

**PERFORMANCE OF CONCRETE BASED WATER FILTRATION
SYSTEM: INFLUENCE OF REDUCED GRAPHENE OXIDE AND
ACCELERATED CARBONATION**

A THESIS

submitted by

MURUGAN M.

for the award of the degree

of

DOCTOR OF PHILOSOPHY



BUILDING TECHNOLOGY AND CONSTRUCTION MANAGEMENT DIVISION

DEPARTMENT OF CIVIL ENGINEERING

INDIAN INSTITUTE OF TECHNOLOGY MADRAS

JULY 2017

THESIS CERTIFICATE

This is to certify that the thesis titled “**PERFORMANCE OF CONCRETE BASED WATER FILTRATION SYSTEM: INFLUENCE OF REDUCED GRAPHENE OXIDE AND ACCELERATED CARBONATION**”, submitted by **Murugan M.**, to the Indian Institute of Technology Madras, Chennai for the award of the degree of **Doctor of Philosophy**, is a bona fide record of the research work done by him under my supervision. The contents of this thesis, in full or in parts, have not been submitted to any other Institute or University for the award of any degree or diploma.

Dr. Manu Santhanam

(Research Guide)

Professor

Department of Civil Engineering

Indian Institute of Technology Madras

Chennai, Tamil Nadu 600 036, India

Place: Chennai

Date: 05 July 2017

ACKNOWLEDGEMENT

I am thankful to my research guide Prof. Manu Santhanam, Department of Civil Engineering, IIT Madras for his constant encouragement and valuable guidance throughout my research work.

I am extremely grateful to Prof. Surendra P. Shah (Northwestern University, USA), Prof. T. Pradeep (IIT Madras), Prof. Ravindra Gettu (IIT Madras), and Dr. Mathava Kumar (IIT Madras) for their valuable suggestions and constructive criticism.

I express my sincere thanks to the doctoral committee members, Prof. Devdas Menon (IIT Madras), Prof. Srinivasan Chandrasekaran (IIT Madras), Dr. Pijush Ghosh (IIT Madras) and Dr. Radhakrishna G. Pillai (IIT Madras) for their suggestions regarding various aspects of my research work.

My sincere thanks to Prof. S.R. Gandhi (former), Prof. A. Meher Prasad (former) and Prof. K. Ramamurthy (current), Head of the Civil Engineering Department, IIT Madras for providing excellent facilities in the department.

I would like to thank the BTCM office staffs for their timely help. My deepest sense of gratitude to all the supporting staff in the BTCM laboratory for their constant support given to me for the successful completion of my experimental work.

I am thankful to all the Research Scholar and Project Staff of the Metallurgical and Materials Engineering, Civil Engineering (Geotechnical Division, and Environmental and Water Resources Engineering Division) and Chemistry departments of IIT Madras for their help and support.

My sincere thanks to all my friends and fellow BTCM researchers at IIT Madras for their suggestions, discussions and help rendered during different stages of my research work.

This work is dedicated to my family. Without the support of my father Mr. S. Muthu and my elder sister Ms. M. Anandham, my dream of doing Ph.D. at IIT Madras would not have been materialised.

MURUGAN M.

ABSTRACT

Keywords: Porous concrete; pore connectivity; X-ray tomography; acid attack; dissolution and decalcification; alteration phases; hydraulic retention time; chemical precipitation

Fresh and clean water is essential for the survival of human life. In India, the release of industrial effluents into the surface and ground water reserves is increasing significantly. The untreated water from these reserves is found unsafe for human consumption, irrigation and industrial needs. The present study attempted to develop a concrete based water filtration system that can remove the most common and toxic heavy metals, especially lead (Pb^{2+}), from aqueous solutions. This water filtration system was based on porous cement concrete, which allows the water to percolate under gravity through the interconnected voids available inside the porous material. The influence of reduced graphene oxide (rGO), an emerging nanomaterial, on the filtration characteristics was also studied.

Graphene is a 2-dimensional planar sheet of single atom thickness having sp^2 bonded carbon atoms arranged in a honeycomb lattice pattern. In this study, rGO (that has properties close to pristine graphene) was synthesized from natural graphite using modified Hummers' method. The effect of rGO sheets on mechanical properties and microstructure of cement pastes, in comparison to alumina and silica nanoparticles was first evaluated in normal curing conditions as well as in aggressive acidic environment, which is known to cause calcium leaching. The addition of the nanomaterials was able to refine the pore structure of 28-day cured cementitious pastes and also increased the resistance to leaching of cementitious matrix after storage in acidic solution for 28 days.

Next, porous concrete was designed for the controlled levels of permeability similar to the permeability range of conventional sand filters that are used in wastewater treatment plants. The permeability and compressive strength of the porous concrete developed in this study was 7.98 ± 3.83 cm/min and 22.96 ± 0.76 MPa respectively. The size of voids in this concrete was found to fall within 126 μm to 14.8 mm. A 2-dimensional image based approach was followed in this study to determine the size of voids in the porous concrete.

The effect of carbonation on the characteristics of water passed through the porous concrete was then assessed. Tap water, distilled water, dilute solutions containing HCl and NaOH

were passed through the cylindrical porous concrete specimens of size 100×150 mm ($\phi \times H$) after initial curing as well as after an accelerated carbonation exposure. Three water quality indicators such as pH, turbidity and the concentration of calcium ions remaining in the filtrate were analysed. The pH and turbidity of the filtrate were decreased significantly because of concrete carbonation in all the cases. The amount of calcium ions remaining in the filtrate was decreased only in case of distilled and tap water. Aqueous solutions containing lead, cadmium, mercury and chromium were passed through the carbonated porous concretes. Out of the four, lead and cadmium were retained substantially in such concretes because of metal carbonate precipitation. The remaining part of the study was therefore limited to investigating the removal of lead (Pb^{2+}) by the plain and 0.06 wt% rGO modified porous concretes.

After several trials to assess the influence of hydraulic retention time on the efficiency of the filtration process, a filtration system with porous concrete was developed. In this system, three individual cylindrical specimens of size 100×150 mm ($\phi \times H$) were arranged in series with progressively decreasing levels of hydraulic head (30 cm, 7.5 cm and 0 cm). Aqueous solution having lead concentration of 8 mg/L was passed through these concretes under continuous flow for a period of 60 minutes. This filtration arrangement was able to remove nearly 98% of heavy metal (Pb^{2+}) from the acidic aqueous media by chemical precipitation. However, the introduction of rGO was found to have no strong influence on the removal of heavy metal (Pb^{2+}) which may be due to the lesser availability of rGO sheets on the surfaces of the flow channels in porous concrete. A comparison of the costs of the newly developed system with the conventional methods for lead removal was also performed, and thus clearly indicated the porous concrete system presents a cost-effective alternative to the current methods. The easy availability of concrete making materials, as well as the ease of fabrication of such filters makes them a viable solution to the needs of water filtration systems especially in rural areas.

TABLE OF CONTENTS

ACKNOWLEDGEMENT	i
ABSTRACT	ii
LIST OF TABLES	ix
LIST OF FIGURES	x
ABBREVIATIONS	xxii
NOTATION	xxiii
CHAPTER 1	01
INTRODUCTION	01
1.1 Problem statement	01
1.2 Objective and scope	02
1.3 Research methodology	03
1.4 Outline of thesis	06
CHAPTER 2	08
LITERATURE REVIEW	08
2.1 Introduction	08
2.2 Health hazards of heavy metals contamination	08
2.3 Lead contamination in Indian rivers	10
2.4 Porous cement concrete – an overview	11
2.4.1 Brief description.....	11
2.4.2 Typical mixture proportioning	11
2.4.3 Permeability or infiltration rate or percolation rate	16
2.4.4 Pore structure related features inside the material	18
2.4.5 Water filtration performance of porous cement concrete system	20
2.4.6 Sediment blockages inside the porous concrete.....	22
2.5 Phase changes in the cementitious binder exposed to acidic environment	24
2.6 Phase changes in the cementitious binder exposed to CO₂ environment	26
2.7 Graphene, graphene oxide and reduced graphene oxide	28
2.8 Graphene for water purification	30
2.8.1 Heavy metals.....	30
2.8.2 Dyes, radionuclides, pesticides and bacteria.....	32

2.9 Performance of graphene oxide modified cementitious composites	34
2.10 Summary of literature review and research needs.....	38
CHAPTER 3	40
MATERIALS AND METHODS	40
3.1 Introduction	40
3.2 Materials used	40
3.2.1 Cement, aggregate and superplasticizer	40
3.2.2 Reduced graphene oxide, alumina and silica nanoparticles.....	41
3.3 Analysis of water quality	46
3.3.1 pH and turbidity	46
3.3.2 Inductivity coupled plasma – mass spectrometry	48
3.4 Microanalytical studies	50
3.4.1 Scanning electron microscopy and optical microscopy	50
3.4.2 3-D X-ray computed tomography	54
3.4.3 Thermal analysis	60
3.4.4 Nanoindentation	61
3.4.5 Mercury intrusion porosimetry	64
3.4.6 X-ray diffraction	66
3.4.7 Fourier transform infrared spectroscopy	68
3.5 Summary	69
CHAPTER 4	70
EFFECT OF GRAPHENE, ALUMINA AND SILICA NANOPARTILCES	
ON THE PROPERTIES OF OPC PASTE.....	70
4.1 Introduction	70
4.2 Specimen preparation	70
4.3 Experimental program.....	72
4.4 Analysis of pore structure.....	73
4.5 Results and discussion	85
4.5.1 Mini slump spread, mechanical strengths and water sorptivity test	85
4.5.2 Alterations in the pore structure.....	87
4.5.3 Scanning electron microscopy images	90
4.6 Summary	95

CHAPTER 5	96
EFFECT OF GRAPHENE, ALUMINA AND SILICA NANOPARTICLES ON THE DETERIORATION CHARACTERISTICS OF OPC PASTE EXPOSED TO ACIDIC ENVIRONMENT	96
5.1 Introduction	96
5.2 Acid immersion test	96
5.3 Results and discussion	97
5.3.1 Analysis of phase changes by FTIR and XRD	97
5.3.2 Quantification of phase changes by TGA	101
5.3.3 Pore structure by porosimetry	102
5.3.4 Imaging the alteration phases by optical microscopy and X-ray CT	105
5.3.5 Nanomechanical properties by nanoindentation	111
5.3.6 Microstructural assessment by SEM/EDS	116
5.4 Summary	141
 CHAPTER 6	 142
MIXTURE PROPORTIONING, SPECIMEN PREPARATION AND TESTING OF POROUS CONCRETE	142
6.1 Introduction	142
6.2 Specimen preparation	142
6.3 Experimental program	147
6.3.1 Falling head permeability test	148
6.3.2 Compressive strength test	149
6.3.3 Determination of void size using image analysis approach	149
6.4 Results and discussion	153
6.4.1 Trial based experimental design	153
6.4.2 Properties of porous concrete	155
6.5 Summary	165
 CHAPTER 7	
EFFECT OF CARBONATION ON THE CHARACTERISTICS OF WATER PASSED THROUGH POROUS CONCRETE	166
7.1 Introduction	166
7.2 Accelerated carbonation exposure	169

7.3 Experimental methods	171
7.3.1 Repeat cycle permeability testing	171
7.3.2 Bentonite clay loading test.....	172
7.4 Results and discussion	174
7.4.1 Characteristics of distilled water and tap water, and dilute HCl and NaOH solutions after passage through the porous concrete.....	174
7.4.2 Toxic metal pollutants.....	181
7.4.3 Bentonite clay loading test results	184
7.5 Summary	186
 CHAPTER 8	 188
EFFECT OF REDUCED GRAPHENE OXIDE ON THE FILTRATION PERFORMANCE OF POROUS CONCRETE	188
8.1 Introduction	188
8.2 Specimen preparation	191
8.3 Constant head permeability test	193
8.4 Results and discussion	194
8.4.1 Effect of reduced graphene oxide on the lead removal.....	194
8.4.2 Effect of hydraulic retention time on the lead removal	197
8.5 Proposed design and cost estimate of concrete based water filtration system for heavy metals removal	201
8.5.1 Design and execution of concrete based filtration system to filter the heavy metals from industrial effluents	201
8.5.2 Cost estimation of plain and graphene modified porous concrete	206
8.6 Summary	210
 CHAPTER 9	
CONCLUSIONS	211
9.1 Summary of the project work	211
9.2 Specific conclusions	212
9.2.1 Effect of graphene, alumina and silica nanoparticles on the properties of Portland cement paste.....	212
9.2.2 Effect of graphene, alumina and silica nanoparticles on the deterioration characteristics of Portland cement paste exposed to acidic environment...	213

9.2.3 Design of porous concrete having controlled levels of hydraulic conductivity	213
9.2.4 Effect of carbonation on the characteristics of water percolated through the porous cement concrete	214
9.2.5 Effect of reduced graphene oxide on the filtration performance of concrete based water filtration system.....	215
9.3 Major contributions from this study	215
9.4 Recommendations for further study.....	216
REFERENCES.....	218
LIST OF PAPERS ON THE BASIS OF THIS THESIS.....	236
DOCTORAL COMMITTEE.....	238
CURRICULUM VITAE.....	239

LIST OF TABLES

Table 1.1	Brief descriptions of the major tasks that were involved in the present study	04
Table 2.1	Effect of heavy metals on human health as described by Singh et al. (2011)	09
Table 2.2	Different processes followed to remove the heavy metals from water as described by Singh et al. (2011)	10
Table 2.3	Common aggregate gradings for porous concrete (ASTM C33 2011).....	12
Table 2.4	Typical ranges of material proportions in porous concrete (ACI 522R 2010)	13
Table 2.5	Removal of radionuclides from water using GO/rGO based composites.....	34
Table 3.1	List of important wave numbers that can be detected in the spectra of hydrated cementitious materials (Barnett et al. 2002)	69
Table 4.1	Experimental results of the different pastes that were prepared in the present study	85
Table 4.2	Porosimetry results of the 28-day cured cementitious pastes	87
Table 5.1	Amounts of portlandite, calcite and bound water in the t+0 and t+28 pastes that were calculated from their TGA plots	102
Table 5.2	Pore related features of t+0 and t+28 pastes determined using porosimetry	105
Table 6.1	Details of the different concrete mixes that were prepared for this study	154
Table 7.1	Characteristics of drinking water conforming to IS 10500 (2012)	186
Table 8.1	Estimation of materials cost of 0.06 wt% graphene modified cylindrical porous cement concrete specimen	206
Table 8.2	Cost of filtration arrangement comprising of three numbers of porous concretes (of 0.00157 m ³) exposed to accelerated CO ₂ environment.....	208
Table 8.3	Details of commercially available filtration methods with the porous cement concrete that was proposed in this study.....	209

LIST OF FIGURES

Figure 1.1	Methodology followed in this study.....	06
Figure 2.1	Effect of aggregate size on the pore structure of porous concrete section.....	12
Figure 2.2	Relationship between porosity and paste content of porous concrete (ACI 522R 2010).....	13
Figure 2.3	Relationship between porosity and percolation rate of porous concrete (ACI 522R 2010).....	14
Figure 2.4	Relationship between the compressive strength and porosity (ACI 522R 2010).....	14
Figure 2.5	A sample of fresh porous cement concrete mixture prepared with (a) low, (b) optimum and (c) high amounts of water (Tennis et al. 2004)	15
Figure 2.6	Falling head permeability test set up that is recommended to measure the permeability of porous concrete (Olek et al. 2003).....	16
Figure 2.7	Comparison of the experimentally determined and predicted permeabilities of porous concretes having low and paste content in them (Sumanasooriya and Neithalath 2011)	17
Figure 2.8	Variation of pore area fraction and paste area fraction along the depth of porous concrete section having 19% porosity (Sumanasooriya and Neithalath 2011).....	19
Figure 2.9	Infiltration of stormwater runoff through the interconnected voids available inside the porous concrete pavement	20
Figure 2.10	Schematic illustration of concrete based reactive column that was used for the treatment of acid mine drainage (Shabalala et al. 2017) ...	21
Figure 2.11	Schematic diagram illustrating sediment clogging that is likely to disrupt the water movement in permeable concrete.....	22
Figure 2.12	Flow of steps that were involved in the assessment of pore clogging in the porous concrete pavement by image based approach (Kayhanian et al. 2012)...	23
Figure 2.13	Porosity profile of two different parking lots that were less and highly clogged due to the deposition of fine sediments (Kayhanian et al. 2012)	23
Figure 2.14	Schematic illustration of a cut section of cement paste exposed to HNO ₃ environment (Pavlik 1994)	25
Figure 2.15	Schematic diagram showing the evolution of a thin layer of calcite on a portlandite substrate in a moist environment (Galan et al. 2015)	27
Figure 2.16	Graphene, the building block of other carbon allotropes that include 0-D fullerene, 1-D carbon nanotube and 3-D graphite (Geim and Novoselov 2007).....	28

Figure 2.17	Schematic illustration of the synthesis of reduced graphene oxide using modified Hummers' method	29
Figure 2.18	Kinetics of Hg(II) adsorption by different adsorbents (Sreeprasad et al. 2011) .	31
Figure 2.19	Schematics illustrating the possible interactions between (a) GO – MB (b) GO – MV (c) GO – Rhodamine B (RB) and (d) RGO – OG dyes (Ramesha et al. 2011).....	33
Figure 2.20	Schematic representation of the reaction between the –COOH groups of graphene and hydration products of cement (Pan et al. 2015).....	35
Figure 2.21	SEM images of 28-day cured cementitious pastes modified using (a) 0.01 wt% and (b) 0.05 wt% GO sheets in them respectively (Lv et al. 2014)	36
Figure 2.22	AFM image illustrating the plain and GO modified cementitious mortar (Horszczaruk et al. 2015)	37
Figure 2.23	Modulus of elasticity of the plain and GO modified cementitious mortar that was determined using AFM technique (Horszczaruk et al. 2015)	37
Figure 3.1	Particle size distribution of coarse aggregate that was used in the preparation of porous concrete modified using graphene nanosheets.....	41
Figure 3.2	EDS spectra showing the presence of different elements in the reduced graphene oxide, alumina and silica nanoparticles	42
Figure 3.3	Micrograph illustrating the agglomerated reduced graphene oxide sheets that were synthesized in this study using modified Hummers' method.....	42
Figure 3.4	Micrograph illustrating the agglomerated alumina nanoparticles that were procured from Sigma Aldrich, India	43
Figure 3.5	Micrograph illustrating the agglomerated silica nanoparticles that were procured from Sigma Aldrich, India	43
Figure 3.6	TEM image of reduced graphene oxide, indicating a wrinkled surface texture.....	45
Figure 3.7	Graphene oxide and reduced graphene oxide; both were dissolved in distilled water	46
Figure 3.8	General scheme of infrared Turbidimeter	47
Figure 3.9	CyberScan pH 510 Meter and the standard calibration solutions having pH 4.01, 7 and 10.01 that were used in this study.....	47
Figure 3.10	Eutech TN 100 IR Turbidimeter and the standard calibration solutions having turbidity of 800 NTU, 100 NTU, 20 NTU and 0.02 NTU that were used in this study	48
Figure 3.11	Schematic diagrams illustrating the layout of ICP – MS ..	49
Figure 3.12	Photograph of ICP – MS that was used in this study	49
Figure 3.13	Layout of Emcrafts Genesis 2100 Scanning Electron Microscope.....	51

Figure 3.14	Micrograph illustrating the fractured surface of 3-day cured cementitious matrix modified using 0.06 wt% reduced graphene oxide sheets	52
Figure 3.15	Micrograph illustrating the fractured surface of 7-day cured cementitious matrix modified using 0.06 wt% reduced graphene oxide sheets	52
Figure 3.16	Emcrafts Genesis 2100 Scanning Electron Microscope that was used in this study	53
Figure 3.17	Olympus BX41 optical microscope that was used in this study	54
Figure 3.18	Photograph and general scheme of the GE phoenix v tome x s X-ray computed tomography instrument that was used in this study.....	55
Figure 3.19	Isosurface image of cement paste sample illustrating the entrapped air voids and the solid phase revealed by X-ray CT.....	57
Figure 3.20	Isosurface image of porous concrete illustrating the interconnected and entrapped voids and the solid phase revealed by X-ray CT.....	58
Figure 3.21	Volume rendered view of cement paste sample illustrating the different volume of voids that were present inside the matrix after curing for 3 days	59
Figure 3.22	Photograph and general scheme of power compensated type DSC	60
Figure 3.23	TGA plot of 28-day cured cement paste sample that was prepared using a w/c ratio of 0.32.....	61
Figure 3.24	Schematic illustration of the elastic-plastic deformation in the material which occurs due to indentation.....	62
Figure 3.25	Hysitron TI Premier Nanoindenter.....	63
Figure 3.26	Micrograph illustrating the Berkovich tip.....	63
Figure 3.27	Indent on the surface of ceramic sample left by a Berkovich tip.....	64
Figure 3.28	Thermo Scientific Pascal 140/440 series Mercury intrusion porosimetry instrument that was used in this study.....	65
Figure 3.29	Identification of major characteristics like threshold diameter, most likely diameter and total percolated pore volume from the MIP plot	66
Figure 3.30	Bruker D8 Model X-ray diffraction instrument that was used in this study	67
Figure 3.31	PerkinElmer Spectrum One FTIR instrument that was used in this study.....	68
Figure 4.1	Different solutions containing graphene, alumina and silica nanoparticles and DLS test result of those solutions.....	71
Figure 4.2	Mini slump spread and water sorptivity test	72
Figure 4.3	Reconstructed and isosurface CT image of the control paste of size 10 × 10 × 10 mm and their greyscale histograms	74
Figure 4.4	Reconstructed 3-D CT image and its transparent view illustrating the presence of voids in the control paste specimen of 10 × 10 × 10 mm	75
Figure 4.5	Reconstructed 3-D CT image and its transparent view illustrating the presence of voids in the RGO paste specimen of 10 × 10 × 10 mm	76

Figure 4.6	Reconstructed 3-D CT image and its transparent view illustrating the presence of voids in the Al ₂ O ₃ paste specimen of 10 × 10 × 10 mm.....	77
Figure 4.7	Reconstructed 3-D CT image and its transparent view illustrating the presence of voids in the SiO ₂ paste specimen of 10 × 10 × 10 mm.....	78
Figure 4.8	Transparent view of the CT image illustrating the presence of different sizes of spherical shaped air void inside the cementitious matrix.....	79
Figure 4.9	Colour-coded 3-D CT images of the cement paste obtained before and after porosity analysis using the software VGStudio Max	80
Figure 4.10	Colour-coded 3-D CT images illustrating the presence of voids having volume in between 0.07 mm ³ to 0.75 mm ³ in the paste specimens	81
Figure 4.11	Colour-coded 3-D CT images illustrating the presence of voids having volume in between 0.01 mm ³ to 0.75 mm ³ in the paste specimens	82
Figure 4.12	Closer view of the analysed CT image illustrating the rainbow colours attributed to the voids having different volume in the cementitious matrix	83
Figure 4.13	Closer view of the analysed CT image illustrating the interconnected voids inside the cementitious matrix.....	83
Figure 4.14	Closer view of the analysed CT image illustrating the entrapped air void having irregular and rough texture	84
Figure 4.15	Closer view of the analysed CT image illustrating the presence of different sizes of spherical voids in the cementitious matrix.....	84
Figure 4.16	Micrograph illustrating the presence of poorly dispersed silica nanoparticles in the cementitious matrix	86
Figure 4.17	Distribution of void sizes in the control paste after curing for 28 days	88
Figure 4.18	Distribution of void sizes in the RGO paste after curing for 28 days	88
Figure 4.19	Distribution of void sizes in the Al ₂ O ₃ paste after curing for 28 days.....	89
Figure 4.20	Distribution of void sizes in the SiO ₂ paste after curing for 28 days.....	89
Figure 4.21	Micrograph illustrating the fractured surface of 28-day cured control paste.....	90
Figure 4.22	Micrograph illustrating the morphology of C-S-H in the control paste after curing for 28 days	90
Figure 4.23	Micrograph illustrating the presence of graphene sheet in the RGO paste	91
Figure 4.24	Micrograph showing the presence of hexagonal crystals in the RGO paste	92
Figure 4.25	Micrograph illustrating the presence of needle like crystals in the RGO paste	92
Figure 4.26	Micrograph showing the formation of thick rod shaped crystals in the Al ₂ O ₃ paste	93
Figure 4.27	Micrograph illustrating the cloud like calcium silicate hydrate in the Al ₂ O ₃ paste	93

Figure 4.28	Micrograph illustrating the C-S-H having homogeneous texture and the growth of needle shaped crystals from such hydrate in the SiO ₂ paste.....	94
Figure 5.1	Mid-infrared spectra of the t+0, t+10 and t+28 control paste	97
Figure 5.2	Mid-infrared spectra of the t+0, t+10 and t+28 RGO paste	97
Figure 5.3	Mid-infrared spectra of the t+0, t+10 and t+28 Al ₂ O ₃ paste	98
Figure 5.4	Mid-infrared spectra of the t+0, t+10 and t+28 SiO ₂ paste	98
Figure 5.5	XRD pattern of the t+0, t+10 and t+28 control paste.....	99
Figure 5.6	XRD pattern of the t+0, t+10 and t+28 RGO paste.....	99
Figure 5.7	XRD pattern of the t+0, t+10 and t+28 Al ₂ O ₃ paste	100
Figure 5.8	XRD pattern of the t+0, t+10 and t+28 SiO ₂ paste	100
Figure 5.9	TGA pattern of the t+0 pastes	101
Figure 5.10	TGA pattern of the t+28 pastes	101
Figure 5.11	Porosimetry result of t+0 and t+28 control paste	103
Figure 5.12	Porosimetry result of t+0 and t+28 RGO paste	103
Figure 5.13	Porosimetry result of t+0 and t+28 Al ₂ O ₃ paste.....	104
Figure 5.14	Porosimetry result of t+0 and t+28 SiO ₂ paste.....	104
Figure 5.15	Digital photographs illustrating the cut sections of t+0, t+28 and t+56 pastes.....	106
Figure 5.16	Optical micrographs illustrating the degraded zone in the t+28 pastes	107
Figure 5.17	Optical micrograph of pastes showing the alteration phases and cracks that were formed in their matrices.....	108
Figure 5.18	CT images illustrating the alteration phases and cracks that were formed in the control paste after storage in HNO ₃ solution for a period of 28 days	109
Figure 5.19	CT slice showing the location of degradation front in the t+28 pastes	110
Figure 5.20	Optical micrograph illustrating the polished section of the control paste.....	111
Figure 5.21	Micrograph showing the polished section of grey zone in the control paste	112
Figure 5.22	Scanning probe microscopy image illustrating the depth of indentation in the polished surfaces of control paste	112
Figure 5.23	SPM image illustrating the indentation performed in the polished surface of control paste	113
Figure 5.24	SPM image illustrating the five numbers of indentation that were performed in the polished surface of control paste for estimating the statistical variance	113
Figure 5.25	Schematic diagram illustrating the different zones which are likely to be formed in the hardened cement paste after storage in HNO ₃ solution.....	114
Figure 5.26	Load versus depth of indentation curve of the different zones in the control paste after storage in 0.5 M HNO ₃ solution for a period of 28 days.....	114

Figure 5.27	Young's modulus and hardness of the t+0 paste and different zones in the t+28 pastes determined using nanoindentation technique.....	115
Figure 5.28	Line scan result showing the distribution of major elements in the cut section of control paste (t+28).....	116
Figure 5.29	Low and high magnification SEM images illustrating the alteration phases in the transition zone of control paste (t+28).....	117
Figure 5.30	EDS result of the alteration phases in the control paste (t+28).....	118
Figure 5.31	Micrograph illustrating the formation of long crack between the degraded layer and unaffected material (t+28)	118
Figure 5.32	Micrographs illustrating the different zones that were formed in the control paste after storage in 0.5 M HNO ₃ solution for a period of 28 days.....	119
Figure 5.33	EDS spectra of the different zones in the t+28 paste	120
Figure 5.34	Micrograph illustrating the presence of graphene sheets in the transition zone of RGO paste (t+28)	121
Figure 5.35	Micrograph illustrating the presence of thick, acicular crystals in the transition zone of RGO paste (t+28)	121
Figure 5.36	Micrograph and EDS result of the alteration phases that were formed in the transition zone of RGO paste (t+28)	122
Figure 5.37	Micrograph illustrating the formation of cracks in the grey zone of t+56 paste (RGO) which could be due to the effect of decalcification induced shrinkage.....	123
Figure 5.38	Micrograph illustrating the alteration phases that were formed in the transition zone of RGO paste (t+56)	123
Figure 5.39	Micrograph illustrating the formation of prismatic crystals in the degraded layer of RGO paste (t+56)	124
Figure 5.40	Micrograph illustrating the presence of dendritic cluster crystals in the degraded layer of RGO paste (t+56)	124
Figure 5.41	Micrograph illustrating the presence of alteration phases having different morphology in the RGO paste (t+56).....	125
Figure 5.42	Micrograph illustrating the growth of dendritic cluster shaped crystals matured from the prismatic shaped compounds in the RGO paste (t+56).....	125
Figure 5.43	Micrograph and EDS result of the prismatic compounds that were formed in the transition zone of RGO paste (t+56).....	126
Figure 5.44	Micrograph and EDS result of the dendritic compounds that were formed in the transition zone of RGO paste (t+56).....	127
Figure 5.45	Micrograph and EDS result of the grey zone in the Al ₂ O ₃ paste (t+28)	128
Figure 5.46	Micrograph illustrating the degraded layer in the Al ₂ O ₃ paste (t+28)	129
Figure 5.47	EDS result of the degraded layer in the Al ₂ O ₃ paste (t+28).....	130

Figure 5.48	Micrograph illustrating the formation of needle like compounds in the transition zone of the Al ₂ O ₃ paste (t+28)	130
Figure 5.49	Micrograph and EDS result illustrating the plate like crystalline compounds that were formed in the transition zone of Al ₂ O ₃ paste (t+28).....	131
Figure 5.50	Micrographs illustrating the presence of voids in the Al ₂ O ₃ paste (t+28)	132
Figure 5.51	Micrograph and EDS result illustrating the formation of prismatic crystals inside the void of Al ₂ O ₃ paste (t+28)	133
Figure 5.52	Low and high magnification SEM images illustrating the presence of agglomerated silica nanoparticles in the SiO ₂ paste (t+28).....	134
Figure 5.53	EDS result illustrating the presence of agglomerated silica particles in the cut section of SiO ₂ paste (t+28).....	135
Figure 5.54	Micrograph illustrating the formation of alteration phases in the transition zone of SiO ₂ paste (t+28)	135
Figure 5.55	Micrograph illustrating the presence of spherical particles and radiated, thin plate like compounds in the transition zone of SiO ₂ paste (t+28).....	136
Figure 5.56	Micrograph illustrating the closer view of the non-uniform, radiated leaf like compounds that were formed in the transition zone of SiO ₂ paste (t+28) .	136
Figure 5.57	Micrograph and EDS result illustrating the closer view of the alteration phases that were formed in the transition zone of SiO ₂ paste (t+28).....	137
Figure 5.58	Micrograph illustrating the poorly dispersed silica nanoparticles in the transition zone of SiO ₂ paste (t+28)	138
Figure 5.59	Micrograph illustrating the formation of well defined, prismatic crystals in the transition zone of SiO ₂ paste (t+28)	138
Figure 5.60	Micrograph illustrating the formation of spherical crystals in the transition zone of SiO ₂ paste (t+28)	139
Figure 5.61	Micrograph illustrating the formation of thin plate like and spherical crystalline compounds in the transition zone of SiO ₂ paste (t+28).....	139
Figure 5.62	Micrograph and EDS result of the spherical crystals having cavity in the middle of its structure in the SiO ₂ paste (t+28).....	140
Figure 6.1	Aggregates of different sizes were separated using standard set of sieves conforming to IS 460-1 (1985).....	143
Figure 6.2	Dry blending the cement and aggregate in a laboratory concrete mixer.....	143
Figure 6.3	Each layer in the concrete specimen was filled by weighing the fresh concrete and then poured inside the cylindrical shaped iron mould	144
Figure 6.4	Consolidation was done using Marshall hammer having foot diameter, drop weight and free fall of 98.4 mm, 4.54 kg and 457 mm respectively	144
Figure 6.5	A collar arrangement was fixed to consolidate the top concrete layer that was poured inside the cylindrical shaped iron mould	145

Figure 6.6	Top concrete layer was levelled and finished using a hand-held metal float....	145
Figure 6.7	Mass of fresh and hardened porous concrete including mould was measured using a weigh balance of 0.01 g accuracy for density calculation	146
Figure 6.8	Porous concrete specimens of size 100 × 200 mm demolded after 24 hours from the mixing time of ingredients.....	146
Figure 6.9	Porous concrete specimens were cured in tap water for a period of 7 days before testing	147
Figure 6.10	Non-permeable top and bottom concrete edges of about 25 mm thick in the specimen were removed using diamond-tipped saw ...	147
Figure 6.11	Porous concrete specimens of size 100 × 150 mm after sectioning using Diamond-tipped saw	148
Figure 6.12	Determination of permeability of porous concrete using falling head permeability test set up which is similar to the set up suggested by Sonebi and Bassuoni (2013).....	148
Figure 6.13	Schematic diagram illustrating the series of steps that were followed to analyse the CT slice using image analysis software	150
Figure 6.14	Feret diameter measurement of the polygons in the 2-D CT slice of the porous cement concrete	151
Figure 6.15	Plain and analysed CT image obtained from the software Image Pro Premier 9.1	152
Figure 6.16	A typical slice from the CT and the void related features that were determined using image analysis approach	153
Figure 6.17	3-D CT image of the porous concrete specimen which was reconstructed using the software named VolumeGraphics Studio Max 2.2.....	155
Figure 6.18	3-D Reconstructed CT image which was sectioned along horizontal and vertical axis and then processed to delineate the voids inside the material using the software VolumeGraphics Studio Max 2.2	156
Figure 6.19	3-D Reconstructed CT image randomly sectioned along the primary axes and then processed to clearly illustrate the porous structure inside the material.....	157
Figure 6.20	3-D Reconstructed CT image sectioned out into a cuboid and then processed to show the porous structure inside the material	158
Figure 6.21	Closer view of the CT image illustrating the co-existence of interconnected and disconnected voids inside the porous concrete specimen.....	159
Figure 6.22a	Porosity profiles of three M ₅ category porous concrete specimens of size 40 × 100 mm	160
Figure 6.22b	Porosity profiles of the remaining M ₅ category concrete specimens of size 40 × 100 mm	161

Figure 6.23	3-D Reconstructed CT image illustrating the aggregates of different sizes that were packed inside the porous concrete specimen	162
Figure 6.24	Selective chemical attack of the porous concrete specimen by storage in 0.5 M HNO ₃ solution	163
Figure 6.25	Comparison of permeability of M ₅ specimens with the existing literature.....	164
Figure 7.1	Alteration in the pH of distilled water which was used for storage	166
Figure 7.2	Alteration in the turbidity of distilled water which was used for storage	167
Figure 7.3	Phase alteration which is likely to occur in the flow channels of porous cement concrete when exposed to carbon dioxide from the atmosphere.....	168
Figure 7.4	Carbonation test chamber that was used in this study.....	169
Figure 7.5	Micrograph illustrating the presence of Ca(OH) ₂ and calcite crystals in the fractured surface of porous concretes after initial curing as well as after an accelerated carbonation exposure	170
Figure 7.6	Schematic illustration of the repeat cycle permeability testing of cylindrical porous concrete specimen of size 100 × 150 mm	171
Figure 7.7	Schematic illustration of the highly turbid solution passed through the porous concrete specimen mounted in the permeability test set up	172
Figure 7.8	Particle size distribution of dry bentonite clay and the highly turbid bentonite containing solution that was prepared for this study	173
Figure 7.9	Alteration in the pH of distilled water passed through the porous concrete after initial curing as well as after an accelerated carbonation exposure, for ten repeat cycles.....	174
Figure 7.10	Alteration in the pH of tap water passed through the porous concrete after initial curing as well as after an accelerated carbonation exposure, for ten repeat cycles.....	174
Figure 7.11	Alteration in the turbidity of distilled water passed through the porous concrete after initial curing as well as after an accelerated carbonation exposure, for ten repeat cycles	175
Figure 7.12	Alteration in the turbidity of tap water passed through the porous concrete after initial curing as well as after an accelerated carbonation exposure, for ten repeat cycles.....	175
Figure 7.13	Calcium ions remaining in the filtrate obtained through the porous concrete specimens tested using distilled water, after initial curing as well as after an accelerated carbonation exposure, for ten repeat cycles	176
Figure 7.14	Calcium ions remaining in the filtrate obtained through the porous concrete specimens tested using tap water, after initial curing as well as after an accelerated carbonation exposure, for ten repeat cycles	176

Figure 7.15	Alteration in the pH of dilute HCl solution passed through the porous concrete after initial curing as well as after an accelerated carbonation exposure, for ten repeat cycles	177
Figure 7.16	Alteration in the pH of dilute NaOH solution passed through the porous concrete after initial curing as well as after an accelerated carbonation exposure, for ten repeat cycles	177
Figure 7.17	Alteration in the turbidity of dilute HCl solution passed through the porous concrete after initial curing as well as after an accelerated carbonation exposure, for ten repeat cycles	178
Figure 7.18	Alteration in the turbidity of dilute NaOH solution passed through the porous concrete after initial curing as well as after an accelerated carbonation exposure, for ten repeat cycles	178
Figure 7.19	Calcium ions remaining in the filtrate obtained through the porous concrete specimens tested using dilute HCl solution, after initial curing as well as after an accelerated carbonation exposure, for ten repeat cycles	179
Figure 7.20	Calcium ions remaining in the filtrate obtained through the porous concrete specimens tested using dilute NaOH solution, after initial curing as well as after an accelerated carbonation exposure, for ten repeat cycles	179
Figure 7.21	Chromium ions remaining in the filtrate obtained through the porous concrete specimens after accelerated carbonation exposure tested using the solution containing potassium dichromate	181
Figure 7.22	pH (of filtrate) and mercury ions remaining in the filtrate obtained through the porous concrete specimens after accelerated carbonation exposure tested using the solution containing mercuric chloride	182
Figure 7.23	pH (of filtrate) and cadmium ions remaining in the filtrate obtained through the porous concrete specimens after accelerated carbonation exposure tested using the solution containing cadmium sulfate	182
Figure 7.24	pH (of filtrate) and lead ions remaining in the filtrate obtained through the porous concrete specimens after accelerated carbonation exposure tested using the solution containing lead nitrate	183
Figure 7.25	Change in the turbidity of bentonite containing solution after percolation through the porous concrete specimen that was reused for ten times	184
Figure 7.26	Permeability of the porous concrete specimen, measured after each passage of the bentonite containing solution	184
Figure 7.27	Schematic diagram illustrating the bentonite particles that were physically trapped inside the tortuous, interconnected voids of the porous cement concrete	185

Figure 8.1	Schematic illustration of the presence of graphene nanosheets, carbonate and hydroxyl species along the flow channels of porous cement concrete.....	189
Figure 8.2	Schematic illustration of the lead removal by porous concrete (a) presence of $\text{Ca}(\text{OH})_2$ and CaCO_3 on the pore channel surfaces (b-d) passage of $\text{Pb}(\text{NO}_3)_2$ solution through the flow channels results in the precipitation of lead hydroxide and lead carbonate	190
Figure 8.3	Sonication was done to the solution containing graphene using Sonics VCX-750 Vibra Cell Ultra Sonic Processor mode probe sonicator and freshly prepared graphene modified porous concrete mixture.....	191
Figure 8.4	Micrograph illustrating the binder surface in the 7-day cured porous cement concrete.....	192
Figure 8.5	Micrograph illustrating the binder surface in the porous concrete after an accelerated carbonation exposure.....	192
Figure 8.6	Constant head permeability testing of porous concrete	193
Figure 8.7	Lead ions remaining in the filtrate after passage of lead nitrate solution through the 7-day cured control and RGO specimens maintained with a constant head of 30 cm.....	194
Figure 8.8	Lead ions remaining in the filtrate after passage of lead nitrate solution through the carbonated control and RGO specimens maintained with a constant head of 30 cm.....	195
Figure 8.9	Lead ions desorbed in the filtrate after subsequent passage of distilled water through the 7-day cured control and RGO specimens maintained with a constant head of 30 cm.....	195
Figure 8.10	Lead ions desorbed in the filtrate after subsequent passage of distilled water through the carbonated cured control and RGO specimens maintained with a constant head of 30 cm	196
Figure 8.11	Lead ions remaining in the filtrate after passage of first filtrate through the 7-day cured control and RGO specimens maintained with a constant head of 30 cm	197
Figure 8.12	Lead ions remaining in the filtrate after passage of first filtrate through the carbonated control and RGO specimens maintained with a constant head of 30 cm	198
Figure 8.13	Lead ions remaining in the filtrate after passage of first filtrate through the 7-day cured control and RGO specimens maintained with a constant head of 7.5 cm.....	198
Figure 8.14	Lead ions remaining in the filtrate after passage of first filtrate through the carbonated control and RGO specimens maintained with a constant head of 7.5 cm	199

Figure 8.15	Lead ions remaining in the filtrate after passage of second filtrate through the 7-day cured control and RGO specimens tested with a trickling head of aqueous solution.....	200
Figure 8.16	Lead ions remaining in the filtrate after passage of second filtrate through the carbonated control and RGO specimens tested with a trickling head of aqueous solution.....	200
Figure 8.17	Filtration arrangement illustrating the series of porous concretes with decreasing levels of hydraulic head for the purpose of removing heavy metals from aqueous solutions	202
Figure 8.18	Lead ions remaining in the filtrate after passage of solution having lead concentrations of 9.4 mg/L through the 7-day cured control and RGO specimens maintained with a trickling head of solution.....	203
Figure 8.19	Lead ions remaining in the filtrate after passage of solution having lead concentrations of 9.4 mg/L through the carbonated cured control and RGO specimens maintained with a trickling head of solution.....	203
Figure 8.20	Industries that are major sources of lead containing effluents	204
Figure 8.21	Schematic illustration of the treatment process which is proposed to filter the heavy metals and suspended particles from the industrial effluent.....	205

LIST OF ABBREVIATIONS

w/c	water to cement ratio
P	Portlandite
AFm	Monosulfate
AFt	Ettringite
CSH	Calcium silicate hydrate
CH	Calcium hydroxide
RH	Relative humidity
PCE	Polycarboxylate ether
XRD	X-ray diffraction
SEM	Scanning electron microscopy
EDS	Energy dispersive spectroscopy
OM	Optical microscopy
CT	Computed tomography
TG / DSC	Thermo gravimetric / differential scanning calorimetry
ICP-MS	Inductivity coupled plasma – mass spectrometry
TGA	Thermo gravimetric analysis
SPM	Scanning probe microscopy
MIP	Mercury intrusion porosimetry
FTIR	Fourier transform infrared spectroscopy
NI	Nanoindentation
NTU	Nephelometric turbidity unit
M	Molarity
C	Calcite
C ₃ S	Tricalcium silicate
C ₂ S	Dicalcium silicate
GSV	Greyscale value
OPC	Ordinary Portland cement
SE / BSE	Secondary electron / back scattered electron mode

LIST OF NOTATIONS

SiO_2	Silica nanoparticles
Al_2O_3	Alumina nanoparticles
rGO	Reduced graphene oxide
GO	Graphene oxide
HNO_3	Nitric acid
RGO	Porous concrete modified using reduced graphene oxide
\varnothing	Diameter
E	Young's modulus
H	Hardness
$\text{Pb}(\text{NO}_3)_2$	Lead (II) nitrate
2-D / 3-D	2-dimensional / 3-dimensional
t+0	Cement paste specimen that was cured for 28 days
t+10	t+0 specimens after storage in HNO_3 solution for 10 days
t+28	t+0 specimens after storage in HNO_3 solution for 28 days
t+56	t+0 specimens after storage in HNO_3 solution for 56 days

CHAPTER 1

INTRODUCTION

1.1 PROBLEM STATEMENT

In India, rapid industrialization due to unplanned growth is severely polluting the land, water and air. The discharge of toxic heavy metals from different sources such as mining, battery manufacturing, electroplating, galvanizing and rubber processing, copper picking, paint and pigment producing and agricultural practices resulting in the discharge of fertilizer and pesticides into the surface waters are increasing substantially. The heavy metals mainly present in these sources include lead, cadmium, copper, chromium, nickel and zinc. Water containing these heavy metals is unsafe for human consumption and the intake of such heavy metals may affect the central nervous system, modify the blood composition, and cause severe damage to liver, kidney, lungs and other vital organs. According to IS 10500 (2012), the maximum permissible limit of Pb, Cd, Cu and Zn in drinking water is 10 µg/L, 3 µg/L, 50 µg/L and 5000 µg/L. In 2014, Central Water Commission, Govt. of India conducted survey on the quality of major Indian rivers and thereby found the Pb, Cd and Cu concentration in Ramganga (48.92 µg/L), Yamuna (4 µg/L Cd) and Rapti (180.7 µg/L), respectively had exceeded the desirable limits. However, the Zn concentration was reported to be within the limits (Status of Trace and Toxic Metals in Indian Rivers 2014).

The conventional treatment methods that are practiced in the industries for the removal of heavy metals include adsorption, precipitation, ion exchange, oxidation, reduction, electrolysis and reverse osmosis. However, the major drawbacks that affect the practice of those treatment methods are high initial capital cost, operational and maintenance costs. These drawbacks can be overcome by developing new methods and materials for water filtration, which can be made with inexpensive and locally available ingredients.

The easy access to concrete making materials and the ease of fabrication in concrete makes it a possible candidate for the development of water filtration systems. Enhanced porosity concrete or porous concrete, is a way forward in this regard. Applications of porous cement concrete in the form of parking lots, green house floors, tennis courts, zoo areas, low volume

roads, patios, shoulders, noise barriers, slope stabilization, drains, swimming pool decks and friction course for pavements are increasing significantly.

United States Environmental Protection Agency has recognized that porous concrete is a good option among other stormwater management practices. Apart from managing the stormwater, porous concrete also decreases the urban heat island effect, ground water contamination and vehicular noise substantially. The flow channels in porous concrete, which is highly alkaline, can retain the heavy metals from the aqueous solution after passage, and thereby causes such metals to precipitate within the matrix of the porous material. These channels can also physically trap the motor oil, suspended solids, and nitrogen and phosphorus which cause the eutrophication problem in lakes and rivers (Brown et al. 2011, Lee et al. 2013, Park and Tia 2004).

Graphene, graphene oxide, and graphene oxide based nanocomposites are extensively studied in the existing literature because of their super adsorbing behaviour towards a wide variety of toxic contaminants such as fertilizer, dyes, pesticides and heavy metals such as mercury, arsenic, lead and cadmium present in the aqueous solutions.

The present study attempts to develop a concrete based water filtration system that can retain the heavy metals from the industrial effluent. Although the characteristics of water obtained through the porous concrete have been studied earlier, the utility of such concretes for water filtration is still not clearly understood, as several challenges exist in this regard, including (i) its filtration mechanism with respect to certain metal contaminants, (ii) chemical degradation because of its contact with the aggressive aqueous media, (iii) concrete carbonation and (iv) sediment blockage.

Further, the addition of nanomaterials such as reduced graphene oxide (rGO) into the porous concrete matrix and its effect on the filtration performance needs to be examined to explore the potential for such systems to be used in the field of water treatment.

1.2 OBJECTIVES AND SCOPE

The objectives of this study are three-fold:

- Investigation of the influence of reduced graphene oxide on the properties of Portland cement paste in comparison to alumina and silica nanoparticles.

- Design and preparation of porous cement concrete having controlled levels of hydraulic conductivity desired for water filtration purposes.
- Investigation of filtration of toxic heavy metals through the porous cement concrete modified using reduced graphene oxide.

Materials in this study are restricted to one cement (ordinary Portland cement 53 grade), one coarse aggregate (crushed granite), and three nanomaterials such as reduced graphene oxide, alumina and silica nanoparticles. The scope of this study is limited to investigate the removal of heavy metals, especially lead (Pb^{2+}) by the plain and 0.06 wt% rGO modified porous cement concretes, which are designed to have the filtration rate similar to the sand filters used in water and wastewater treatment plant. X-ray computed tomography scans are performed to analyse the pore related properties such as voids size and surface porosity of plain porous concrete. The water quality tests are limited to pH, turbidity, and concentration of calcium and lead ions remaining in the filtrate after passage through the plain porous concrete.

This study is restricted to 3-dimensional image analysis technique and mercury intrusion porosimetry to analyse the pore structure of 28-day cured OPC (ordinary Portland cement) pastes modified using 0.02 wt% rGO, 0.2 wt% alumina and 4 wt% silica nanoparticles, which are compared with the control mix. All these four pastes are prepared with a w/c ratio and polycarboxylate ether (PCE) based superplasticizer of 0.32 and 0.05 wt% respectively. Furthermore, the deterioration characteristics of those four pastes after storage in acidic solution for 28 and 56 days are analysed using characterisation techniques, which are limited to Fourier transform infrared spectroscopy (FTIR), X-ray diffraction (XRD), thermogravimetric analysis (TGA), mercury intrusion porosimetry (MIP), optical microscopy (OM), 3-D X-ray computed tomography (CT), scanning electron microscopy (SEM) and nanoindentation.

1.3 RESEARCH METHODOLOGY

The present study was limited to investigate the Pb removal in plain and rGO modified porous concrete systems. The Pb containing solution is acidic and thereby it can deteriorate the binder phase (alkaline in nature) in such concretes. Thus, the role of rGO in the binder phase exposed to highly aggressive acidic environments needs to be studied prior to the investigation on the Pb removal in porous concrete systems. In regards to this, the research

methodology of the present study was divided into two levels, namely, investigations on the effect of rGO nanosheets (which is also referred as ‘graphene’ in this study) in cement paste, and then investigations related to the Pb removal (filtration performance) in rGO modified porous concrete. The methodology of these two levels is described in Table 1.1 and then pictorially illustrated in Figure 1.1 and Figure 1.2.

Table 1.1 Brief descriptions of the major tasks that were involved in the present study

Tasks involved	Brief description of the task
Level I	
Influence of rGO on the properties of cement paste	The effect of graphene, alumina and silica nanoparticles on the properties of Portland cement paste were studied by performing tests such as compressive and flexural strength, and water sorptivity test. Additionally, the effect of these nanomaterials on the pore structure of cement paste was analysed using MIP and 3-D imaging with X-ray CT.
Deterioration characteristics of rGO modified cement paste	The nanomaterial (graphene, alumina and silica nanoparticles) - modified cementitious pastes were exposed to acidic environment for 56 days. The rate of deterioration after acid storage was assessed at different time periods using MIP and TGA respectively. Additionally, the alteration phases in the cut section of the degraded pastes were imaged using SEM/EDS, OM and X-ray CT.
Level II	
Preparation of porous concrete having controlled levels of hydraulic conductivity	In the level II, the porous concrete desired for water filtration was developed and then the characteristics of filtrate after passage were analysed. Finally, the Pb removal in rGO modified porous concrete was investigated. ACI 522R (2010) has reported the typical mixture proportions of porous concrete. Trial based experimental design was followed in this study for proportioning the porous concrete mixture. Next, the preparation procedure of porous concrete was marginally modified from the ACI procedure, to attain a porous

	concrete mixture with controlled levels of hydraulic conductivity which could be desired for water filtration purposes.
Determination of the properties of porous concrete	The essential features of porous concrete system such as void size and its distribution, permeability, density and compressive strength were determined. The connected voids inside such porous material was imaged by X-ray CT.
Effect of carbonation on the quality of water passed through the porous concrete	Dilute solutions containing hydrochloric acid (HCl) and sodium hydroxide (NaOH), and distilled water and tap water were passed through the cylindrical porous concrete specimens after initial curing as well as after an accelerated CO ₂ exposure. The filtrate collected from the porous concrete was again passed through the specimens ten times. After each pass, three water quality indicators such as pH, turbidity and concentration of calcium ions remaining in the filtrate were analysed using ICP-MS.
Selection of model pollutant for experimental investigation	Aqueous solutions containing lead, cadmium, chromium and mercury were passed through the porous concrete specimens. Lead and cadmium were significantly trapped by the porous concrete. This study was restricted to lead for investigations on rGO modified porous concrete.
Filtration performance of rGO modified porous concrete	Aqueous solution having lead concentration of 8 mg/L was passed through a filtration arrangement consisting of three porous concretes that were arranged in series with progressively decreasing levels of constant head (H, H/4 and 0). This investigation was performed for a period of 60 minutes. Additionally, the material cost of this filtration system was also calculated and then compared with the commercially available filtration methods.

LEVEL I	01 Synthesis of reduced graphene oxide using modified Hummers' method
	02 Effect of graphene, alumina and silica nanoparticles on the properties and pore structure of OPC paste <ul style="list-style-type: none"> ✓ Mini slump test ✓ Compressive strength test ✓ Flexural strength test ✓ Water sorptivity test
	<ul style="list-style-type: none"> ✓ Mercury porosimetry (< 100 μm) ✓ 3-D Image analysis approach (≥ 100 μm)
	03 Effect of graphene, alumina and silica nanoparticles on the deterioration characteristics of OPC paste exposed to acidic environment <ul style="list-style-type: none"> ✓ Analysis of binder phases using TGA, FTIR and XRD ✓ Analysis of pore structure by mercury porosimetry ✓ Imaging the alteration phases using 3-dimensional X-ray CT, optical microscopy and SEM/EDS ✓ Determination of nanomechanical properties by nanoindentation
LEVEL II	04 Porous cement concrete – its mixture design, specimen preparation and testing methods <ul style="list-style-type: none"> ✓ Falling head permeability test, density measurement and compressive strength ✓ Determination of voids size using 2-dimensional image based approach ✓ Imaging the interconnected voids inside the porous concrete using 3-dimensional X-ray CT
	05 Effect of carbonation on the characteristics of water passed through the porous concrete <ul style="list-style-type: none"> ✓ Porous concrete exposed to accelerated CO₂ environment ✓ Repeat cycle permeability testing to investigate on the physical characteristics of distilled and tap water, dilute HCl and NaOH solutions after passage ✓ Bentonite clay loading test to investigate on the sediment blockage after passage
	06 Effect of reduced graphene oxide on the filtration performance of porous concrete <ul style="list-style-type: none"> ✓ Constant head permeability test to investigate on the removal of heavy metals after passage ✓ Proposed design of concrete based water filtration arrangement for the industries that are major sources of lead containing effluents

Figure 1.1 Methodology followed in this study

1.4 OUTLINE OF THESIS

This report is composed of nine chapters. The present chapter deals with the problem statement, objectives and scope, and methodology used in this study. The second chapter provides a detailed review of the literature covering the different applications of porous concrete and the test methods involved in determining their pore structure features. Additionally, their filtration performance is also reviewed. The performance of rGO in the fields of water treatment is also briefly reviewed. Based on a critical analysis of the literature, the needs for research are brought about at the end of the chapter. The materials and the principles of microanalytical and water quality testing techniques involved in this study are discussed in the third chapter. As stated earlier, the research methodology consists of two different levels – (1) to investigate the effect of rGO on the properties of cementitious matrix and (2) to investigate on the removal of heavy metals in plain and rGO modified porous concrete system.

The experimental investigations on the influence of rGO on the properties of Portland cement paste in comparison to popularly reviewed nanomaterials including alumina and silica nanoparticles are discussed in the fourth chapter. The deterioration characteristics of these 28-day cured pastes after storage in acidic solution for a period of 56 days were analysed using microanalytical studies and the findings are presented in the fifth chapter. The next chapter discusses the mixture design, specimen preparation and testing of porous concrete having controlled levels of hydraulic conductivity desired for water filtration purposes. The effect of concrete carbonation on the characteristics of water after passage is discussed in the seventh chapter. Investigations on the Pb removal in plain and rGO modified porous concrete specimens are discussed in the eighth chapter. The last chapter provides the specific conclusions and the scope for future investigations.

CHAPTER 2

LITERATURE REVIEW

2.1 INTRODUCTION

Heavy metals including Pb, Cd, Cu and Zn can form metal complexes with the hydroxyl and carbonate species that are available in the flow channels of porous cement concrete system. Application of nanotechnology in such system would be a new field of study. This combination can emerge as a potential candidate in removing the toxic heavy metals and inorganic dyes from industrial effluents. The present study is limited on understanding the effectiveness of Pb removal in plain and rGO (nanomaterial) modified pervious concrete system. The relevant literature is reviewed in this chapter.

The first section discusses the health hazards of heavy metals contamination and Pb contamination in Indian rivers. The subsequent section explains the porous concrete system; its mixture design, preparation, testing and maintenance methods, and filtration performance. In the long run, the porous concrete systems are likely to carbonate naturally and thereby phase alterations occur. This change influences the filtrate characteristics after passage. The possible alterations in the microstructure of carbonated binder phases are discussed. Apart from this, such phases in porous concrete system are likely to deteriorate after passage of acidic aqueous solutions. This deterioration is reviewed from the relevant literature and then discussed in the subsequent section. The last section covers the review of graphene and its composites, which are popular in the field of water treatment. The influence of graphene oxide (GO) on the properties of cementitious materials is also reviewed.

2.2 HEALTH HAZARDS OF HEAVY METALS CONTAMINATION

Due to rapid industrialization, heavy metal contamination is a growing problem worldwide. Toxic heavy metals that are of particular concern in the industrial effluents include arsenic, cadmium, lead, chromium, manganese, mercury, zinc and copper. Table 2.1 lists the effect of those heavy metals on human health, along with their acceptable limits.

Table 2.1 Effect of heavy metals on human health as described by Singh et al. (2011)

Heavy metals	Major sources of contamination	Influence on human health	Acceptable limit (mg/L)
Arsenic	Fungicides, metal smelters and pesticides	Dermatitis and bronchitis poisoning	0.02
Cadmium	Electroplating, fertilizer, batteries containing Cd and Ni, welding nuclear fission plant and pesticides	Lung and kidney disease, increase in blood pressure, bronchitis, gastrointestinal problems, bone marrow and renal dysfunction	0.06
Lead	Automobile emission, paint, mining, coal burning, smoking and pesticide	Fatal infant encephalopathy, sensor neural deafness, mental retardation in children, developmental delay, congenital paralysis and acute or chronic damage to the nervous system, epilepticus, liver, kidney, gastrointestinal damage	0.1
Chromium	Mineral sources and mines	Irritability, fatigue problems and damage to the central nervous system	0.05
Manganese	Fuel addition, metals welding, ferromanganese production	Major damage to central nervous system and breathing problems	0.26
Mercury	Batteries containing Hg, paper industries and pesticides	Protoplasm poisoning , minor psychological changes, acrodynia characterized by pink hands and feet, abortion and damage to central nervous system	0.01
Zinc	Pipe manufacturing, metal plating, refineries and brass manufacture	Damage to nervous system, zinc fumes have corrosive effect on human skin	15
Copper	Pesticide, metal piping and chemical industry	Liver and kidney failure, Anemia, stomach and intestinal irritation	0.1

Ion exchange method is found effective in removing the aforementioned heavy metals from the industrial effluent. Different processes that are in practice are listed in Table 2.2.

Table 2.2 Different processes followed to remove the heavy metals from contaminated water as described by Singh et al. (2011)

Contaminant	Filtration agent	Significant method	Other methods preferred
Heavy metals in Water	Conductive electroactive polymers (polypyrrole and polyaniline), calcium alginate particles, Dithiocarbamates, chitosan-capped gold nanoparticles and natural zeolites	Ion exchange	Complexation, immobilization, complexation, biosorption and bioremediation
Mercury	Bentonite and activated carbon	Ion exchangers	Precipitation, extraction and reduction
Chromium	Activated carbon	Ion exchange adsorbents	Surface absorption, ion-exchange, reverse osmosis and chemical sedimentation
Arsenic	Poly vinyl alcohol, hydroxypropylcellulose and polypyrrole	Oxidation	Capacitive deionization, use of adsorbents and surfactants

2.3 LEAD CONTAMINATION IN INDIAN RIVERS

Lead (Pb^{2+}) has been identified to be the most common and toxic heavy metal discharged into the natural water from sources like battery manufacturing, metal plating, soldering, paint and pigment producing and oil refining (Axtell et al. 2003, Kul and Koyuncu 2010). As per Bureau of Indian Standards (IS 10500 2012), the maximum permissible limit of Pb in drinking water is 10 $\mu\text{g/L}$. In May 2014, Central Water Commission, Govt. of India had reported that the Pb concentrations in eight Indian rivers such as Brahmani, Ganga, Ghagra, Gomti, Mahanadi, Ramganga, Rapti and Yamuna were found exceeding the acceptable

limits. This increase was observed in most of the water quality monitoring stations situated along these rivers.

In particular, the Moradabad water quality station (Lat. 28°20' and 29°16' N – Long. 78°24' and 79°0' E) on Ramganga River during June, 2012 had recorded a very high level of Pb concentration up to 48.92 µg/L (Status of Trace and Toxic Metals in Indian Rivers 2014). This polluted water on consumption can cause several health disorders like kidney diseases, chromosome and nervous damage, even leading to death (Kazi et al. 2008). Water treatment methods that are typically adopted in the industries for the Pb removal include adsorption, precipitation, ion exchange, oxidation, reduction, electrolysis and reverse osmosis (Kul and Koyuncu 2010). However, the major drawbacks involved in practicing these methods are high initial capital cost, operational and maintenance costs.

2.4 POROUS CEMENT CONCRETE – AN OVERVIEW

2.4.1 Brief description

Porous concrete is made of cement, gap graded or single sized coarse aggregate, water and little or no fine aggregate (ACI 522R 2010). This concrete possesses better thermal insulation capacity, higher permeability, lower drying shrinkage and unit weight. However, the high porosity decreases the compressive, tensile and bond strengths of concrete (Ghafoori and Dutta 1995, Malhotra 1976). Various advantages in laying porous concrete roadways include stormwater regulation and pollution control, decrease in interaction noise between tire and pavement, water and air percolation to the tree roots, reduction of glare on road surfaces, increase in parking facilities because of optimization of water retention areas. Although this concrete has multiple benefits, its application is limited because of the potential challenges that are involved like specialised construction practices, extended curing time, absence of standardised test methods, special attention in case of high ground water table and expansive soils (ACI 522R 2010).

2.4.2 Typical mixture proportioning

Porous concrete with the desired performance can be achieved only based on trial and error (ACI 522R 2010, Lian and Zhuge 2010, Marolf et al. 2004, Meininger 1988, Yang and Jiang

2003). In the case of porous concrete, the amount of water and binder contents are proportioned to only coat and bind the aggregates together in such porous matrix (Tennis et al. 2004). The aggregate size, shape and texture influences the permeability of porous concrete (Mehta and Aïtcin 1990). The porosity of such concrete can decrease when the matrix is packed with higher amounts of small sized aggregates, as schematically shown in Figure 2.1. This may tend to increase the tortuosity of flow channels in porous concrete.

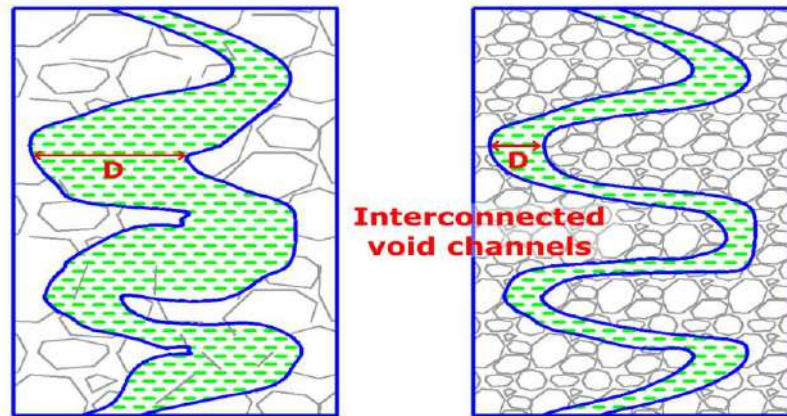


Figure 2.1 Effect of aggregate size on the pore structure of porous concrete section

The coarser aggregate content (> 4.75 mm) in porous concrete is narrowly graded, to allow the rapid percolation of water. It can also be achieved by decreasing the amount of fine aggregate. The most common gradings of coarse aggregate that are used in the porous concrete mix are #67 (19 to 4.75 mm), #7 (12.5 to 4.75 mm), #8 (9.5 to 2.36 mm) and #89 (9.5 to 1.18 mm) conforming to ASTM C33 (2011), and these are shown in Table 2.3.

Table 2.3 Common aggregate gradings for porous concrete (ASTM C33 2011)

Size number (Nominal size)	Amounts finer than each laboratory sieve, mass percent							
	25 mm	19.0 mm	12.5 mm	9.5 mm	4.75 mm	2.36 mm	1.18 mm	300 μ m
67 (19.0 to 4.75 mm)	100	90-100	-	20-55	0-10	0-5	-	-
7 (12.5 to 4.75 mm)	-	100	90-100	40-70	0-15	0-5	-	-
8 (9.5 to 2.36 mm)	-	-	100	85-100	10-30	0-10	0-5	-
89 (9.5 to 1.18 mm)	-	-	100	90-100	20-55	5-30	0-10	0-5

The aggregate sizes are found to be varying from 25 mm to 300 μm . It can be seen that the gradings 8 and 89 have a small amount of fine aggregate in them. This may decrease the air voids content in the porous material. Table 2.4 specifies the typical proportions that can be used in the design of porous concrete mix.

Table 2.4 Typical material proportions in porous concrete (ACI 522R 2010)

Details	Proportions in kg/m^3
Cementitious materials	270 to 415
Aggregate	1190 to 1480
w/c ratio, by mass	0.27 to 0.34
Aggregate : cement, by mass	4 to 4.5 : 1
Fine : coarse aggregate, by mass	0 to 1 : 1

These values are considered in the design of concrete systems having porosities ranging from 15% to 35%. Below 15% porosity, it is argued that the pores or voids in concrete may not be interconnected significantly and thereby rapid percolation of water is disrupted (Meininger 1988). Figures 2.2 to 2.4 show the relationship between the paste content, porosity, percolation rate, compaction effort and compressive strength of porous concrete.

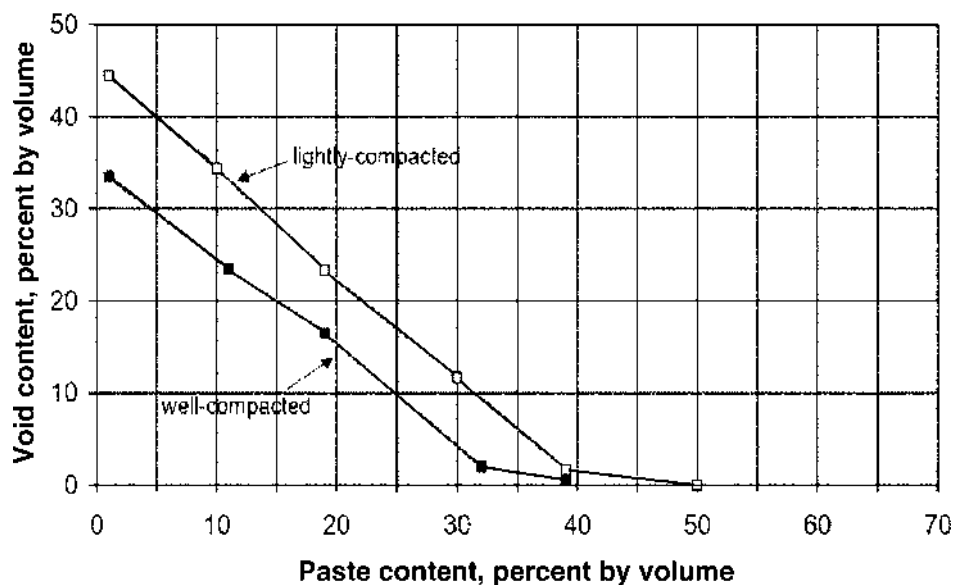


Figure 2.2 Relationship between porosity and paste content of porous concrete (ACI 522R)

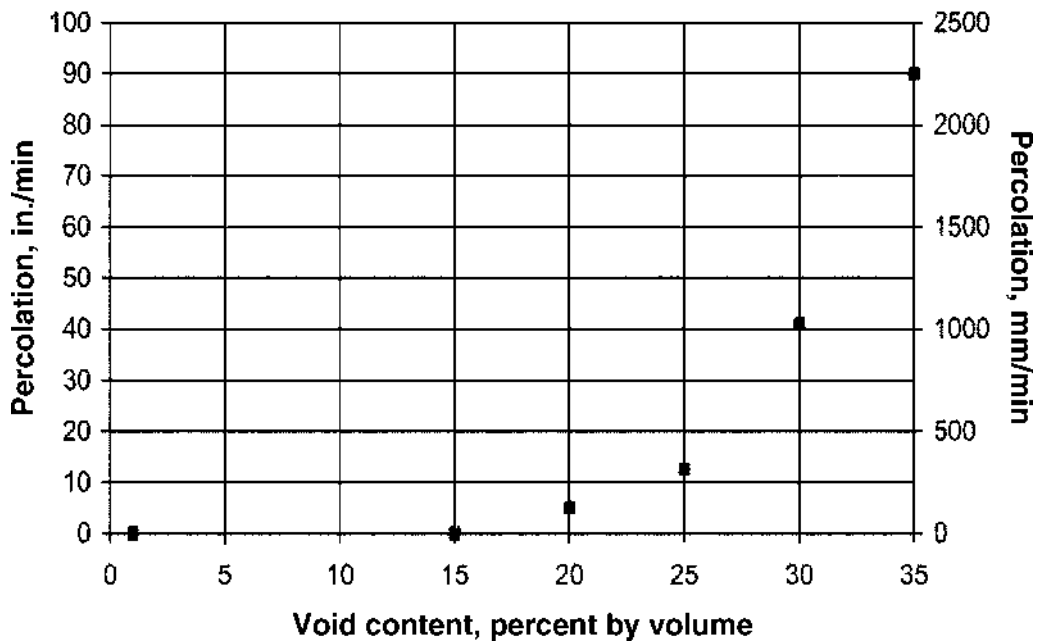


Figure 2.3 Relationship between porosity and percolation rate of porous concrete (ACI 522R)

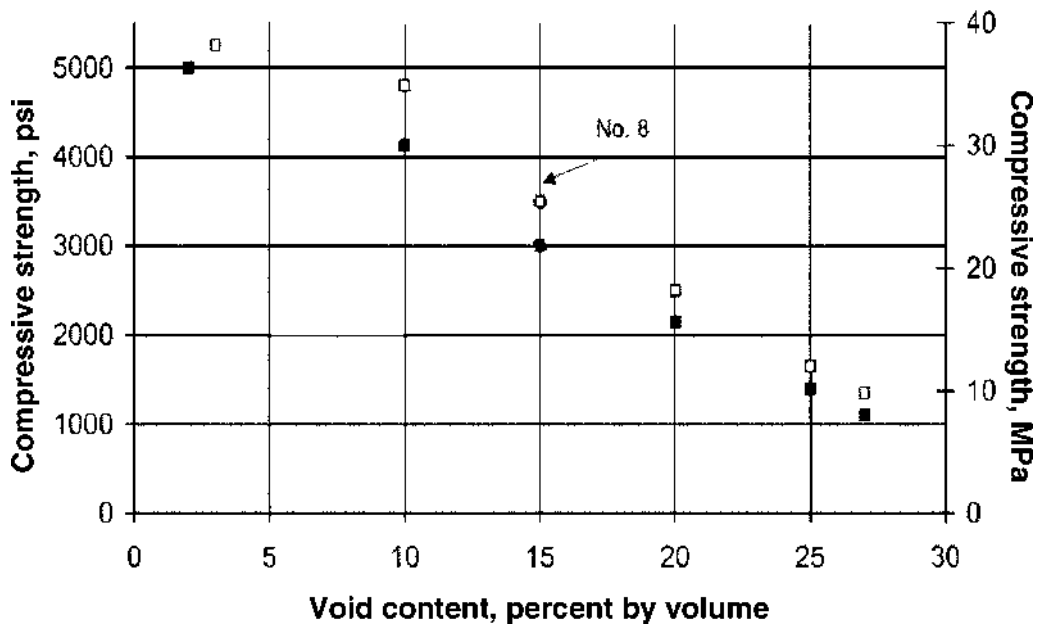


Figure 2.4 Relationship between the compressive strength and porosity (ACI 522R 2010)

The amount of paste content and compaction energy applied to the porous concrete mix influences the percolation rate. Although the increase in those amounts enhance the compressive strength, the resultant decrease in porosity affects the permeability (percolation rate) of the system. Unlike conventional concrete, the relationship between the compressive

strength and w/c ratio is not clear for porous concrete. Figure 2.5 compare a handful of fresh porous concretes having increased amount of water content in them (Tennis et al. 2004).

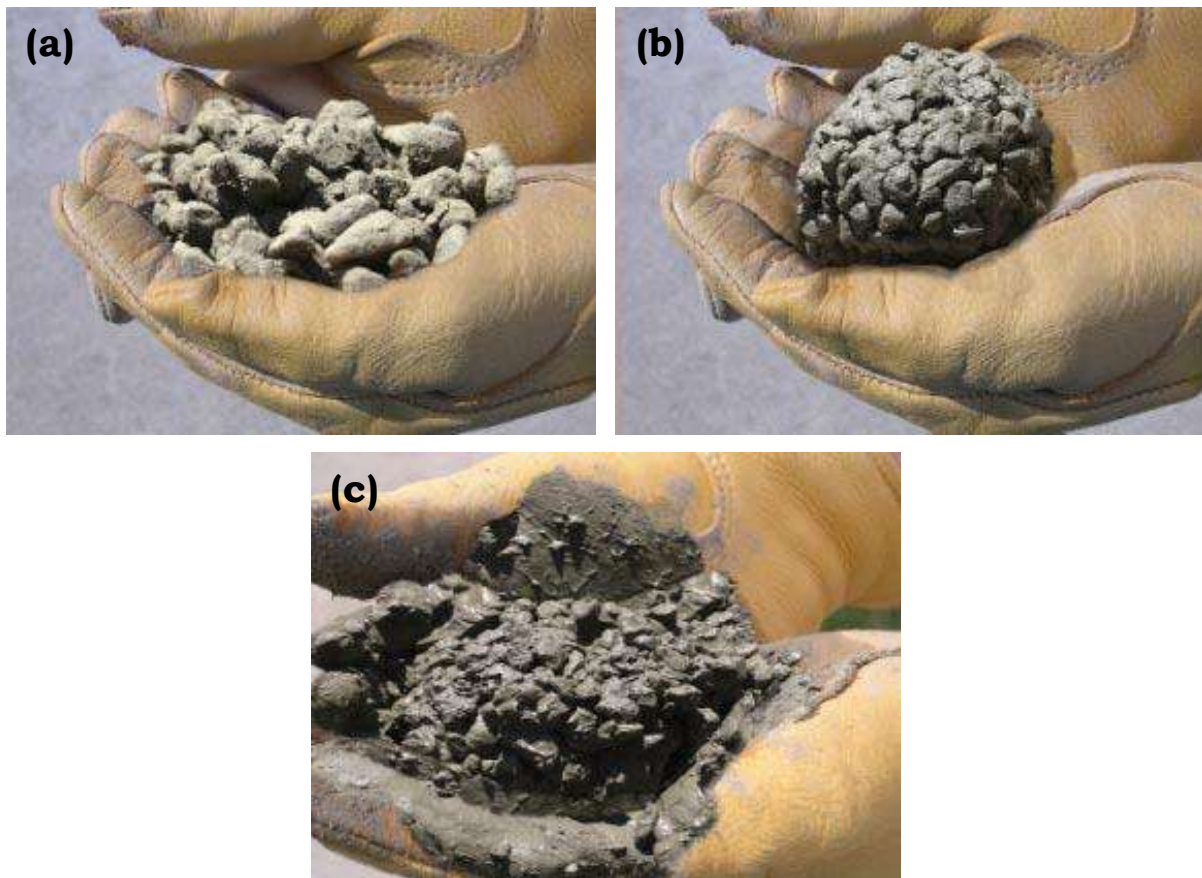


Figure 2.5 A sample of fresh porous cement concrete mixture prepared with (a) low, (b) optimum and (c) high amounts of water (Tennis et al. 2004)

It can be noticed from the photographs that the water content needs to be tightly controlled to avoid bleeding of cement slurry and also to maintain sufficient bond in between the aggregates (Tennis et al. 2004). For laboratory scale investigations, the porous concrete is consolidated using mechanical compactors such as Proctor and Marshall Hammer conforming to AASHTO T 180 (2015) and AASHTO T 245 (2015) respectively. The degree of porosity in concrete system can be altered by varying the numbers of layers and blows applied to the fresh concrete mixture (Sumanasooriya et al. 2012).

Cylindrical porous concrete specimens with lower and higher compaction efforts were prepared and their porosity, strength and density were determined in a study (Bury et al. 2006). Fresh concrete was poured inside a cylindrical iron mould for the entire depth and then

five blows were applied over its surface using the Marshall Hammer. This loose packing was termed as low compaction effort.

Porous concretes having higher compaction effort were achieved by dividing the fresh concrete into three equal layers inside the mould. After pouring each layer of the fresh concrete, twenty six blows were applied over each layer using the hammer (Badoe et al. 2003, Bury et al. 2006). Suleiman et al. (2006) have reported that the compressive strength of porous concrete was decreased up to 11% when the vibration amplitude of the compactor was reduced from 0.127 to 0.086 mm.

2.4.3 Permeability or infiltration rate or percolation rate

The falling head permeability test principle is often followed in measuring the permeability of porous concrete (Huang et al. 2010, Kayhanian et al. 2012, Neithalath et al. 2006, Shu et al. 2011, Sonebi and Bassuoni 2013). The test set up recommended in ACI 522R (2010) is shown in Figure 2.6.

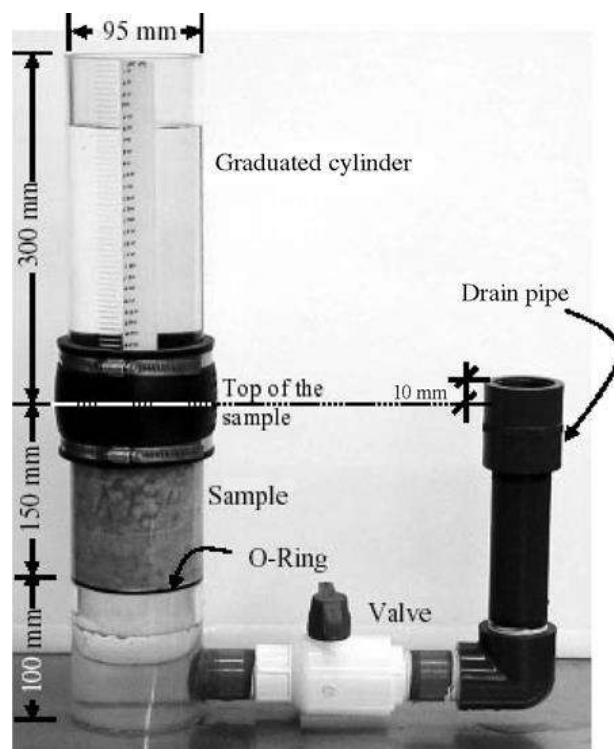


Figure 2.6 Falling head permeability test set up that is recommended to measure the permeability of porous concrete (Olek et al. 2003)

This test apparatus is seen to be relatively easier to fabricate and rapid in yielding test results that are interpreted using Darcy's law of flow in homogeneous porous materials. The permeability of a porous medium is dependent on the pore volume and its connectivity whereas the porosity is a volumetric property of the material. Kozeny-Carman equation (Neithalath et al. 2006), relates the porosity and permeability of a porous material which is shown in Equation 2.1.

$$\text{Permeability, } K = (N^3) / (F \times \tau^2 \times S^2 \times (1 - N)^2) \quad - (2.1)$$

where N is the porosity, τ is the tortuosity which is the inverse of connectivity; F and S are factors to account for different pore shapes and the specific surface area of pores respectively. In a study, porous concretes having low and high paste content were prepared and then experimentally tested for their permeability. Additionally, the permeability value was also predicted using Katz-Thompson equation, which is better explained in Sumanasooriya and Neithalath (2011). Figure 2.7 compares the experimentally determined and predicted permeabilities of the different mixtures having low and high paste content in them.

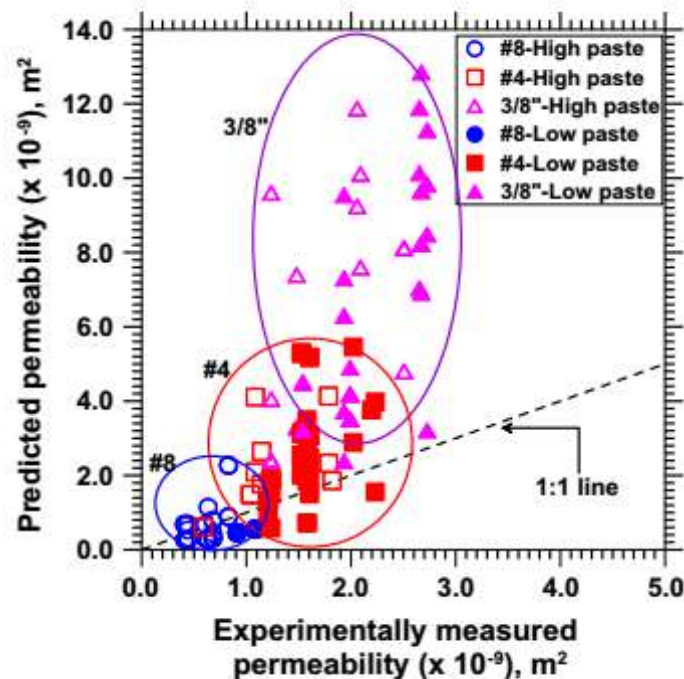


Figure 2.7 Comparison of the experimentally determined and predicted permeabilities of porous concretes having low and high paste content in them (Sumanasooriya and Neithalath 2011)

Good correlation between the experimentally measured and predicted permeabilities of the different mixtures was observed in the study, as shown in the plot. Porous concretes having high paste content showed lower permeabilities. However, the concrete mixture having 3/8” aggregates (size of aggregates used were finer than 9.5 mm) and high paste content was not following the trend, which could be due to the formation of larger amounts of small sized pores and thereby predicts higher permeability. As reported in Sumanasooriya et al. (2012), and Sumanasooriya and Neithalath (2009), the increase in the amount of binder content had decreased the porosity of porous concrete because of localized paste clogging. This effect may increase the tortuosity of flow channels and thus reduces the water permeability.

The high paste content also decreased the connectedness of pore structure in the concrete system. The design of porous concrete having higher amounts of paste content and compaction effort, the usage of small sized aggregates and its grading can also lead to low permeability because of reduction in permeable pore spaces in the system (Ćosić et al. 2015, Mahboub et al. 2009, Marolf et al. 2004, Obla and Sabnis 2009, Tan et al. 2015).

2.4.4 Pore structure related features inside the material

In a porous cement concrete system, the total porosity can be divided into interconnected pores, capillary and dead-end pores. The application of image processing and analysis technique to determine the size of pores and its distribution in the light weight and porous concretes is described in several studies (Ćosić et al. 2015, Kuang et al. 2011, Nambiar and Ramamurthy 2007, Neithalath et al. 2010, Sumanasooriya and Neithalath 2009). Two-dimensional and three-dimensional images of porous concrete sections were obtained either using flatbed scanner or X-ray computed tomography. The pore related features such as porosity, pore size and its distribution, specific surface area and pore connectivity in those images (either 2-D or 3-D) were determined using stereological and morphological methods supported with image analysis software (Sansalone et al. 2008, Sumanasooriya and Neithalath 2009).

Sumanasooriya and Neithalath (2011) adopted a colour threshold procedure on the 2-D images to determine the variation of pore and paste area fractions along the depth of porous concrete having high paste contents. Figure 2.8 compare the variation of pore and paste area fraction along the depth of a concrete mixture having 19% porosity.

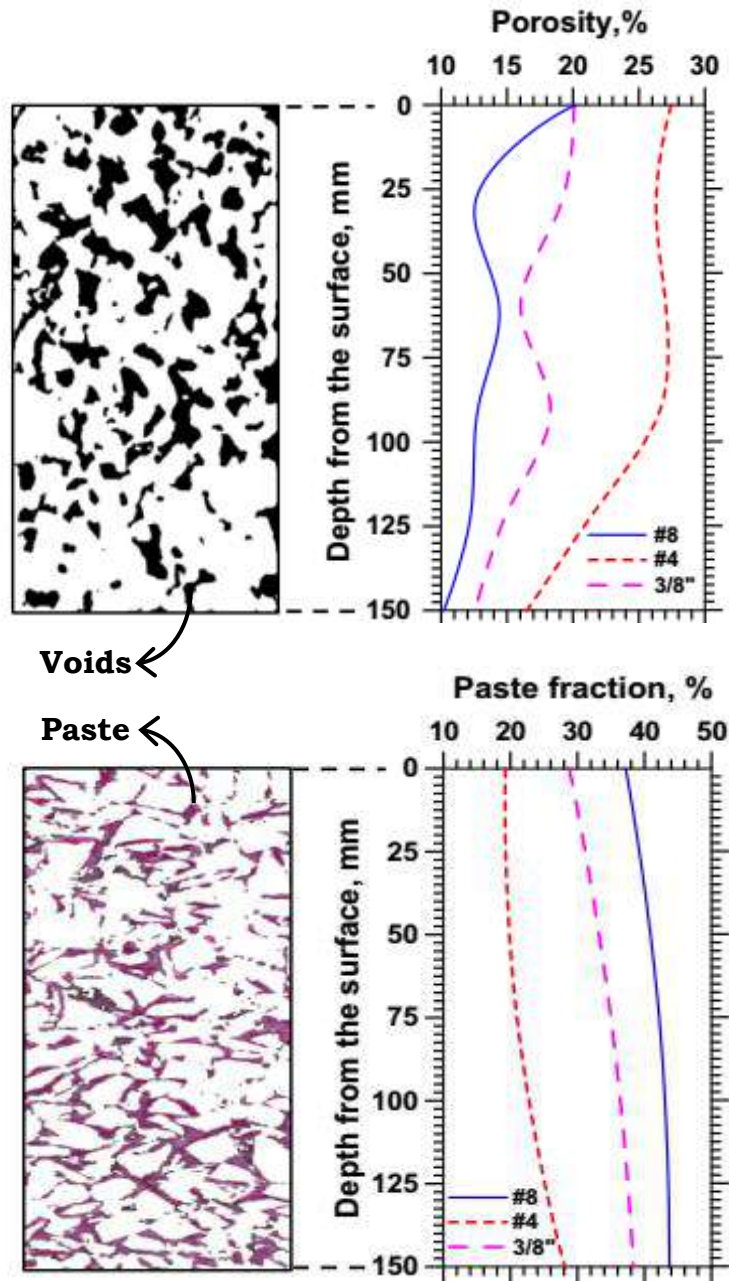


Figure 2.8 Variation of pore area fraction (top image) and paste area fraction (bottom image) along the depth of porous concrete section having 19% porosity (Sumanasooriya and Neithalath 2011)

At the bottom of the section, the pore area fraction decreases and paste area fraction increases which confirm the influence of paste clogging. Pore tortuosity is defined as the ratio of effective length of the flow path to the specimen length. Mostly, this ratio is more than 1. The tortuosity predicted using Kozeny-Carman model was seen to correlate well with the

tortuosity along the vertical section of porous concrete determined using image analysis technique (Zhong et al. 2016).

2.4.5 Water filtration performance of porous cement concrete system

Figure 2.9 schematically illustrates a porous concrete pavement that could result in the infiltration of stormwater runoff through the interconnected voids present inside the material.

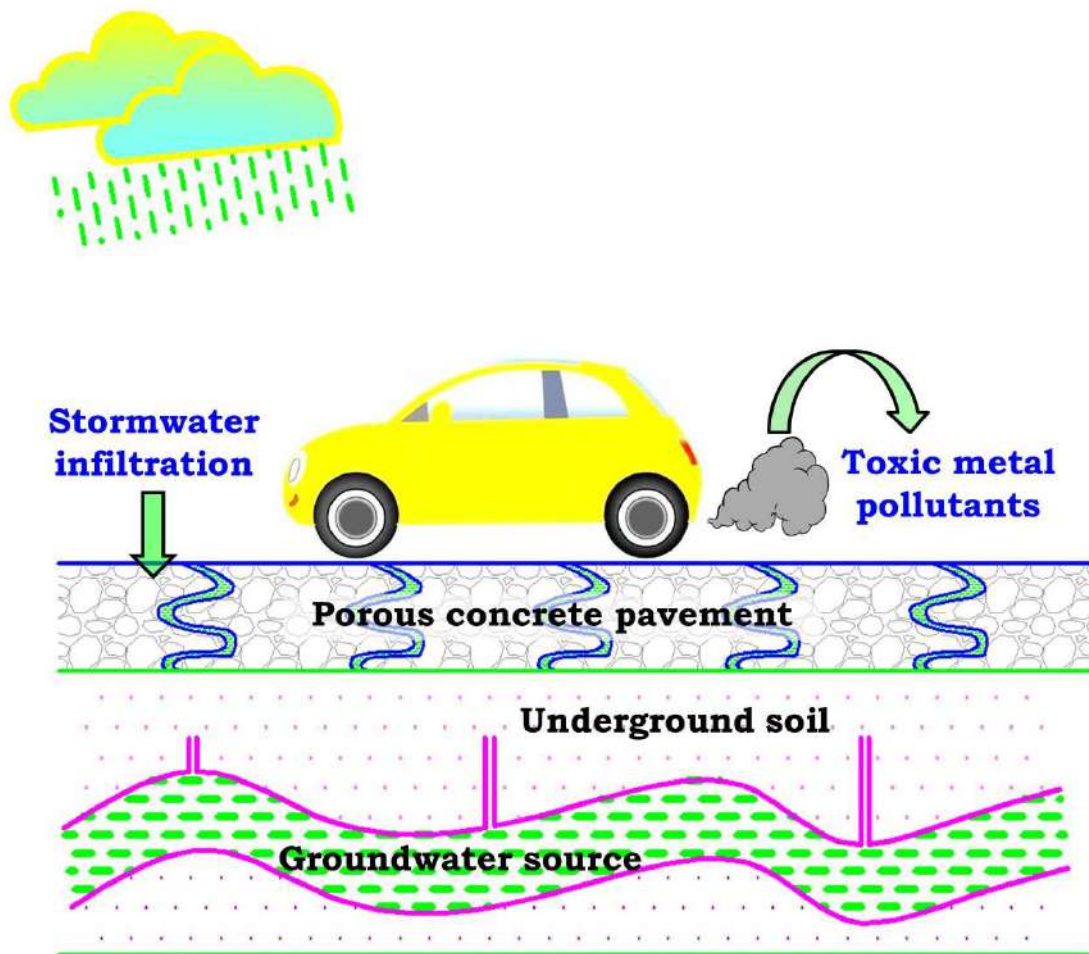


Figure 2.9 Infiltration of stormwater runoff through the interconnected voids available inside the porous concrete pavement

Stormwater runoff from urban roads and car parks contain dissolved pollutants like heavy metals, hydrocarbons, phosphorus, oil, nitrogen and so on (Hwang et al. 2016, Sansalone et al. 2012). In particular, the presence of dissolved heavy metals such as Zn, Pb, Cu, Ni, Cr, Cd and Fe are found to be dominant and their infiltration severely affects the ground and surface

water reserves (Hwang et al. 2016). Low impact development practices like bio-retention, rain garden, constructed wetland, tree box filter and permeable concrete pavement decrease the entry of toxic metals from the runoff into the ground environment (Chandrappa and Biligiri 2016, Maniquiz-Redillas and Kim 2016). Haselbach et al. (2014) have reported that the porous cement concrete could retain 90% and 87% of Zn and Cu from the simulated runoff at lab conditions over the testing period. Solpuker et al. (2014) passed an aqueous solution containing Pb, Cu and Zn through the porous concrete and Pb was found to be immobilized better than the remaining metals. Leaching of the immobilized ions was found to be greater when the pH was less than 8 (Solpuker et al. 2014).

The application of porous concrete barriers could remove 30% sulfate, 99% Fe, 50% to 83% manganese and 30% total dissolved solids from the acid mine drainage (Ekolu et al. 2014). This barrier was able to decrease the Al, Fe, Mn, Co and Ni contaminants significantly from the drainage of gold mines and coalfields. Additionally, the cement based system increased the pH of drainage and thus remained alkaline (9 to 12) throughout the investigation (Shabalala et al. 2017). Figure 2.10 schematically demonstrate the concrete based reaction column that was used to treat the acid mine drainage.

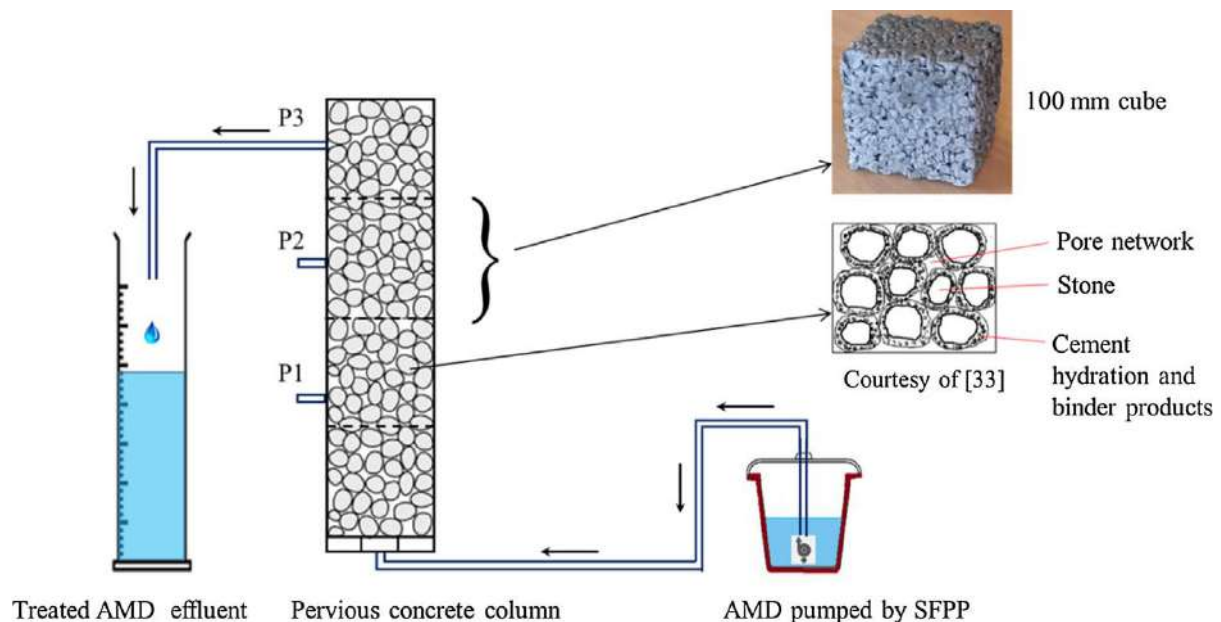


Figure 2.10 Schematic illustration of concrete based reactive column that was used for the treatment of acid mine drainage (AMD – acid mine drainage, SFPP – submersible fish pond pump, P1, P2, P3 – sampling ports 1, 2, 3) (Shabalala et al. 2017)

A permeable concrete pavement at Canada was widely tested for its filtration performance. Even under cold conditions, this pavement was able to retain the Cu, Pb and Zn ions from the stormwater runoff. This suggests that the removal of toxic heavy metals is independent of climatic conditions (Huang et al. 2016). Chemical precipitation of metal hydroxides could be the dominant metal removal mechanism (Shabalala et al. 2017). The metal ions are also likely to be removed due to complexation and solids formation with the carbonate (CO_3^{2-}) species that are attached to calcium in the concrete (Haselbach et al. 2014). However, the removal of fine suspended particles is due to water trapping and physical adsorption (Kuang et al. 2007). A laboratory investigation showed that the permeable asphalt pavement was also found to retain the Cu, Zn, Pb and Cd metal pollutants from the runoff (Jiang et al. 2015).

Besides heavy metals, the porous concrete could remove suspended solids, nitrogen and phosphorus and thus decrease the ill-effects of eutrophication in lakes and rivers (Brown et al. 2011, Park and Tia 2004). This porous medium was also found to trap the motor oil from simulated runoff (Lee et al. 2013). An attempt to remove Cu from aqueous solution using porous geopolymers that was prepared using fly ash, 30% iron ore tailing by weight, and H_2O_2 (foaming agent) was found encouraging at higher temperature ($40\text{ }^\circ\text{C}$) with the pH value of 6.0 (Duan et al. 2016).

2.4.6 Sediment blockages inside porous concrete

Commonly, the stormwater runoff consists of fine sand, dirt and debris that are sourced from vehicles and the nearby environment. The percolation of such water through the porous concrete pavements could gradually affect its hydraulic performance because of pore clogging or sediment blockage. Figure 2.11 schematically illustrates the sediment clogging that is likely to disrupt the water movement in permeable concrete.

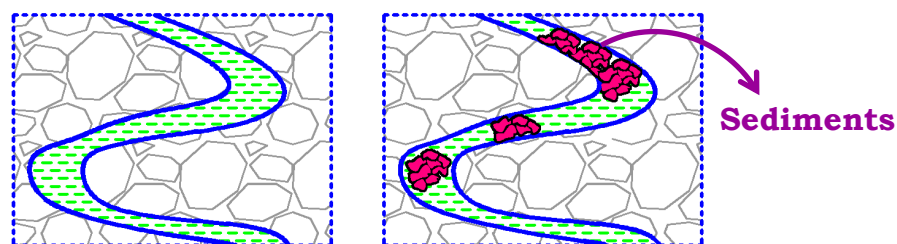


Figure 2.11 Schematic diagram illustrating sediment clogging that is likely to disrupt the water movement in permeable concrete

The pore clogging along the cut section of porous concrete from different parking lots were assessed using X-ray computed tomography (CT) images aided with image analysis technique, which is illustrated in Figure 2.12 (Manahiloh et al. 2012). Figure 2.13 compares the porosity profile of concrete from the parking lots along its depth.

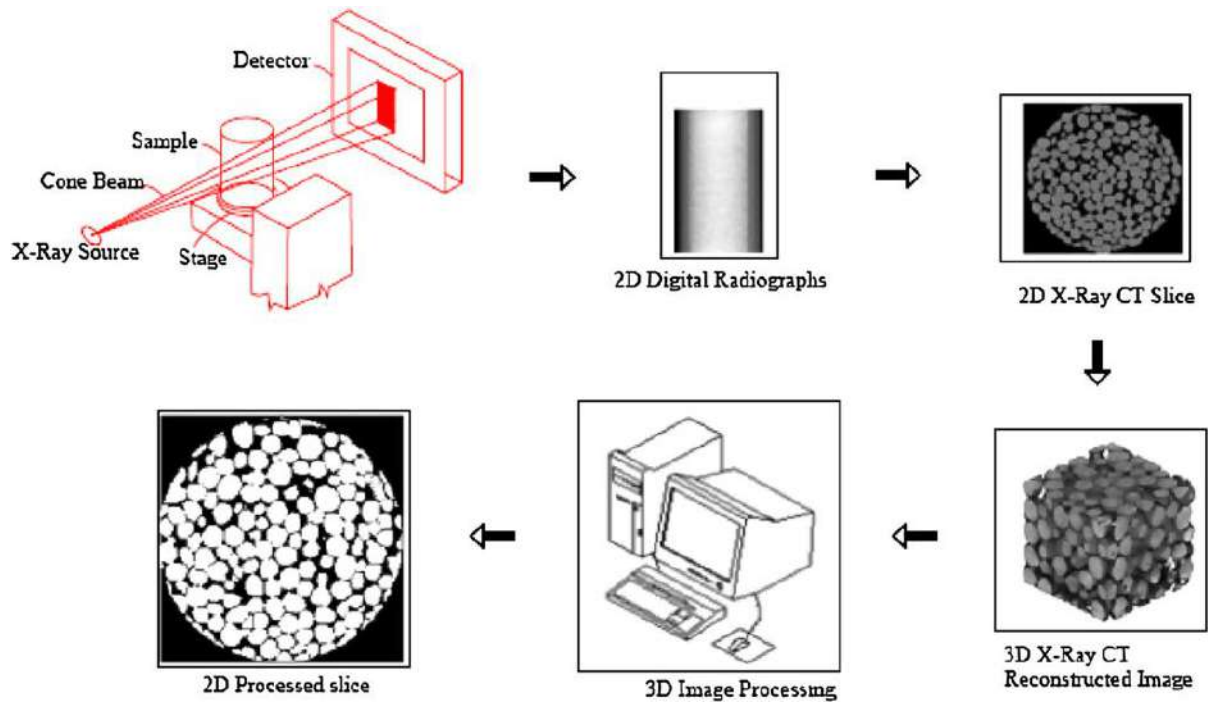


Figure 2.12 Flow of steps that were involved in the assessment of pore clogging in the porous concrete pavement by image based approach (Kayhanian et al. 2012)

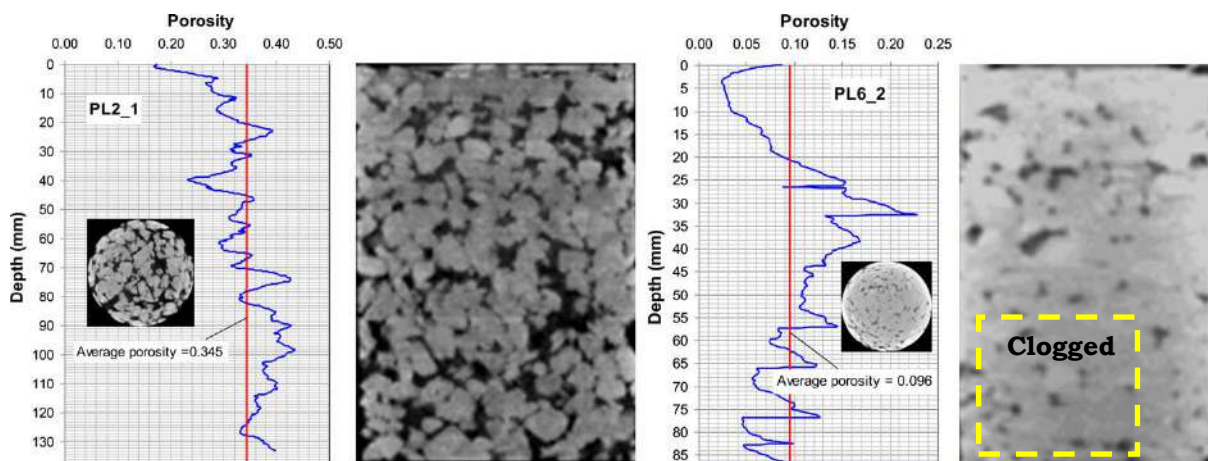


Figure 2.13 Porosity profile of two different parking lots that were less (left image) and highly clogged (right image) due to the deposition of fine sediments (Kayhanian et al. 2012)

The sediment blockages and their location in the pore structure of porous concrete sections were clearly delineated using the CT images. Around 25 mm from the top surface of concrete was reported to be highly clogged (solidified due to alternate wet and dry cycles) than the remaining portions in the vertical section (Kayhanian et al. 2012). Industrial hand-held vacuum cleaning, pressure washing and milling are found to be used in recovering the permeability of old porous concrete pavements. In particular, milling up to 2.5 cm has significantly restored the permeability of a 21 year old porous asphalt pavement in Sweden (Winston et al. 2016).

A combination of vacuuming and sonication was able to recover the permeability up to 96 to 99% in porous cement concrete (Sansalone et al. 2012). Chopra et al. (2009) have reported that the performance of pressure washing was found better than the vacuum cleaning for the recovery of permeability in low traffic roads. Surface sweeping and subsequent rinsing with plain water was found efficient in removing the kaolin, bentonite and red clay deposits that were clogged inside the porous concrete (Haselbach 2009). Up to 66% of clogged sediment particles were removed from the porous concrete by reverse flushing with water at a low pressure of 3.5 kPa (Shirke and Shuler 2009).

2.5 PHASE CHANGES IN CEMENTITIOUS BINDERS EXPOSED TO ACIDIC ENVIRONMENT

Chemical warehouses, nuclear industry structures, underground tunnels and radioactive waste disposal structures made of cement concrete are commonly exposed to aggressive solutions (Alexander et al. 2013, Bertron et al. 2005, Fan et al. 2016, Gutberlet et al. 2015). The binder phase in these structures is highly stable in alkaline conditions ($\text{pH} > 11.5$), which is brought about by the ionic species available in the pore solution (OH^- , Ca^{2+} and alkali ions such as Na^+ and K^+). Diffusion of H^+ ions from the external solution disturbs the neutrality of the pore solution and thus decreases the pH of porous medium (Camilleri 2011, Pavlík 1994, Revertegat et al. 1992, Schwotzer et al. 2015). Under lowered pH conditions, calcium leaching occurs, which is a combined diffusion – dissolution – precipitation process (Bertron et al. 2005, Jain and Neithalath 2009, Moranville et al. 2004).

According to Berner's diagram (Berner 1988), the calcium to silica (Ca/Si) ratio is in direct relationship with the amount of Ca^{2+} ions in the pore solution. The decrease in this ratio

forces the dissolution of calcium hydroxide (C-H) and subsequently calcium silicate hydrate (C-S-H) gel. Their dissolution is also dependent on the chemical equilibrium of calcium – silicate – water system (Alexander et al. 2013, Zivica and Bajza 2001). This decalcification increases the pore connectivity of C-S-H gel and changes the equilibrium Ca/Si ratio which substantially decreases the concrete strength. Along with these phases, the remaining hydrates like calcium aluminate hydrate (C-A-H), ettringite (AF_t) and monosulphate (AF_m) are reported to lose the soluble calcium from their well-defined structure. Aluminate and ferrite phases dissolve at much lower pH values than the release of Ca²⁺ ions from the C-H and C-S-H gel. This late dissolution releases Al³⁺ and Fe³⁺ ions into the external solution (Beddoe and Dorner 2005). The rate of degradation is primarily dependent on the acid type and its concentration and the chemical composition of binder. In the present study, the effect of nanomaterials including reduced graphene oxide (rGO) on the deterioration characteristics of cement paste exposed to nitric acid (HNO₃) environment is investigated. Thus, it is of interest to describe some studies that have addressed this issue. Pavlík (1994) had earlier described the HNO₃ attack of cement paste, which is schematically reproduced in the Figure 2.14.

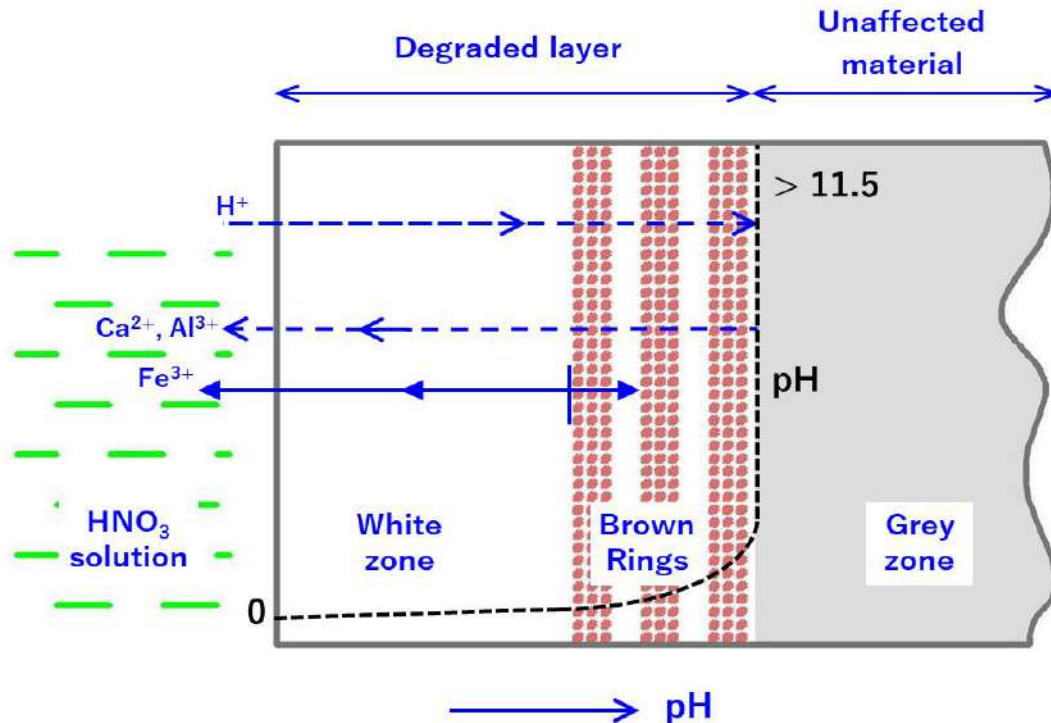


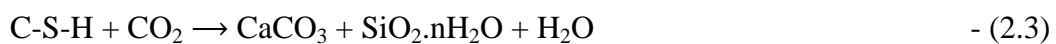
Figure 2.14 Schematic illustration of a cut section of cement paste exposed to HNO₃ environment (Pavlík 1994)

HNO₃ attack on cementitious binder produces Ca(NO₃)₂ (calcium nitrate) salts which are highly soluble. This attack is characterised by the formation of insoluble precipitates surrounding the unaffected material. The pH in the degraded layer changes from the low values of external solution to the highly alkaline unaffected material. The precipitates are made of Si, Fe and traces of Al, and are highly porous, soft and have surface cracks in them. These shallow cracks may occur because of drying of gels that have undergone decalcification. Si and Fe based precipitates are found to be white and brown in colour respectively whereas the undamaged grey material is still occupied with the normal hydrates (Chandra 1988, Chatveera and Lertwattanaruk 2014, Fan et al. 2016, Gutberlet et al. 2015, Pavlík 1994, Pavlík 1994, Pavlík 1996, Shi and Stegemann 2000, Zivica and Bajza 2001). The outermost siliceous gel is structurally amorphous and precipitates when the Ca²⁺ concentrations are lesser than 2 mol/m³ in the pore solution (Gaitero et al. 2008). The intermediate brown discolouration is probably governed by the precipitation of Fe(OH)₃ (Gutberlet et al. 2015).

Gaitero et al. (2009), Mondal et al. (2010), Singh et al. (2013) have reported that the addition of nano silica into cementitious composites had strongly decreased the rate of calcium leaching. This degradation was controlled because of pore refinement and pozzolanic conversion as reported in Gaitero et al. (2008). The introduction of silica nanoparticles could increase the average length of silicate chains in the C-S-H gel. This change stabilized the calcium in the system and thus decreased the porosity (Gaitero et al. 2006).

2.6 PHASE CHANGES IN CEMENTITIOUS BINDERS EXPOSED TO CO₂ ENVIRONMENT

Concrete carbonation is a natural phenomenon. The CO₂ that enters in the pores of the cementitious matrix is likely to dissolve in the interstitial solution (pH ~ 13.5) and thereby alters the chemical balance between the solution and binder phases (Villain et al. 2007). Major phase changes that could occur while carbonation includes conversion of portlandite and C-S-H gel to CaCO₃ which is shown in Equations 2.2 and 2.3 (Thiery et al. 2007).



This final product, CaCO_3 has three commonly occurring crystalline polymorphs: calcite, vaterite and aragonite. The carbonation of C-H involves three major steps: (1) dissolution of C-H; (2) absorption of CO_2 and formation of carbonate ions; and (3) chemical reaction and precipitation. This C-H carbonation is mainly dependent on the porosity and moisture content of the binder phase. Figure 2.15 schematically illustrate the evolution of calcite layer on a portlandite substrate in a moist environment.

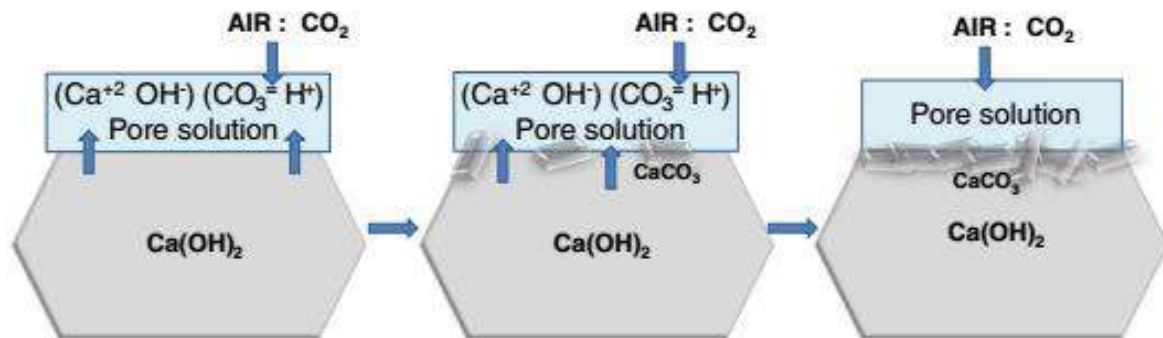


Figure 2.15 Schematic diagram showing the evolution of a thin layer of calcite on a portlandite substrate in a moist environment. The water film is coloured in blue and its thickness relates to the relative humidity (~ 53 to 75%) (Galan et al. 2015)

Although C-H initially undergoes rapid carbonation, its rate of reaction decreases with time because of the formation of thin layer of CaCO_3 on the surface of C-H crystals. Subsequently, the decalcification of C-S-H gel due to carbonation results in the formation of highly porous amorphous silica gel and various polymorphs of CaCO_3 (Groves et al. 1990).

The C-S-H carbonation rate is greatly dependent on the CO_2 concentration and environmental conditions (Šauman 1971). However, the remaining calcium bearing phases such as C-H, ettringite, and aluminates could undergo maximum amounts of carbonation, irrespective of the CO_2 concentration (Hyvert et al. 2010). The carbonation rate is higher in C-S-H gel having low Ca/Si ratio surrounding the high density C-S-H (Sevelsted and Skibsted 2015). The formation of calcite layer with the residual C-S-H could largely prevent the inner C-S-H from being fully carbonated (Morales-Florez et al. 2012).

The decalcification of ettringite due to carbonation results in the formation of gypsum and alumina gel (Nishikawa et al. 1992). The carbonation of ettringite produces vaterite like CaCO_3 crystals (Fernández-Carrasco et al. 2012). At low temperature, the CO_2 ingress could

aid in the production of thaumasite ($\text{CaCO}_3 \cdot \text{CaSO}_4 \cdot \text{CaSiO}_3 \cdot 15\text{H}_2\text{O}$) in the near surface regions of concrete exposed to sulphate environment. This thaumasite seems to remain stable at highly basic conditions ($\text{pH} > 12.0$) and thereby only minor amounts of CaCO_3 are detected in this condition (Jallad et al. 2003).

2.7 GRAPHENE, GRAPHENE OXIDE AND REDUCED GRAPHENE OXIDE

Graphene, a 2-D planar sheet of single atom thickness having sp^2 bonded carbon atoms arranged in a honeycomb lattice pattern, gives excellent in-plane mechanical (modulus of elasticity 1100 GPa), thermal (conductivity 5300 W/mK), optical transparent, and electrical (conductivity 2000 S/cm) properties. Layers of graphene sheets that are stacked on top of each other form graphite having an interplanar spacing of 0.335 nm (Singh et al. 2011). Graphene is the building block of other carbon allotropes such as 0-D fullerene (curving), 1-D carbon nanotube (rolling) and 3-D graphite (stacking) which is illustrated in Figure 2.16.

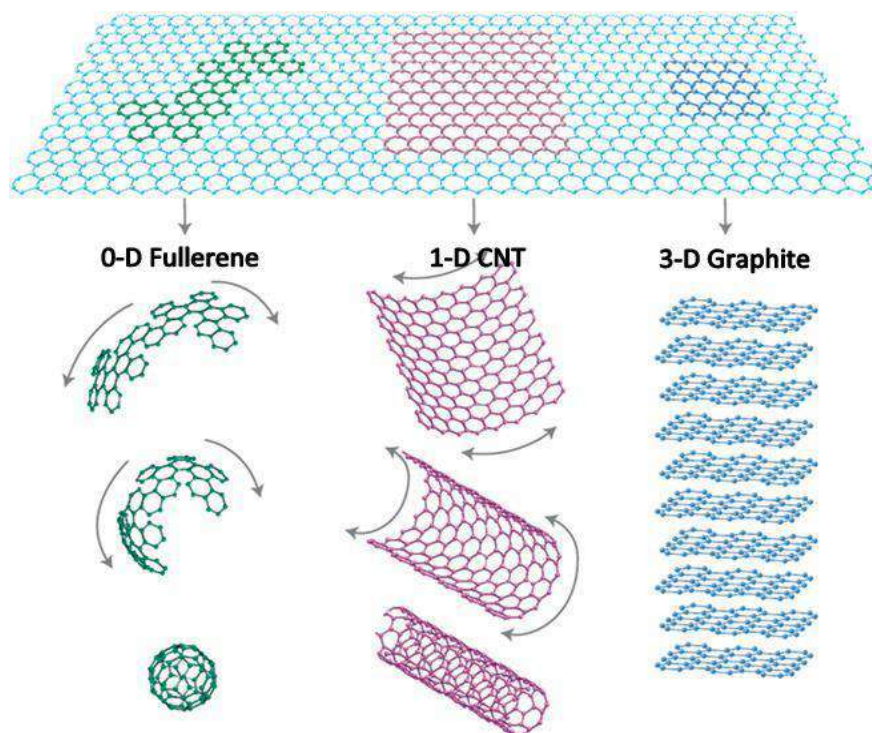


Figure 2.16 Graphene, the building block of other carbon allotropes that includes 0-D fullerene, 1-D carbon nanotube and 3-D graphite (Geim and Novoselov 2007)

Liquid phase exfoliation, oxidation of graphite, mechanical exfoliation, and epitaxial growth such as chemical vapour deposition and thermal decomposition of silicon carbide (SiC) are

the synthesizing methods that have been developed to produce a single layer or few layers of graphene (Wei and Liu 2010). The manipulation of graphene at large scale is particularly achieved with the synthesis of graphene oxide (GO) by modified Hummers' method (Hummers and Offeman 1958, Li et al. 2008). Figure 2.17 demonstrate the extraction of reduced graphene oxide from natural graphite using modified Hummers' method.

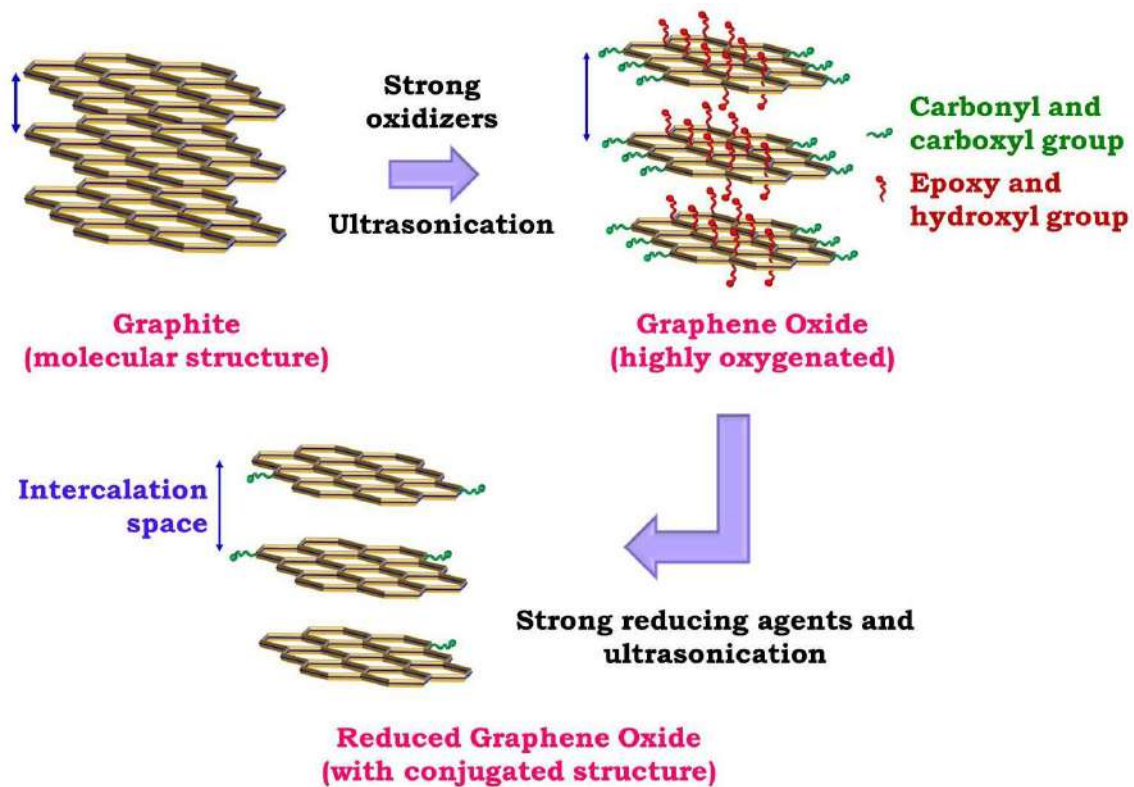


Figure 2.17 Schematic illustration of the synthesis of reduced graphene oxide using modified Hummers' method

This method produces chemically converted graphene sheets where its basal planes are decorated with epoxide and hydroxyl groups, in addition to carbonyl and carboxyl groups located at the edges (Konios et al. 2014). These planar sheets are likely to form stable colloids through electrostatic stabilization and can readily be dispersed in water, without the need for any polymeric or surfactant stabilizers (Kuila et al. 2012). The covalent behaviour of C-O bonds affects the sp^2 conjugation of the hexagonal graphene lattice, making GO an insulator. This GO could be made conductive by removing the oxygen containing groups that are attached on its surfaces through hydrazine reduction under controlled conditions (Li et al. 2008). The resultant material is termed as 'Reduced' Graphene Oxide (rGO) where the

important electrical properties have been partially restored. The availability of metal salts and acids can neutralize the charges on the GO sheets that are likely to cause agglomeration or even restacking to form graphite. The reduction process has a strong influence on the GO solubility and stability by significantly removing those residual electrolytes and thus made the sheets electrostatically more stable (Li et al. 2008).

2.8 GRAPHENE FOR WATER PURIFICATION

Water can be made potable in multiple ways that include filtration, osmosis, adsorption, desalination, disinfection and sedimentation. Among them, adsorption holds major advantages and it is often preferred for the purification of industrial effluents (Kemp et al. 2013). Graphene, a promising adsorbent is found effective in water purification because of its higher surface area, antibacterial properties and lesser cytotoxicity than the carbon nanotubes. However, its immediate use for practical applications (such as water purification) is still limited due to the difficulty in large scale synthesis and post treatment handling, which include solid-liquid separation (Sreeprasad et al. 2013). Recent studies have indicated that graphene, graphene oxide and graphene modified nanocomposites could remove different toxic pollutants such as dyes (rhodamine B, orange G, methyl violet, methylene blue), pesticides and halogenated compounds, heavy metals (arsenic, lead, cobalt, cadmium, mercury, chromium), radionuclides and bacteria from the aqueous solution. Additionally, water desalination could also be done using graphene through capacitive deionization (CDI) method (Sreeprasad and Pradeep 2012).

2.8.1 Heavy metals

Heavy metals, even at low concentration, are believed to be risky for human beings. The adsorption mechanism provides flexibility in the design, operation and treatment of contaminated water by the filtration membranes. The adsorbents can be regenerated with an appropriate desorption process that is of low maintenance cost, high efficiency and ease of operation (Hua et al. 2012). An attempt of synthesizing graphene oxide (GO) modified ferric hydroxide was found encouraging in the removal of arsenate ions from the water at the pH range of 4 to 8 (Zhang et al. 2010). Arsenic is naturally present in water either in trivalent As(III) or in pentavalent As(V) state. The rGO modified magnetite (M-rGO) having super

paramagnetic behaviour at room temperature has a strong binding capacity for As(III) and As(V) that are present in aqueous solutions. This adsorption is likely to occur when the pH of solution is neutral (Chandra et al. 2010). Zhao et al. (2011) and Zhao et al. (2011) have suggested that the oxygen containing groups on the surfaces of GO sheets played an important role in the adsorption of Pb(II), Cd(II) and Co(II) ions from aqueous solutions. Hence, at higher pH, this adsorption was significant because of additional surface complexation that takes place in between the metal ions and the oxygen containing groups on GO surfaces.

Chromium in water exists either in trivalent Cr(III) or in hexavalent Cr(VI) state. Graphene based nanocomposites, having magnetic properties, are found better in removing Cr(VI) from aqueous solution. This adsorption of chromic acid (HCrO_4^-) on the surfaces of magnetic graphene nanocomposite was found to occur only at low pH (1 to 3) (Zhu et al. 2011). Substantial amounts of Hg(II) were removed from aqueous solution by the use of rGO-metal/metal oxide composites. These composites were formed through a redox like reaction between rGO and the metal precursor. The composites such as rGO-Ag and rGO-MnO₂ were anchored on river sand (RS) using chitosan (Ch) as the binder and thereby such composites were applied in water purification. Removal of Hg(II) using these composites was found to be two fold higher than the plain rGO sheets (Sreeprasad et al. 2011). Figure 2.18 shows the kinetics of Hg(II) adsorption by different adsorbents.

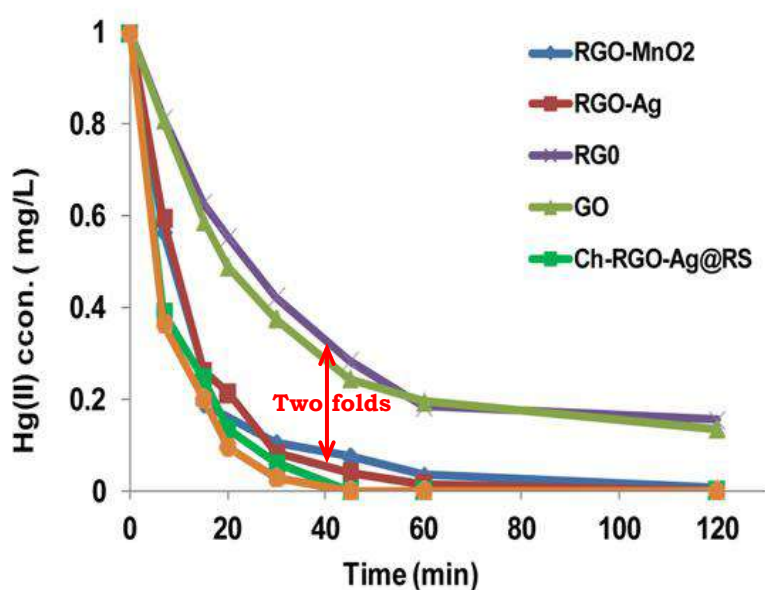


Figure 2.18 Kinetics of Hg(II) adsorption by different adsorbents (Sreeprasad et al. 2011)

2.8.2 Dyes, radionuclides, pesticides and bacteria

Disposal of effluent from industries such as dyestuff, textiles, plastics, leather, rubber cosmetics and pharmaceutical into natural waters are increasing significantly (Özdemir et al. 2015). These effluents are highly coloured, low in chemical oxygen demand (COD) and high in biological oxygen demand (BOD), which is found toxic to aquatic environment (Kadirvelu et al. 2000). The dyes having a complex chemical structure are found to be stable to light, heat and oxidation agents (Kapdan and Kargi 2002). Activated carbon is dominantly used for the decolourisation of industrial effluents. GO has been recently found popular in treating the coloured water because of its higher adsorption potential than the activated carbon (Sharma 2015). The negative charge on the surfaces of GO could adsorb cationic dyes such as methylene blue (MB) and methyl violet (MV) significantly from aqueous solutions. Additionally, the removal of oxygen containing groups from the GO produces rGO, which could remove anionic dyes such as orange G (OG) (Ramesha et al. 2011). Figure 2.19 schematically show the removal of dyes on the surfaces of GO and rGO respectively.

While up to 95% of the cationic dyes were removed using GO sheets, the removal efficiency was found negligible for anionic dyes. In case of rGO, the removal efficiency of anionic dyes was found to be up to 95%, while it was nearly 50% for cationic dyes (Ramesha et al. 2011). This adsorption was mainly because of electrostatic and/or van der Waals' type interactions depending on the system. Hazardous dyes like basic red 12 and methyl orange from aqueous solutions were removed using GO sheets (Robati et al. 2016). Organic dyes could also be removed using rGO decorated magnesium hydroxide having mesoporous structure (Li et al. 2011).

Globally, the shortage of fossil fuels is mitigated using the production of nuclear energy. This process generates radioactive nuclear waste. The release of this hazardous waste (radionuclides such as ^{137}Cs , ^{235}U , ^{90}Sr and ^{129}I) into the environment may contaminate the food chain and thus seriously affect the human health. The radionuclides could be removed using GO/rGO based composites. This adsorption is mainly dependent on the pH of solution. Recent literature has reported on the removal of radionuclides from drinking water using GO/rGO based materials, and some main results are listed in Table 2.5.

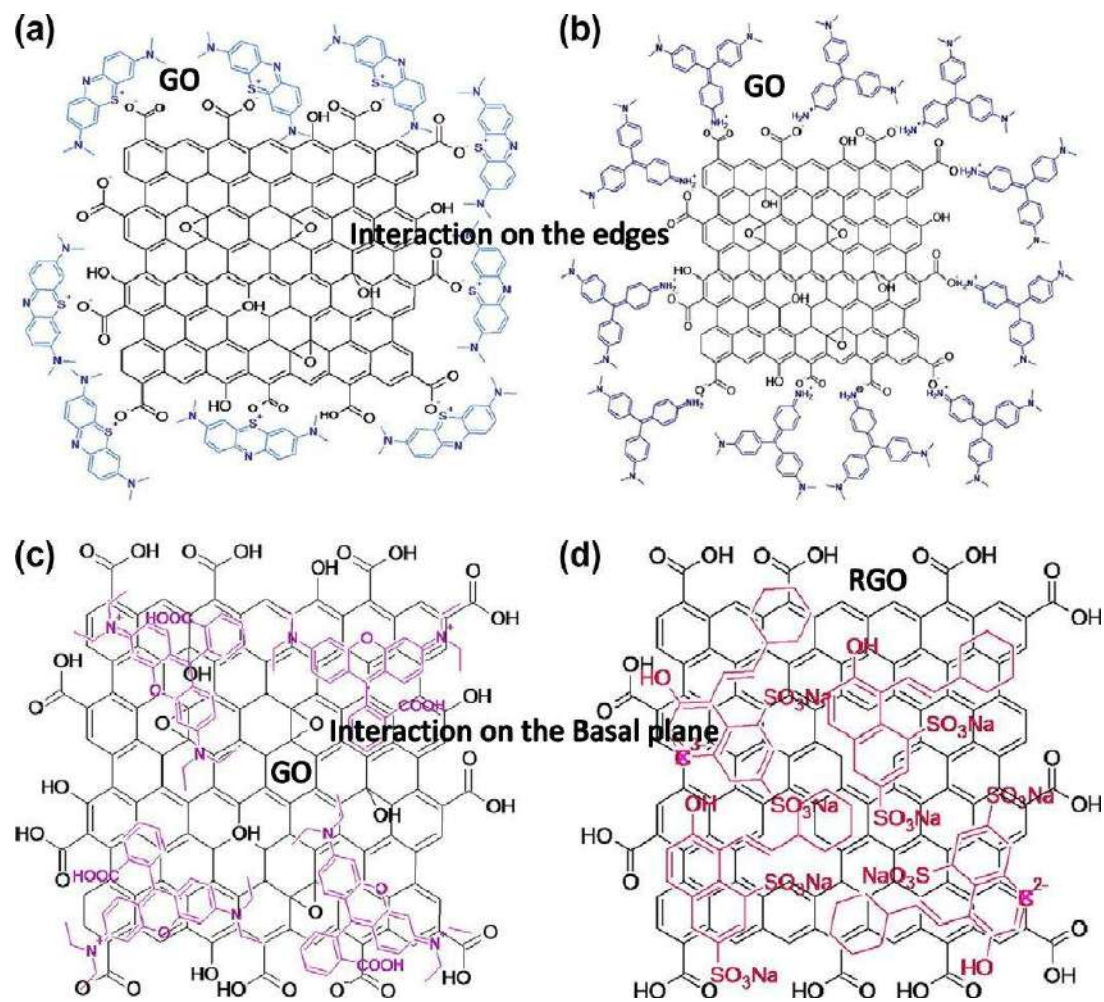


Figure 2.19 Schematics illustrating the possible interactions between (a) GO – MB (b) GO – MV (c) GO – Rhodamine B (RB) and (d) rGO – OG dyes (Ramesha et al. 2011)

Table 2.5 Removal of radionuclides from water using GO/rGO based composites

Material	Adsorbate	pH	Maximum adsorption capacity in mg/g	References
GO	U(VI)	4.0	208.33	(Ding et al. 2014)
GO	Th(IV)	2.6	214.6	(Bai et al. 2014)
GO	Sr(II)	6.5	23.83	(Romanchuk et al. 2013)
Fe ₃ O ₄ /GO	U(VI)	5.5	69.49	(Zong et al. 2013)
rGO	Th(IV)	3.0	47.72	(Pan et al. 2013)

Pesticides are often used in agricultural fields, golf courses, forested and landscaped areas. The residue from such pesticides is likely to dissolve in runoff and thus contaminate the surface and ground water. This water on consumption is highly carcinogenic to humans (Nagappa and Chandrappa 2007). rGO substrate has a strong influence to adsorb pesticides such as endosulphan, chlorpyrifos and malathion from drinking water (Maliyekkal et al. 2013). Organo phosphorus pesticides could be removed from aqueous solution using graphene coated silica (Liu et al. 2013).

Graphene, an antibacterial agent could remove *Escherichia coli* (*E. coli*) from the drinking water. This removal is greatly dependent on the morphology and lateral dimensions of graphenic sheets. The presence of GO could weaken the metabolic activity of *E. coli* and thus kill those micro-organisms. The larger GO sheets exhibit higher antimicrobial behaviour than the small sized sheets because of their potential to cover the maximum of the cell surfaces (Liu et al. 2011).

2.9 PERFORMANCE OF GRAPHENE OXIDE MODIFIED CEMENTITIOUS COMPOSITES

The movement of deleterious ions through the pore network of cementitious materials could be decreased using nanosized materials having higher surface area (Kawashima et al. 2013, Pacheco-Torgal and Jalali 2011, Sanchez and Sobolev 2010). From the existing literature, it can be noticed that the modification of cementitious composites using nanomaterials such as

multiwalled carbon nanotubes, carbon nanofibre, alumina and silica nanoparticles substantially improved the mechanical and durability properties (Barbhuiya et al. 2014, Said et al. 2012, Tyson et al. 2011, Yazdanbakhsh et al. 2010).

Nanoparticles with higher surface area are found to adsorb the free water significantly, providing the potential for higher chemical reactivity with the binder phases (Sanchez and Sobolev 2010). Subsequently, the nanomaterials are perceived to act as nucleation sites for the progressive growth of hydration crystals at early ages and thus decreasing the fraction of unhydrated cement (Li et al. 2015, Lv et al. 2013, Makar and Chan 2009). The addition of superplasticizer can compensate the loss in workability and also assists in reducing the agglomeration of nanomaterials that is caused because of van der Waals' attraction. (Konsta-Gdoutos et al. 2010, Metaxa et al. 2013, Pan et al. 2015, Quercia et al. 2012).

Among nanomaterials, the investigations on graphene oxide as an additive are becoming popular (Chuah et al. 2014, Gong et al. 2014, Lv et al. 2014, Pan et al. 2015). Figure 2.20 shows the reaction that can occur in between the carboxylic acid groups of graphene and hydration products of cement.

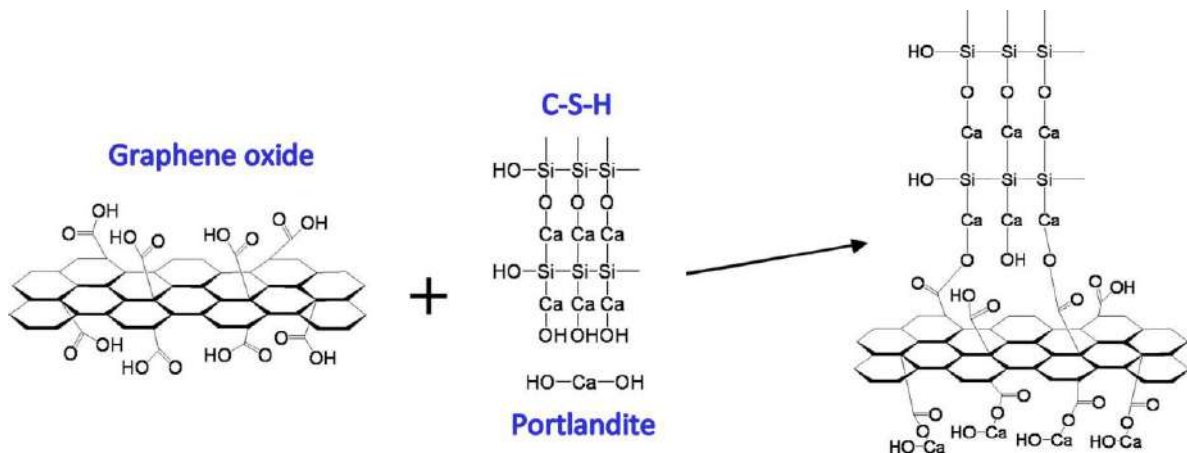


Figure 2.20 Schematic representation of the reaction between the -COOH groups of graphene and hydration products of cement (Pan et al. 2015)

Wang et al. (2016) have commented that the -COOH groups in GO sheets react with the Ca^{2+} based hydrates, thus forming a 3-D network structure. The formation of this structure improves the strength related properties; on the other hand, the GO sheets that are highly conductive decrease the resistivity of cementitious matrix (Sharma and Kothiyal 2016). The gel pores (1 to 10 nm) are an indication of pore system in C-S-H gel. GO addition has been

reported to increase the amount of gel pores, which indicates greater production of C-S-H gel. Both N₂ desorption and Mercury porosimetry investigations revealed such changes in the pore structure (Gong et al. 2014, Pan et al. 2015). The minor additions of 0.03 wt% GO in cement paste increased the amounts of portlandite and non-evaporable water content up to 6% and 9% respectively. The compressive, tensile and flexural strengths of this GO modified composite were found increased up to 38%, 79% and 60% than the control mix respectively (Pan et al. 2015). Figure 2.21 shows the alterations in the microstructure of 28-day cured GO modified cementitious composites.

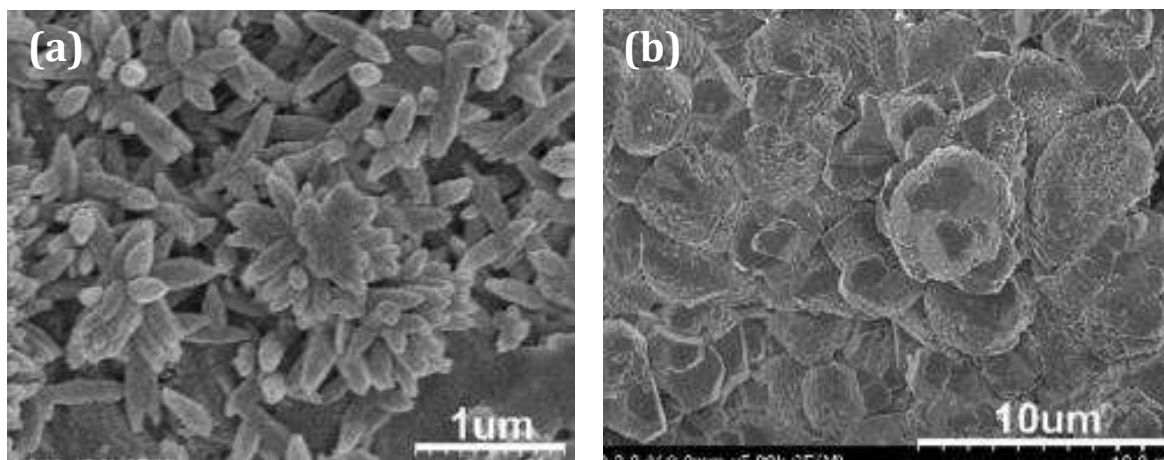


Figure 2.21 SEM images of 28-day cured cementitious pastes modified using (a) 0.01 wt% and (b) 0.05 wt% GO sheets in them respectively (Lv et al. 2014)

Dendritic clusters and polyhedral hydration crystals were seen to be formed at low and high GO dosages respectively in 28-day cured cementitious pastes (Lv et al. 2014). Graphene oxide at low dosages (0.05 vol% of concrete) had increased the acid resistance of cement concrete pipes substantially that were particularly designed for sanitary sewer environments. The diffusion of aggressive ions was delayed because of the addition of GO sheets having planar geometry and higher surface area (Peyvandi et al. 2013).

Du and Dai Pang (2015) and Mohammed et al. (2015) suggested that the tortuosity of diffusion paths was increased because of the presence of graphene nanoplatelets (GNP) in the cementitious mortar. The addition of 2.5 wt% GNP in cement mortar had decreased the water penetration depth, chloride diffusion and migration coefficients up to 64%, 70% and 30% significantly than the control mix respectively. Mohammed et al. (2016) have reported that the mass loss of 0.06 wt% GO modified cement mortar due to free thaw cycles was reduced

by 68.7% compared to the control mix. The presence of graphene sheets could have arrested the propagation of nanocracks that were initiated because of frost damage. Figure 2.22 and Figure 2.23 compares the modulus of elasticity of reference and 3 wt% GO modified cement mortar that was determined using Atomic Force Microscopy (AFM).

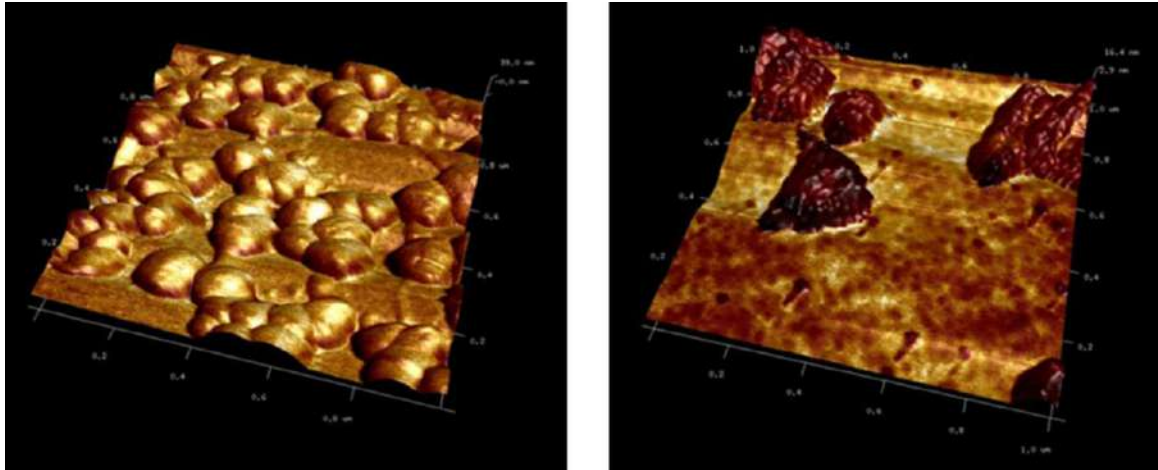


Figure 2.22 AFM image illustrating the plain (left image) and GO modified cementitious mortar (right image) (Horszczaruk et al. 2015)

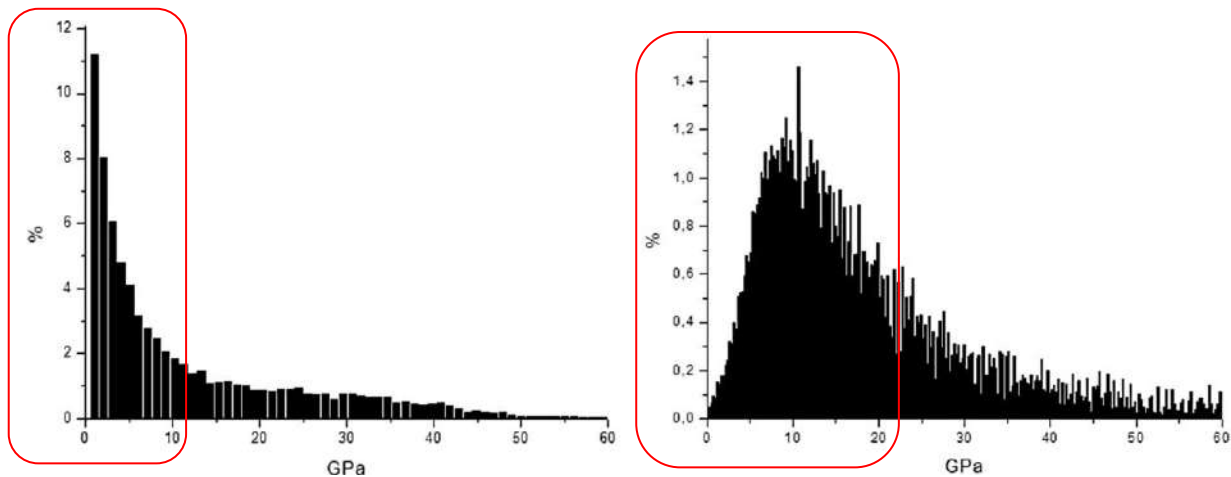


Figure 2.23 Modulus of elasticity of the plain (left image) and GO modified cementitious mortar (right image) that was determined using AFM technique (Horszczaruk et al. 2015)

The elastic modulus was noticed to be higher in GO modified cement mortar (5 to 20 GPa) than the reference mix (1 to 10 GPa). This suggests that the addition of GO sheets had enhanced the mechanical properties of the nanocomposite. (Horszczaruk et al. 2015).

2.10 SUMMARY OF LITERATURE REVIEW AND RESEARCH NEEDS

Application of nanotechnology in cementitious composites for water filtration purposes would be a novel attempt and thereby add a new dimension to the existing scientific literature. Graphene oxide (GO), which is a strong adsorbent, seems to be effective in removing the different pollutants such as heavy metals, dyes, pesticides and bacteria from aqueous solutions. The subsequent passages summarize the information gathered in the review of literatures, and bring out the needs for further study.

The first section of the review covered the heavy metals contamination in drinking water, its sources, health hazards, desirable limits and treatment methods. This was followed with a review on the material design and behaviour of porous concrete. Particularly, the capability of porous concrete pavement to retain the heavy metals from stormwater runoff was discussed. The binder phase of this porous material is likely to alter (carbonate) when exposed to CO₂ from the environment. This phase change would affect the characteristics of aqueous solutions after passage. In regards to this, a brief review of the possible changes in the binder phase when exposed to CO₂ from the atmosphere was presented. Further, the deterioration of concrete after passage of aggressive acidic solutions was also reviewed. The subsequent sections covered the effects of GO on the properties of cementitious materials; its adsorption potential towards various toxic contaminants in the water was discussed in this chapter. From the review of literature, the major challenges that are involved in the application of cement concrete based water filtration system to filter the heavy metals from the industrial effluents are listed below:

- **Need for a porous concrete system having maximum hydraulic retention time to retain the heavy metals from aqueous solutions**

The major design variables, which can increase the hydraulic retention time of porous cement concrete, need to be identified scientifically. Cementitious binder is the major ingredient that traps the heavy metals in porous concrete. Trial based experimental design is necessary to maximise the amounts of cementitious binder in the mixture, without affecting the void connectivity in porous material. Modification of cementitious materials can be attempted to trap the different toxic pollutants effectively from the industrial effluents. Preparatory guidelines to achieve a porous concrete with controlled levels of hydraulic conductivity for the laboratory environment is lacking. An image based

approach is found necessary to analyse the pore related properties such as voids size, surface porosity, and volume fraction of interconnected and disconnected voids in the porous concrete. Furthermore, imaging of voids connectivity inside such porous concrete needs further attention.

- **Need to have a fundamental understanding on the effect of graphene in cementitious composites through scientific approach**

Studies on the effect of reduced graphene oxide, alumina and silica nanoparticles on the pore structure (comprising of pores and voids) of cementitious matrices is necessary. Clear understanding of the deterioration characteristics due to soft water (acid) attack in cementitious matrices modified using reduced graphene oxide, alumina and silica nanoparticles is needed. The performance evaluation of paste systems using changes in pH and mass, and microanalytical studies such as SEM, OM, X-ray CT, nanoindentation, TGA and MIP need to be conducted to explore the deterioration mechanisms associated with the interactions between hydrated phases and acidic solution at different time periods. The dispersion effect of rGO of different concentrations in the cement paste systems needs to be studied. Additionally, the effects on rheology and fracture toughness of the cementitious matrix should also be investigated.

- **Need for a scientific approach to understand the quality of filtrate obtained through the porous cement concrete modified using reduced graphene oxide**

The effect of concrete carbonation on the physical characteristics of water such as pH, turbidity and hardness after passage needs to be analysed. Investigation of the effect of sediment blockage on the hydraulic properties of porous cement concrete is necessary. The filtration performance of porous concrete modified using reduced graphene oxide, which is a new field of study, needs to be explored scientifically. Fundamental mechanisms which trap the heavy metals on binder phases have to be addressed at a microstructural level. Adsorption of heavy metals onto cementitious binder has to be studied using batch-adsorption process. The influence of contact time, pH and adsorbent dosage on the adsorption process also needs to be studied. A comparison between the porous concrete and commercially available water filtration methods in terms of cost and performance is lacking.

CHAPTER 3

MATERIALS AND METHODS

3.1 INTRODUCTION

The present study investigates the filtration properties of porous cement concrete modified using reduced graphene oxide (rGO) nanosheets. The details of the raw materials used in its preparation are discussed in this chapter. This is followed by a discussion of the techniques - inductively coupled plasma – mass spectrometry (ICP-MS), pH and turbidity, which were used to analyse the quality of filtrate obtained through the porous concrete specimens. This chapter also discusses in detail, the principles and methods of the microanalytical studies involved in the characterization of rGO modified cementitious matrix exposed to aggressive environments; the characterization techniques include scanning electron microscopy (SEM), optical microscopy (OM), X-ray computed tomography (CT), mercury intrusion porosimetry (MIP), thermogravimetric analysis (TGA), Fourier transform infrared spectroscopy (FTIR), X-ray diffraction (XRD) and nanoindentation.

3.2 MATERIALS USED

This section describes the properties of the concrete ingredients which include cement, aggregate and superplasticizer that were used in this study. Additionally, the different nanomaterials such as reduced graphene oxide, alumina and silica nanoparticles that were added into the cementitious matrix are also described.

3.2.1 Cement, aggregate and superplasticizer

53 Grade ordinary Portland cement (62.16 wt% CaO, 20.95 wt% SiO₂, 5.14 wt% Al₂O₃, 3.06 wt% Fe₂O₃, 3.08 wt% SO₃, 1.33 wt% MgO and 0.009 wt% Cl) and crushed granite coarse aggregate conforming respectively to IS 12269 (2013) and IS 383 (1970) were used in the present study. The specific surface area of cement, determined using Blaine's apparatus conforming to ASTM C204 (2011), was 340 m²/kg. The specific gravity (SSD) and water

absorption of coarse aggregate were found to be 2.77 and 0.42% as per the methods prescribed in IS 2386-3 (1963). Figure 3.1 illustrates the size distribution profile of coarse aggregates that were used in the preparation of porous concrete modified using graphene nanosheets.

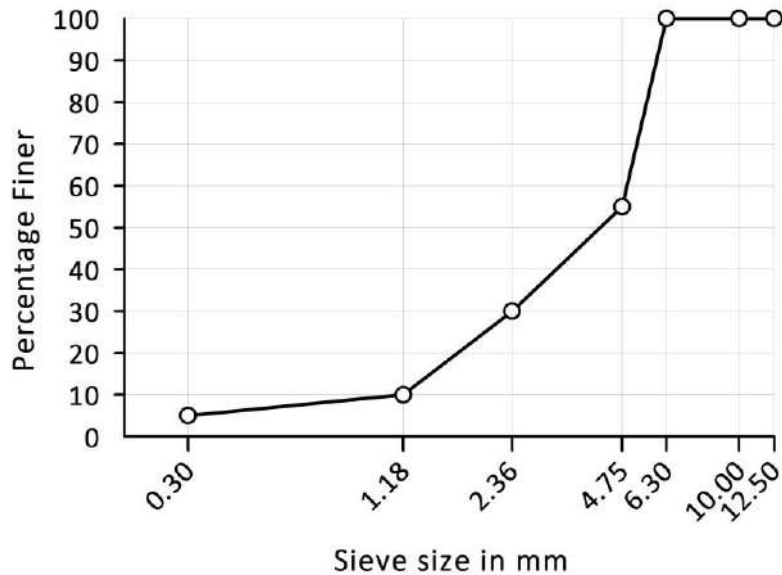


Figure 3.1 Particle size distribution of coarse aggregate that was used in the preparation of porous concrete modified using graphene nanosheets

Polycarboxylate ether based superplasticizer (solids content of 40.86%) and distilled water having pH of 6.64 and 6.98 respectively were the remaining materials used in the preparation of porous concrete.

3.2.2 Reduced graphene oxide, alumina and silica nanoparticles

The effect of graphene on the properties of cementitious paste was investigated in comparison to popularly reviewed nanomaterials such as dry nano alumina and colloidal nano silica. The alumina and silica nanoparticles were procured from Sigma Aldrich, India. The mean particle size and specific surface area of these nanomaterials were specified by the manufacturers as 50 nm and 40 m²/g, and 12 nm and 225 m²/g respectively. In this study, the graphene was synthesized at large scale using a top-down approach. The chemical elements present in the raw nanomaterials were verified using SEM/EDS analysis. Figures 3.2 to 3.5

illustrate the EDS (energy dispersive spectroscopy) spectra and micrographs of agglomerated graphene, alumina and silica nanoparticles respectively that were used in this study.

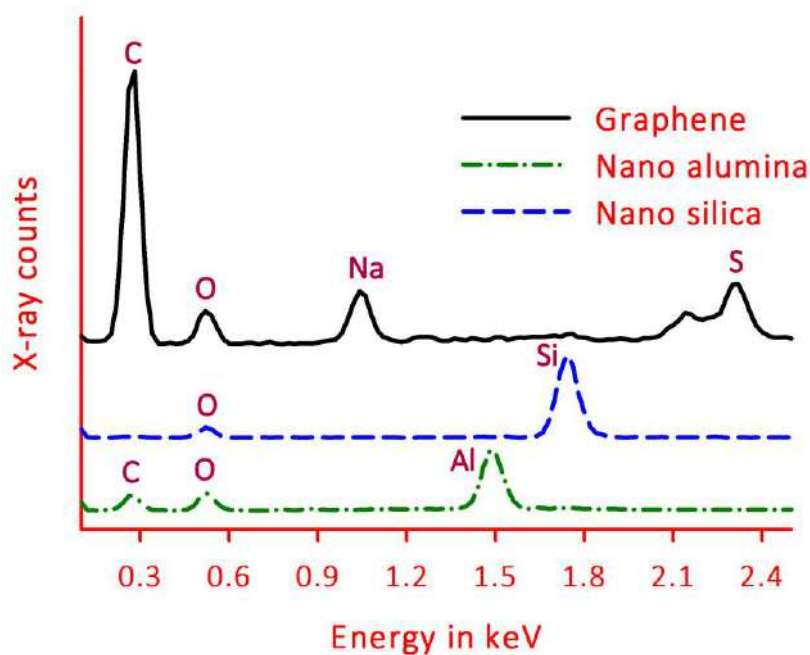


Figure 3.2 EDS spectra showing the presence of different elements in the reduced graphene oxide (rGO), alumina (Al_2O_3) and silica (SiO_2) nanoparticles

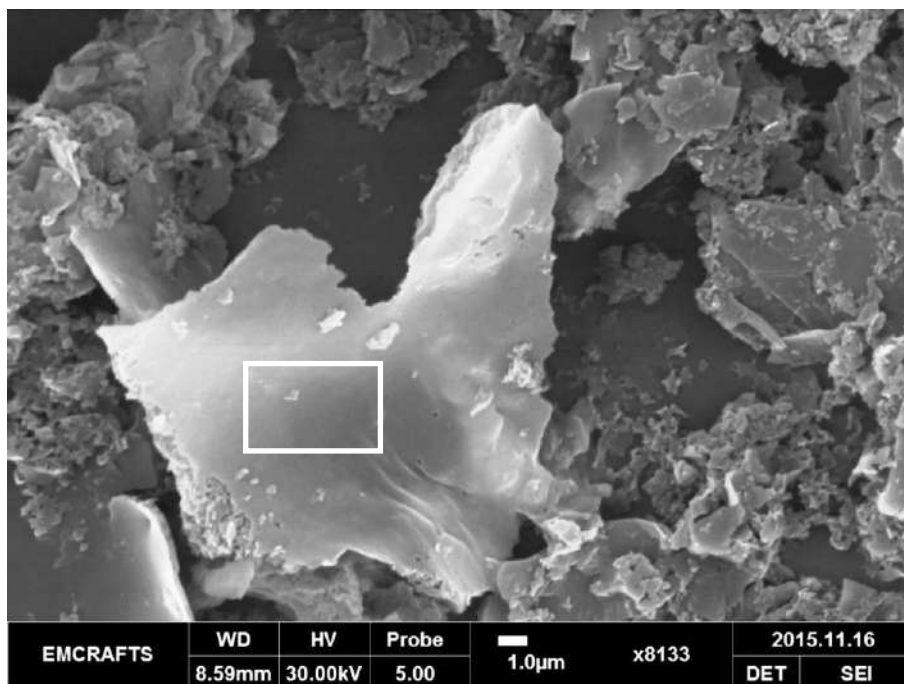


Figure 3.3 Micrograph illustrating the agglomerated reduced graphene oxide sheets that were synthesized in this study using modified Hummers' method

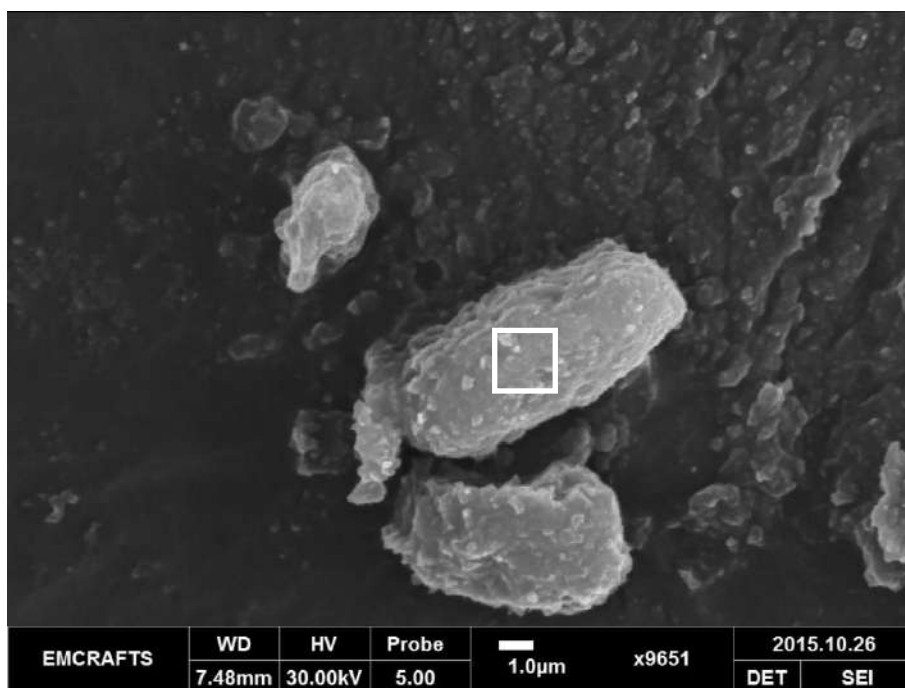


Figure 3.4 Micrograph illustrating the agglomerated alumina nanoparticles that were procured from Sigma Aldrich, India

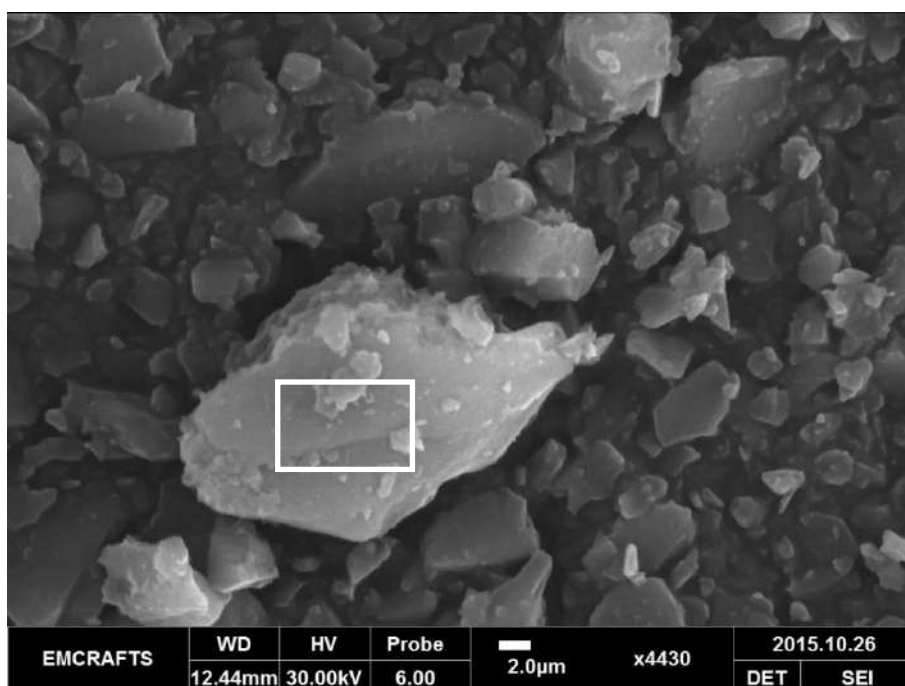


Figure 3.5 Micrograph illustrating the agglomerated silica nanoparticles that were procured from Sigma Aldrich, India

When agglomerated, the wrinkled graphene sheets were multi-stacked and the remaining nanomaterials were found to be irregular shaped particles. These inferences were found useful while locating the bundled nanomaterials in the pastes at the time of SEM imaging. The following sections describe the extraction of reduced graphene oxide from natural graphite using modified Hummers' method.

Preparation of graphene oxide (GO)

Firstly, a solution containing 25 mL of concentrated H_2SO_4 , 5 g of $\text{K}_2\text{S}_2\text{O}_8$ and 5 g of P_2O_5 was stirred constantly in a 250 mL beaker maintained at 80 °C. Once these reactants were completely dissolved, 6 g of graphite powder was gradually added to the mixture and left under constant stirring for 5 hours. This hot mixture was cooled at room temperature and next diluted using 1 L of distilled water. The resultant solution was left undisturbed overnight and then filtered and washed subsequently to remove the excess acids present in the mixture. The solids obtained after the removal of acids were dried overnight in air.

Secondly, 230 mL of concentrated H_2SO_4 was added to this pre-oxidized graphite maintained at 5 °C in an ice bath. 15 g of KMnO_4 was gradually added to this mixture, while maintaining the temperature below 10 °C. The resultant solution was stirred for 2 hours at 35 °C and then diluted using 1 L of distilled water, which was once again stirred for 2.5 hours. To this mixture, 25 mL of 30% H_2O_2 and 1.5 L of distilled water were further added and then left undisturbed up to 24 hours. The supernatant was removed and the remaining was centrifuged and washed using 10% HCl , and distilled water for several times. After this centrifugation process, the resultant solids (precipitate) were dried and then a 2 wt% (w/v) dispersion was prepared in distilled water. Dialysis was done to this dispersion to remove the excess salts and acid and next diluted to extract 0.5 wt% (w/v) graphene oxide (GO).

Preparation of sulphonated reduced graphene oxide (rGO)

Pre-reduction, sulfonation and post-reduction were the three major stages that were involved in extracting the reduced graphene oxide using redox reaction. The pre-reduction of GO was done to remove the oxygen functionalities by adding Na_2CO_3 (5 wt%) and 800 mg of NaBH_4 and the mixture was then heated at 80 °C for 60 minutes. The resultant mixture was cooled, centrifuged, washed with water several times and again re-dispersed in distilled water. 20 mg

of Sulfanilic acid and 8 mg of sodium nitrite dissolved in 0.25% NaOH solution were added to the resultant mixture. This was stirred well and then 4 mL of 0.1 M HCl solution was added such that the reaction mixture was kept in an ice bath under stirring. Once again, the mixture was cooled, centrifuged, washed with water several times and again re-dispersed in distilled water. This sulfonation was done to increase the solubility of graphene oxide in water. The reduction process of GO was schematically illustrated in the Figure 2.17 of Chapter 2. Post-sulfonation, the majority of oxygenated groups that were attached to the graphene surfaces were removed by adding 40% hydrazine hydrate ($\text{NH}_2\text{NH}_2 \cdot \text{H}_2\text{O}$) (5mL) to the resultant solution, which was heated at 95 °C for 24 hours under constant stirring. This hot mixture was cooled, centrifuged, washed with water several times and again re-dispersed in distilled water. Finally, the rGO (0.5 wt%) was dialysed and retained as stock solution. TEM image of this rGO, indicating a wrinkled surface texture is illustrated in Figure 3.6.

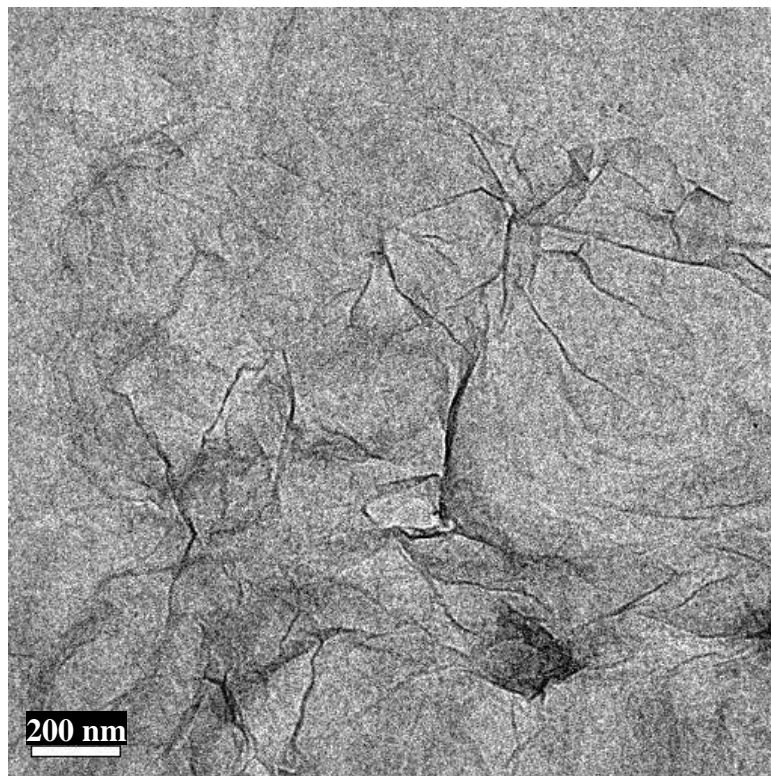


Figure 3.6 TEM image of reduced graphene oxide, indicating a wrinkled surface texture (the image was obtained using JEOL 3010 Transmission Electron Microscope)

This rGO, which is electrostatically stable and has adsorption properties alike pristine graphene, was used in the present study to modify the porous cement concrete. Figure 3.7

shows a photograph illustrating the change in colour when the graphene oxide was reduced using hydrazine hydrate.



Figure 3.7 Graphene oxide (left image) and reduced graphene oxide (right image); both were dissolved in distilled water

3.3 ANALYSIS OF WATER QUALITY

3.3.1 pH and turbidity

pH is a measure of the hydrogen ion concentration of an aqueous solution. A typical pH meter has two components namely an electronic meter and a pH probe. This probe consists of one reference electrode and one glass electrode. The immersion of this probe in an aqueous solution causes a potential difference between the two electrodes and thereby pH is measured. The electronic meter interprets the potential difference and converts it to a scale of 0 to 14. Every time before use, the pH meter is calibrated using standard solutions of pH 4.01, 7 and 10.01. This calibration is then verified by measuring the pH of deionized water.

Turbidity is a measure of the degree to which the water loses its clarity due to the availability of suspended particulates. It is measured using turbidity meter which operates by the principle of light scattering or transmission. This meter employs a light beam and a light detector set to one side (90°) of the source beam which is schematically shown in Figure 3.8.

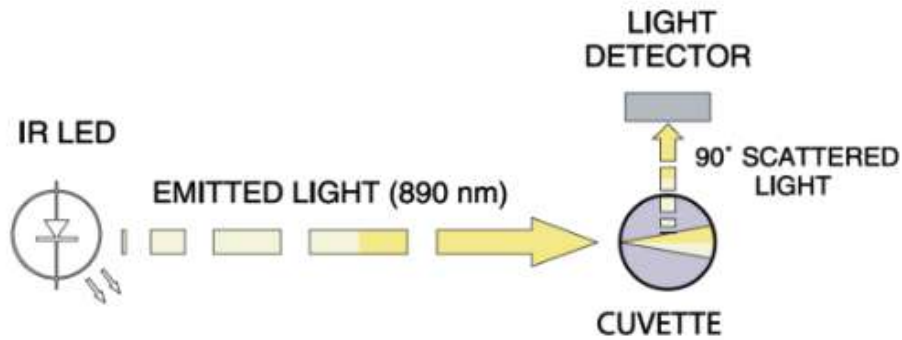


Figure 3.8 General scheme of infrared (IR) Turbidimeter (this image was reproduced from the source - <http://hannainst.com/hi98713-iso-turbidity-portable-meter.html>)

The results are shown in NTU (Nephelometric Turbidity Unit). The meter is calibrated using calibration solutions of turbidity 800 NTU, 100 NTU, 20 NTU and 0.02 NTU, before conducting measurements on the test solutions. The physical characteristics such as pH and turbidity of water percolated through the porous concrete were measured using CyberScan pH 510 Meter and Eutech TN100 IR Turbidimeter. Photographs of these instruments are shown in Figure 3.9 and Figure 3.10.

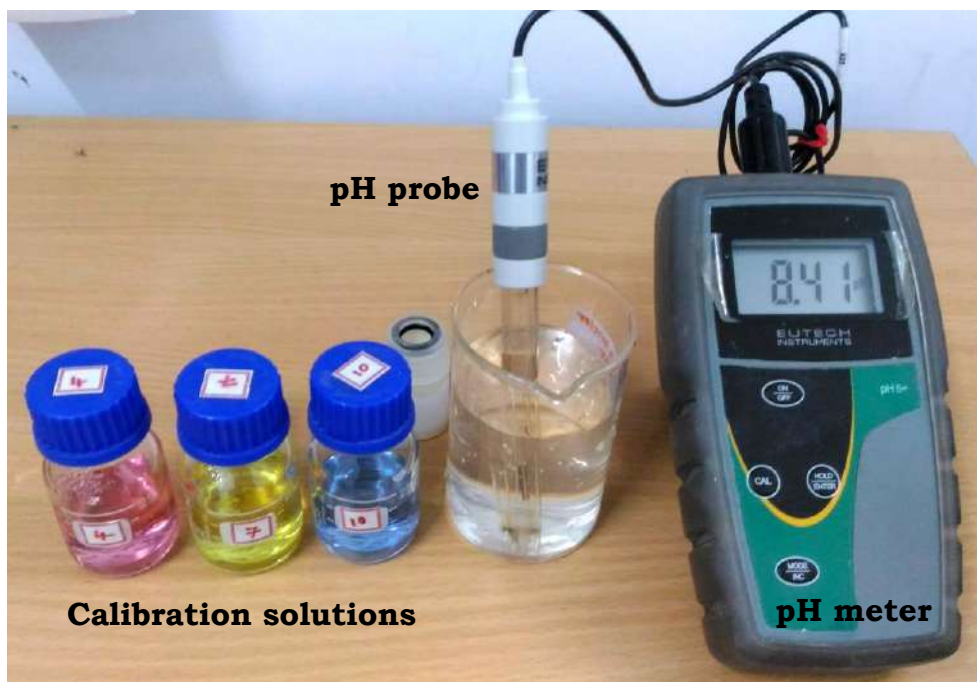


Figure 3.9 CyberScan pH 510 Meter and the standard calibration solutions having pH 4.01, 7 and 10.01 that were used in this study



Figure 3.10 Eutech TN100 IR Turbidimeter and the standard calibration solutions having turbidity of 800 NTU, 100 NTU, 20 NTU and 0.02 NTU that were used in this study

3.3.2 Inductively coupled plasma – Mass spectrometry (ICP-MS)

In this present study, the concentration of calcium ions and heavy metals such as lead, cadmium, mercury and chromium remaining in the filtrate obtained through the porous concrete specimens were analysed using ICP-MS (NexION 300X - Perkin Elmer. Plasma source: Argon, 18 L/min flow rate). The water samples containing these heavy metals were diluted with ultrapure water and next acidified using 2% HNO₃ solution. This acid treatment was done to remove the presence of volatile substances in the water sample. The calibration standards were prepared using a multi-element standard containing 30 elements. Figure 3.11 and Figure 3.12 show the general scheme and photograph of ICP-MS that was used in this study respectively.

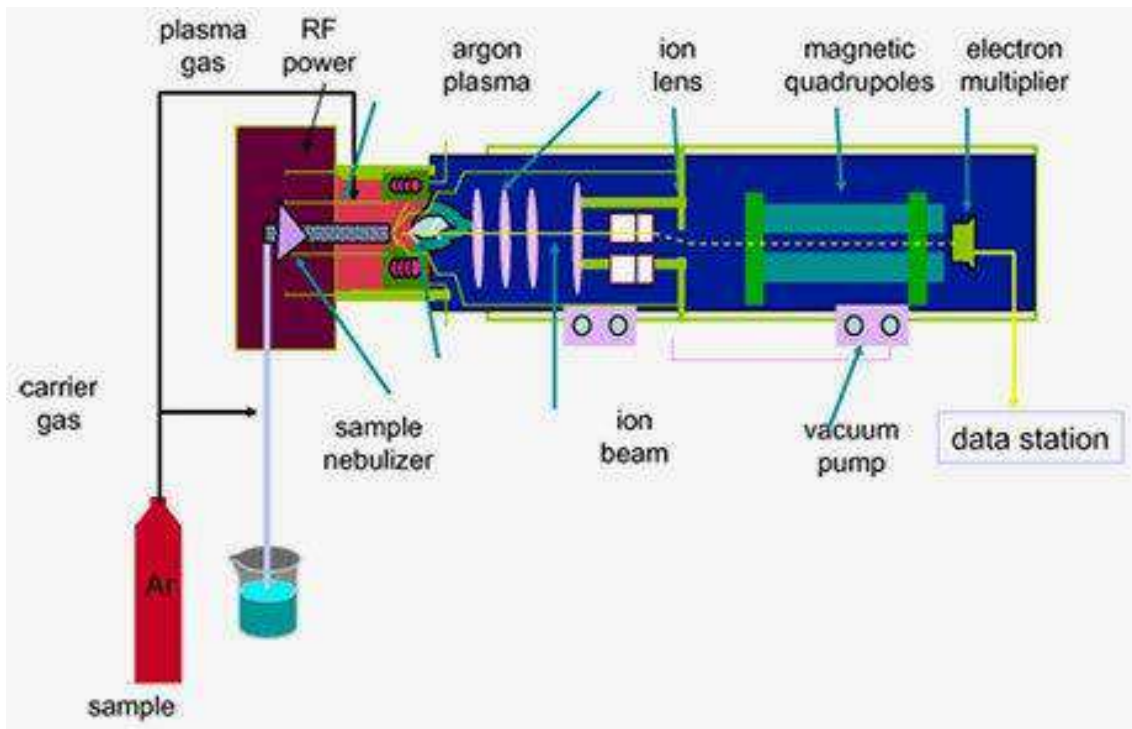


Figure 3.11 Schematic diagram illustrating the layout of ICP-MS (this image was reproduced from the source - https://www.emdmillipore.com/US/en/water-purification/learning-centers/applications/inorganic-analysis/icp-ms/_e2b.qB.s7QAAAFAniQQWTtN,nav)



Figure 3.12 Photograph of ICP-MS (NexION 300X - Perkin Elmer. Plasma source: Argon, 18 L / min flow rate) that was used in this study

This analysis technique combines a high temperature inductively coupled plasma (ICP) source with a mass spectrometer (MS). The heat source (ICP) converts the atoms of the elements in the liquid sample to ions. Next, these ions are separated and identified using mass spectrometer.

The major components of ICP-MS are injector, nebulizer, plasma torch, triple cone, quadrupole and detectors. The water sample is introduced into high-energy plasma which is composed of electrons and positively charged argon ions. In the plasma source, the material separates into individual atoms and thereby these atoms can lose electrons and become charged positive ions. Majority of the elements ionize efficiently in the hot plasma. There is a small metal plate placed at the center of the ion beam, which reflects the photons away from the detector. Then the ion beam enters the quadrupole mass analyser. In the quadrupole, the ions are separated on the basis of their mass to charge ratio. Each element has its own characteristic isotopes and masses and thereby produces its own mass spectrum.

ICP-MS is fast, precise and sensitive compared to atomic absorption techniques. It can precisely detect the heavy metals concentration in drinking water. However, the elemental analysis using ICP-MS is likely to be affected by the trace contaminants from the glassware and reagents (Beauchemin 2010).

3.4 MICROANALYTICAL STUDIES

Different characterisation techniques were used in this study to investigate the effect of nanomaterials on the microstructure of cement pastes exposed to acidic environment. The working principle of these techniques is described in the following sub-sections.

3.4.1 Scanning electron microscopy and optical microscopy

The morphology and distribution of phases in the solid material can be studied using scanning electron microscopy. In this technique, the specimen is scanned at a very fine scale with a focused beam of electrons, which results in the production of secondary electrons (SE), backscattered electrons (BSE) and X-rays. This study used two models of scanning electron microscope (SEM), namely Emcrafts Genesis 2100 and FEI Quanta 400 FEG. Figure 3.13 schematically shows the layout of an SEM.

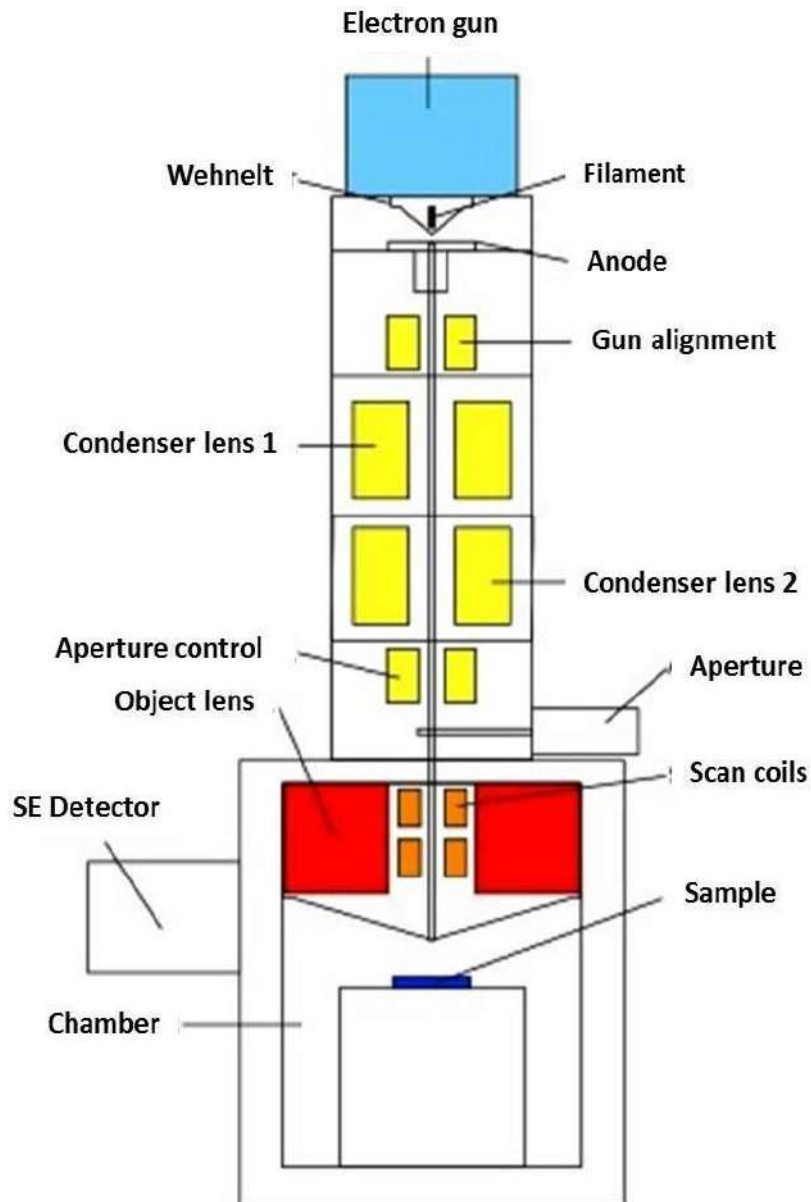


Figure 3.13 Layout of Emcrafts Genesis 2100 Scanning Electron Microscope

In the case of SE mode, an inelastic collision between the primary electrons and the loosely bound outer shell electrons of the surface atoms of the sample results in the emission of secondary electrons. These secondary electrons are captured by an Everhart-Thornley detector and the resultant image on a CRT screen helps in the visualization of the morphology or texture of the sample at a fine scale. However, the contrast of such images is highly dependent on the amounts of secondary electrons that can be emitted from the sample. In the SE image, the crest and valley regions appear brighter and darker respectively. The SE images can reveal the alterations in phases, and precipitation of new crystalline products in

the cementitious matrix exposed to aggressive environment. Figure 3.14 and Figure 3.15 show the micrograph of cementitious matrix obtained from FEI Quanta 400 FEG and Emcrafts Genesis 2100 respectively.

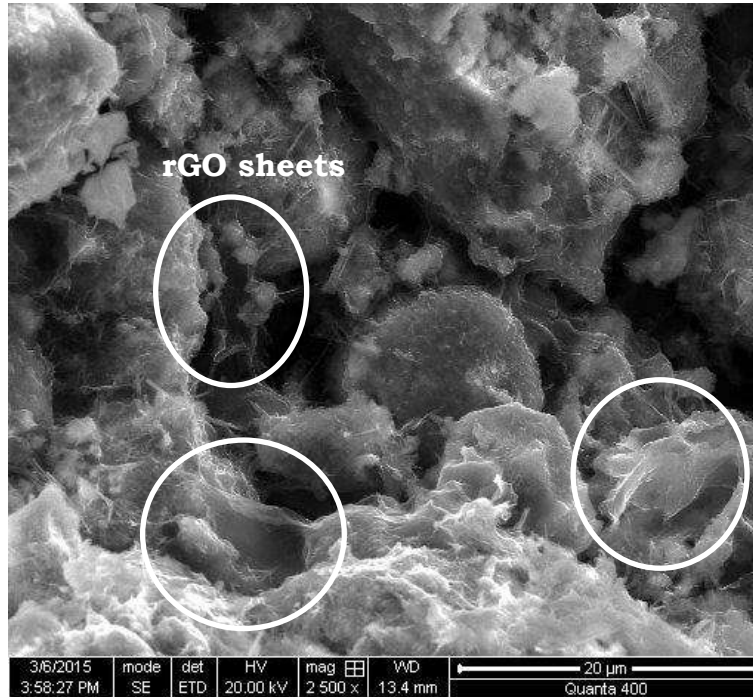


Figure 3.14 Micrograph illustrating the fractured surface of 3-day cured cementitious matrix modified using 0.06 wt% reduced graphene oxide (rGO) sheets

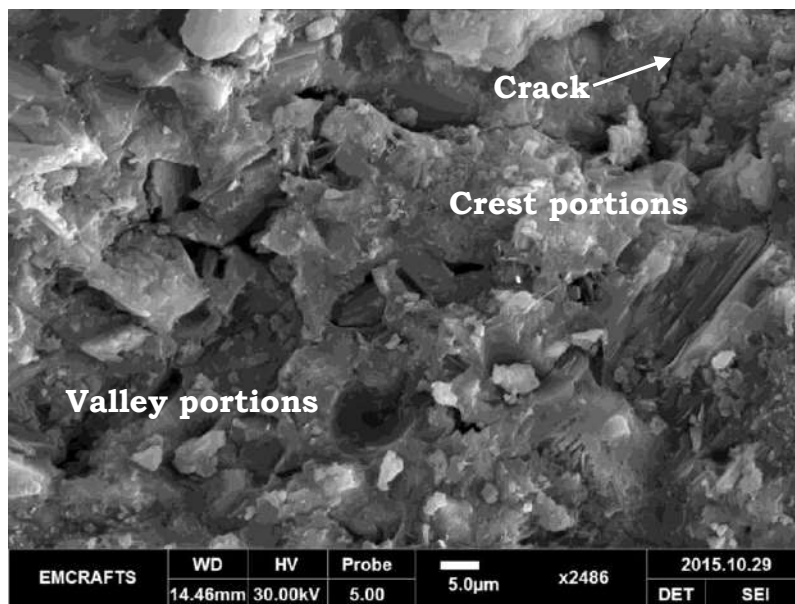


Figure 3.15 Micrograph illustrating the fractured surface of 7-day cured cementitious matrix modified using 0.06 wt% reduced graphene oxide (rGO) sheets

In general, any optical petrographic microscope is equipped with reflected and transmitted modes of operation. This study used imaging in reflected mode to visualise the alteration phases in the cement paste exposed to aggressive environments. This study used Olympus BX41 optical microscope, which was capable of 40X, 100X, 400X and 1000X magnifications because of multiple objective lenses. The trinocular head enabled the capture of images with a digital camera. Photographs of SEM and OM that were used in this study are shown in Figure 3.16 and Figure 3.17.



Figure 3.16 Emcrafts Genesis 2100 Scanning Electron Microscope that was used in this study



Figure 3.17 Olympus BX41 optical petrographic microscope that was used in this study

3.4.2 3-D X-ray computed tomography (CT)

X-ray CT is a non-destructive technique which is used to visualise the interior features within the scanned object, and also to acquire digital information on their 3-D geometries. In this study, the CT scans were done using GE phoenix v|tome|x s X-ray tomography machine which works according to Beer-Lambert law. This law relates the intensity of transmitted radiation (I) to the intensity of incident radiation (I_0), the linear attenuation co-efficient of the scanned material (μ) and the distance travelled through the material (t), which is illustrated in Equation 3.1.

$$I = I_0 \cdot \exp\left(-\int \mu \cdot(t)dt\right) \quad - (3.1)$$

The X-ray CT machine is composed of an X-ray source, detectors and a rotational geometry arrangement. The transmitted X-rays have a customised intensity dependent on the overall linear attenuation characteristics of the solid object, which is being scanned. Figure 3.18 shows the photograph and layout of 3-D X-ray CT instrument that was used in this study.

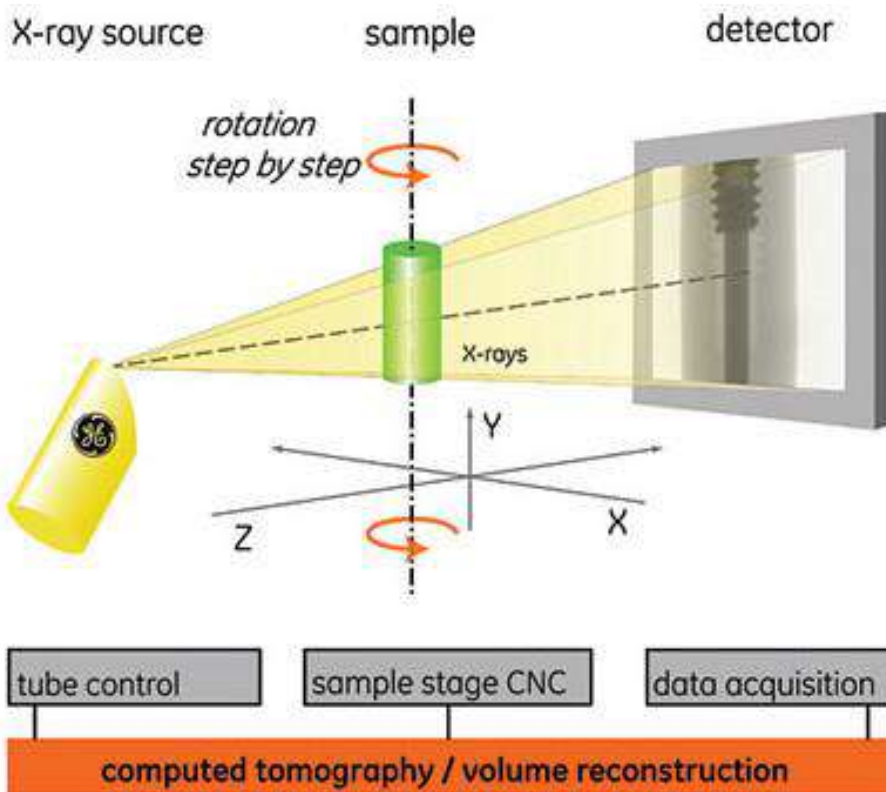


Figure 3.18 Photograph (top image) and general scheme (bottom image) of the GE phoenix v|tome|x s X-ray computed tomography instrument that was used in this study (this image was reproduced from the source – <http://www.qualitymag.com/articles/92672-industrial-x-ray-ct-quality-control-from-the-lab-to-the-production-floor>)

The CT imaging consists of focussing X-rays at an object from multiple orientations and measuring the decrease in the intensity along a series of linear paths. A specific algorithm is next used to reconstruct the distribution of X-ray attenuation within the scanned material. The reconstructed CT image is a 3-dimensional matrix of relative attenuation values. The additional insights from this CT data can be extracted using visualisation techniques such as ‘isocontouring’ and ‘volume rendering’.

Isocontouring

In general, isolines are those which have constant characteristic value on the surface of 3-dimensional scalar field and thereby such lines help to visualise the distribution of scalar quantities over the surface, which is representing a 3-dimensional analog of an isoline. These kind of constant valued curves and surfaces (isosurface) from the 3-dimensional scalar fields could be separated by applying isocontouring technique (DeFloriani and Spagnuolo 2008). The use of such technique on the CT data of a scanned material can help in separating the specific phases (voids or pores) having same CT value. It works similar to the topographic maps constructed from the gridded data (Ketcham and Carlson 2001).

Volume rendering

A digital image is generally composed of pixels (picture elements). In contrast, a CT image is composed of voxels (volume elements). In the case of volume rendering, each voxel in the volume is reserved by a greyscale (red-green-blue colour) and an opacity, which is based on the CT number. This number indicates a normalised value of the calculated X-ray absorption coefficient of a pixel in a computed tomogram. It is expressed in terms of Hounsfield units, where the CT numbers of water and air are 0 and 1000 respectively. Some voxels in the 3-dimensional CT image can be turned invisible when their opacity is set to zero and thereby the observer is able to visualise the non-transparent materials of interest through such voxels (Ketcham and Carlson 2001). Figures 3.19 to 3.21 show the images that were processed using such techniques for this study.

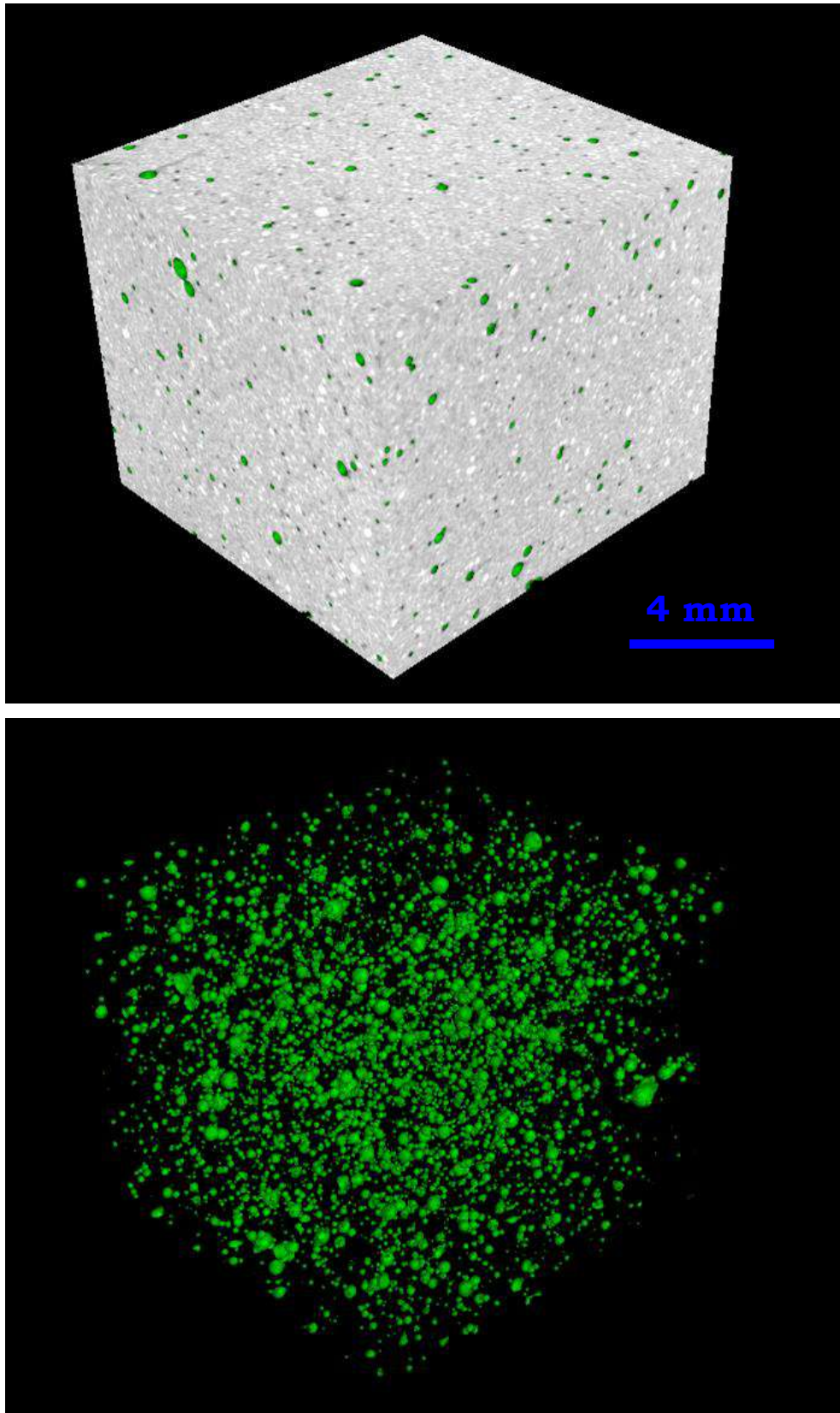


Figure 3.19 Isosurface image of cement paste sample illustrating the entrapped air voids (green in colour) and the solid phase (grey in colour) revealed by X-ray CT

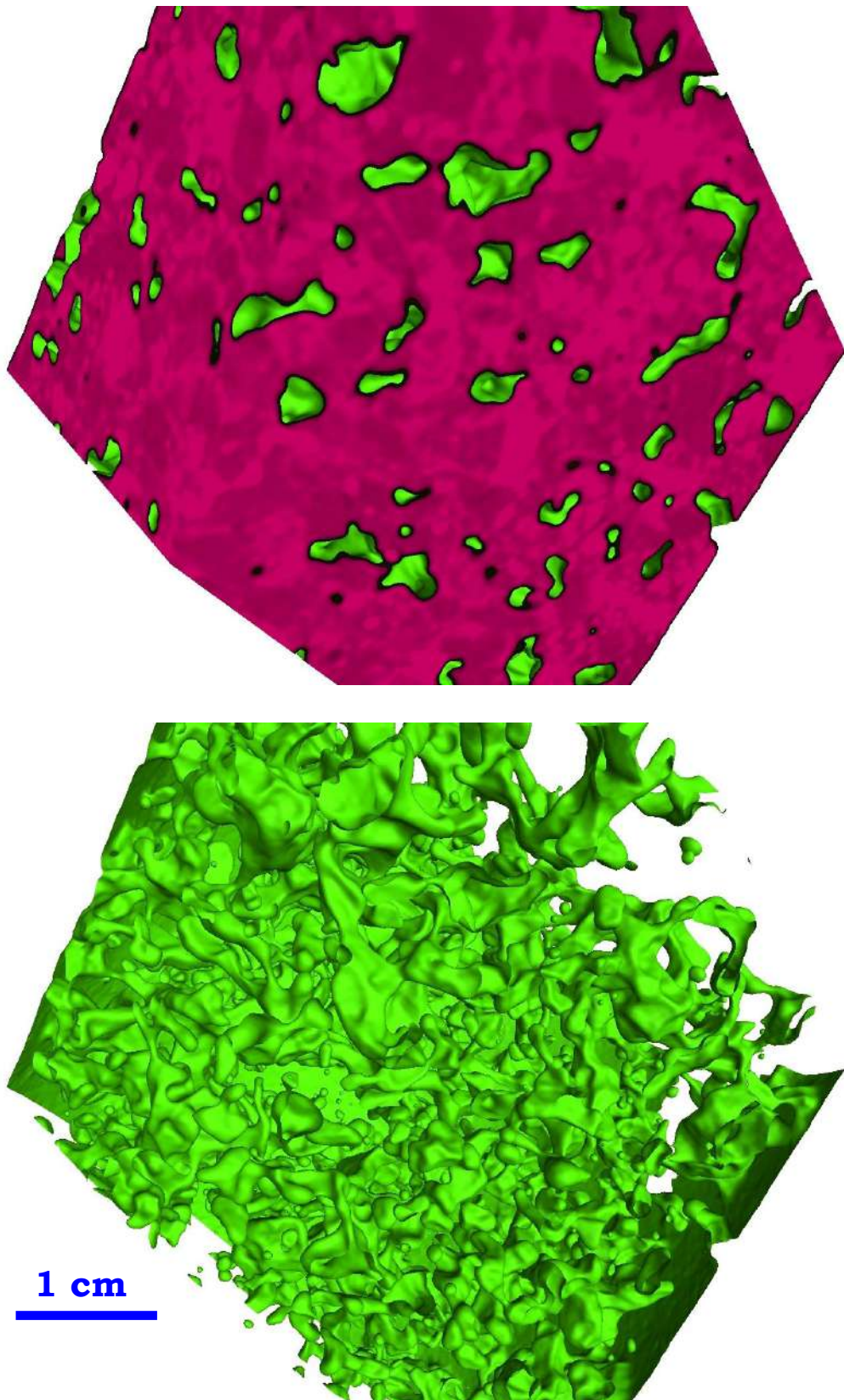


Figure 3.20 Isosurface image of porous concrete illustrating the interconnected and entrapped voids (green in colour) and the solid phase (pink in colour) revealed by X-ray CT

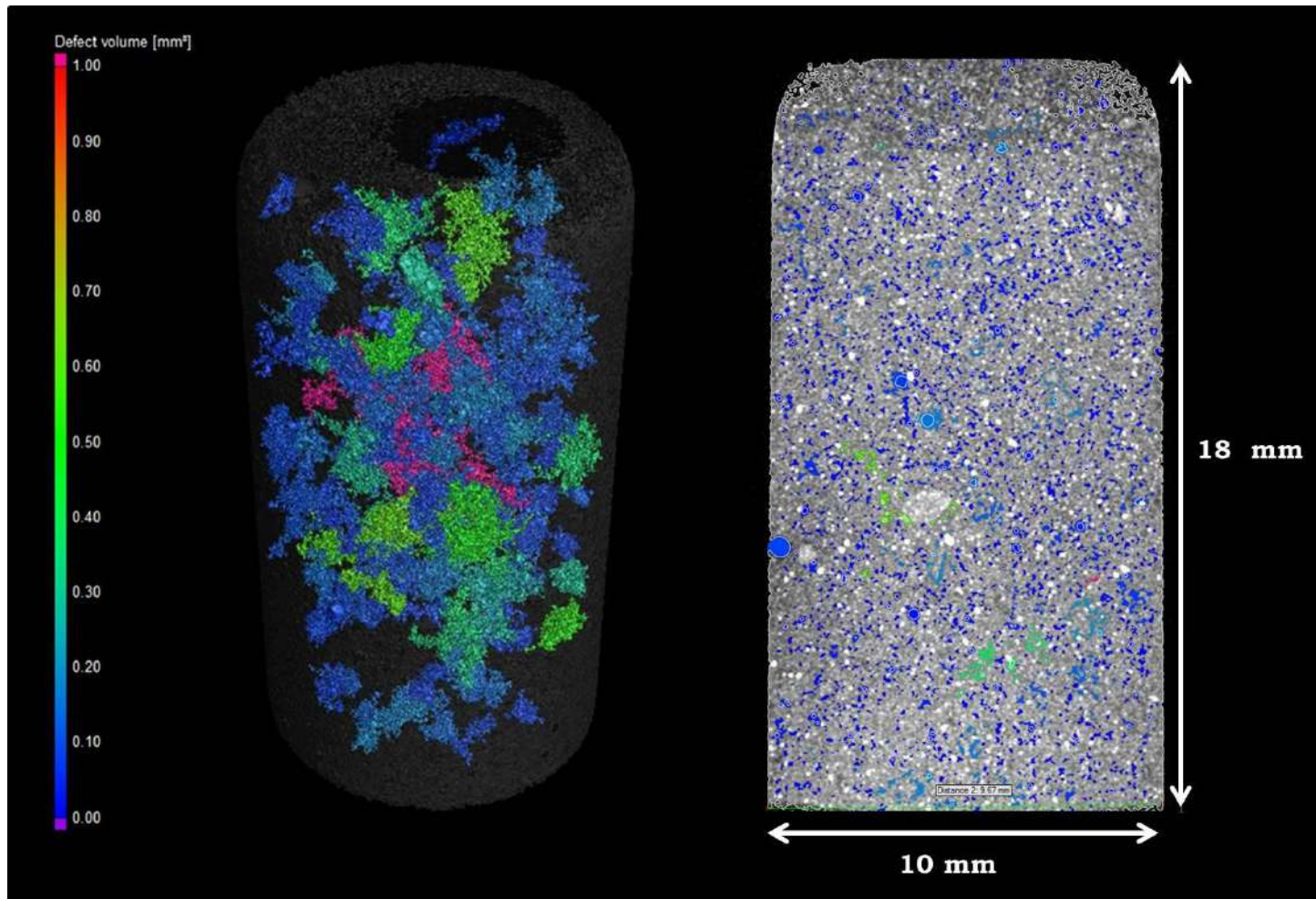


Figure 3.21 Volume rendered 2-D and 3-D views of cement paste sample illustrating the different volume of voids that were present inside the matrix after curing for 3 days

3.4.3 Thermal analysis

In this study, a combined Thermo-Gravimetry / Differential Scanning Calorimetry (TG/DSC) instrument (model named Netzch STA 409 TC) was used to determine the amounts of portlandite, calcite and non-evaporable water content available in the cementitious pastes exposed to acidic environment. Differential scanning calorimetry (DSC) measures the change in heat flow into a sample and a reference material, as a function of time and temperature in a controlled environment. Simultaneously, the rate of change in their masses is measured by Thermogravimetric analysis (TGA). Figure 3.22 shows the photograph and general scheme of power compensated type differential scanning calorimetry, which has a separate furnace for the sample and reference material.

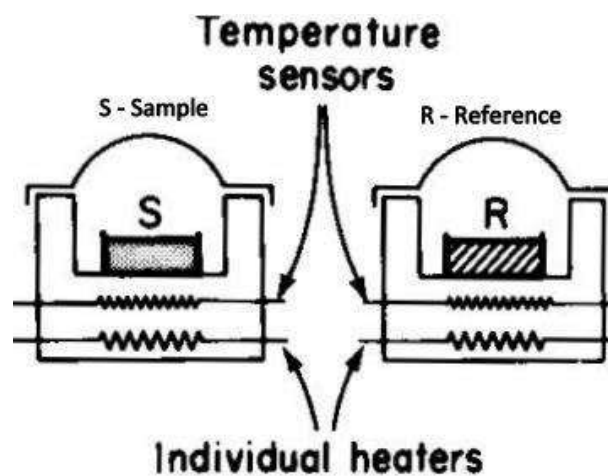
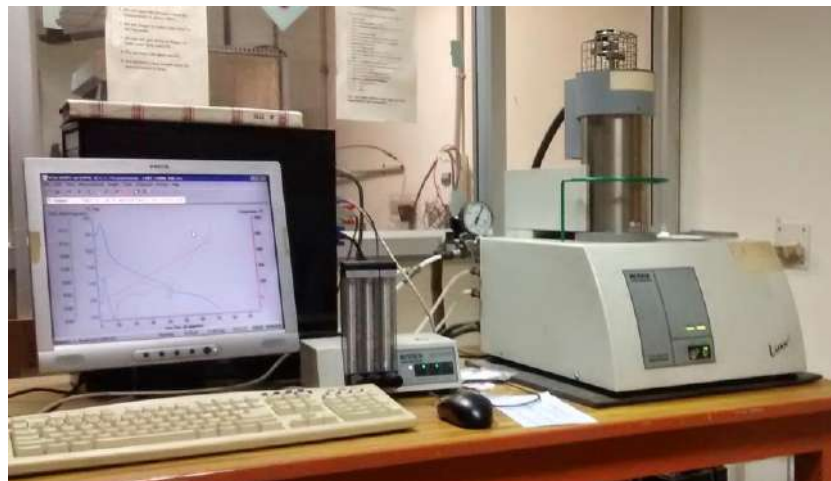


Figure 3.22 Photograph (top image) and general scheme (bottom image) of power compensated type DSC

The TG/DSC instrument is built with a differential detector, signal amplifier, furnace, temperature controller, gas control device and data acquisition device. Alumina crucibles were used in this study because of their capability to remain stable at very high temperature (~ 1000 °C). In this study, the 28-day cured cement pastes were ground and then passed through 75 µm standard sieve. The powdered samples were next heated up to 1000 °C at a rate of 10 °C per minute in an inert (N₂) environment. The amounts of bound water, portlandite and calcite present in such samples were determined using thermal analysis. Figure 3.23 illustrate the TGA pattern of 28-day cured cement paste sample that was prepared using a w/c ratio of 0.32.

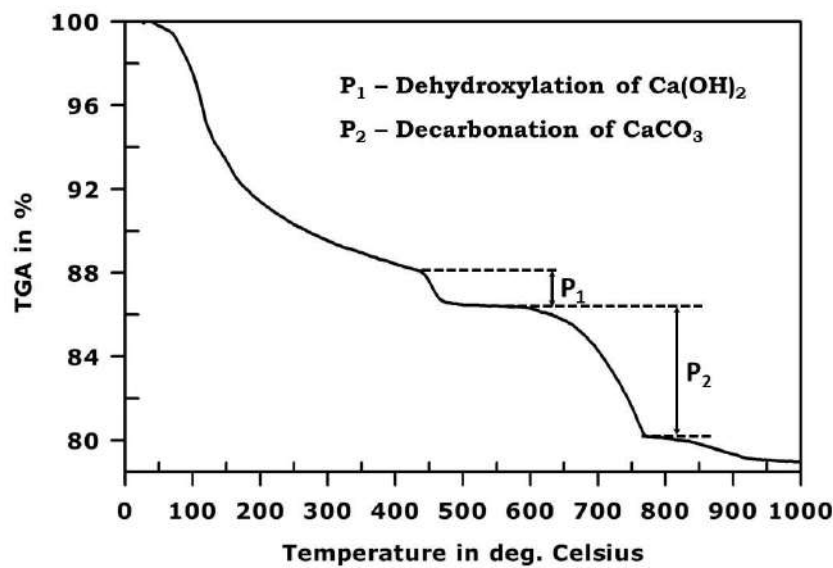


Figure 3.23 TGA plot of 28-day cured cement paste sample that was prepared using a w/c ratio of 0.32

P₁ and P₂ in the TGA plot indicate the gravimetric change due to Ca(OH)₂-dehydroxylation (430 to 480 °C) and CaCO₃-decarbonation (600 to 780 °C) respectively. Additionally, the amounts of bound water in such sample is characterised by the mass loss between 105°C and 975°C, discounting the mass loss that is associated with the decomposition of CaCO₃.

3.4.4 Nanoindentation

The nanoindentation technique helps in determining the mechanical properties such as Young's modulus, fracture toughness, hardness, creep, phase transformation, residual stresses and energy absorption of materials at the nanometer level. The nanomechanical properties of

pastes exposed to acidic environment were determined in this study using Hysitron TI Premier Nanoindenter. This technique produces an imprint in the material by applying a continuously increasing force with a very small indenter tip. Due to this indentation, the sample undergoes elastic-plastic deformation which is schematically shown in Figure 3.24.

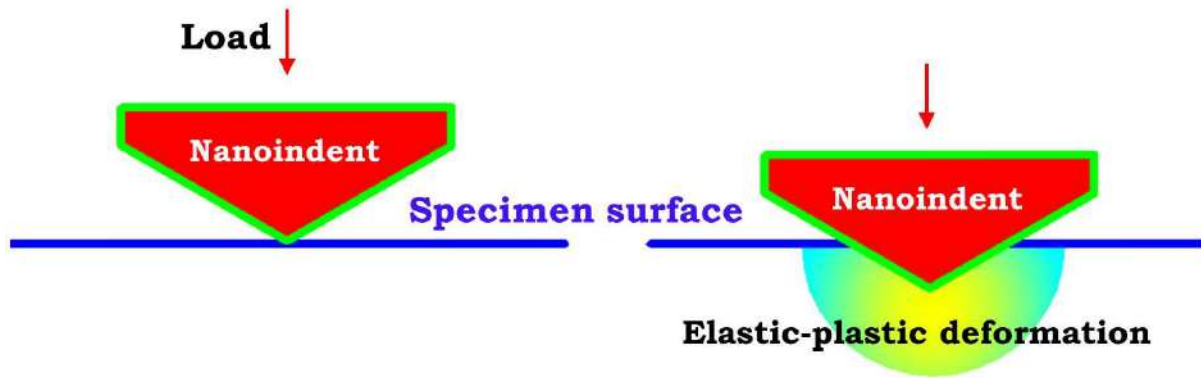


Figure 3.24 Schematic illustration of the elastic-plastic deformation in the material which occurs due to indentation

Berkovich tip (three-sided pyramid tip) was used in this study to investigate on the polished surfaces of cementitious matrix. The hardness and Young's modulus is determined as a function of load, as illustrated in Equations 3.2 and 3.3 respectively (Mallikarjunachari 2016).

$$\text{Hardness, } H = P / A_c \quad - (3.2)$$

$$A_c \text{ is a function of 'h}_c\text{' } = C_1 h_c^2 + C_2 h_c + C_3 h_c^{1/2} + C_4 h_c^{1/4} + \dots$$

$$\text{Reduced Young's modulus, } E_r = (\pi / 2\beta) \times (S / (A_c)^{1/2}) \quad - (3.3)$$

Where, P_{\max} is the maximum load applied, A_c is the contact area at such load, ' h_c ' is the indentation depth and $S = (dP / dh)$ is the initial slope of the unloading segment in the load-displacement curve. C_1 , C_2 , C_3 , C_4 and β are constants that are used to calculate the nanomechanical properties. The effect of both loading and unloading is considered to determine the Young's modulus of the material. Figures 3.25 to 3.27 illustrate the photograph of the nanoindentation instrument that was used in this study, micrograph of Berkovich tip and the indent mark in the surface of solid sample.

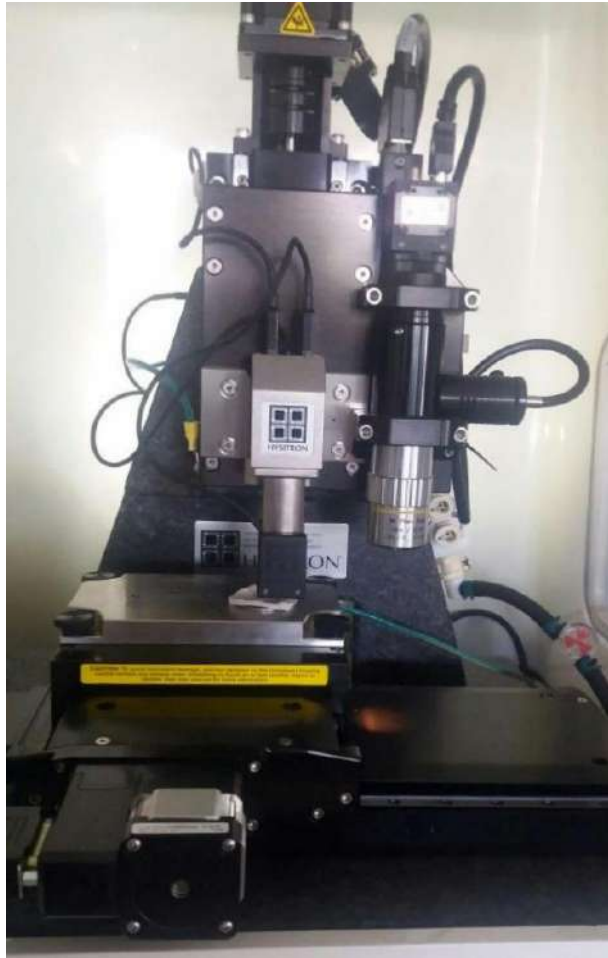


Figure 3.25 Hysitron TI Premier Nanoindenter

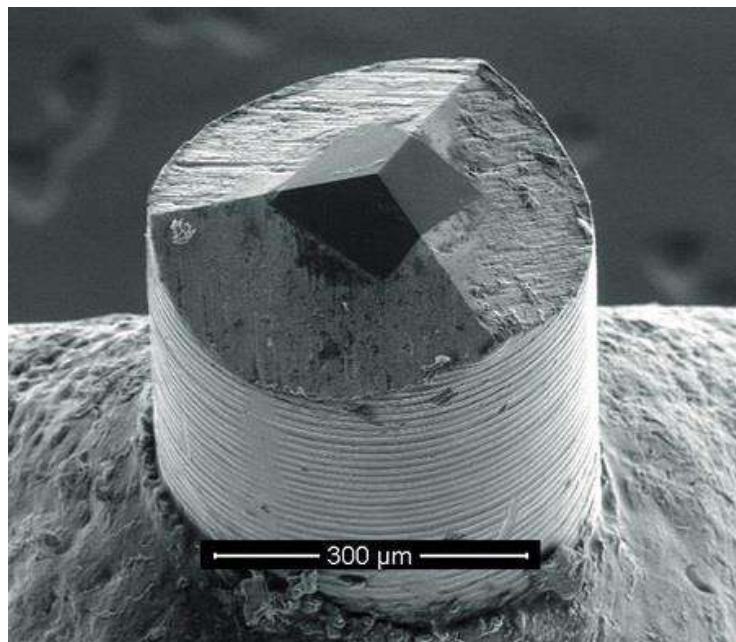


Figure 3.26 Micrograph illustrating the Berkovich tip (this image was obtained from the source - <http://bm3.unl.edu/hysitron-nanoindenter>)

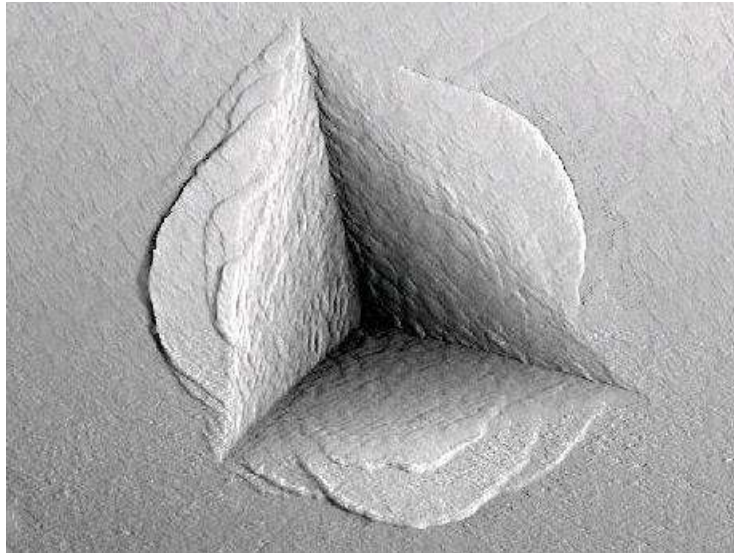


Figure 3.27 Indent on the surface of ceramic sample left by a Berkovich tip
(<http://mars.es3inc.com/themarssolver/dem.php>)

3.4.5 Mercury intrusion porosimetry

The complex pore structure of hydrated cementitious materials is characterised using mercury intrusion porosimetry which is based on the intrusion of a non-wetting liquid (mercury) into porous structures under increasing pressure. This liquid intrusion is opposed by the surface tension and thereby an external pressure is applied to compensate the pressure difference over the mercury meniscus in the pores. The MIP technique is based on the Washburn equation that relates the pore radius and pore pressure, as mentioned in Equation 3.4.

$$P = - (2 \times \gamma \times \cos \theta) / r \quad - (3.4)$$

Where, P , γ , θ and r indicates the pore pressure, surface tension of mercury, contact angle and capillary radius respectively. Thermo Scientific Pascal 140/440 series MIP instrument, which is shown in Figure 3.28, was used in this study to determine the alteration in the pore structure of cementitious paste modified using reduced graphene oxide, alumina and silica nanoparticles.



Figure 3.28 Thermo Scientific Pascal 140/440 series Mercury Intrusion Porosimetry instrument that was used in this study

The MIP results indicate the distributions of pore entry size rather than pore size in the porous samples. Aligizaki (2005) had earlier classified that the pore sizes in the cementitious matrix falling in between 1 nm to 10 nm as gel pores, and greater than 10 nm to 10 μm as capillary pores. Threshold diameter, most likely diameter and total percolated pore volume are the major characteristics which are interpreted from the MIP plots (cumulative pore volume versus pore entry radius). Threshold diameter and most likely diameter is the minimum radius which is geometrically continuous throughout the sample and the pore size that is recorded as the steepest slope in the cumulative intrusion curve respectively. Total percolated pore volume is defined as the maximum pore volume which is recorded through MIP experiments. Figure 3.29 show the identification of these characteristics in the MIP plot.

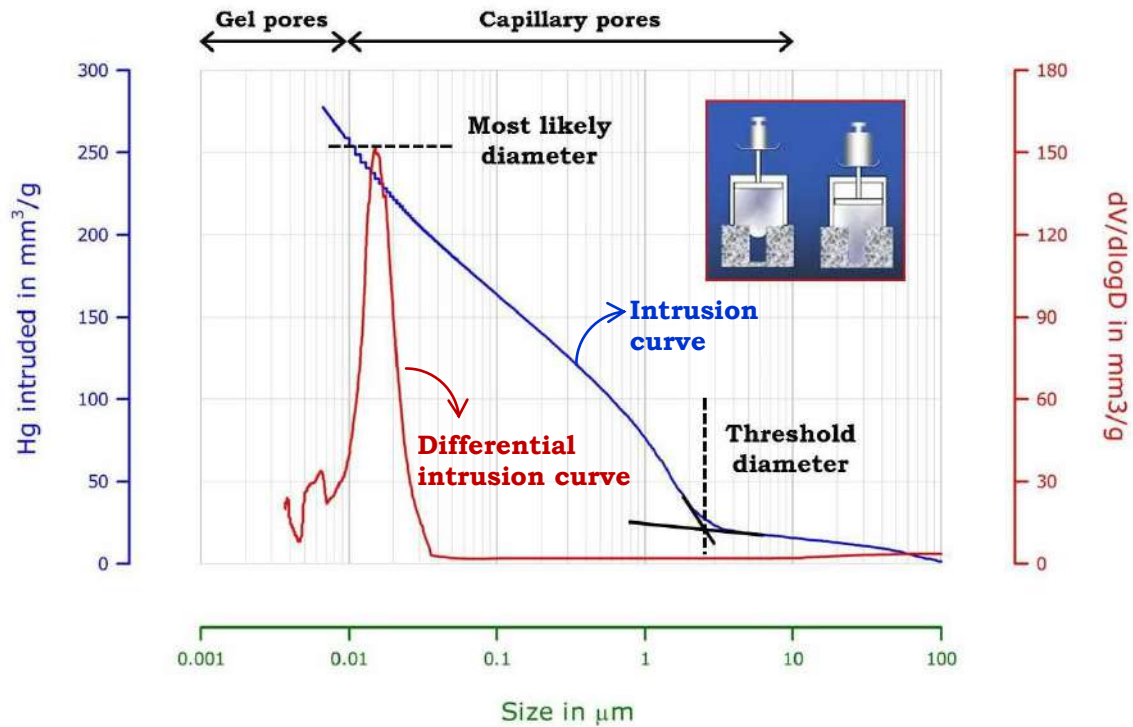


Figure 3.29 Identification of major characteristics like threshold diameter, most likely diameter and total percolated pore volume from the MIP plot

Two curves are indicated in the MIP plot, which are the cumulative intrusion curve and differential intrusion curve. The threshold and most likely diameters are defined as the intersection between the two tangents of the cumulative intrusion curve and the major peak in the differential intrusion curve respectively.

3.4.6 X-ray diffraction

The crystallographic and mineralogical features of a material can be analysed using X-ray diffraction (XRD). This technique was used in the present study to identify the phase changes in the cementitious matrix exposed to acidic environment. The degraded pastes were dried, ground and then sieved through 75 μm standard sieve. The powdered samples were next analysed using a Bruker D8 Model XRD instrument, which is shown in Figure 3.30.



Figure 3.30 Bruker D8 Model X-ray diffraction instrument that was used in this study

X-rays generated by a source (having single wavelength) interact with the atoms in a crystalline material, and the diffracted beams result in producing interference. This interference is constructive when Bragg's law, which is stated in Equation 3.5, is satisfied.

$$n \cdot \lambda = 2 \cdot d \cdot \sin \theta \quad - (3.5)$$

where n , λ , d and θ indicates order of diffraction, wavelength of characteristic X-rays, lattice interplanar spacing of the crystal and X-ray incidence angle (Bragg angle) respectively. This law explains that there is a relationship in between the intensities of the peaks, and disposition and nature of the atoms within the unit cell of the crystalline material.

The diffraction of X-rays by a crystalline material generates an XRD pattern which illustrates the peaks of different intensities at characteristic diffraction angles. The location of such peaks or diffraction angles is found using the size and symmetry of the unit cell through Bragg's law. For qualitative analysis, the XRD pattern is compared to a database of standard patterns of different compounds, which is maintained by the International Joint Committee on Powder Diffraction Standards (JCPDS).

3.4.7 Fourier transform infrared spectroscopy

Fourier transform infrared spectroscopy (FTIR) helps in identifying the presence of certain functional groups in a molecule. In this study, the formation of new compounds in the graphene, alumina and silica modified pastes after storage in acidic solution were analysed using PerkinElmer Spectrum One FTIR instrument, which is illustrated in Figure 3.31.

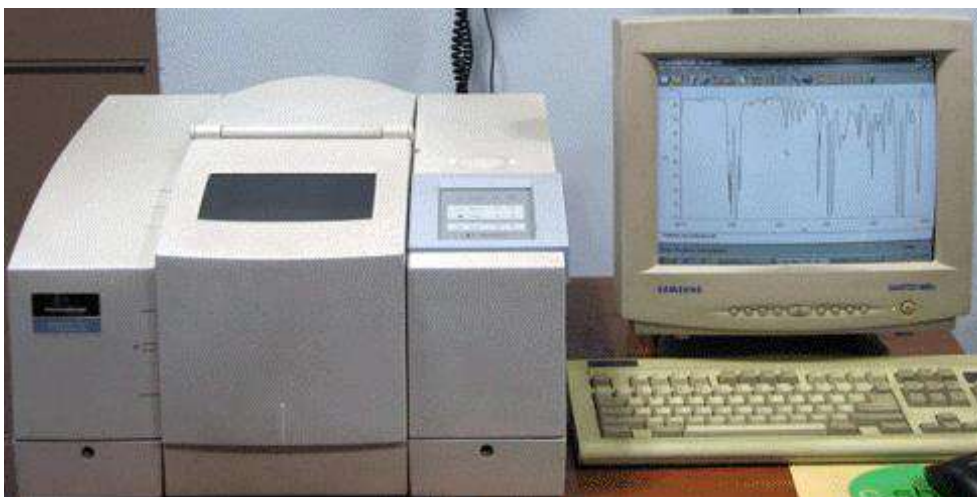


Figure 3.31 PerkinElmer Spectrum One FTIR instrument that was used in this study

In this technique, mid infrared radiation having wavenumber from 4000 cm^{-1} to 400 cm^{-1} is passed through a sample, and some of the radiation is absorbed and some is transmitted through the material. The mid infrared (4000 to 400 cm^{-1}) is used to study the fundamental vibrations of molecular bonds. The instrument uses interferometry which can record the information about the irradiated sample and then the Fourier transform helps in generating the mid infrared spectra of the sample. The detector collects the resulting signal, which is a spectrum illustrating the molecular 'fingerprint' of the sample. Generation of different types of spectral fingerprints suggests that the sample has complex chemical structures. The paste samples (in dried condition) were ground using mortar and pestle and then sieved using $75\text{ }\mu\text{m}$ standard sieve. Next, the powdered samples (finer than $75\text{ }\mu\text{m}$) were prepared for FTIR analysis by grinding a known mass of solid with dried KBr (potassium bromide salts). The resulting powder was then pressed at 2000 psi (140.61 kg/cm^2) for 5 minutes to produce a pellet for analysis. Table 3.1 lists the important wave numbers that are likely to be detected when the hydrated cementitious materials are tested using FTIR.

Table 3.1 List of important wave numbers that can be detected in the spectra of hydrated cementitious materials (Barnett et al. 2002)

Wavenumber in cm^{-1}	Assignment
3600 – 3200	O–H stretch
1680	O–H bend
1400	C–O stretch (CO_3^{2-})
1100	S–O stretch (SO_4^{2-})
940 / 920	SiO_4
875	C–O bend (CO_3^{2-})
850	AlO_6
750	SiO_6 stretch
500	SiO_6 bend

3.5 SUMMARY

Reduced graphene oxide was synthesized in this study by modified Hummers' method. The detailed procedure of this method was explained in this chapter. Additionally, the details of cement, aggregate, alumina and silica nanoparticles were also provided. Further, the working principles of major characterisation techniques such as X-ray CT, SEM, OM, FTIR, XRD, MIP, TGA, ICP-MS and nanoindentation that were used to characterise the nanomaterial-modified cementitious matrix exposed to acidic environment were discussed in this chapter.

CHAPTER 4

EFFECT OF GRAPHENE, ALUMINA AND SILICA NANOPARTICLES ON THE PROPERTIES OF OPC PASTE

4.1 INTRODUCTION

In this chapter, the effect of rGO (which is also named as ‘graphene’ in this study) on the properties of Portland cement paste in comparison to alumina and silica nanoparticles are discussed. The properties of rGO modified cement paste are investigated prior to the addition of such nanomaterial in the porous concrete system. The extent of enhancement of properties of cementitious systems, along with the assessment of the dosage of rGO required for effectiveness is studied. The testing methods used to determine their properties are mini slump test, compressive and flexural strength, and water sorptivity test. Additionally, the influence of these nanomaterials on the pore structure of cement paste was also investigated using mercury intrusion porosimetry (MIP) and 3-dimensional image analysis technique. The morphological changes in the 28-day cured cementitious pastes modified using rGO, alumina and silica nanoparticles were analysed using scanning electron microscopy (SEM).

4.2 SPECIMEN PREPARATION

Distilled water was used in the preparation of four different cement paste mixes having w/c ratio of 0.32. One mix was kept as reference whereas the remaining three mixes were incorporated with reduced graphene oxide, alumina and silica nanoparticles at concentrations of 0.02%, 0.2% and 4% by weight of cement respectively. In this chapter, these mixes were designated as Control, RGO, Al₂O₃ and SiO₂ respectively.

To increase the workability of fresh paste, 0.05 wt% polycarboxylic ether (PCE) based superplasticizer was added in all mixes. The PCE was also expected to increase the dispersion of the nanomaterials. Prior to mixing cement, the solution containing nanomaterials, PCE and distilled water was sonicated using probe sonicator for 30 minutes. Small amounts of sample from these solutions were collected and tested using dynamic light scattering (DLS) method (Horiba Nanopartica SZ-100 instrument was used), the results of

which are shown in Figure 4.1. This technique determines the size distribution profile of particles in suspension.

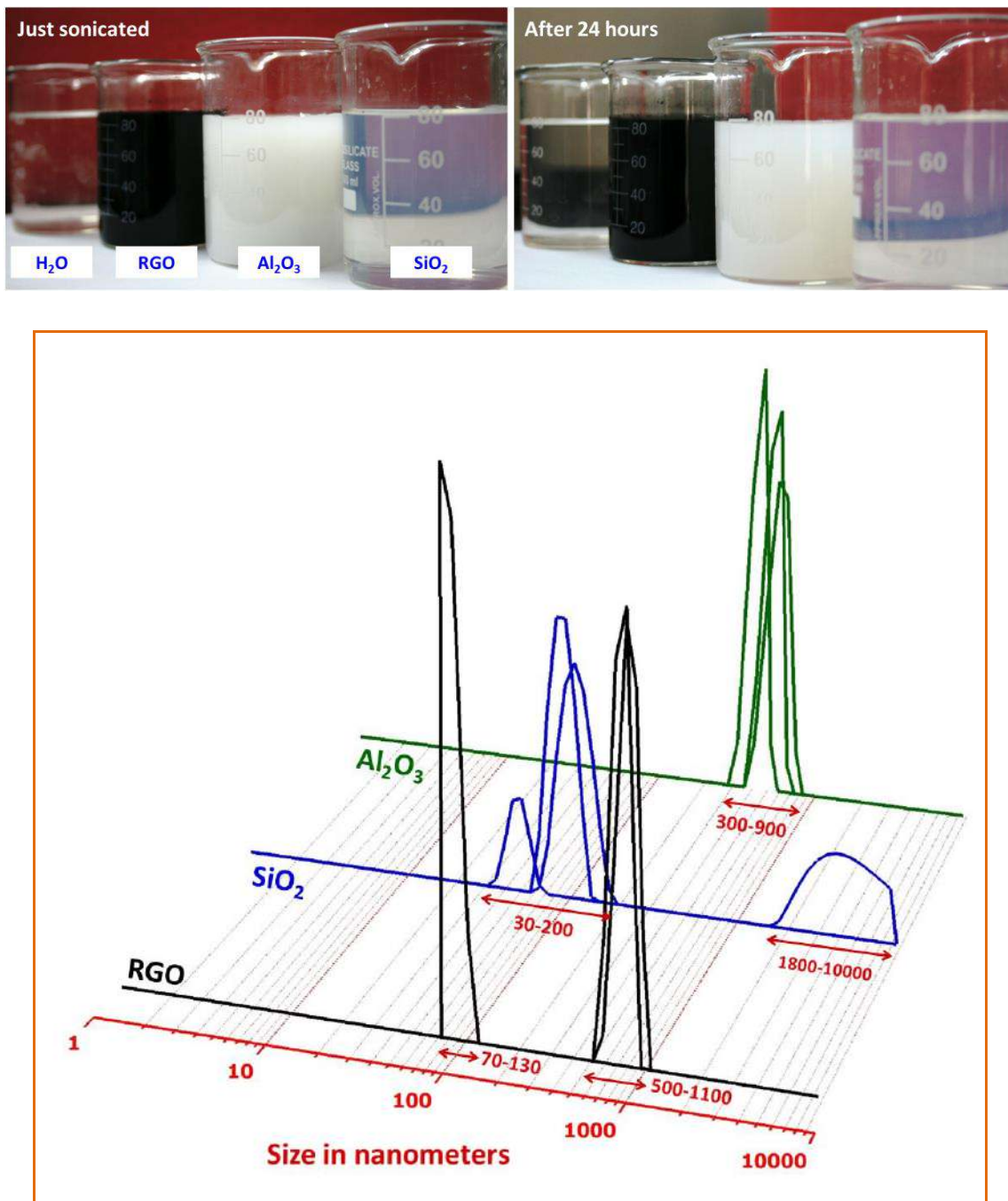


Figure 4.1 Different solutions containing reduced graphene oxide, alumina and silica nanoparticles (top image) and DLS test result of those solutions (bottom image)

The actual particle sizes of alumina and silica nanoparticles as specified earlier (in Chapter 3) were not observed anywhere in the DLS plot. This suggests that those nanomaterials were

agglomerated, possibly because of the use of insufficient superplasticizer (dosage was fixed based on workability of the paste). The majority of graphene sheets synthesized by Modified Hummers' method are reported to have size range in between 5 nm to 1500 nm (Sen Gupta et al. 2011). In this study, the as-synthesized graphene sheets were determined to have two size ranges – 80 to 102 nm and 450 to 1000 nm respectively. The thickness of these sheets cannot be determined effectively using the DLS technique, and thus it is difficult to comment whether the sheets are separate or stacked.

For paste preparation, the ingredients were mixed in a high speed Hobart mixer for 12 minutes. After mixing, the mini slump test was conducted to determine the flowability; the remaining paste was used for casting specimens of size 25 × 25 × 25 mm and 20 × 20 × 160 mm for determining the compressive and flexural strength respectively. Consolidation was performed using a vibration table. The specimens were demolded after 24 hours and then cured in saturated limewater solution at room temperature ($25 \pm 2^\circ\text{C}$) for 7 and 28 days.

4.3 EXPERIMENTAL PROGRAM

A mini slump cone, which is shown in Figure 4.2, was used for determining the workability of cement paste. The procedure specified by Collins et al. (2012) was followed in this study. To determine the compressive and flexural strength, the specimens were tested at a loading rate of 143 N/s and 50 N/s respectively. Both tests were performed using Controls C9842 testing machine on different frames having the capacities of 250 kN and 15 kN respectively.



Figure 4.2 Mini slump spread (left image) and Water sorptivity test (right image)

Water sorptivity test was performed on the paste specimens of size $25 \times 25 \times 12.5$ mm (sliced from the 25 mm cubes) after 7 and 28 days. After curing, the specimens were stored in acetone for the next two days to arrest the hydration followed by air drying for two days. Further, the dried specimens were kept in a shallow tray of size not less than 150×75 mm with roller arrangement as shown in Figure 4.2.

The tray was filled with saturated limewater solution (5 grams per 1 litre of distilled water). The final water level was maintained slightly above the bottom edge of the specimen. The mass of the specimen was measured at specified intervals such as 0, 3, 5, 7, 9, 12, 16, 20 and 25 minutes. Before weighing, the adsorbed water at the specimen surface was removed with a moist cloth. Finally, the vacuum saturated mass of the specimens was measured. The average of three specimens was considered for all tests.

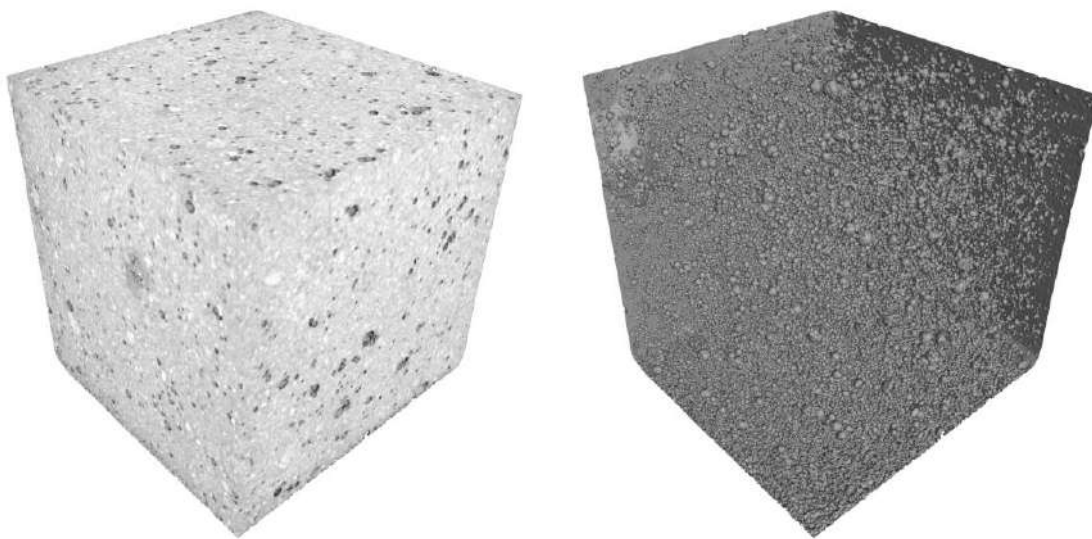
For SEM investigation, the fractured surface of paste sample was analysed using FEI Quanta 400 FEG-SEM and Emcrafts Genesis 2100 – SEM instruments. A gold/palladium layer was coated on the sample to make the surface conductive.

4.4 ANALYSIS OF PORE STRUCTURE

The effect of nanomaterials on the pore structure of OPC (ordinary Portland cement) paste was characterised using MIP and 3-dimensional X-ray CT. Firstly, the distribution of gel pores (< 10 nm) and capillary pores (10 nm to $10 \mu\text{m}$) in a paste specimen of size $7 \times 7 \times 7$ mm was determined using Thermo Scientific Pascal 140/440 series MIP instrument. Secondly, the distribution of pores/voids ($> 100 \mu\text{m}$) in the paste specimen of size $10 \times 10 \times 10$ mm was determined using tomographic images acquired through GE phoenix v|tome|x s 3-D X-ray CT testing machine.

Paste specimens were scanned using an X-ray source generated at a voltage and current of 120 kV and $70 \mu\text{A}$ respectively. The scanning rate was maintained around 4 milliseconds per image for attaining a minimum voxel resolution of $20 \mu\text{m}$ during the image reconstruction. Caesium Iodide based flat panel detector was equipped inside the CT testing machine to convert the X-rays into light. The output data obtained from the X-ray CT run after the end of the scanning period was a 2-D radiograph of the paste specimen. The radiographs were extracted with the help of a data acquisition software named Phoenix datos|x CT. Next, the 2-D data were reconstructed and processed with the software named VGStudio MAX version

2.2 which helps to visualise the 3-D structure of the samples. The reconstructed 3-D CT image, which consists of ‘n’ number of voxels, is a spatial distribution of the linear attenuation coefficient, which is expressed in terms of Greyscale Value (GSV), with brighter and darker regions corresponding to higher and lower value of attenuation coefficient. To visualise the presence of voids inside the cement paste, the GSV of CT image was slightly adjusted. Figures 4.3 to 4.8 show the reconstructed and transparent view of the CT image obtained after GSV adjustments, for paste specimens at 28 days.



Note: At the time of image processing, care was taken to avoid cropping the rear surfaces in the 3-dimensional CT image

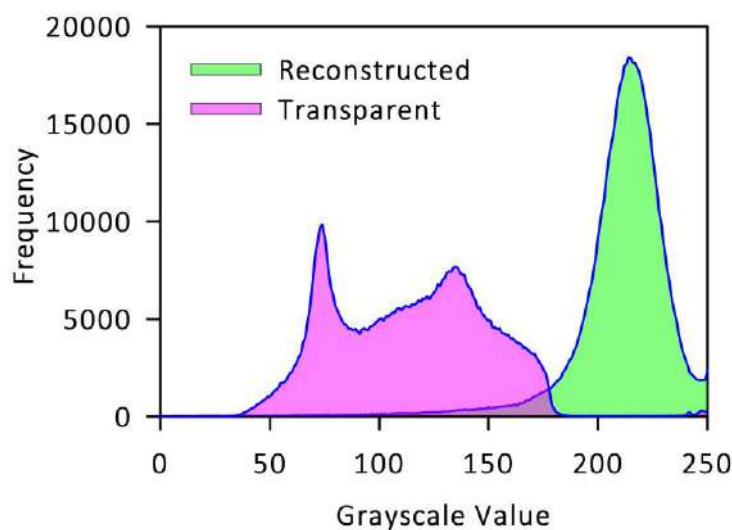


Figure 4.3 Reconstructed and isosurface CT image (top image) of the control paste specimens of size $10 \times 10 \times 10$ mm and their greyscale histograms

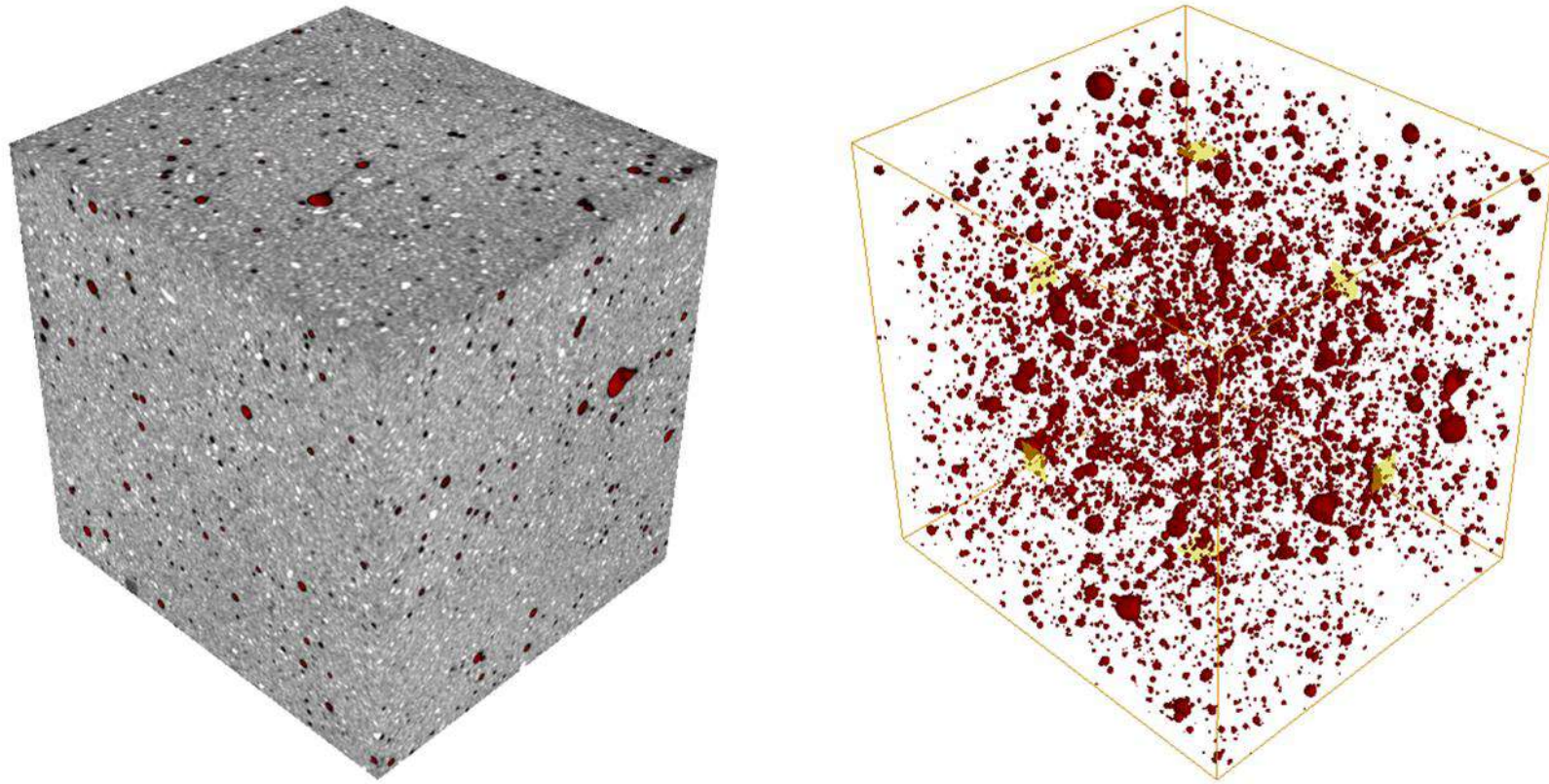


Figure 4.4 Reconstructed 3-D CT image (left image) and its transparent view (right image) illustrating the presence of voids in the control paste specimen of $10 \times 10 \times 10$ mm

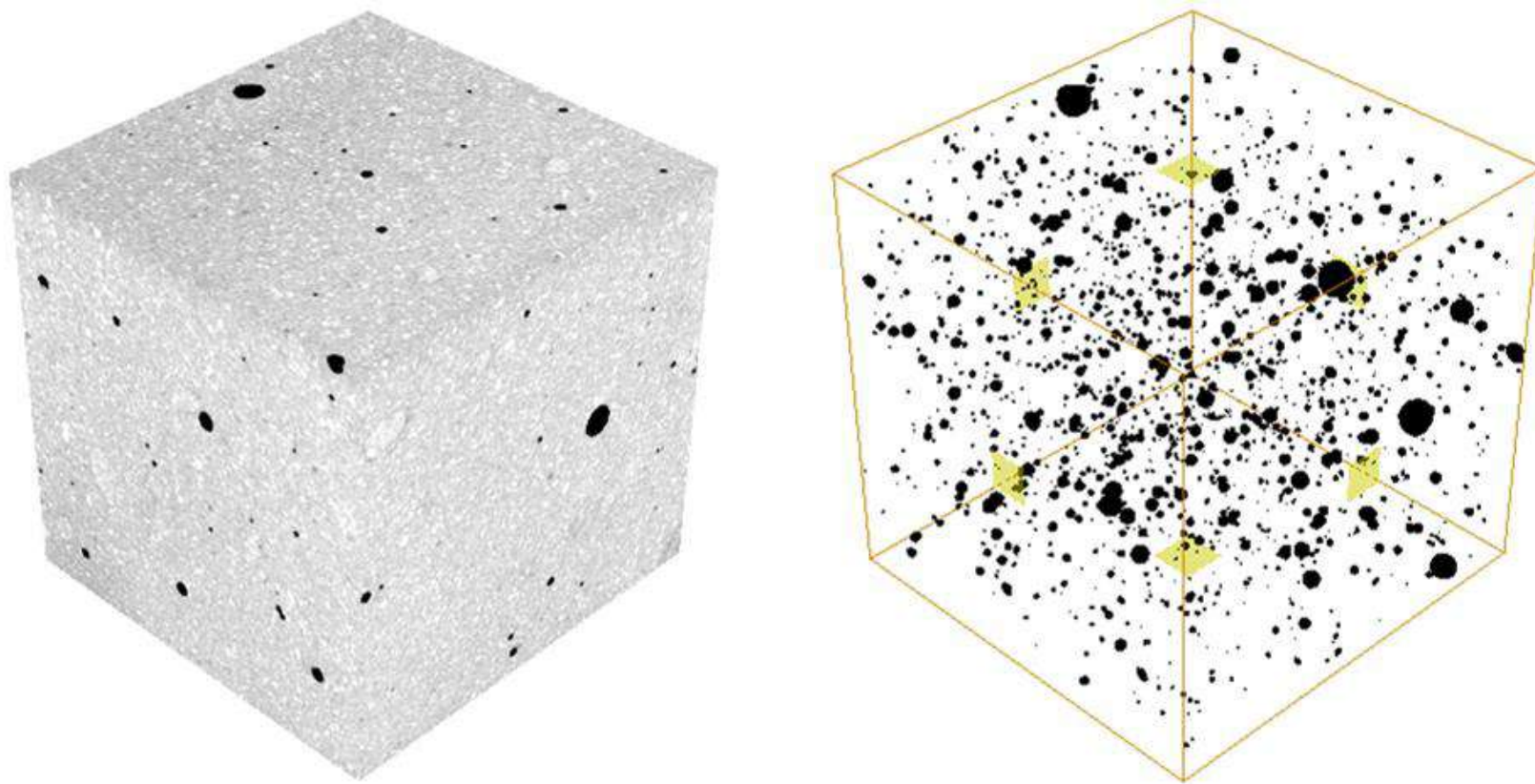


Figure 4.5 Reconstructed 3-D CT image (left image) and its transparent view (right image) illustrating the presence of voids in the RGO paste specimen of $10 \times 10 \times 10$ mm

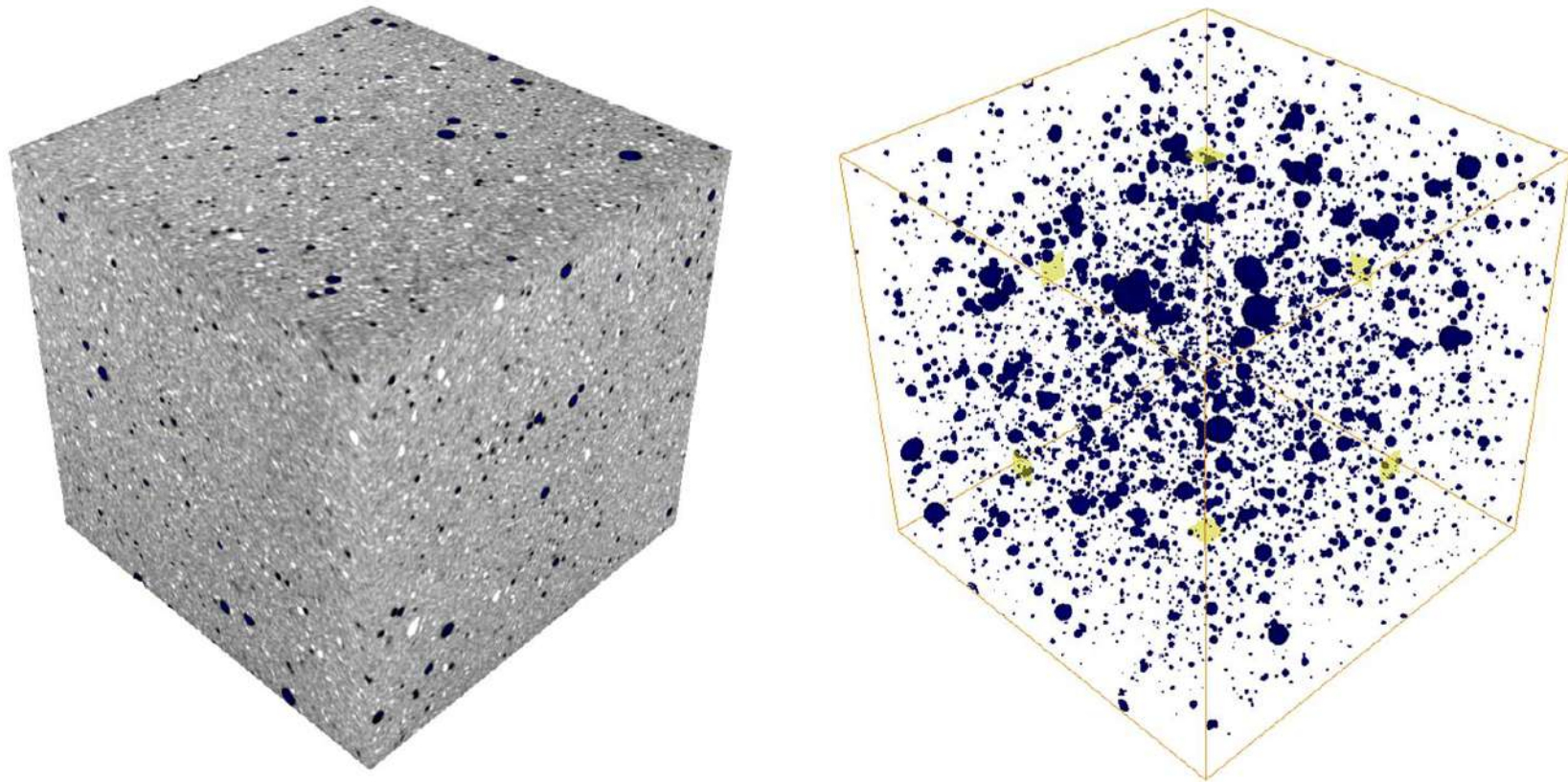


Figure 4.6 Reconstructed 3-D CT image (left image) and its transparent view (right image) illustrating the presence of voids in the Al_2O_3 paste specimen of $10 \times 10 \times 10$ mm

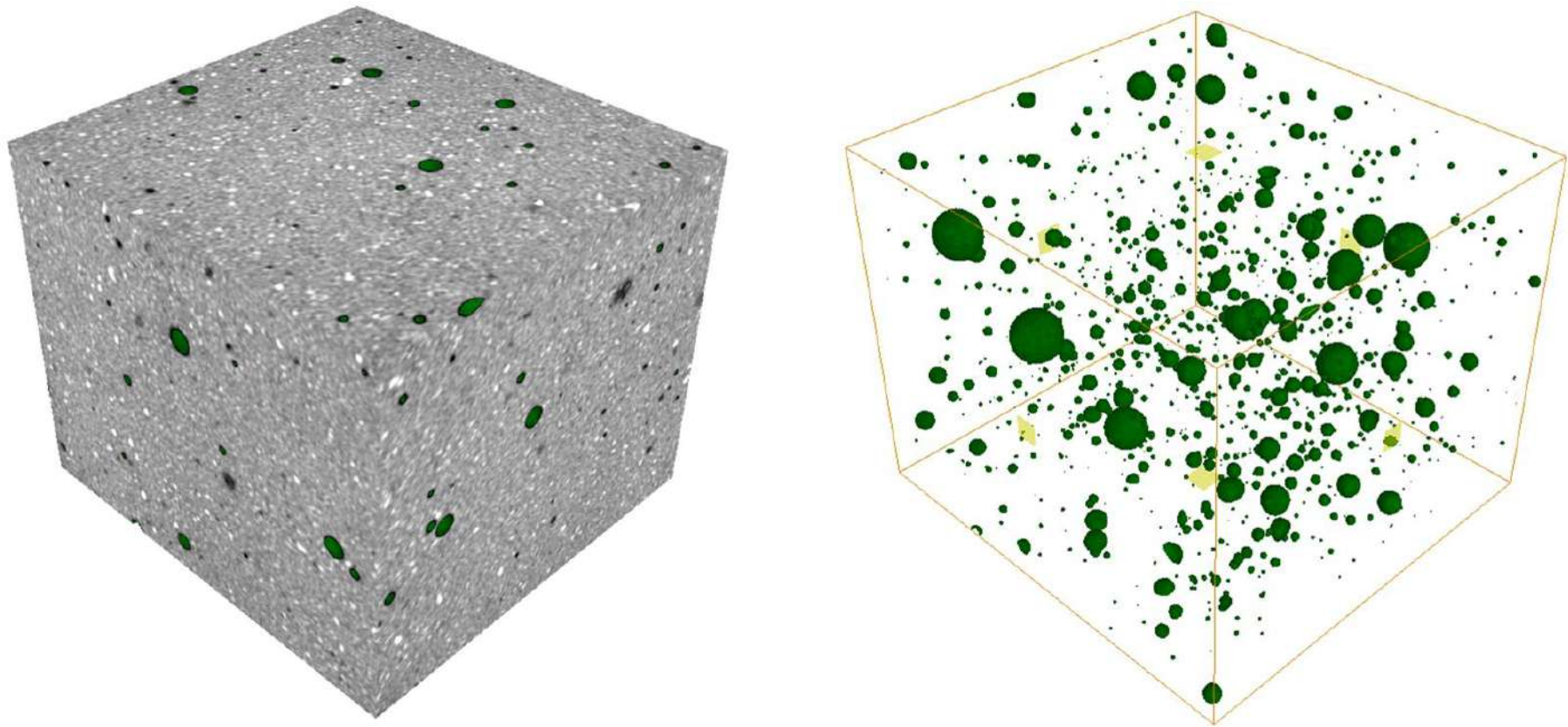


Figure 4.7 Reconstructed 3-D CT image (left image) and its transparent view (right image) illustrating the presence of voids in the SiO_2 paste specimen of $10 \times 10 \times 10$ mm

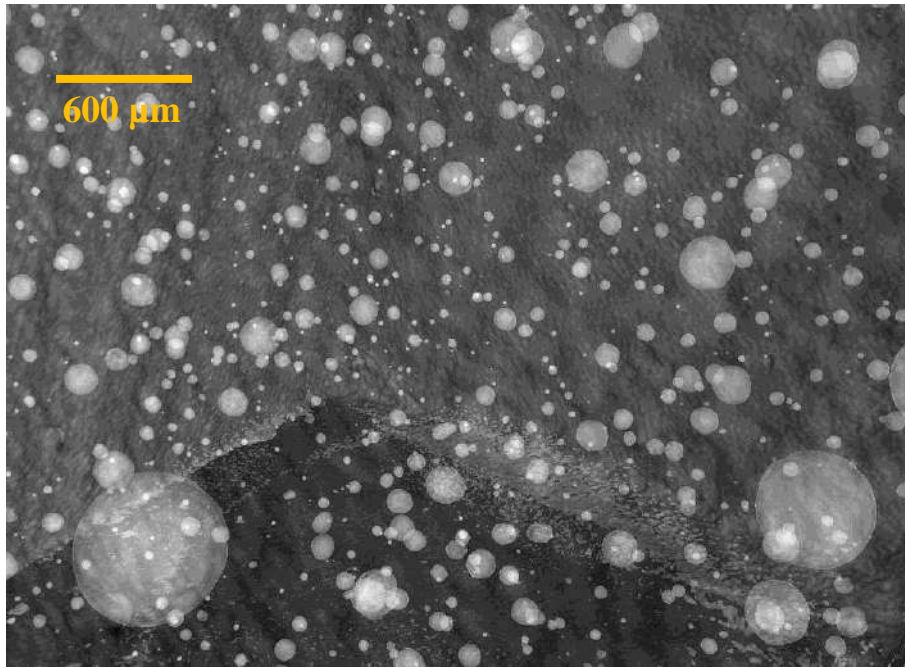


Figure 4.8 Transparent view of the CT image illustrating the presence of different sizes of spherical shaped air void inside the 28-day cured cementitious matrix

The image reconstruction software VGStudio MAX is supplied with an optional add-on module named porosity analysis. This provides a range of algorithms allowing porosity to be located within the object and yields quantitative information about the pores or voids. The module is a bundle of different algorithms and modes which allow to specially investigate the pores with high contrast (air voids) or low contrast (loose material). It also helps to examine the material with open pores that have cut through the cropped surface.

In this study, the analysis module was used on the CT images of the paste specimens to determine the volume and diameter of the voids present inside the material. The only input parameters that are required to run the analysis are the lower and upper bounds of the pore volume that are expected to be present in the material. Since the minimum voxel resolution of the CT image was $20\ \mu\text{m}$, the safe void volume (minimum threshold value) was fixed to have a voxel resolution of $100\ \mu\text{m}$ to avoid misleading results. After running the analysis using the module, the output data consists of parameters such as void volume, void diameter (Feret diameter), voxel counts, and coordinates of the each defect present inside the material. The colour-coded 3-D view of the analysed CT image was also obtained from the software. Figures 4.9 to 4.11 show the different colour-coded CT images of the paste specimens analysed using porosity analysis module.

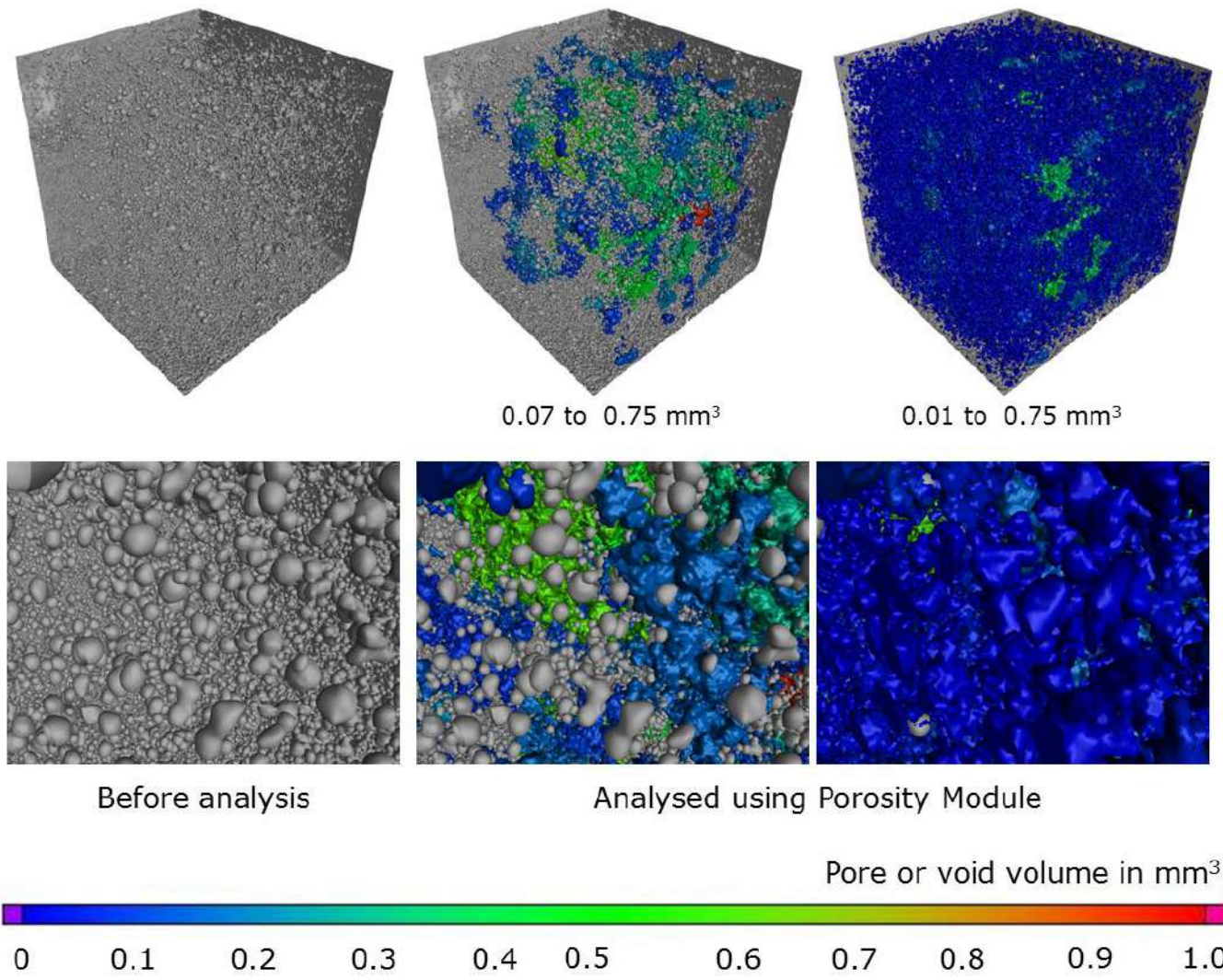


Figure 4.9 Colour-coded 3-D CT images of the cement paste obtained before and after porosity analysis using the software VGStudio MAX

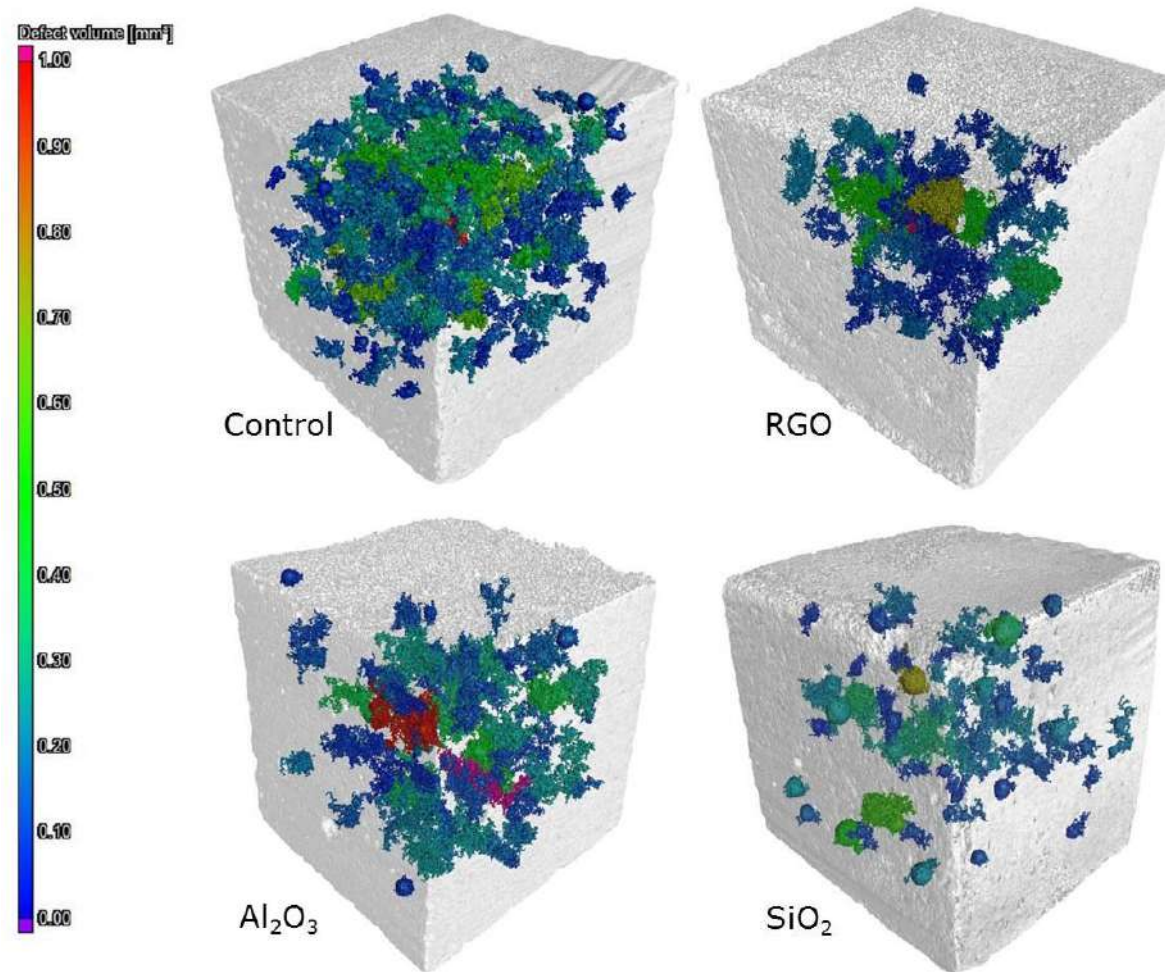


Figure 4.10 Colour-coded CT images (volume rendered) illustrating the presence of voids having volume in between 0.07 mm^3 to 0.75 mm^3 in the paste specimens

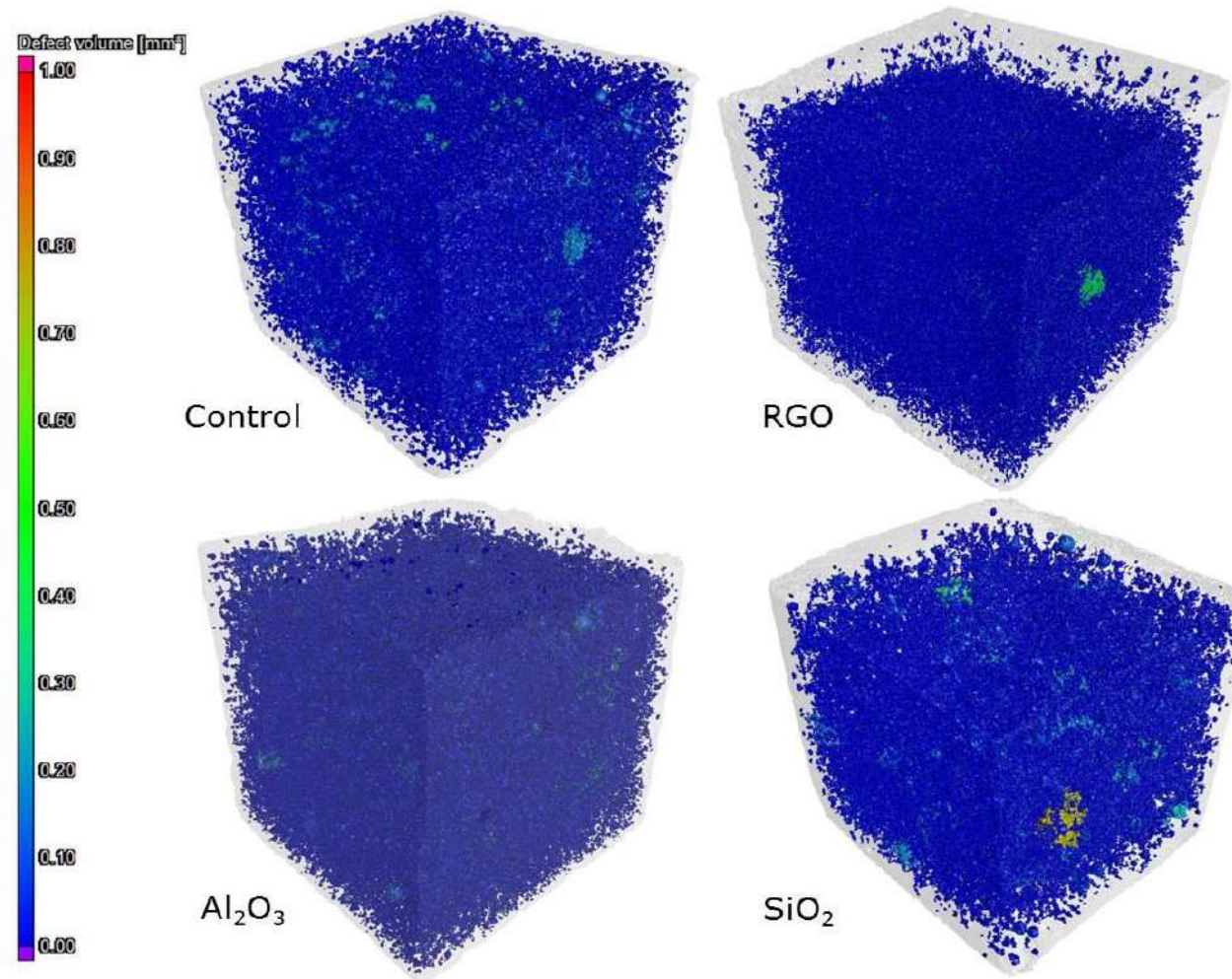


Figure 4.11 Colour-coded CT images (volume rendered) illustrating the presence of voids having volume in between 0.01 mm^3 to 0.75 mm^3 in the paste specimens

From the GSV adjusted CT image, the presence of enclosed voids was clearly visualised. After analysis, the colour change from violet to red indicates the increment in the size of voids. Figures 4.12 to 4.15 show closer views of the analysed CT images, and help to clearly bring out the void features.

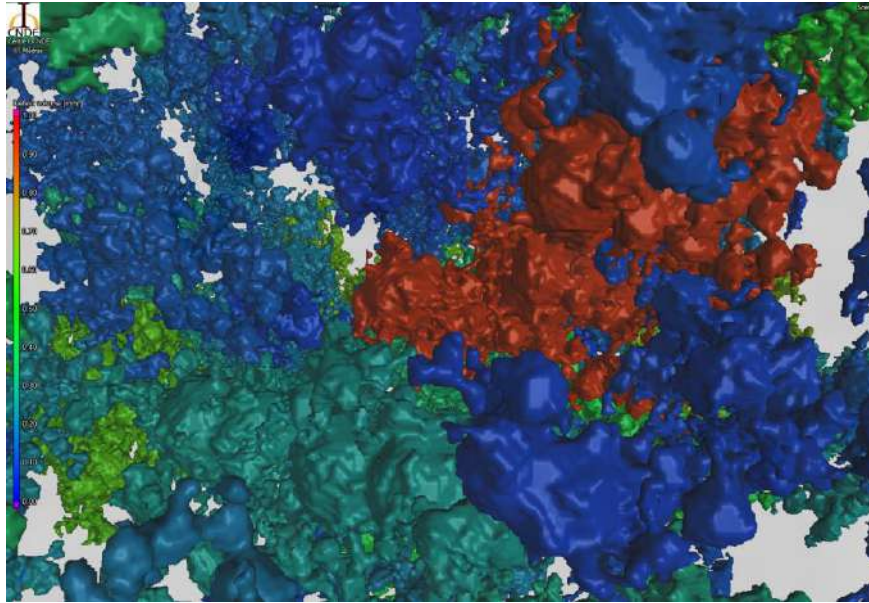


Figure 4.12 Closer view of the analysed CT image illustrating the rainbow colours attributed to the voids having different volume in the cementitious matrix (0.01 mm^3 to 0.75 mm^3)

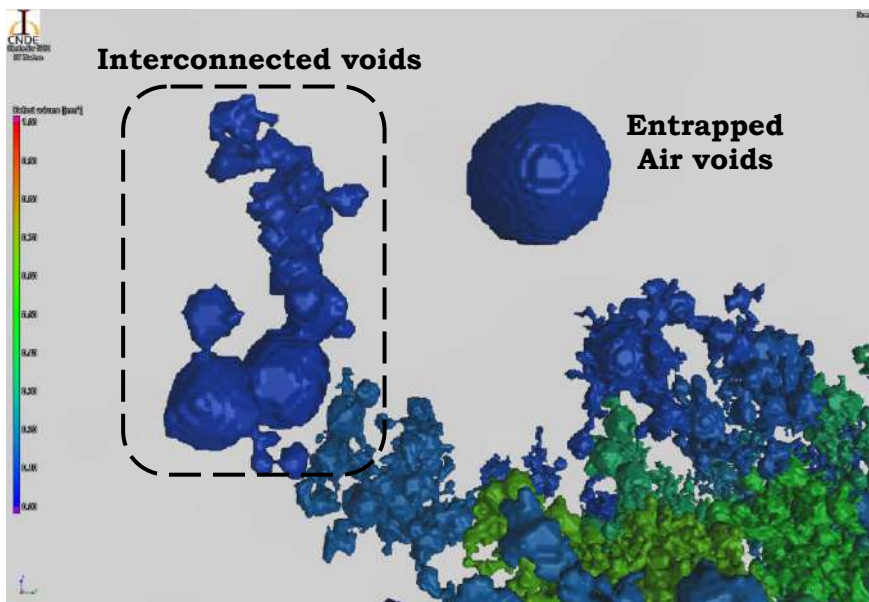


Figure 4.13 Closer view of the analysed CT image illustrating the interconnected voids inside the cementitious matrix

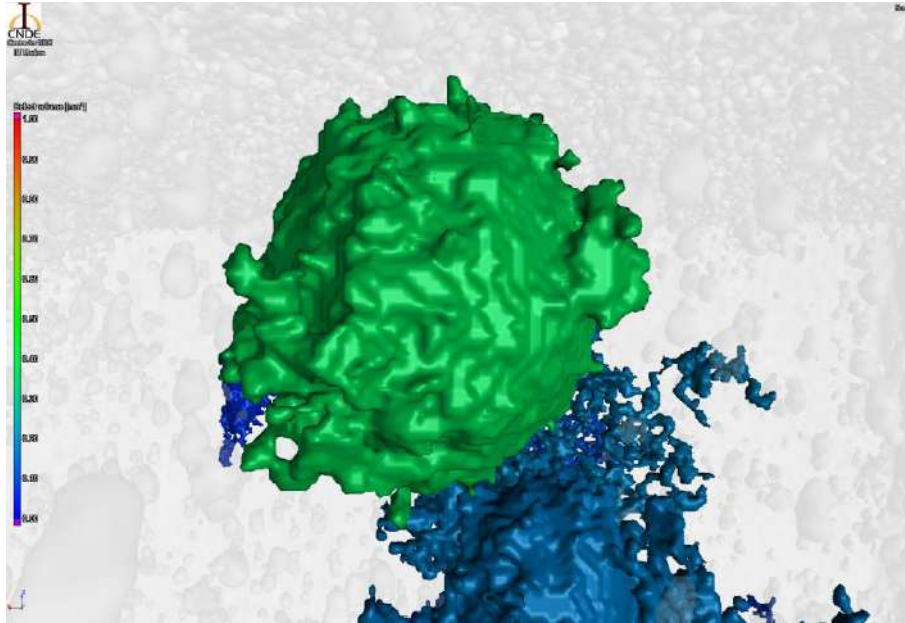


Figure 4.14 Closer view of the analysed CT image illustrating the spherical entrapped air void (the rough texture is due to the resolution of the CT image)

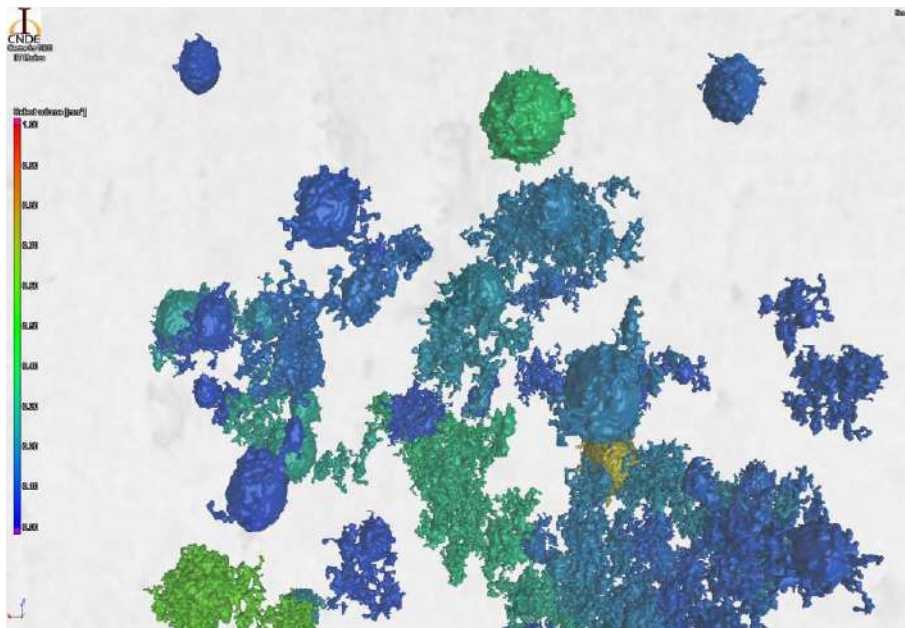


Figure 4.15 Closer view of the analysed CT image illustrating the presence of different sizes of spherical voids in the cementitious matrix

The presence of interconnected voids in the cement paste was clearly noticed in the CT image after analysis. Additionally, the position of these voids in the cementitious matrix was also located using image analysis approach.

4.5 RESULTS AND DISCUSSION

4.5.1 Mini slump spread, mechanical strengths and water sorptivity test

Table 4.1 compares the different experimental results of 7-day (7d) and 28-day (28d) cured cementitious pastes.

Table 4.1 Experimental results of the different pastes that were prepared in the present study

Mix Designation		Control	RGO	Al ₂ O ₃	SiO ₂
Compressive strength in MPa	7d	50.07 ± 1.96	60.01 ± 2.51	66.25 ± 1.03	72.37 ± 0.44
	28d	61.29 ± 2.78	74.97 ± 2.64	75.48 ± 2.54	86.65 ± 3.12
Flexural strength in MPa	7d	5.09 ± 0.79	8.68 ± 0.97	10.40 ± 1.00	11.10 ± 1.05
	28d	10.27 ± 0.59	13.78 ± 0.39	14.33 ± 0.23	11.86 ± 0.68
Mass porosity in %	7d	27.95 ± 2.61	23.49 ± 0.27	25.34 ± 0.84	24.41 ± 1.25
	28d	13.37 ± 0.36	12.92 ± 0.77	13.38 ± 1.00	10.93 ± 0.46
Sorptivity index in mm/hr ^{1/2}	7d	0.78 ± 0.011	0.64 ± 0.027	0.54 ± 0.048	0.70 ± 0.051
	28d	0.11 ± 0.012	0.11 ± 0.009	0.17 ± 0.006	0.19 ± 0.022
Mini slump spread in cm	-	8.5	7.4	7.6	6.5

It can be seen from the results that the spread of reduced graphene oxide, alumina and silica modified fresh pastes was decreased up to 13%, 11% and 24% compared to the control paste respectively, which may be due to loss in free water. The addition of nanomaterials having higher surface area in OPC paste results in the absorption of significant amounts of free water. The addition of graphene, alumina and silica nanoparticles had increased the 7-day compressive and flexural strengths up to 20%, 32%, 45% and 70%, 104%, 118% than the control paste respectively. Further, their 7-day porosity (by mass) and sorptivity rate had decreased up to 20%, 11%, 24% and 18%, 30%, 11% than the control mix respectively. These significant changes were primarily brought about by the nanomaterials acting as nucleation sites for the increased growth and production of cementitious hydrates (Sanchez and Sobolev 2010). In the case of 28 days, the compressive and flexural strengths of reduced

graphene oxide, alumina and silica modified pastes were increased up to 22%, 23%, 41% and 23%, 23%, 4% than the control paste respectively. Their 28-day sorptivity rate had increased up to 4%, 51% and 70% than the control mix respectively. This increase can be attributed to the uptake of moisture by the nanomaterials. The poorly dispersed nanomaterials in the cementitious matrix had marginally increased the porosity of the pastes after 28 days. Despite being agglomerated, the Si particles were fine enough to adequately fill the porosity and improve the packing which may have resulted in the improved strength. A SEM image illustrating the poorly dispersed silica nanoparticles in the cementitious matrix is shown in Figure 4.16.

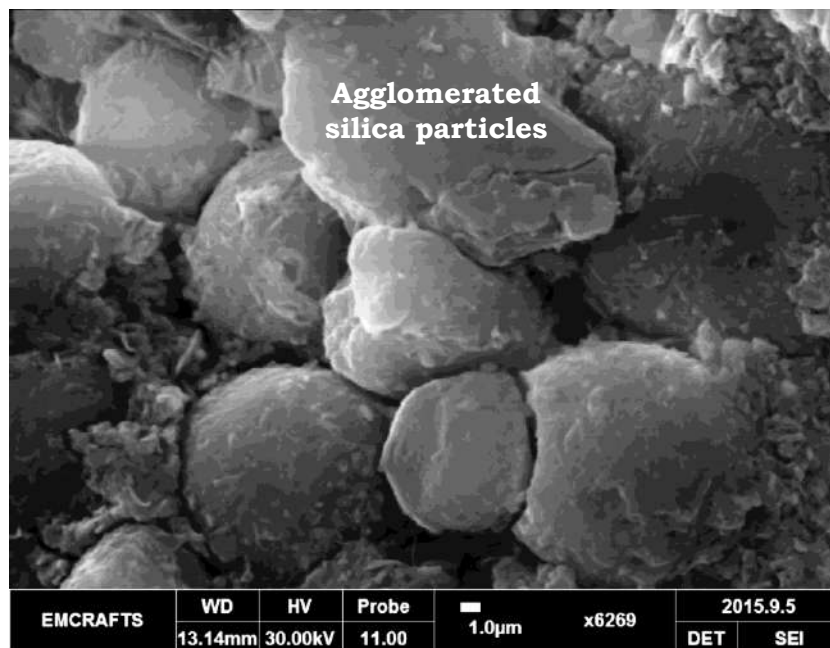


Figure 4.16 Micrograph illustrating the presence of poorly dispersed silica nanoparticles in the 28-day cured cementitious matrix

Among the three nanomaterials, the addition of 2-dimensional graphene sheets even at smaller concentrations (0.02 wt%) was found to be more efficient than the 3-dimensional spherical or angular nanoparticles such as alumina and silica. The good performance of graphene can be attributed to its better dispersion in a polar solvent like water, the shape and size factors, and the presence of functional groups such as carboxyl and hydroxyl on the structure of graphene sheets (Lv et al. 2014, Singh et al. 2011).

4.5.2 Alterations in the pore structure

In this study, the pore sizes in between 3.7 nm to 10 μm were determined using mercury porosimetry. The MIP plot of the pastes are better described in the next chapter which explains about the effect of rGO, alumina and silica nanoparticles on the degradation characteristics of OPC paste exposed to acidic environment. Only an overall assessment is provided here. As mentioned earlier in the section 3.4.5, the pore related features such as threshold and most likely diameters, and the amounts of gel and capillary pores in the 28-day cured cementitious pastes were determined from their MIP plots, which are compared in Table 4.2.

Table 4.2 Porosimetry results of the 28-day cured cementitious pastes

Mix Designation	Control	RGO	Al ₂ O ₃	SiO ₂
Threshold diameter, in nm	26.8	20.7	39.1	28.6
Most likely diameter, in nm	14.7	12.9	27.1	20.4
3.7 nm to 10 nm, Gel pores in mm ³ /g	10.69	14.60	26.97	23.42
10 nm to 10 μm , Capillary pores in mm ³ /g	48.58	33.01	60.58	57.76

The amounts of gel pores in the RGO, Al₂O₃ and SiO₂ pastes had increased up to 37%, 152% and 119% than the control paste respectively. This suggests that the addition of graphene and alumina nanoparticles could have increased the production of C-S-H gel because of their ability to promote nucleation. However, in the case of SiO₂, the pozzolanic reaction of nano silica could have also led to the formation of secondary C-S-H that may also have contributed to the refinement of gel pores. The well dispersed nanomaterials are also likely to refine the capillary pores in the cementitious matrix. Particularly, the addition of 0.02 wt% rGO had decreased the amount of capillary pores up to 32% than the control mix. However, the presence of agglomerated alumina and silica particles had increased the capillary pores (10 nm – 10 μm) up to 25% and 19% than the control mix respectively. Although these nanoparticles were agglomerated, their surfaces would have still promoted the growth and production of C-S-H gel.

The effect of nanomaterials on the size of voids greater than 100 μm was determined using image analysis of the X-ray CT images. Figures 4.17 to 4.20 show the frequency distribution of voids in the 28-day cured cementitious pastes.

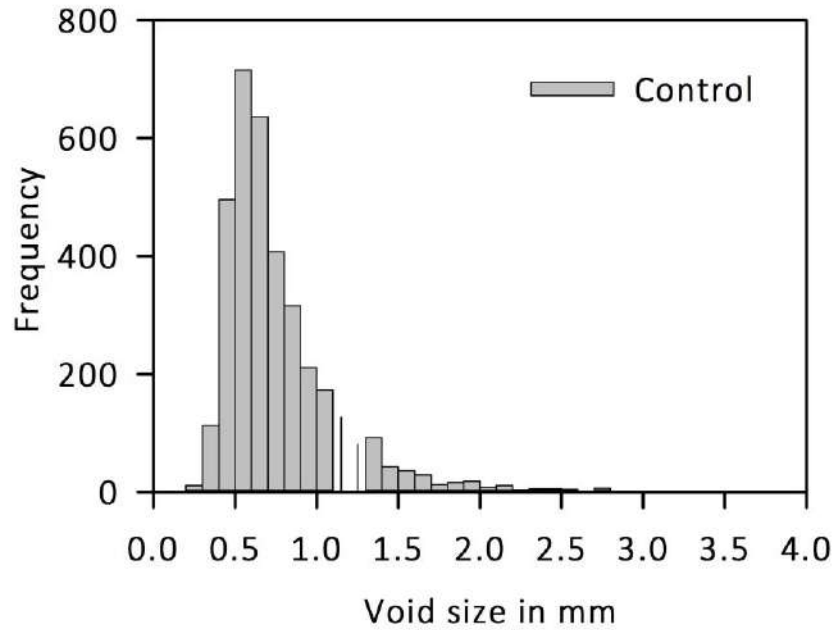


Figure 4.17 Distribution of void sizes in the control paste after curing for 28 days

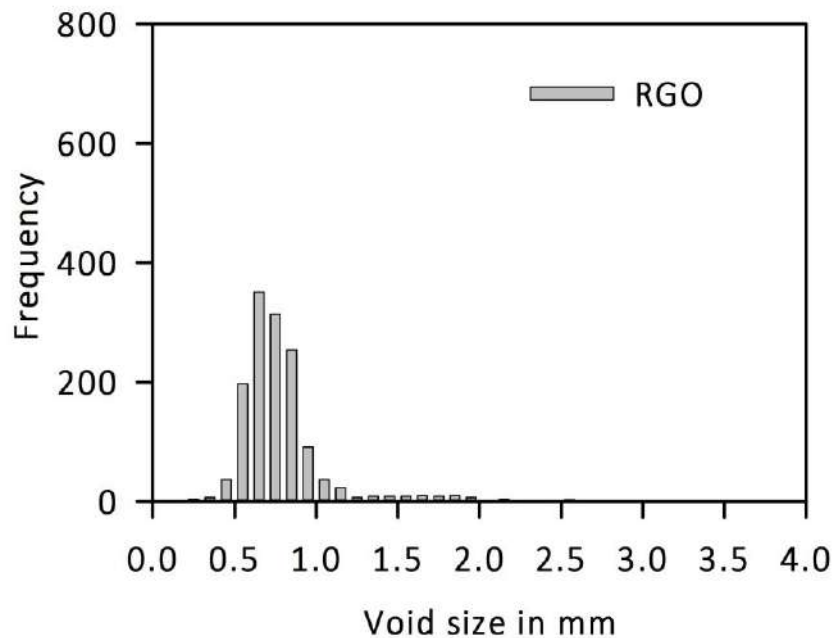


Figure 4.18 Distribution of void sizes in the RGO paste after curing for 28 days

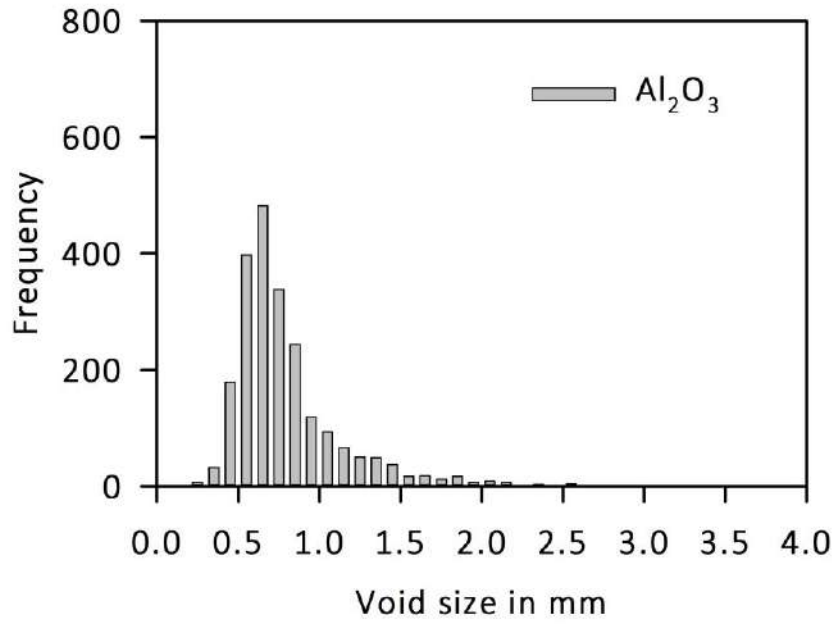


Figure 4.19 Distribution of void sizes in the Al_2O_3 paste after curing for 28 days

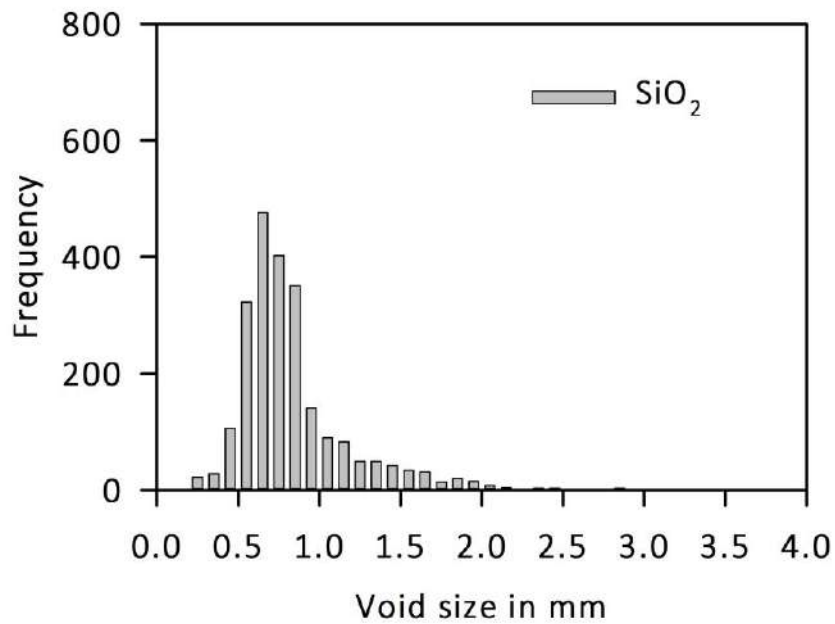


Figure 4.20 Distribution of void sizes in the SiO_2 paste after curing for 28 days

It can be seen from the image analyses that the amounts of voids in the RGO, Al_2O_3 and SiO_2 pastes were decreased substantially than the control paste. In particular, the RGO paste showed better performance when compared to the remaining mixes.

4.5.3 Scanning electron microscopy images

Micrographs illustrating the fractured surface of control and RGO paste after curing for 28 days are presented in Figures 4.21 to 4.25.

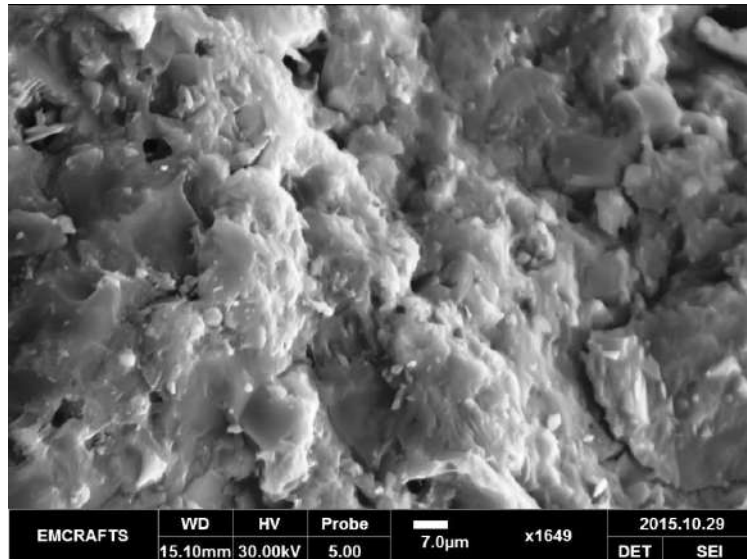


Figure 4.21 Micrograph illustrating the fractured surface of 28-day cured control paste

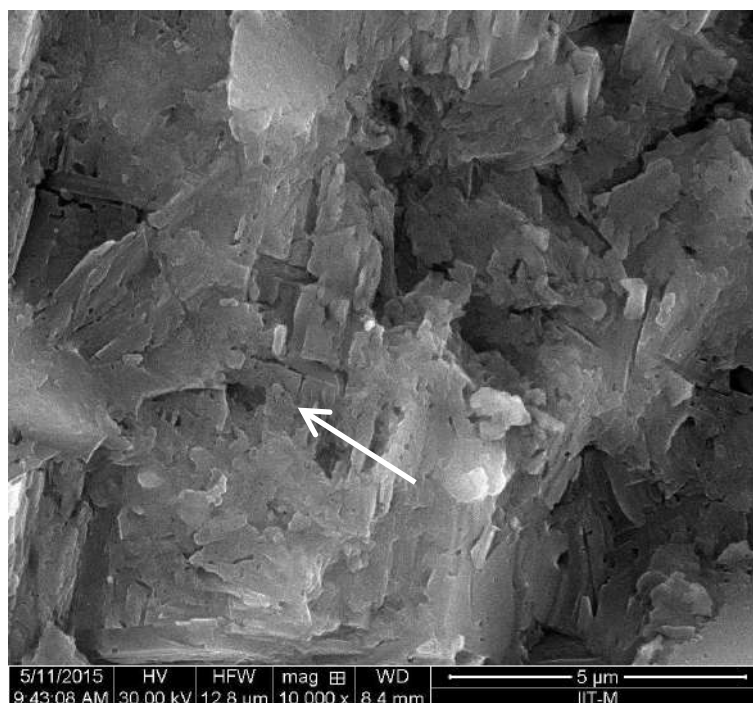


Figure 4.22 Micrograph illustrating the morphology of C-S-H in the control paste after curing for 28 days

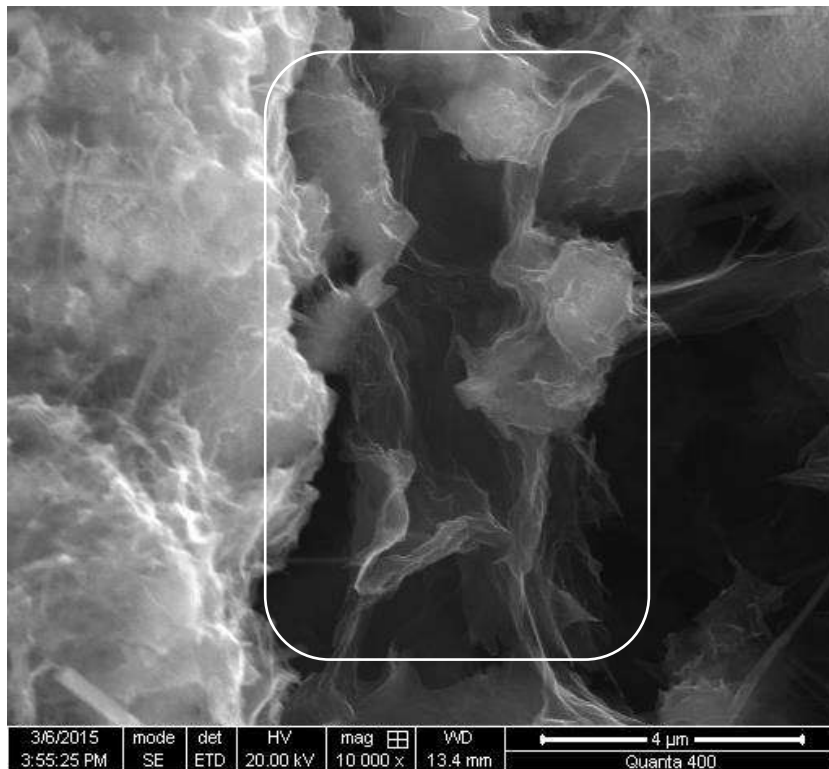
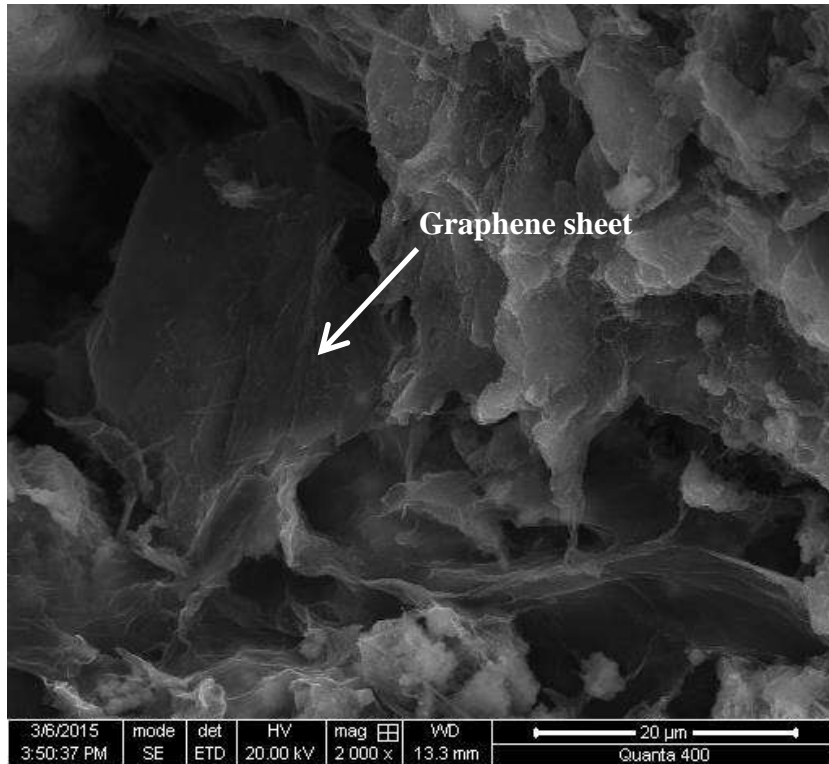


Figure 4.23 Micrograph illustrating the presence of graphene sheet inside the void in the RGO paste (top and bottom image) after curing for 28 days

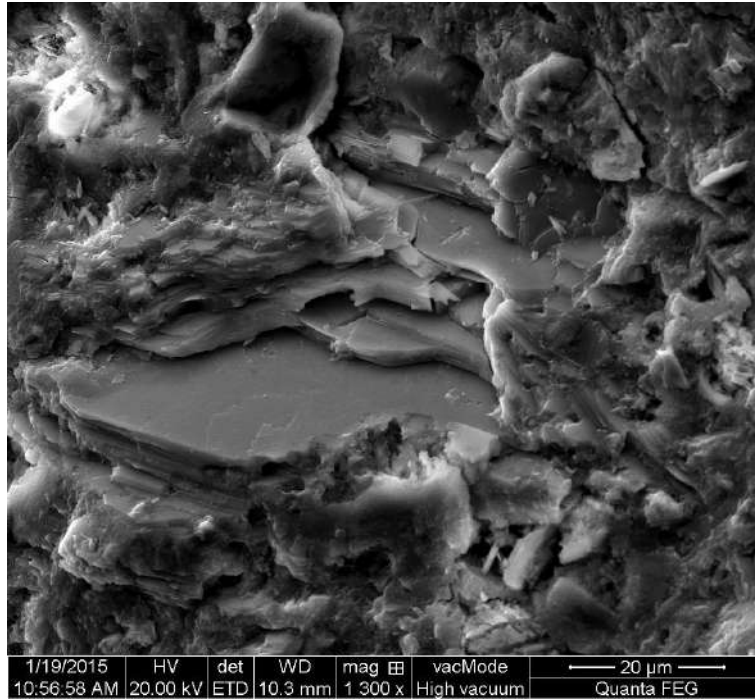


Figure 4.24 Micrograph showing the presence of hexagonal crystals in the RGO paste

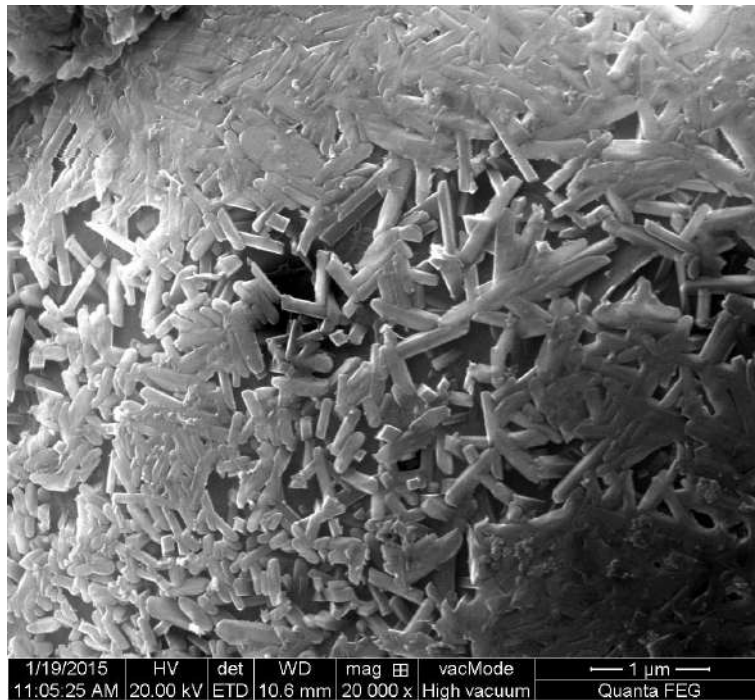


Figure 4.25 Micrograph illustrating the presence of needle like crystals in the RGO paste

Irregularly oriented C-S-H was noticed in the fractured surface of 28-day cured control paste. The presence of wrinkled graphene sheets, hexagonal plate-like crystals and short needle

shaped crystals, attributed to portlandite and ettringite respectively were noticed in the fractured surface of 28-day cured cementitious paste modified using reduced graphene oxide. Micrographs illustrating the fractured surface of 28-day cured cementitious paste modified using alumina nanoparticles are shown in Figure 4.26 to Figure 4.27.

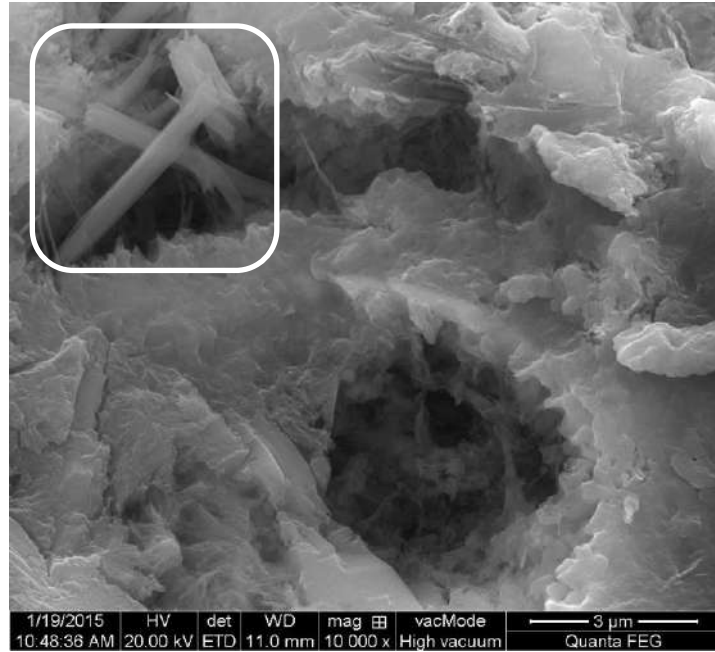


Figure 4.26 Micrograph showing the formation of thick rod shaped crystals in the Al₂O₃ paste

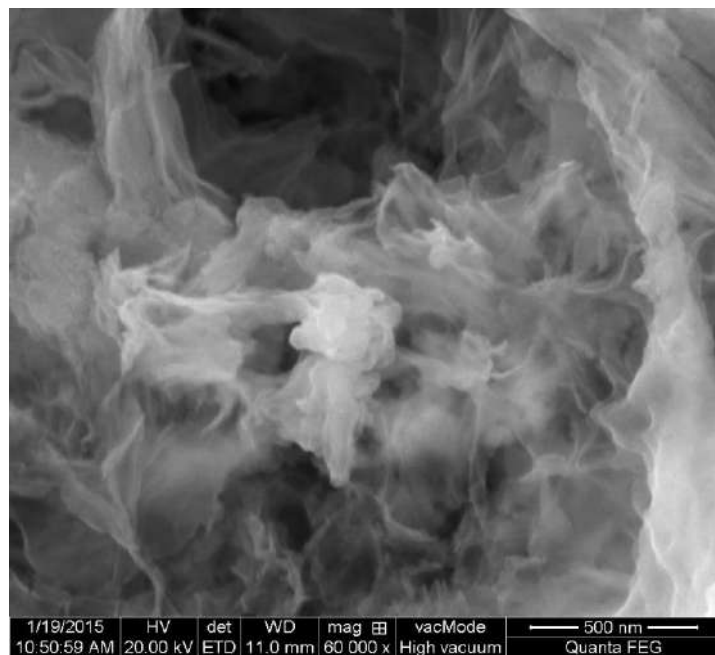


Figure 4.27 Micrograph illustrating the cloud like calcium silicate hydrate in the Al₂O₃ paste

The addition of alumina nanoparticles caused the formation of thin sheet like calcium silicate hydrate having rough texture. Formation of rod shaped crystalline compounds was additionally noticed. A micrograph illustrating the fractured surface of SiO₂ paste is shown in Figure 4.28.

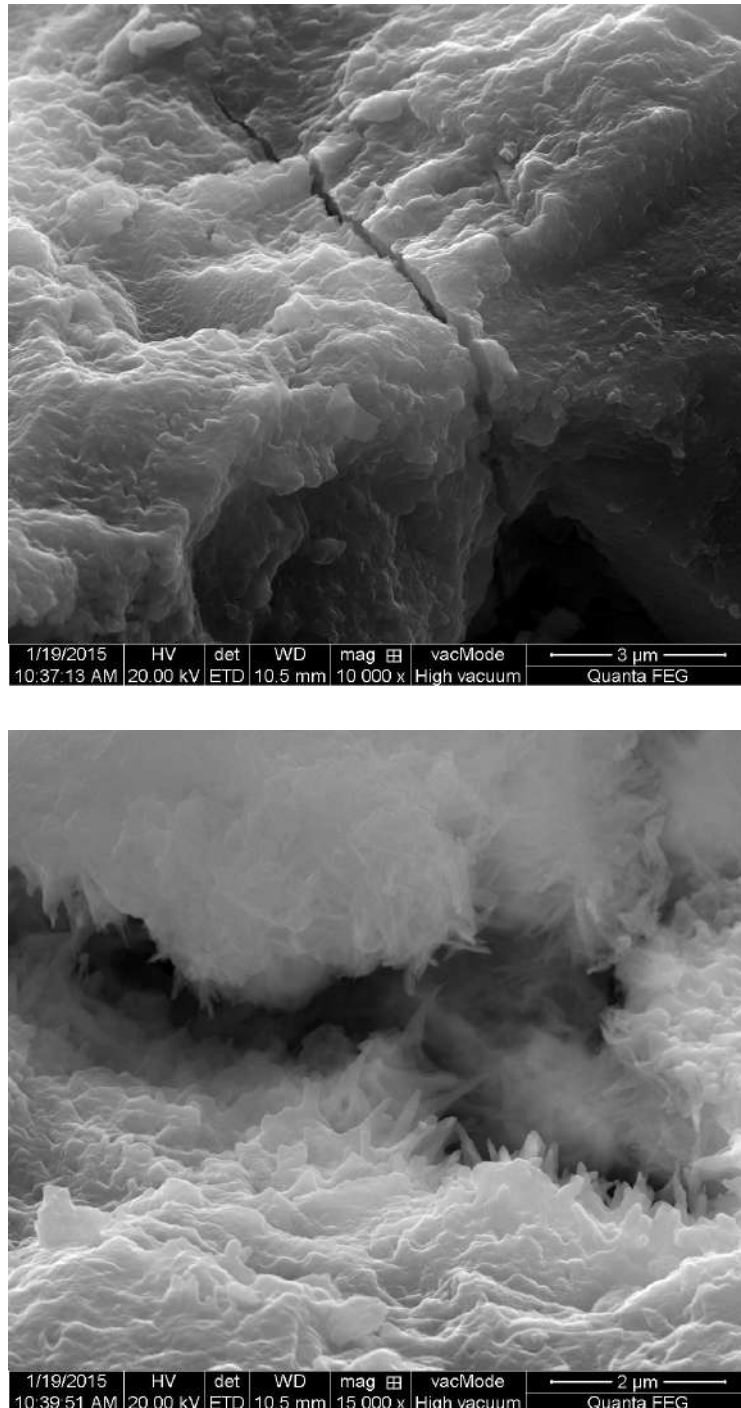


Figure 4.28 Micrograph illustrating the C-S-H having homogeneous texture (top image) and the growth of needle shaped crystals from such hydrate (bottom image) in the SiO₂ paste

The silica nanoparticles may have chemically reacted with the portlandite crystals and thereby produced calcium silicate hydrate having homogeneous texture, which was seen in the fractured surface of SiO_2 paste after curing for 28 days. Additionally, the growth of short needles could be bunches of C-S-H plates collapsed together at the period of drying. The formation of such crystals in the nanomaterial-modified pastes may refine the pore structure and thereby increase the mechanical strengths when compared to control paste.

4.6 SUMMARY

The effect of rGO on the properties of Portland cement paste in comparison to popularly reviewed nanomaterials including nano alumina and nano silica was demonstrated in this chapter. The addition of 0.02 wt% rGO had refined the pore structure and thereby increased the mechanical strength of cement paste. At early ages, the presence of rGO in cement paste had increased the growth and production of binder phases resulting from the large surfaces available for nucleation. In the context of the current project that deals with filtration of heavy metals using porous concrete systems, it would be essential to understand how cementitious composites prepared using such nano additives resist degradation in aggressive conditions brought about by the aqueous solutions containing the pollutants. Therefore, the next chapter demonstrates the role of rGO, nano alumina and nano silica on the deterioration characteristics of 28-day cured cementitious paste after storage in acidic solution for a period of 56 days.

CHAPTER 5

EFFECT OF GRAPHENE, ALUMINA AND SILICA NANOPARTICLES ON THE DETERIORATION CHARACTERISTICS OF OPC PASTE EXPOSED TO ACIDIC ENVIRONMENT

5.1 INTRODUCTION

The effect of rGO on the properties of OPC paste in comparison to alumina and silica nanoparticles was demonstrated in the previous chapter. This chapter explores the influence of these nanoparticles on the resistance of cement paste to acidic environment. This study was undertaken to evaluate the leaching characteristics of cementitious media, which would be of prime importance in water filtration. To investigate this, the 28-day cured cementitious pastes such as Control, RGO, Al₂O₃ and SiO₂ were exposed to highly aggressive nitric acid environment. Different characterisation techniques such as X-ray CT, MIP, TGA, XRD, FTIR, SEM/EDS, nanoindentation and optical microscopy (OM) were used to study the degraded pastes at different time periods.

5.2 ACID IMMERSION TEST

Prismatic specimens of 10 × 10 × 50 mm were prepared using acrylic moulds for the acid immersion test. Apart from the control mix, three paste mixes were incorporated with graphene, alumina and silica nanoparticles at concentrations of 0.02%, 0.2% and 4% by weight of cement respectively. These four mixes were designated as Control, RGO, Al₂O₃ and SiO₂. The preparation procedure of these mixes is already explained in the previous chapter. The prismatic specimens were demoulded after 24 hours from the time of mixing and then cured in saturated limewater solution up to 28 days. In this chapter, the limewater cured specimens are designated as t+0. The t+0 specimens were immersed in 0.5 mol/L HNO₃ solution for a period of 56 days. The acidic solution was replenished frequently to maintain the aggressiveness of the acid. To avoid carbonation, the immersion test was performed inside a glove box, which was purged with inert gas (N₂). The specimens were

taken out after 10, 28 and 56 days of storage, and were designated as t+10, t+28 and t+56 respectively. The collected specimens were then continuously stored in isopropyl alcohol (IPA) to stop the microstructural changes prior to characterisation studies.

5.3 RESULTS AND DISCUSSION

5.3.1 Analysis of phase changes by FTIR and XRD

Prismatic specimens of t+0, t+10 and t+28 pastes were sectioned into multiple slices of size $10 \times 10 \times 10$ mm using diamond-tipped saw. Notably, each slice of the t+10 and t+28 pastes were further sectioned into four halves and thereby majority of such smaller pieces were noticed to be occupied with the degraded layer rather than the unaffected material, which was later ground using mortar and pestle and then sieved through $75 \mu\text{m}$ sieve for FTIR, XRD and TGA studies. Figures 5.1 to 5.4 show the mid infrared spectra of those pastes.

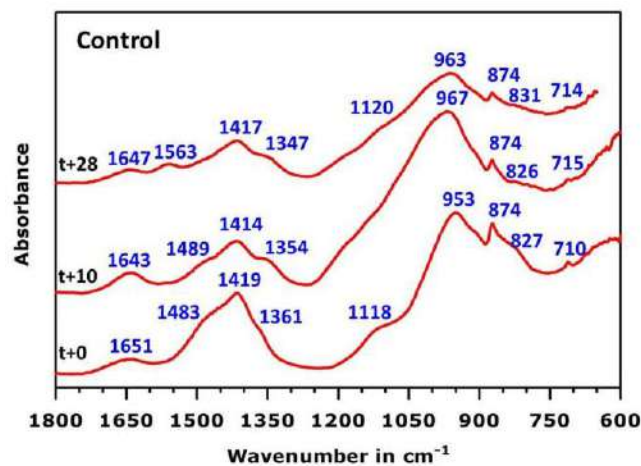


Figure 5.1 Mid infrared spectra of the t+0, t+10 and t+28 control paste

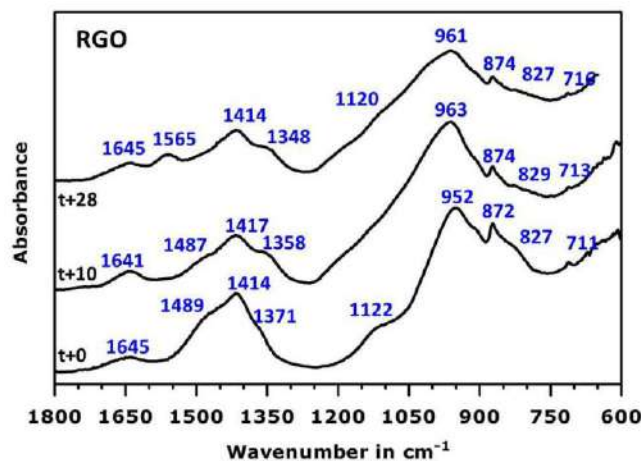


Figure 5.2 Mid infrared spectra of the t+0, t+10 and t+28 RGO paste

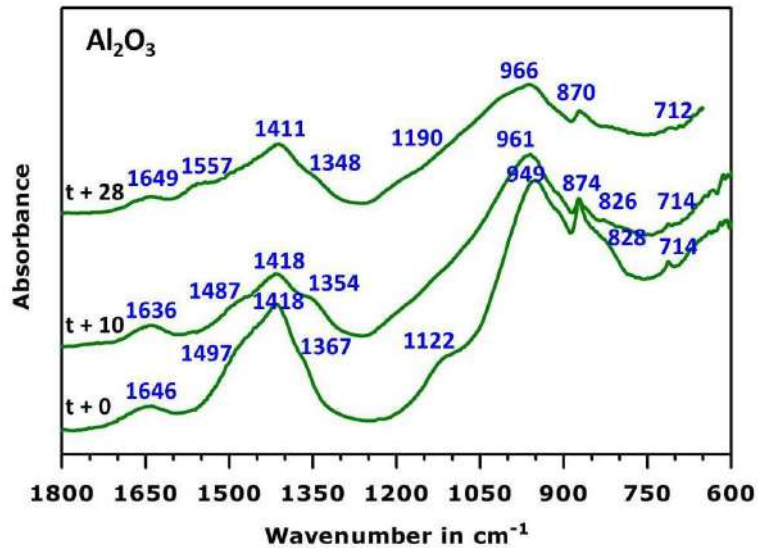


Figure 5.3 Mid infrared spectra of the t+0, t+10 and t+28 Al₂O₃ paste

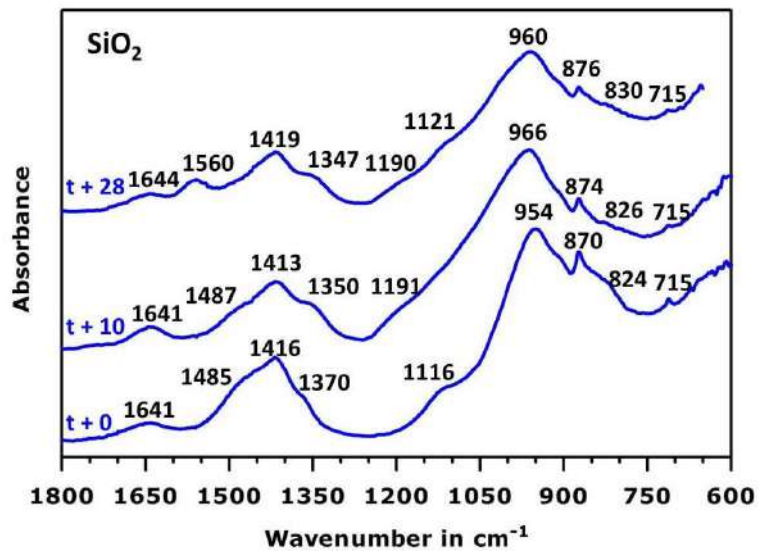


Figure 5.4 Mid infrared spectra of the t+0, t+10 and t+28 SiO₂ paste

The peak attributed to the O-H bend $\sim 1647\text{ cm}^{-1}$ indicated the presence of portlandite in the pastes. This peak intensity was found to be diminishing with an increase in storage time that may be due to the dissolution of Ca(OH)₂ from the pastes after storage in the acidic solution. The peaks attributed to C-O stretch $\sim 1414\text{ cm}^{-1}$ and C-O bend $\sim 874\text{ cm}^{-1}$ showed the formation of calcium carbonate compounds. The presence of silica gel was indicated by the peak at wavenumber 963 cm^{-1} (SiO₄). Lastly, in case of t+28 pastes, the peak attributed to N-O stretch $\sim 1563\text{ cm}^{-1}$ vibration indicated the presence of Ca(NO₃)₂ (calcium nitrate), the compound which could be formed because of reaction between Ca²⁺ leachates and HNO₃ solution. However, the Ca(NO₃)₂ salt, which is highly soluble may not remain stable in the

pastes for prolonged storage time. The XRD patterns of the t+0, t+10 and t+28 pastes are illustrated in the Figures 5.5 to 5.8.

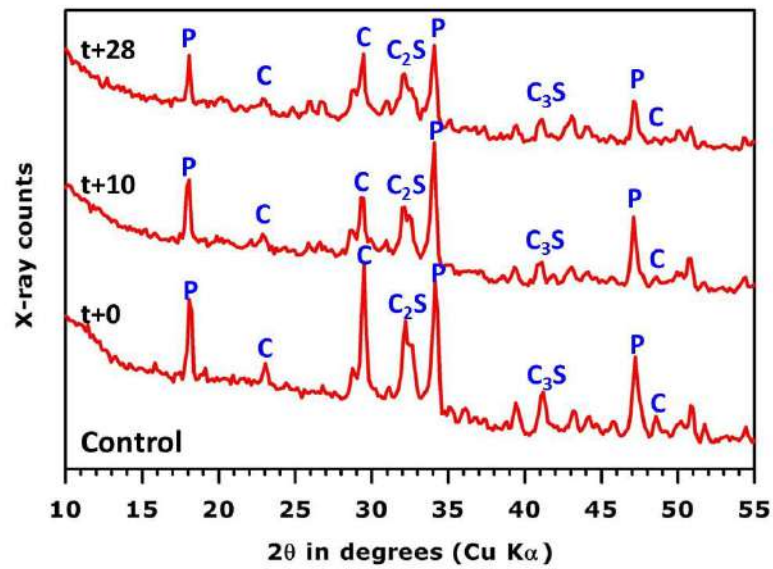


Figure 5.5 XRD pattern of the t+0, t+10 and t+28 control paste

(Note: P – Portlandite, C – calcite, C₂S – dicalcium silicate and C₃S – tricalcium silicate)

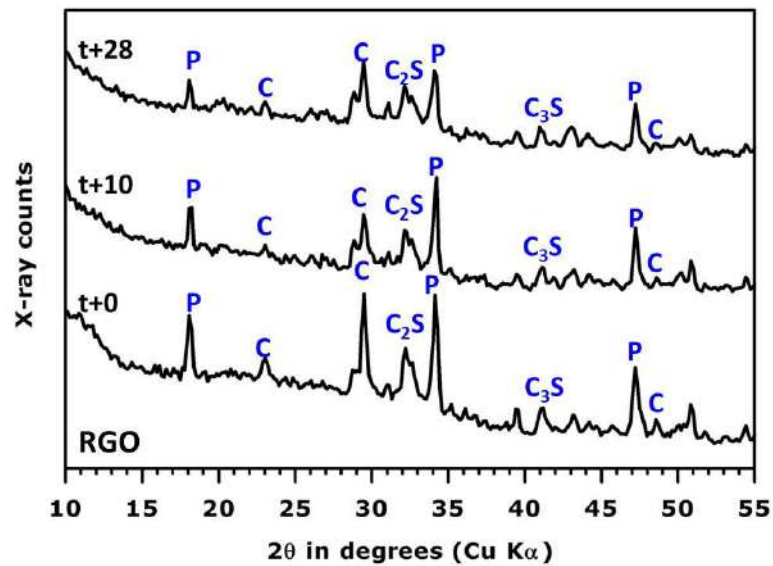


Figure 5.6 XRD pattern of the t+0, t+10 and t+28 RGO paste

(Note: P – Portlandite, C – calcite, C₂S – dicalcium silicate and C₃S – tricalcium silicate)

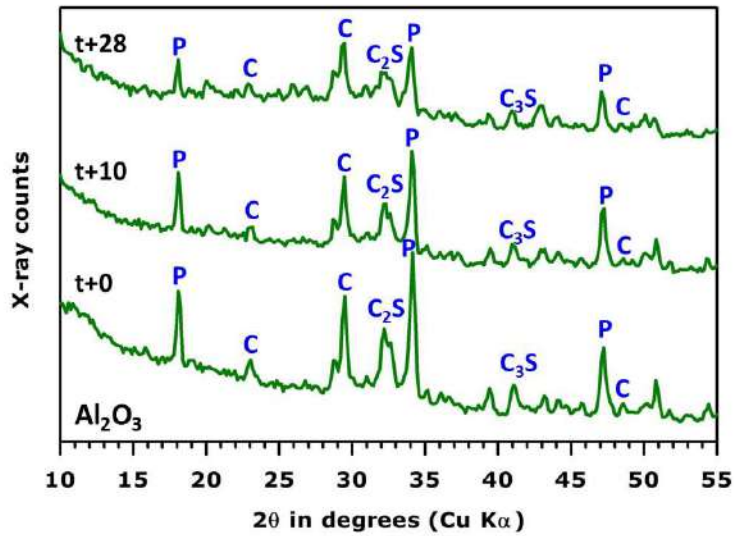


Figure 5.7 XRD pattern of the t+0, t+10 and t+28 Al₂O₃ paste

(Note: P – Portlandite, C – calcite, C₂S – dicalcium silicate and C₃S – tricalcium silicate)

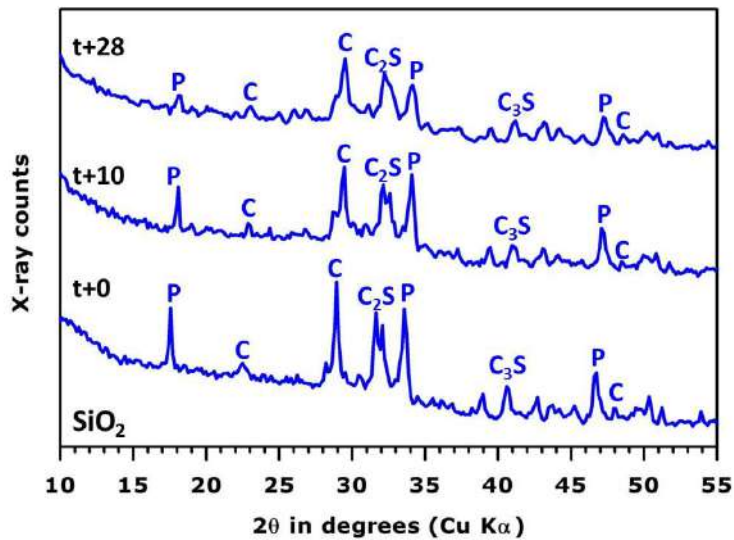


Figure 5.8 XRD pattern of the t+0, t+10 and t+28 SiO₂ paste

(Note: P – Portlandite, C – calcite, C₂S – dicalcium silicate and C₃S – tricalcium silicate)

The peaks at 18.08°, 34.08° and 47.10° 2θ correspond to the presence of portlandite in the pastes. The formation of calcite in the cementitious matrix is indicated by the peaks at 2θ angle of 23.06°, 29.44°, 48.56° and 32.05°, 41.13° respectively. Qualitatively, it can be suggested from the XRD analysis that the amounts of portlandite (P) and calcite (C) were found to be decreased with an increase in storage time. The calcite products are likely to form

when the binder phases react with the CO₂ from the environment. In the t+10 and t+28 pastes, the calcite could have formed after the removal from the acidic solution and before the conduct of XRD.

5.3.2 Quantification of phase changes by TGA

The assessments made with the XRD and FTIR results were better supported with the quantification of binder phases from the TGA study. The powder samples were heated up to 1000 °C at a rate of 10 °C/min in a N₂ environment. The TGA patterns of the t+0 and t+28 pastes are illustrated in Figure 5.9 and Figure 5.10 respectively.

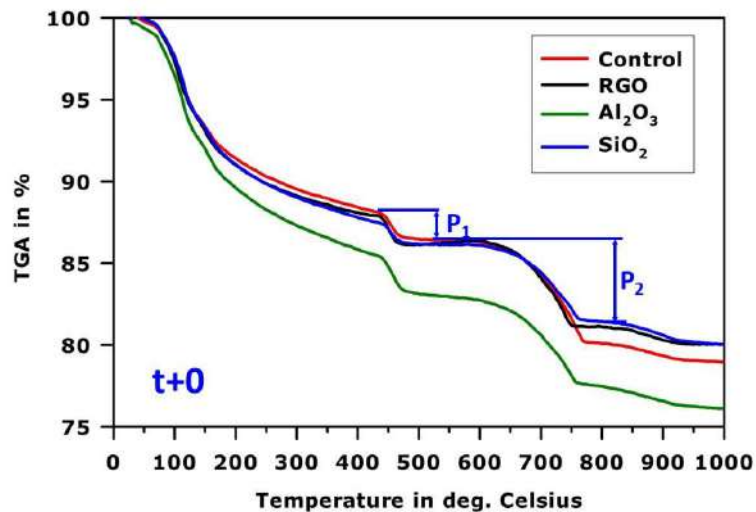


Figure 5.9 TGA pattern of the t+0 pastes

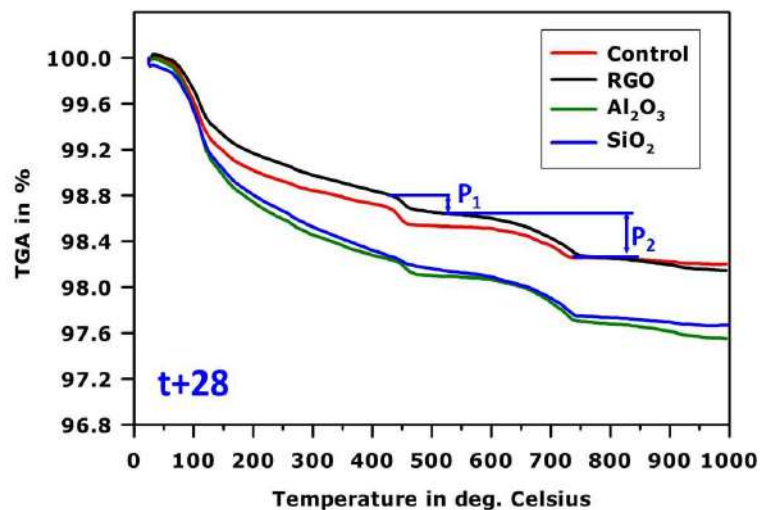


Figure 5.10 TGA pattern of the t+28 pastes

P₁ and P₂ in the TGA plot indicate the gravimetric change due to Ca(OH)₂-dehydroxylation and CaCO₃-decarbonation respectively. Additionally, the amount of bound water is characterised by the mass loss between 105 °C and 975 °C, discounting the mass loss that is associated with the decomposition of CaCO₃. Table 5.1 compares the amounts of portlandite, calcite and bound water available in the t+0 and t+28 pastes that were calculated from their TGA plots.

Table 5.1 Amounts of portlandite, calcite and bound water in the t+0 and t+28 pastes that were calculated from their TGA plots

Mix designation		Control	RGO	Al ₂ O ₃	SiO ₂
% Dehydroxylation of Ca(OH) ₂ ~430 to 480 °C	t+0	5.920	7.194	8.769	4.489
	t+28	0.510	0.724	0.510	0.148
% Decarbonation of CaCO ₃ ~600 to 780 °C	t+0	14.027	11.950	11.516	10.430
	t+28	0.600	0.764	0.798	0.814
% Bound water content ~105 to 975 °C	t+0	11.873	11.446	14.712	12.425
	t+28	1.050	1.151	1.513	1.424

It can be noticed from the TGA results that the amounts of portlandite, calcite and remaining phases were substantially decreased in the pastes after storage in acidic solution for the period of 28 days. Notably, the amounts of bound water in the Control, RGO, Al₂O₃ and SiO₂ pastes at t+28 days were found to be decreased up to 89%, 83%, 86% and 88% when compared to their 28-day cured cementitious pastes respectively. The minor addition of reduced graphene oxide, alumina and silica nanoparticles had reduced the phase changes marginally in the pastes exposed to highly aggressive aqueous media.

5.3.3 Pore structure by porosimetry

The degraded specimen of size 10 × 10 × 10 mm was sliced along its cross section using a Diamond-tipped saw. For MIP testing, the cut section from the middle of the prismatic specimen was used. Figures 5.11 to 5.14 show the porosimetry results of the t+0 and t+28 pastes.

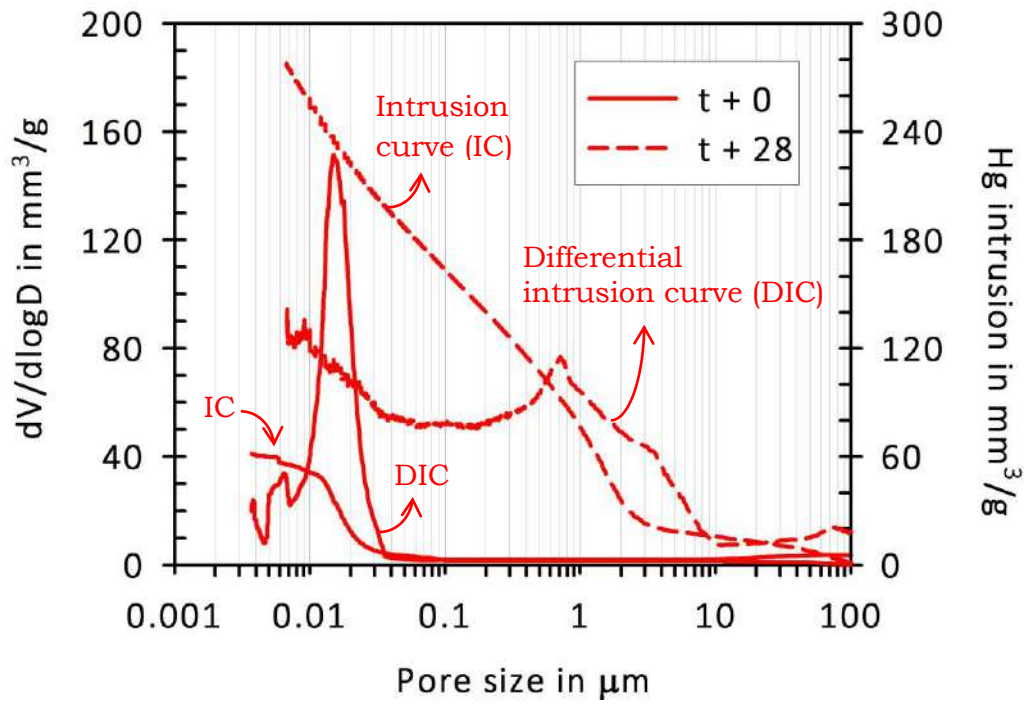


Figure 5.11 Porosimetry result of t+0 and t+28 control paste

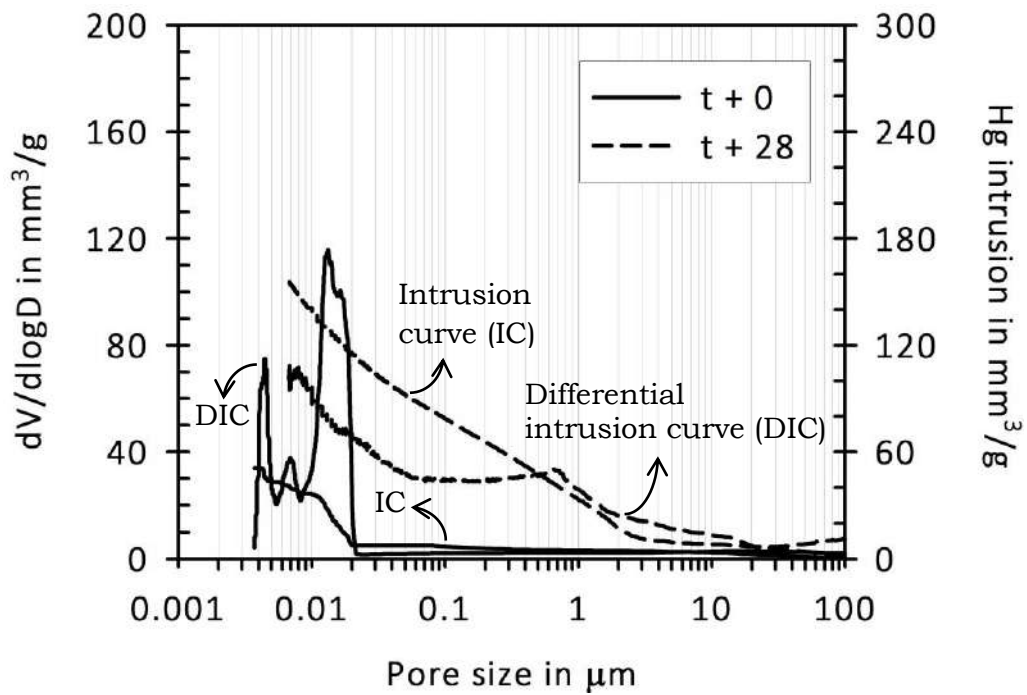


Figure 5.12 Porosimetry result of t+0 and t+28 RGO paste

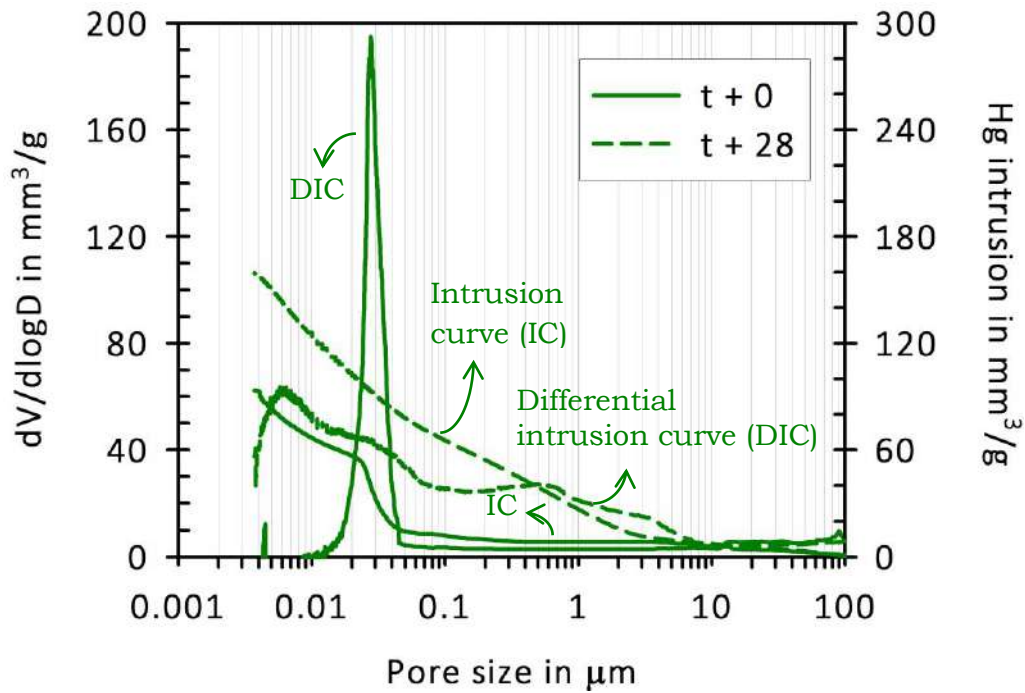


Figure 5.13 Porosimetry result of t+0 and t+28 Al₂O₃ paste

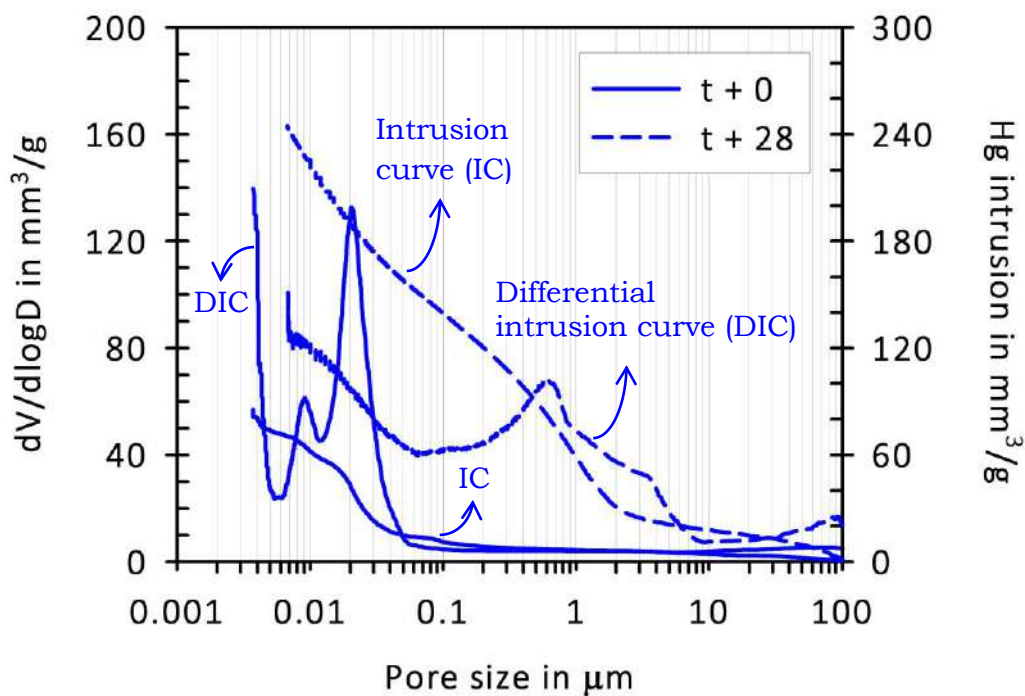


Figure 5.14 Porosimetry result of t+0 and t+28 SiO₂ paste

The MIP results show the cumulative intrusion curve (dashed line) and the differential intrusion curve (solid line), which were plotted together. Aligizaki (2005) had earlier classified that the size of pores falling between 10 nm to 10 μm are capillary pores in the cementitious matrix. The pore size beyond which there is a sudden increase in the mercury

intrusion curve indicates the threshold diameter. The major peak in the differential curve is identified to be the most likely (or critical) diameter. The aforementioned pore related features of the t+0 and t+28 pastes are compared in Table 5.2.

Table 5.2 Pore related features of t+0 and t+28 pastes determined using porosimetry

Mix designation		Control	RGO	Al₂O₃	SiO₂
Threshold diameter in μm	t+0	0.027	0.021	0.039	0.029
	t+28	3.4	2.8	3.6	3.2
Most likely diameter in μm	t+0	0.015	0.013	0.028	0.021
	t+28	0.7	0.7	0.6	0.6
Capillary pores (10 nm to 10 μm) in mm^3/g	t+0	48.6	33.1	60.6	57.8
	t+28	239.9	130.4	116.9	205.4

The MIP results suggest that the pore related features of the pastes were significantly altered because of its exposure to the acidic environment. The threshold diameter of the Control, RGO, Al₂O₃ and SiO₂ pastes after storage in HNO₃ solution was increased up to 126, 133, 92 and 110 times than their 28-day cured cementitious pastes respectively. However, the addition of reduced graphene oxide, alumina and silica nanoparticles resulted in lesser capillary porosity compared to the control paste after storage in acidic solution. In particular, the presence of graphene and nano alumina had decreased the amounts of capillary pores up to 45.6% and 51.2% than the control paste (t+28) respectively. Although the alumina nanoparticles were agglomerated (as previously discussed in the section 4.2), their availability in the paste matrix had considerably delayed the diffusion of deleterious ions and thus decreased the alterations in pore structure.

5.3.4 Imaging of the alteration phases by optical microscopy and X-ray CT

Multiple sections of size 10 × 10 × 10 mm were carefully cut out from the middle of the t+0, t+28 and t+56 pastes and their appearance is shown in Figure 5.15.

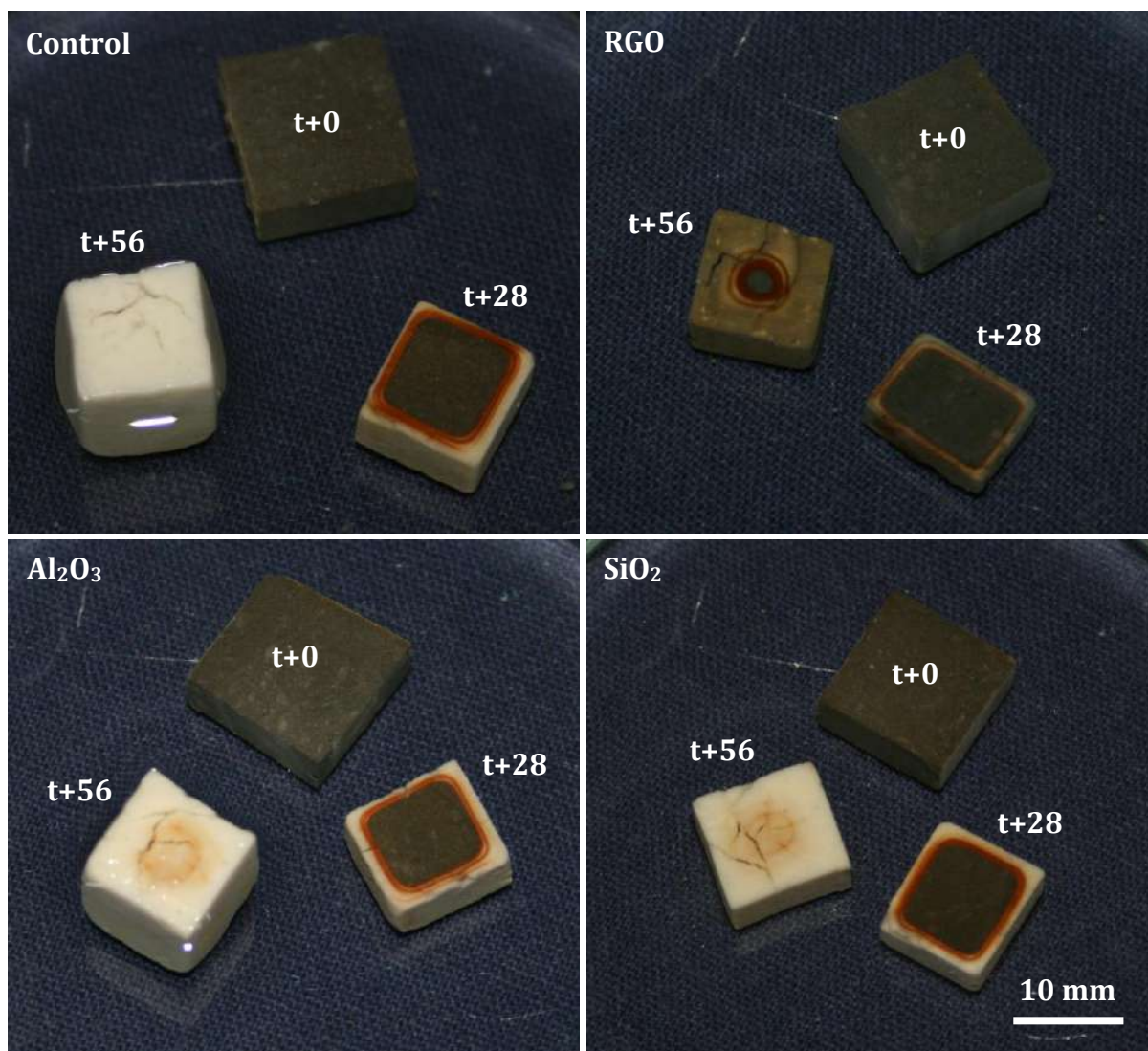


Figure 5.15 Digital photographs illustrating the cut sections of t+0, t+28 and t+56 pastes

The volume of alteration phases increased with an increase in the storage time, which is clearly observed from the photographs. This degradation is governed by Fick's Law of diffusion which states that the leaching fluxes and the position of degradation front is proportional to the square root of storage time in the aggressive solution (Carde et al. 1996, Gutberlet et al. 2015, Nguyen et al. 2007, Pavlík 1994). The cross section of control paste was seen to be completely transformed into white coloured products within 56 days of storage time. However, the brown rings still existed in the Al₂O₃ and SiO₂ pastes at similar storage time.

In the case of RGO paste, a small volume of grey zone surrounded by thin brown rings could be observed. The presence of graphene nanosheets had considerably retarded the movement

of Fe^{3+} ions into the external solution from the degraded specimen. Qualitatively, the photographs suggest that the addition of nanomaterials in OPC paste had delayed the alterations by a perceptible amount when compared to control paste. Figure 5.16 compares the optical micrographs of the t+28 pastes. The relative performance of rGO modified paste was better than Al_2O_3 and SiO_2 pastes.

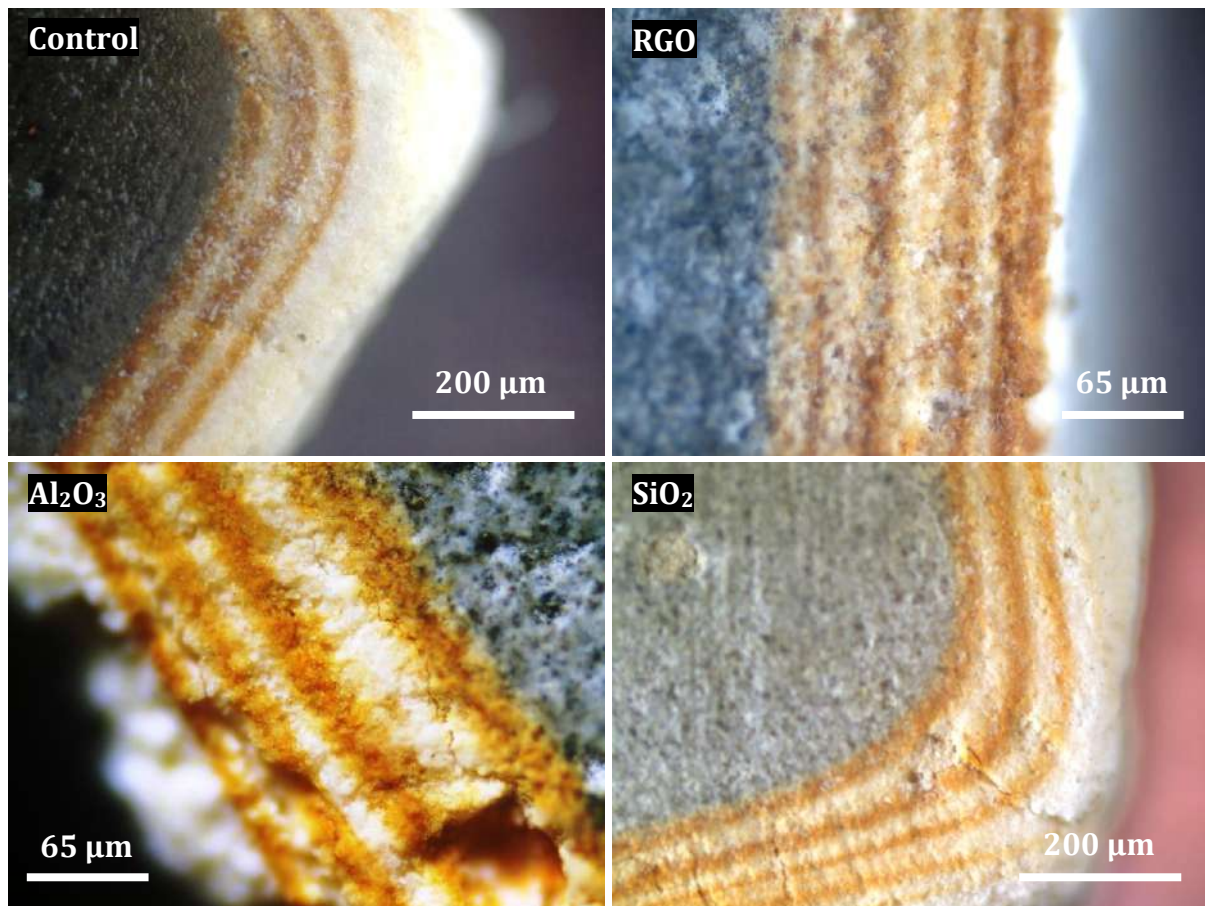


Figure 5.16 Optical micrographs illustrating the degraded zone in the t+28 pastes

Acid attack on the binder phase forms iron based precipitates at the degradation front, which is responsible for the brown discolouration. It appears at locations where the pH of system decreases to 2 or lesser (Pavlík 1994). This study used 0.5 mol/L HNO_3 solution as storage medium and its pH was measured to be zero. The solution was frequently replenished whenever the value increased to 4 or greater. The aggressiveness of this solution had rapidly destabilised the iron based hydrates, which re-precipitated at the degradation front into more than three brown rings of similar thickness situated at equidistant positions.

The intermediate space between the brown ring and the remaining portions in the degraded layer was observed to be occupied with white coloured amorphous silica gel. Figure 5.17 shows the optical micrograph of the t+28 pastes illustrating the alteration phases and the presence of cracks in them.

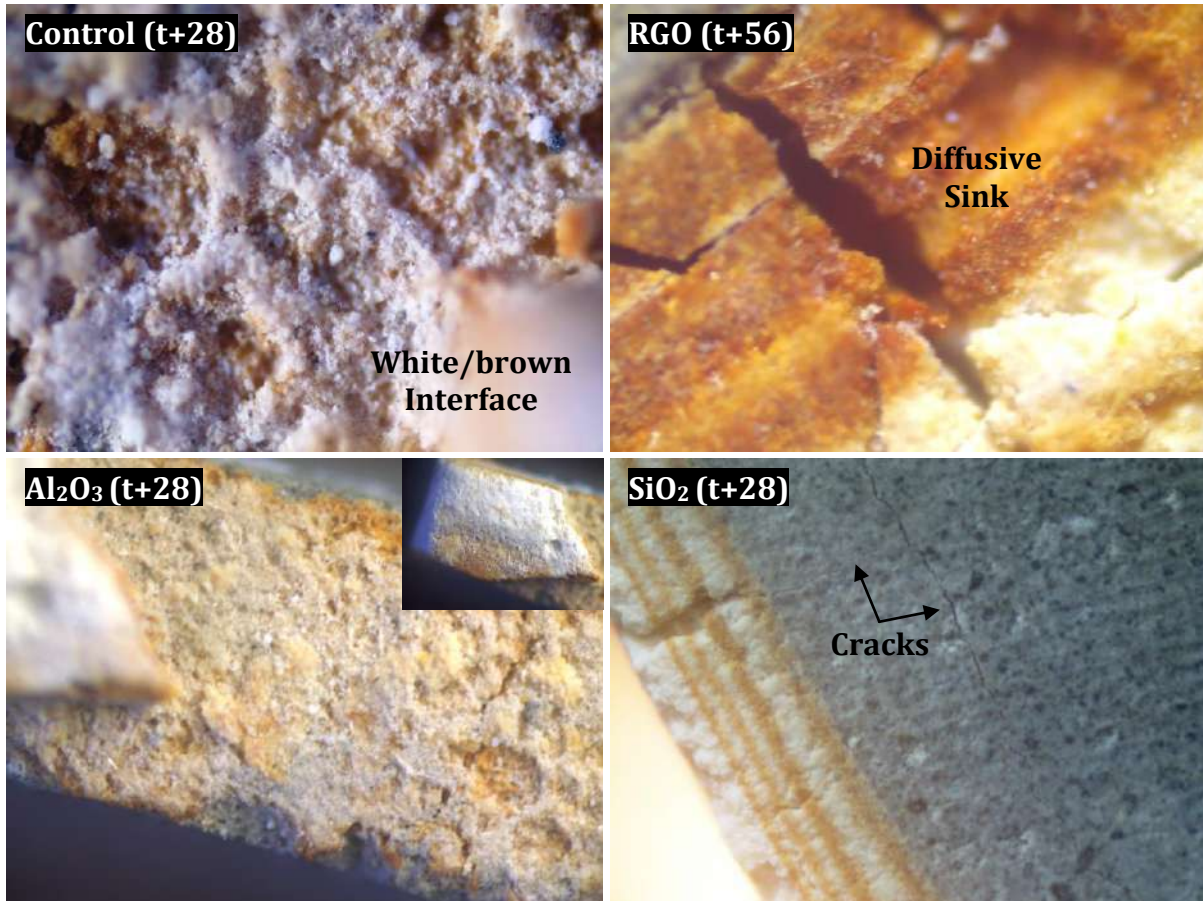


Figure 5.17 Optical micrograph of pastes showing the alteration phases and cracks that were formed in their matrices

At the white/brown zone boundary (seen in the control and Al_2O_3 pastes illustrated in Figure 5.17), Fe^{3+} undergoes two way diffusion, where its concentration partly depletes by a movement into the external solution, and the remaining ions re-precipitate again at the same front or inward as hydroxides. This precipitation marginally increases the pH of the system. For shorter durations, this highly porous mass acts as a barrier which delays the transport of aggressive ions into the proximity of unaffected material (Pavlík 1994).

A wide crack was observed in the micrograph of RGO paste (t+56). The Fe precipitates surrounding this crack could have played the role of a diffusive sink which may have delayed

the ionic movement to the external solution (Mainguy and Ulm 2001). Continuous storage of concrete in aggressive media moves the degradation front inward from the exposed surface. Decalcification advances via the propagation of this front and thus produces a gradient in the Ca/Si ratio. This imbalance acts as driving force for the decalcification induced shrinkage. The generation of differential stresses because of this shrinkage places the exposed surface in tension. The latter induces fracture and crazing at the surfaces (Chen et al. 2006). The crack seen in the unaffected zone of SiO₂ paste (t+28) was formed because of the differential stresses generated by the drying of gels; the possibility of formation of such cracks during specimen preparation cannot be ruled out.

Further, the cut section of the pastes was scanned using GE phoenix v|tome|x s X-ray tomography. Each scan was performed at a voltage and current of 120 kV and 70 μ A respectively. The outcome was the generation of 2-D and 3-D grey scale images of the tested specimen. These images revealed the interior features of the specimen at micrometer scale. Figure 5.18 compares the CT image of control paste tested at time periods t+0 and t+28.

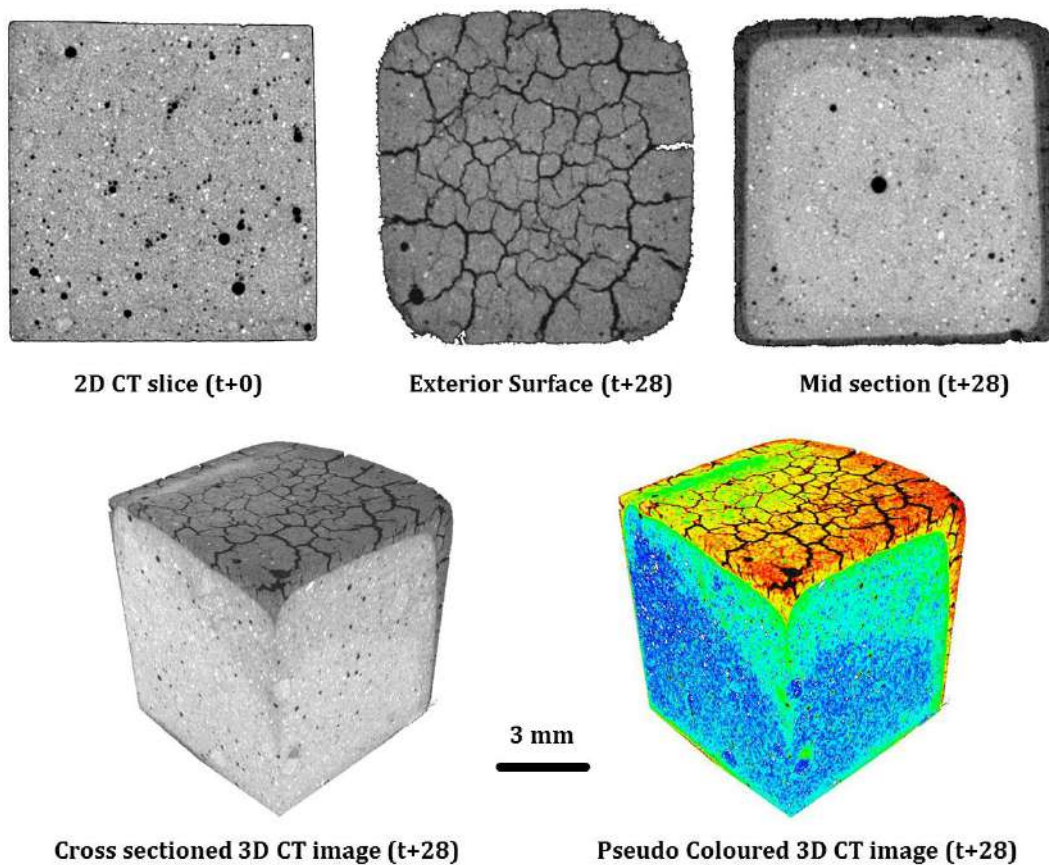


Figure 5.18 CT images illustrating the alteration phases and cracks that were formed in the control paste after storage in HNO₃ solution for the period of 28 days

Dark and bright regions in a CT slice correspond to low and high value of attenuation coefficient. The darker and brighter regions in the CT slice of t+0 paste indicate the presence of air voids and unhydrated phases respectively. After storage in acidic solution, the exterior surface of the specimen was seen to be occupied with shallow cracks which may have formed due to decalcification induced shrinkage. At the mid-section, a highly porous degraded mass surrounding the unaffected material was observed. The inward movement of degradation front from the exterior surface was clearly seen in the 2-D and 3-D CT image of the degraded sample. Pseudo colouring the 3-D CT image was found effective in precisely locating the degradation front in the degraded sample. Figure 5.19 compares the degree of sectional change visualised in the CT slice of the t+28 pastes.

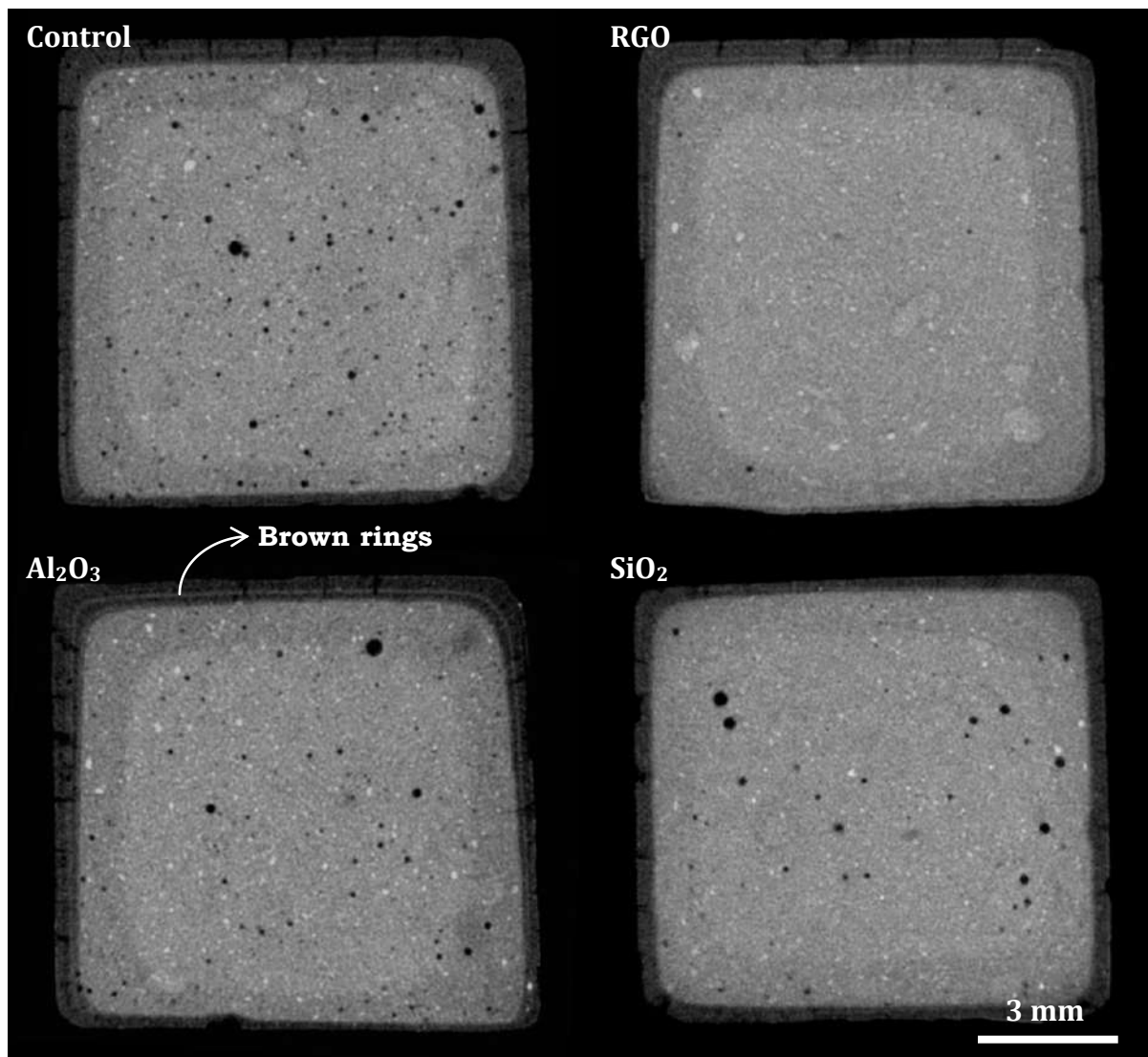


Figure 5.19 CT slice showing the location of degradation front in the t+28 pastes

It can be noticed from the CT slices that the degree of sectional change and the location of degradation front were found to be similar in all pastes (t+28). The occurrence of the brown rings of Fe precipitates in the CT slice was observed to be slightly in contrast within the dark coloured layer. Qualitatively, the degraded layer in the CT slice was visualised to occupy more than 20% of sectional area. This sectional change was observed to be equivalent in all pastes (t+28).

5.3.5 Nanomechanical properties by nanoindentation

For indentation testing, the cut section of prismatic specimen involved impregnation by a low viscosity epoxy using a vacuum impregnation system. Next, coarse polishing was done on the specimen encapsulated by the hardened epoxy polymer to expose the cross section of the specimen. Silicon carbide powder (of # 1000 size) mixed with glycerine/water ratio of 1:3 and cooling lubricant were the consumables utilised to perform the coarse polish. Finally, the sections were fine polished on a lubricated cloth to the desired level using polycrystalline diamond spray of 6 μm , 3 μm and 1 μm size respectively. Micrographs illustrating the polished section of the control paste (t+28) are shown in Figures 5.20 and 5.21.

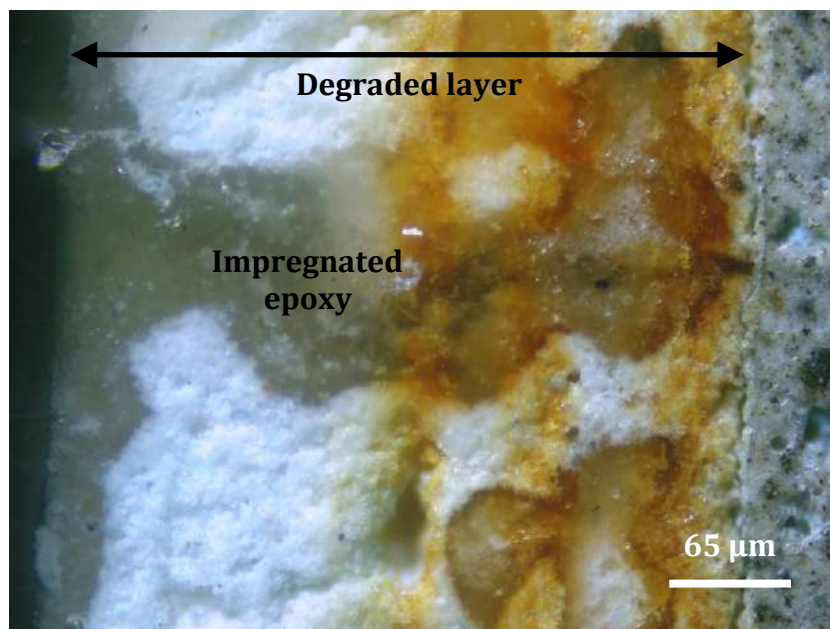


Figure 5.20 Optical micrograph illustrating the polished section of the control paste (t+28)

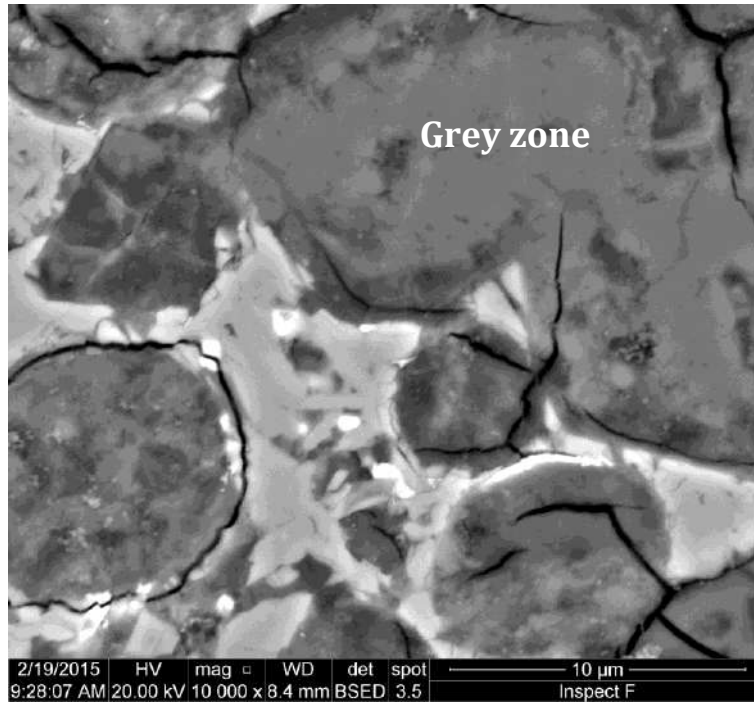


Figure 5.21 Micrograph (SEM in backscatter mode) showing the polished section of grey zone in the control paste (t+28)

A maximum load of 5000 μN capacity was applied using Berkovich tip on the polished sections of t+0 and t+28 pastes. In case of t+28 pastes, the alterations in nanomechanical performance along the cut section comprising of the degraded layer and the unaffected material were assessed by performing multiple indents. Figures 5.22 to 5.24 show the scanning probe microscopy (SPM) image of the indents that were performed on the control paste (t+0).

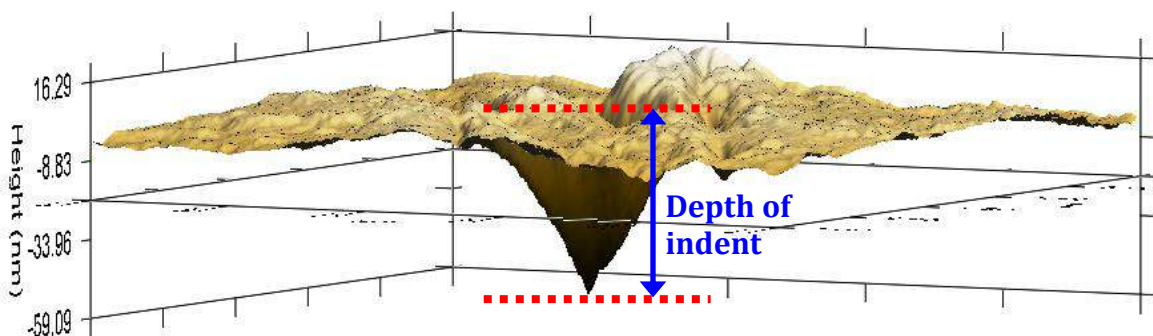


Figure 5.22 Scanning probe microscopy (SPM) image illustrating the depth of indentation in the polished surfaces of control paste (t+0)

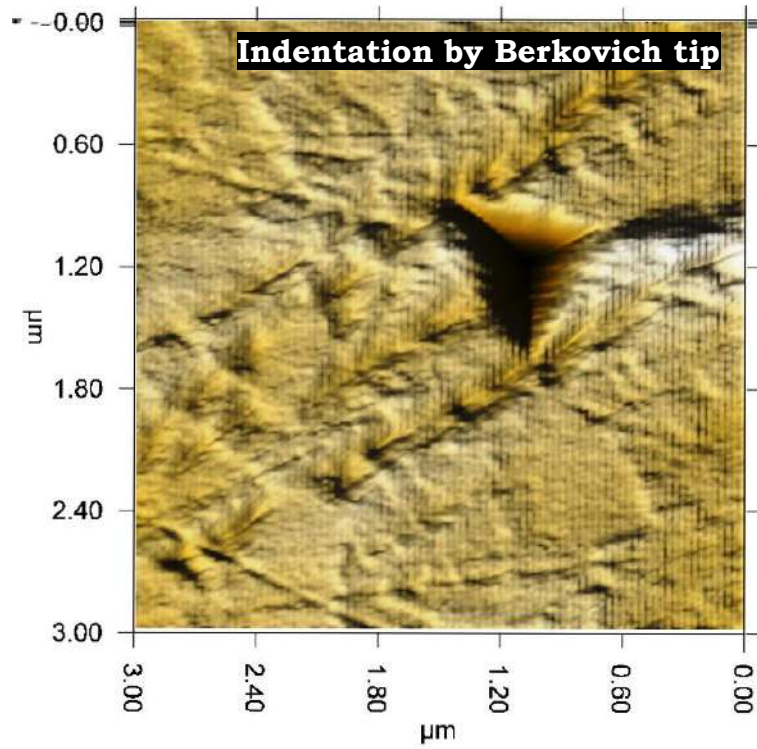


Figure 5.23 SPM image illustrating the indentation performed in the polished surface of control paste (t+0)

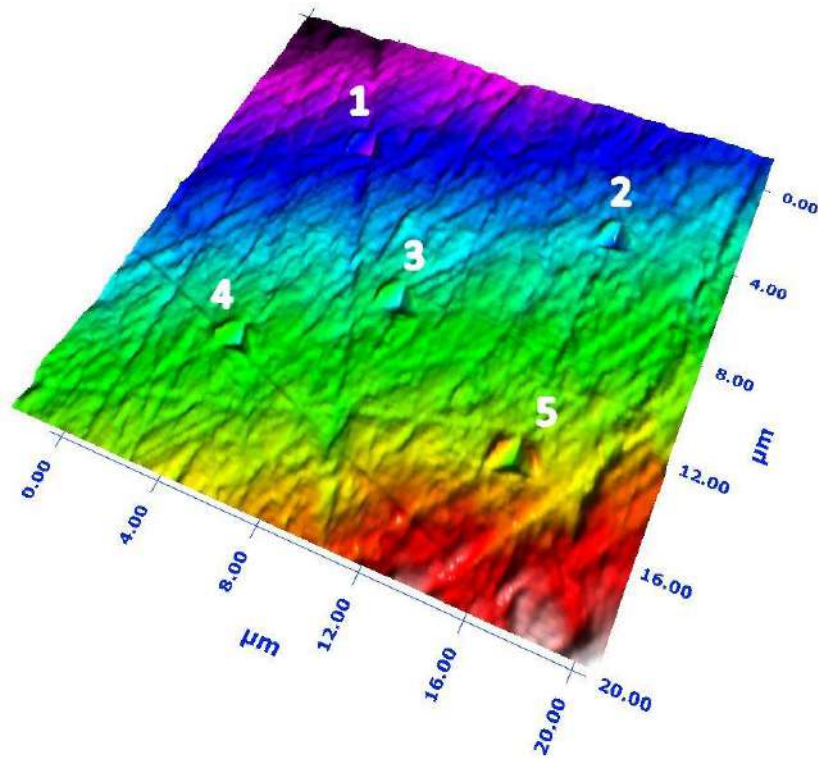


Figure 5.24 SPM image illustrating the five numbers of indentation that were performed in the polished surface of control paste (t+0) for estimating the statistical variance

Figure 5.25 and Figure 5.26 illustrate the schematic diagram of the cut section of t+28 paste and the load displacement curve of indents that were performed in the different zones of such cut section.

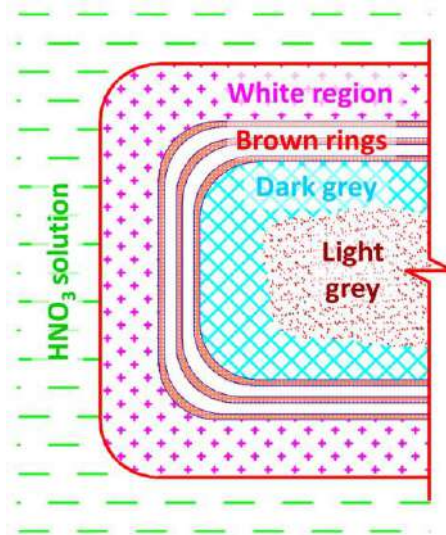


Figure 5.25 Schematic diagram illustrating the different zones which are likely to be formed in the hardened cement paste after storage in nitric acid solution

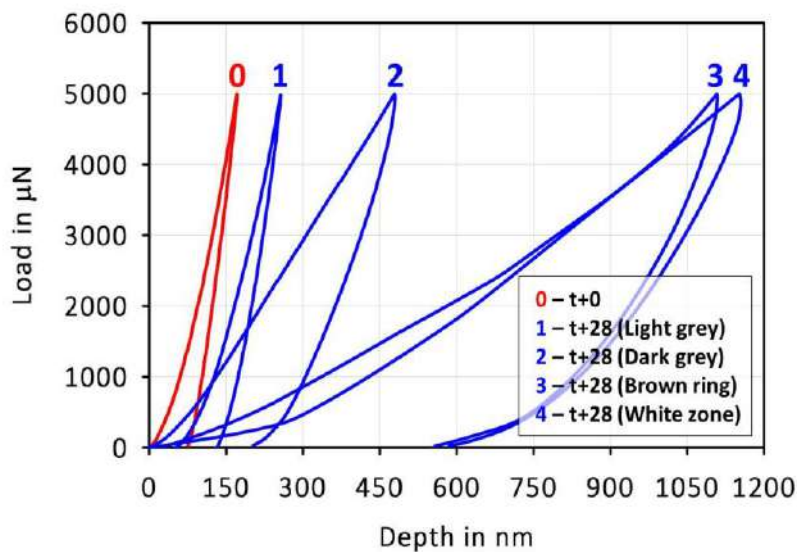


Figure 5.26 Load versus depth of indentation curve of the different zones in the control paste after storage in 0.5 M HNO₃ solution for a period of 28 days

It can be noticed from the load – displacement curves that the degraded layer may be soft when compared to the unaffected material in the control paste (t+28). In the case of t+28 pastes, several pot holes were developed in the hardened epoxy polymer after polish. This could have occurred because of the difference in hardness between the alteration phases and

unaffected material of the degraded specimen. This argument is better supported with the indentation results, which are shown in Figure 5.27.

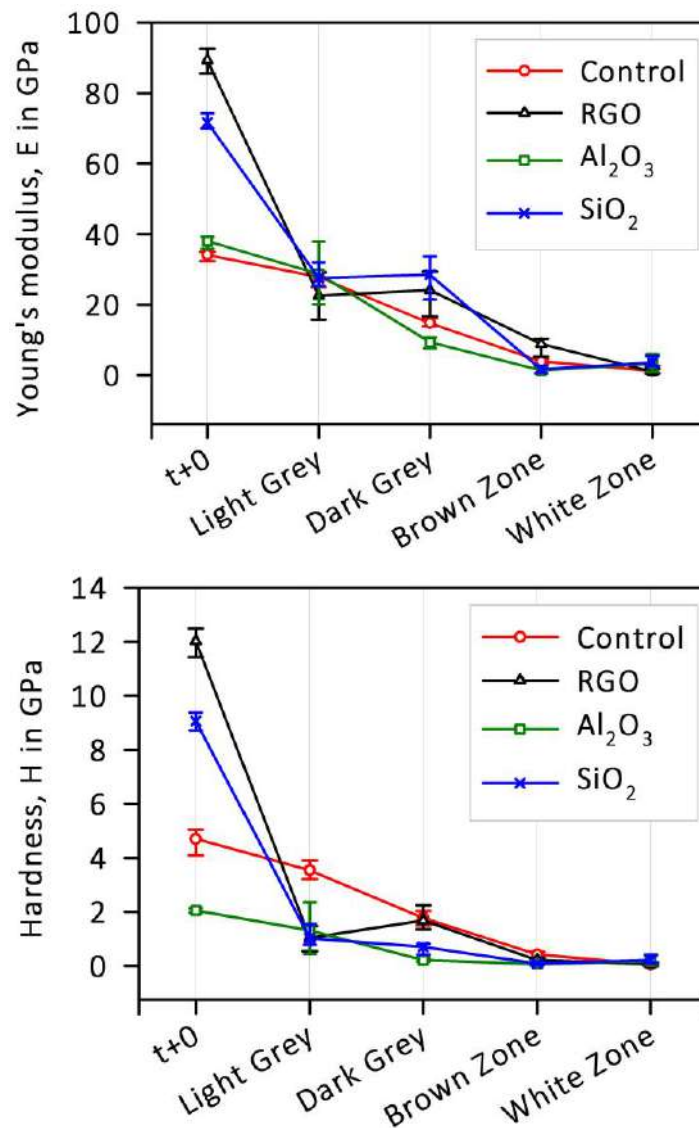


Figure 5.27 Young's modulus (top image) and Hardness (bottom image) of the t+0 paste and different zones in the t+28 pastes determined using nanoindentation technique

The specimen that has undergone acid attack is characterised by the degraded layer (white and brown zone) surrounding the unaffected material. It can be noticed from the E and H results that the nanomechanical performance of the degraded layer was significantly lesser than the unaffected material. This alteration was noticed to be similar in all pastes. Because of this difference in hardness, coupled with the difficulties in proper impregnation with low viscosity epoxy, the t+28 pastes could not be polished up to the desired level for backscattered imaging in the SEM. The average E-modulus values may have been high in

RGO and Al_2O_3 pastes because of the possibility of the tip indenting on unhydrated phases. Velez et al. (2001) demonstrated that the E-Modulus of C_3S , C_2S , C_3A and C_4AF was found to fall within 125 and 145 GPa. The discussion in the section is modified appropriately.

5.3.6 Microstructural assessment by SEM/EDS

The as-polished level of the t+28 pastes that were used for indentation were found to not be appropriate for backscattered imaging, as discussed earlier. Instead, the cut sections were directly used for SEM/EDS analysis (in the Secondary Electron mode). For better resolution of images, gold coating was done over the cut sections to enhance the surface conductivity. In the EDS spectrum, the asterisk (*) symbol indicates gold (Au) which was available because of coating the samples. Elemental line scan was performed on the control paste specimen (t+28). The micrograph and the distribution of major elements in the cut section along the scan are shown in Figure 5.28.

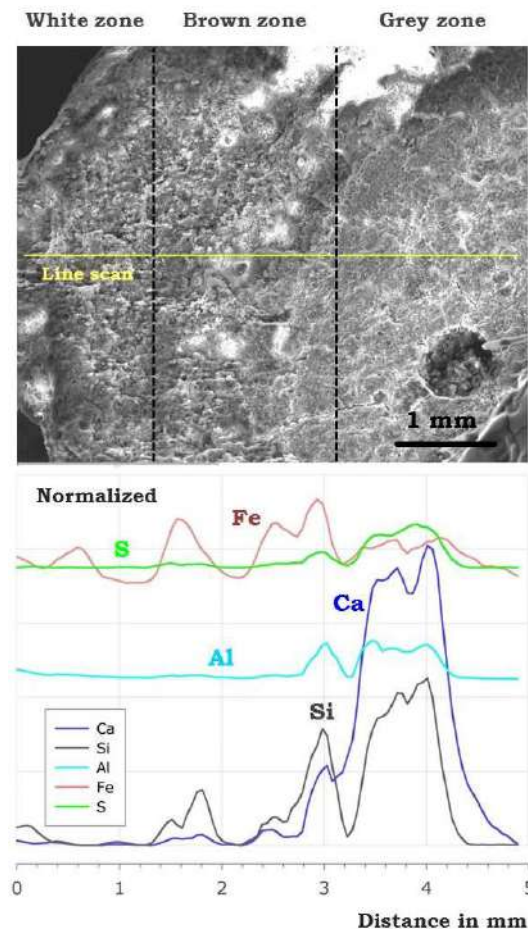


Figure 5.28 Line scan result showing the distribution of major elements in the cut section of control paste (t+28)

The depletion of Ca^{2+} , SO_4^{2-} and Al^{3+} ions in the degraded layer of control paste after storage in acidic solution was noticed from the results of line scan. Fe peaks suggest the precipitation of ferric hydroxide. The remaining portions in the degraded layer were observed to be occupied with amorphous form of silica gel. The degradation front is the location where the calcium starts to deplete because of decalcification and thereby alteration phases may form in such a region. This reactive zone in the cementitious matrix after acid storage is termed as ‘transition zone’ in the present study. The phase changes in the pastes at this location, were mainly assessed using SEM/EDS, and are explained in the following sub-sections.

Control mix

Figure 5.29 and Figure 5.30 show the micrograph and EDS result of the alteration phases in the transition zone of control paste (t+28).

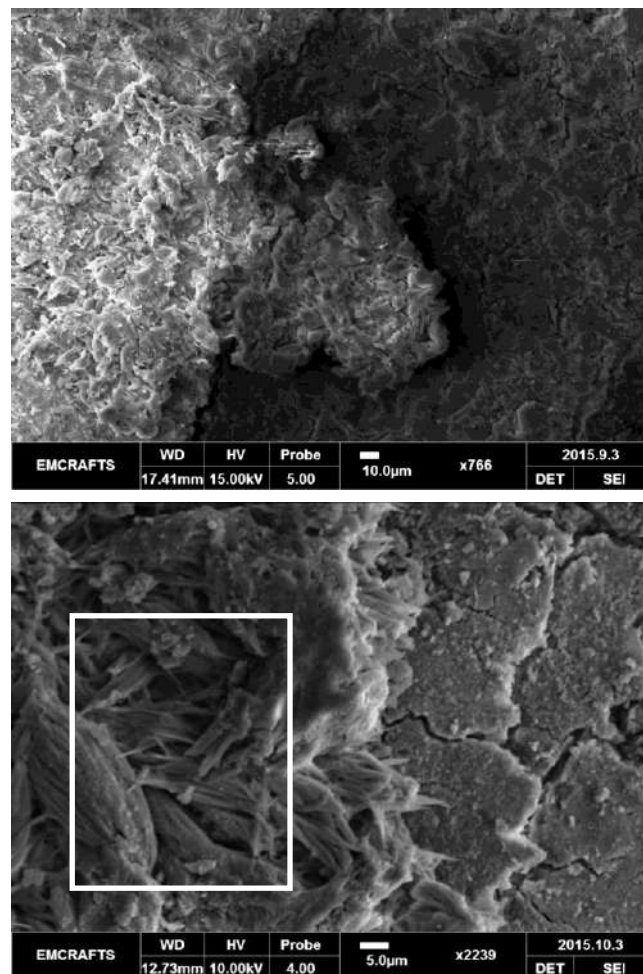


Figure 5.29 Low (top image) and high (bottom image) magnification SEM images illustrating the alteration phases in the transition zone of control paste (t+28)

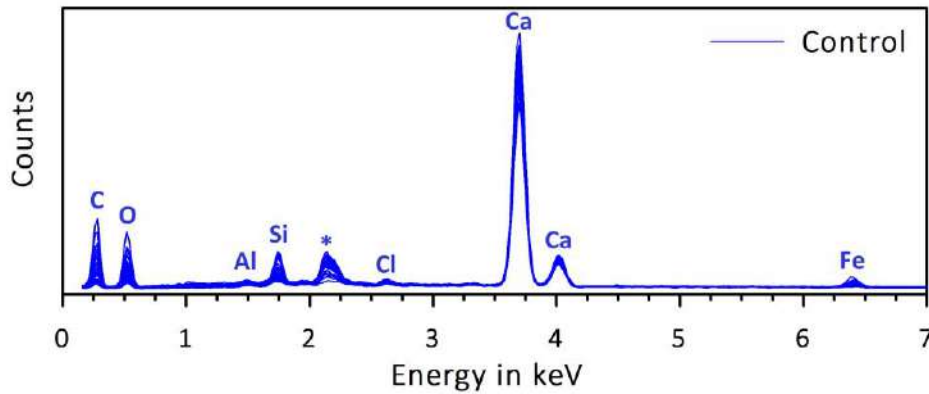


Figure 5.30 EDS result of the alteration phases in the control paste (t+28) – zone indicated by the rectangular box in Figure 5.29

The CO₂ from the environment interacted with the calcium leachates and produced a thick deposit of calcium based compounds having reticulated structure (net like intergrowth) (Figure 5.29). Several EDS points were taken on those alteration phases (zone indicated by the rectangular box) and this analysis confirmed that the deposits were calcite which was precipitated over the degraded layer and undamaged material. Although the acid attack study on paste specimens was performed in a nitrogen environment, and the chances of carbonation during storage in acidic solution would have been negligible, these calcite deposits may have formed after removal from the acidic solution and before the conduct of the SEM/EDS (i.e. during the period of specimen preparation). Figures 5.31 to 5.33 compare the micrograph and EDS result of the different zones in the t+28 paste (control mix).

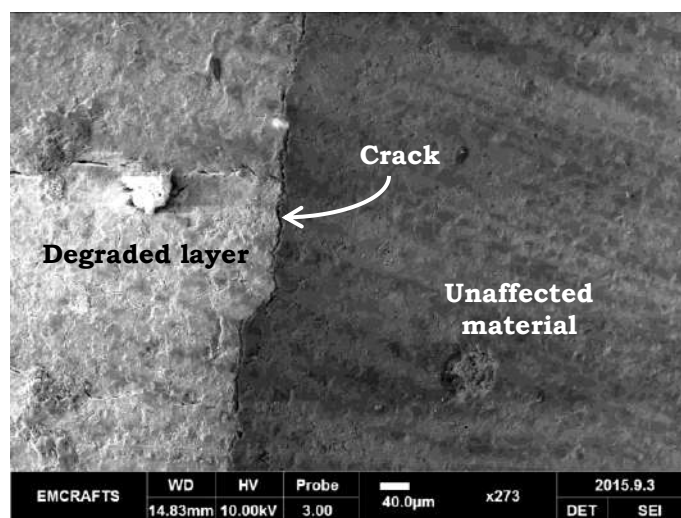


Figure 5.31 Micrograph illustrating the formation of long crack between the degraded layer and unaffected material

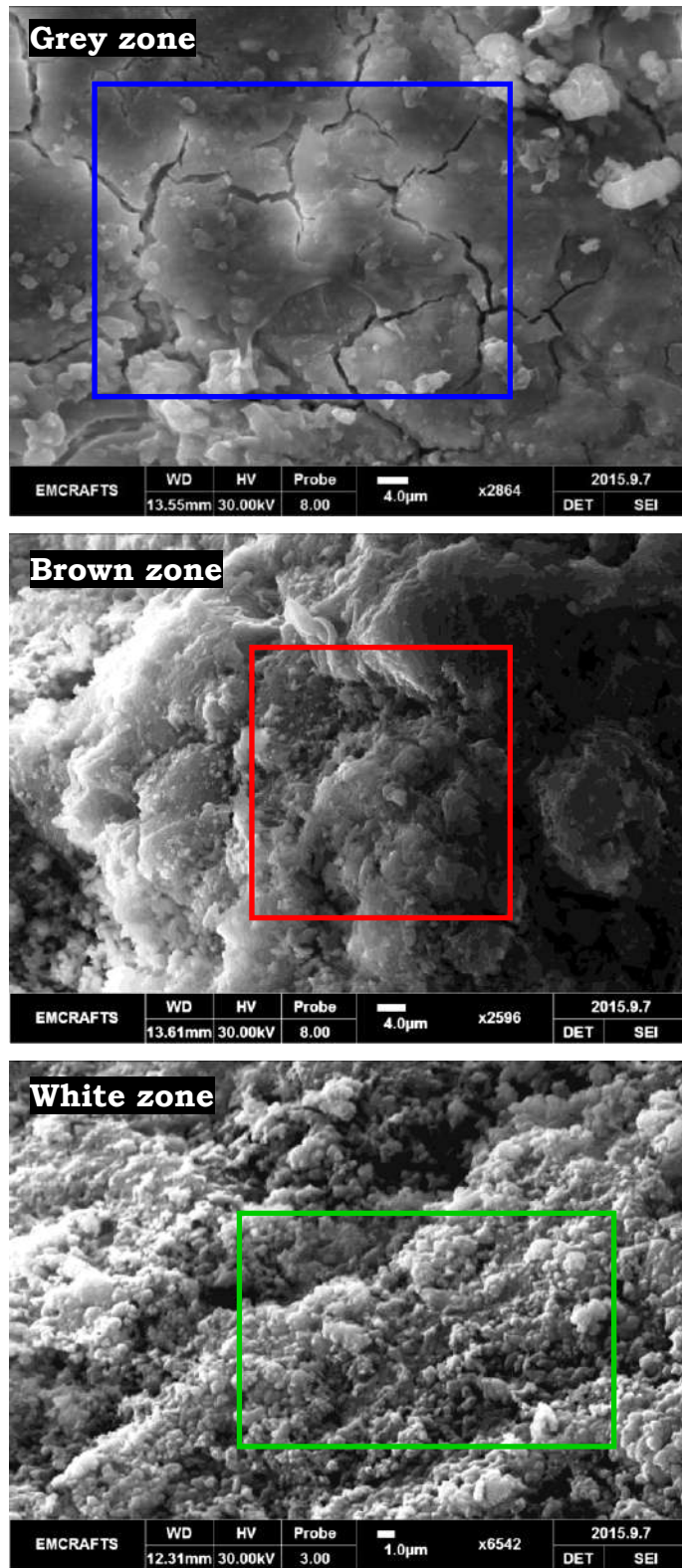


Figure 5.32 Micrographs illustrating the different zones that were formed in the control paste after storage in 0.5 M HNO₃ solution for a period of 28 days

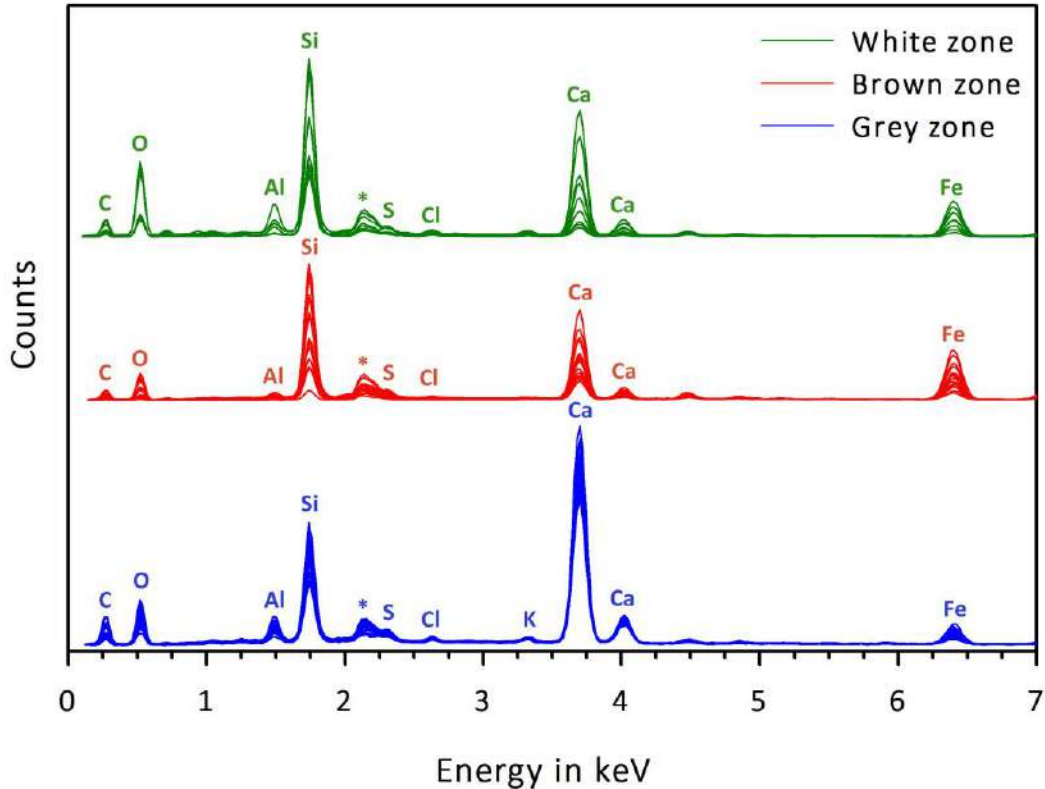


Figure 5.33 EDS spectra of the different zones in the t+28 paste (control mix) – marked by the rectangles in Figure 5.32

HNO₃ attack on cement paste had developed a degraded layer surrounding the unaffected material, which was noticed to be separated by a long crack (Figure 5.31). The unaffected material which is designated as grey zone in this present study was seen to have cracks because of decalcification shrinkage (Figure 5.32). However, as observed from the EDS pattern, there was no alteration of the normal hydrate phases. On the other hand, the highly porous brown and white zones were found to be occupied with Fe and Si based products (Figure 5.33). Acid attack had depleted the Ca²⁺ and Al³⁺ ions in these zones significantly which may have reduced the mechanical strengths of cementitious matrix.

RGO mix

Figures 5.34 to 5.36 show the micrographs and EDS results of the alteration phases that were formed in the transition zone of RGO paste (t+28).

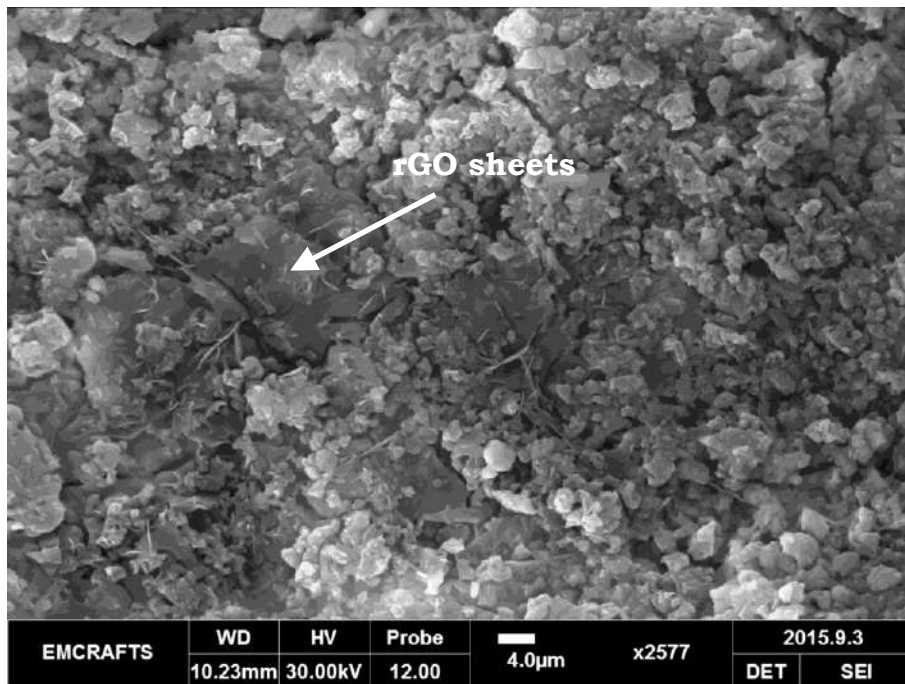


Figure 5.34 Micrograph illustrating the presence of graphene sheets in the transition zone of RGO paste (t+28)

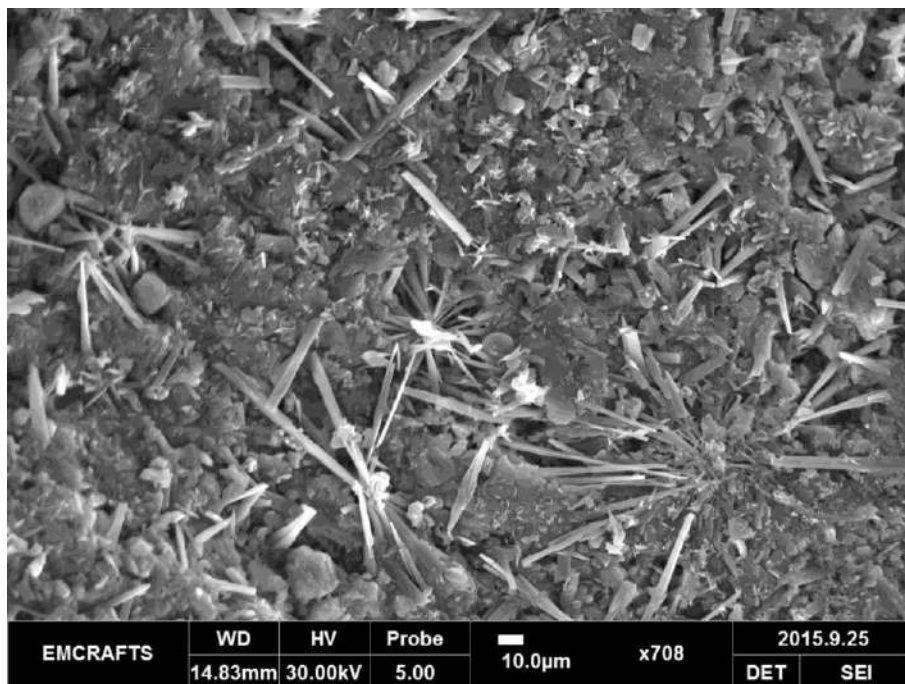


Figure 5.35 Micrograph illustrating the presence of thick, acicular crystals in the transition zone of RGO paste (t+28)

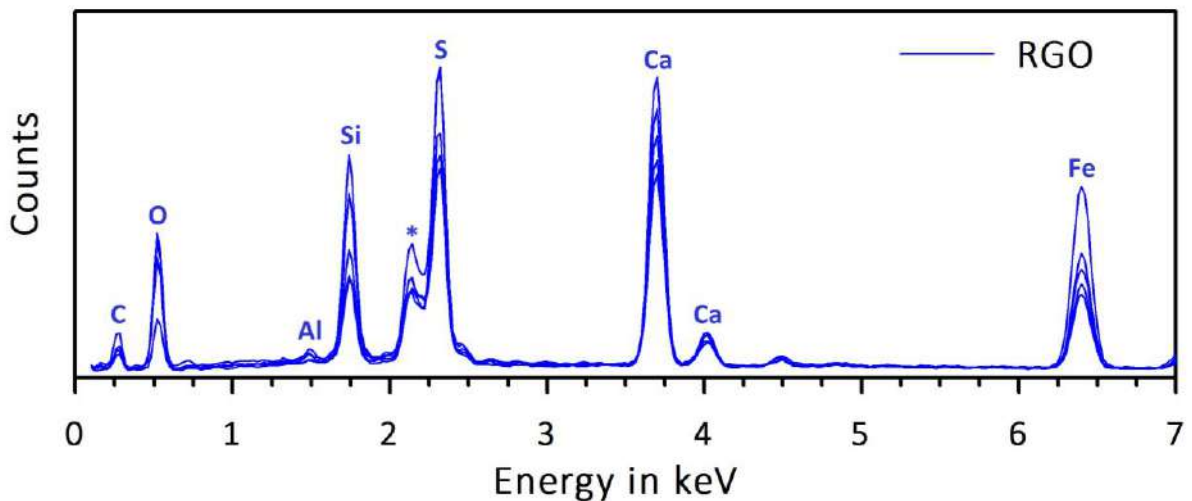
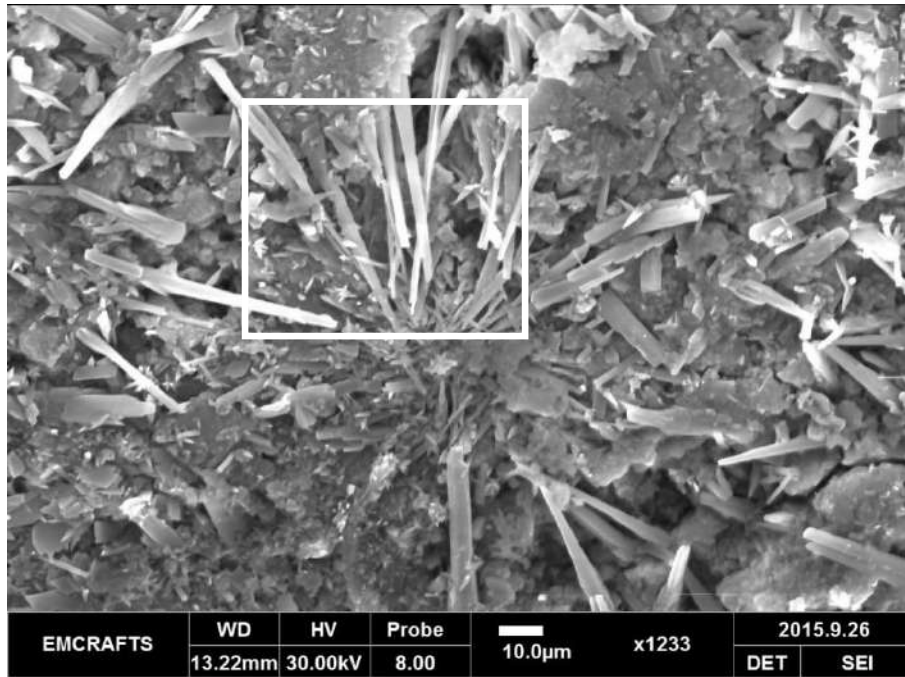


Figure 5.36 Micrograph and EDS result of the alteration phases that were formed in the transition zone of RGO paste (t+28)

The presence of graphene sheets was noticed in the degraded layer (Figure 5.34). Deposits of irregularly oriented long, thick acicular crystals were seen everywhere in the transition zone of the RGO paste (t+28) (Figure 5.35). The EDS result suggests that these crystals were composed of calcium sulfate – silicate – carbonate phase (Figure 5.36). Additionally, it was noticed that this compound had experienced further alterations when the storage time was prolonged for 56 days. Pavlík (1994) has reported that the transition zone in the degraded

paste was found to have pH greater than 11.5. Figures 5.37 to 5.42 illustrate the micrographs of such alteration phases in the RGO paste (t+56).

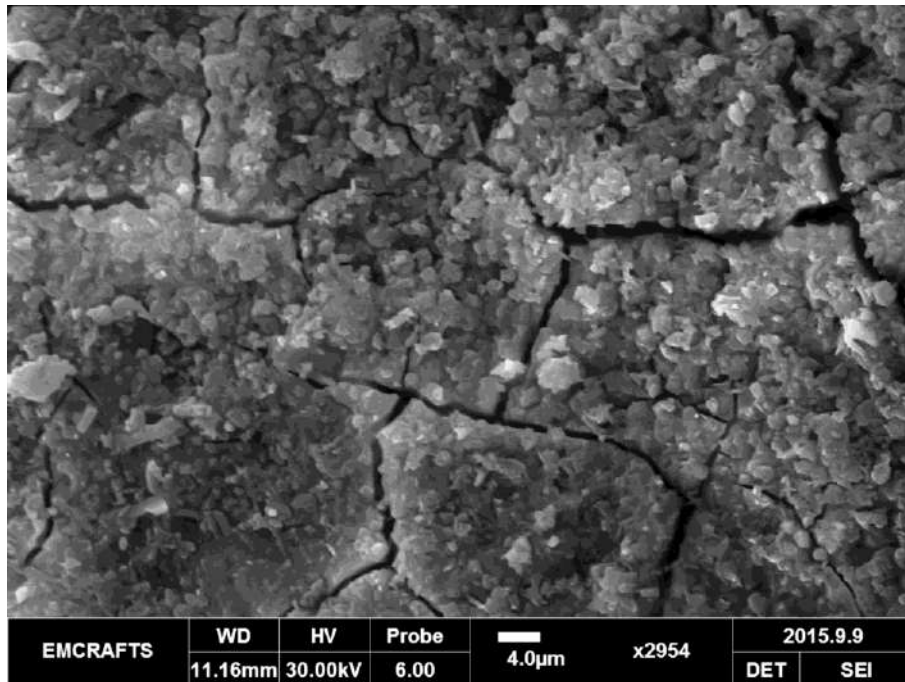


Figure 5.37 Micrograph illustrating the formation of cracks in the grey zone of t+56 paste (RGO) which could be due to the effect of decalcification induced shrinkage

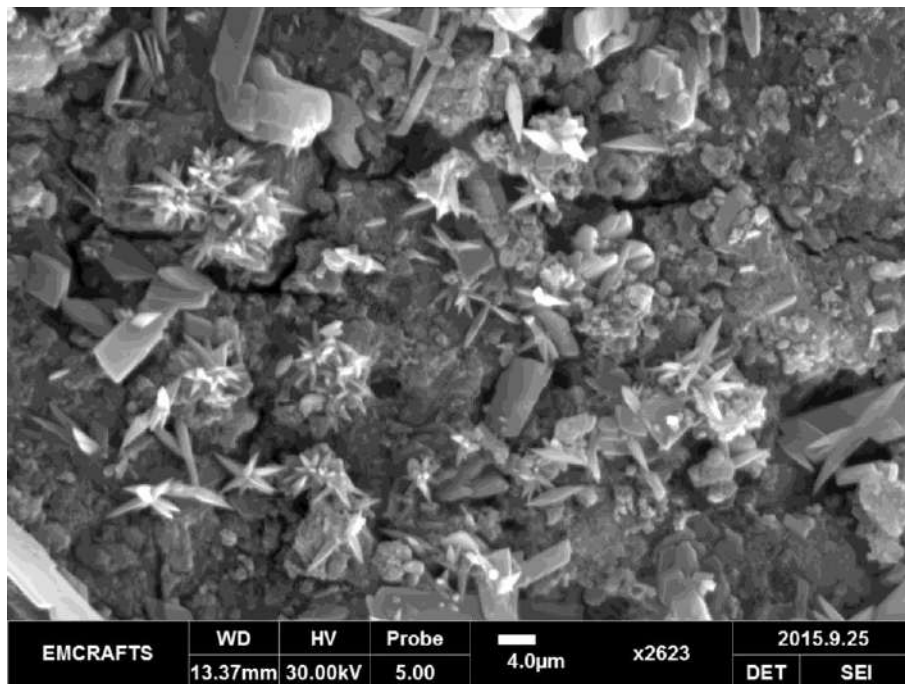


Figure 5.38 Micrograph illustrating the alteration phases that were formed in the transition zone of RGO paste (t+56)

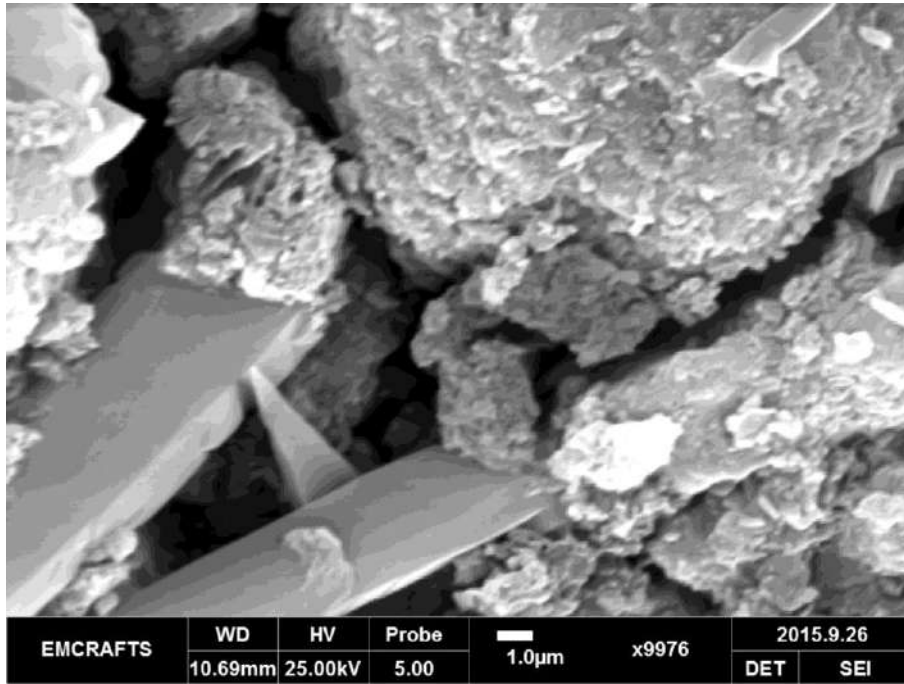


Figure 5.39 Micrograph illustrating the formation of prismatic crystals in the degraded layer of RGO paste (t+56)

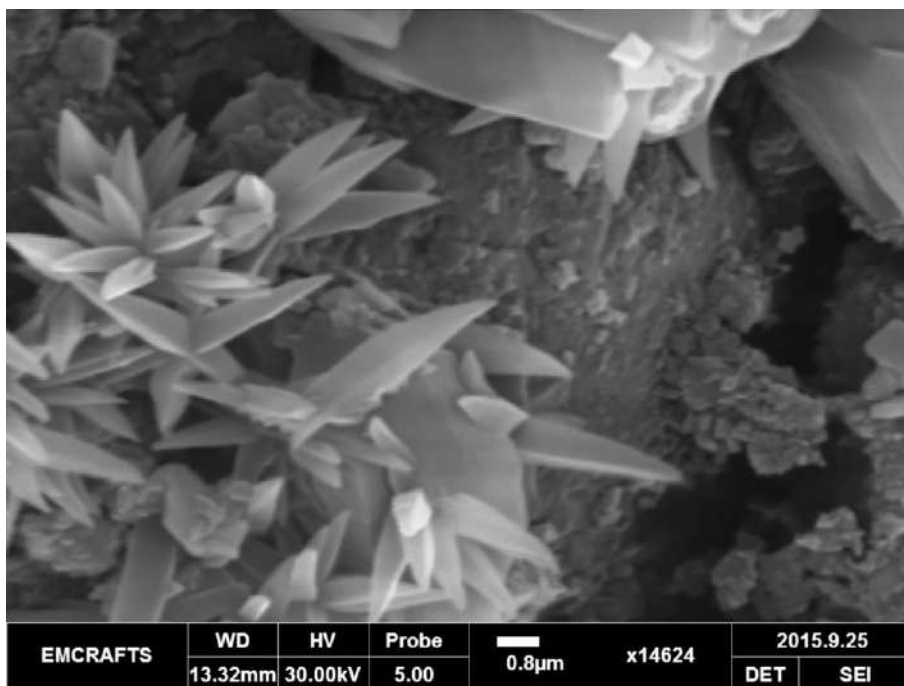


Figure 5.40 Micrograph illustrating the presence of dendritic cluster crystals in the degraded layer of RGO paste (t+56)

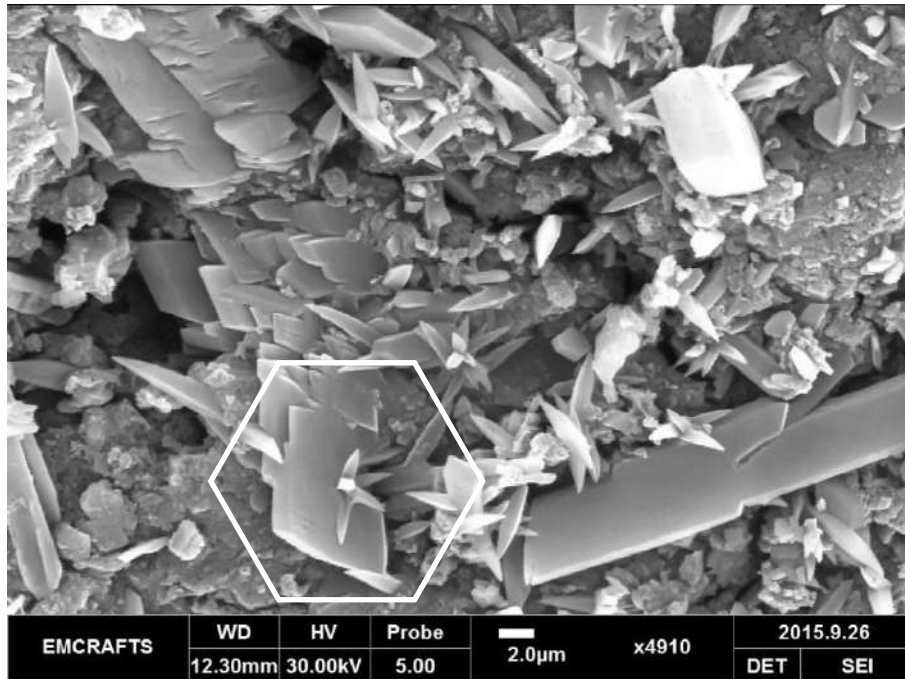


Figure 5.41 Micrograph illustrating the presence of alteration phases having different morphology in the RGO paste (t+56)

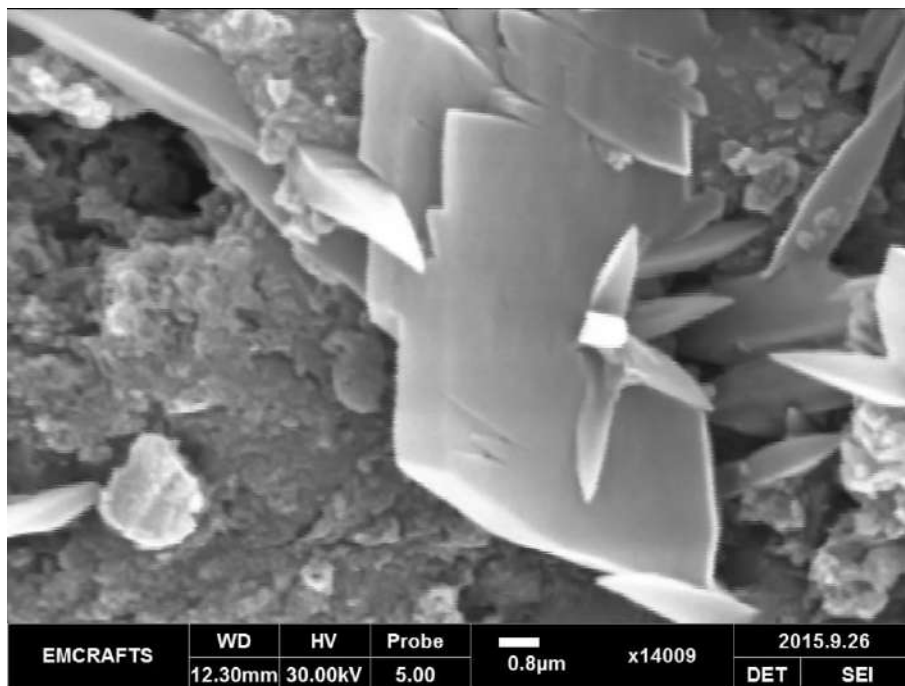


Figure 5.42 Micrograph illustrating the growth of dendritic cluster crystals matured from the prismatic shaped compounds in the RGO paste (t+56)

It can be seen from the micrographs that the dendritic cluster products were found to be matured from the prismatic crystals (Figure 5.42). This effect suggests that the prismatic compounds are prone to further chemical modifications when exposed to the ambient conditions. Figure 5.43 and Figure 5.44 show the micrograph and EDS results of those compounds having different morphology in the RGO paste (t+56).

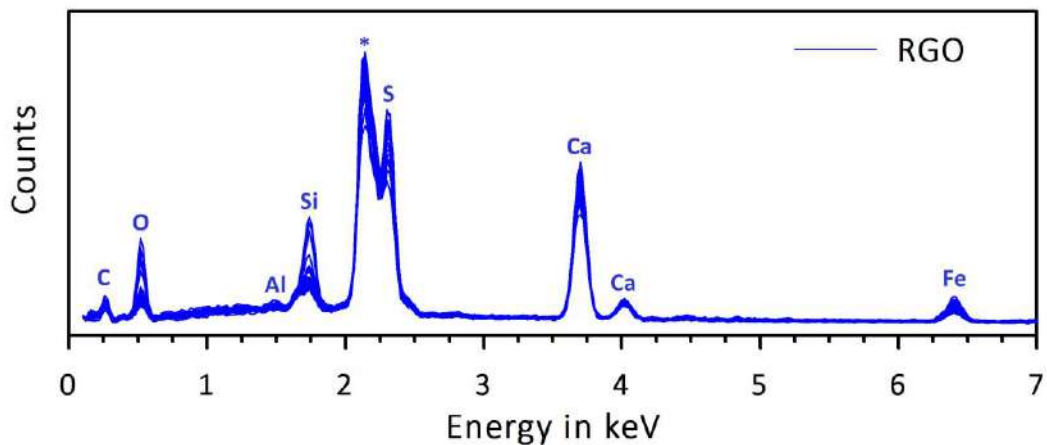
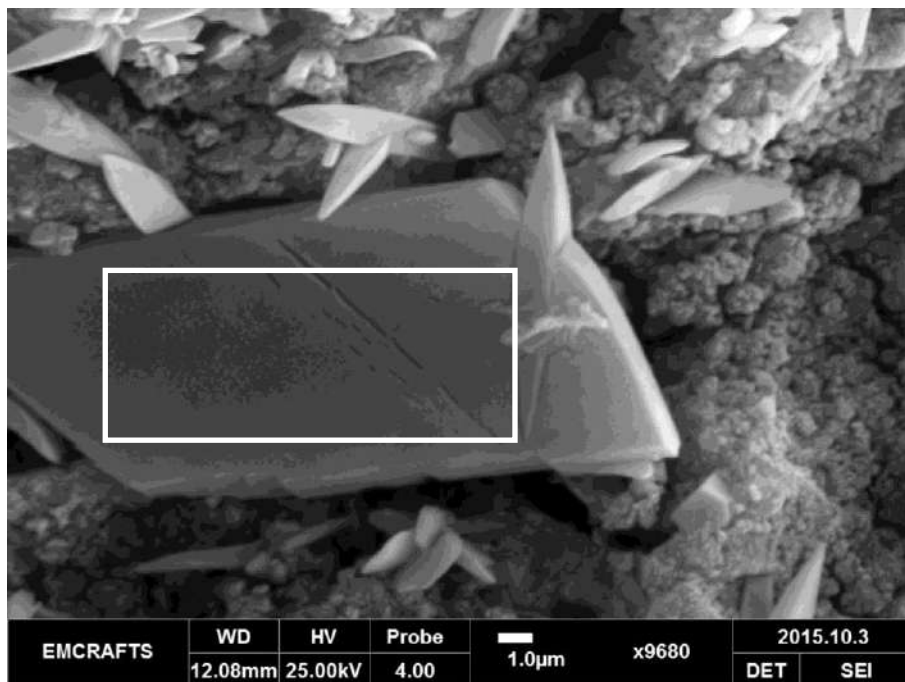


Figure 5.43 Micrograph and EDS result of the prismatic shaped compounds that were formed in the transition zone of RGO paste (t+56)

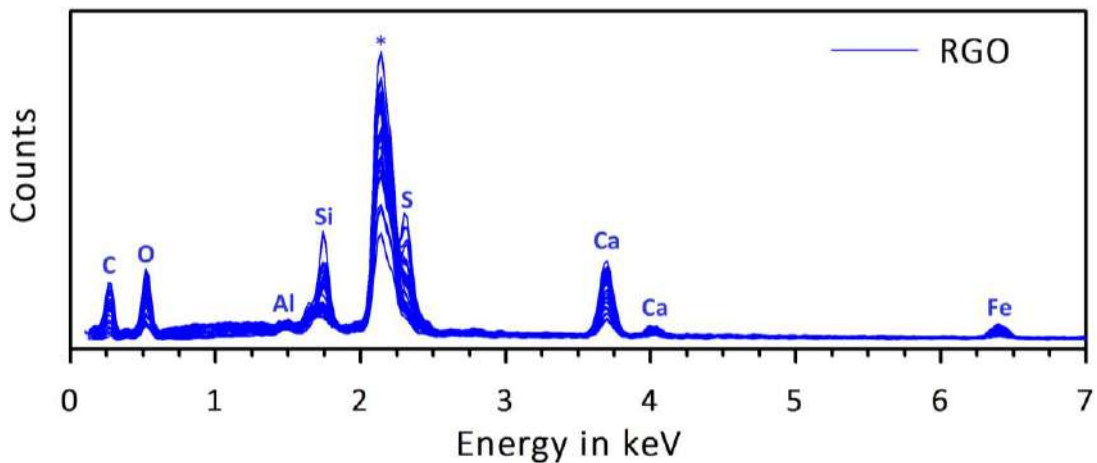
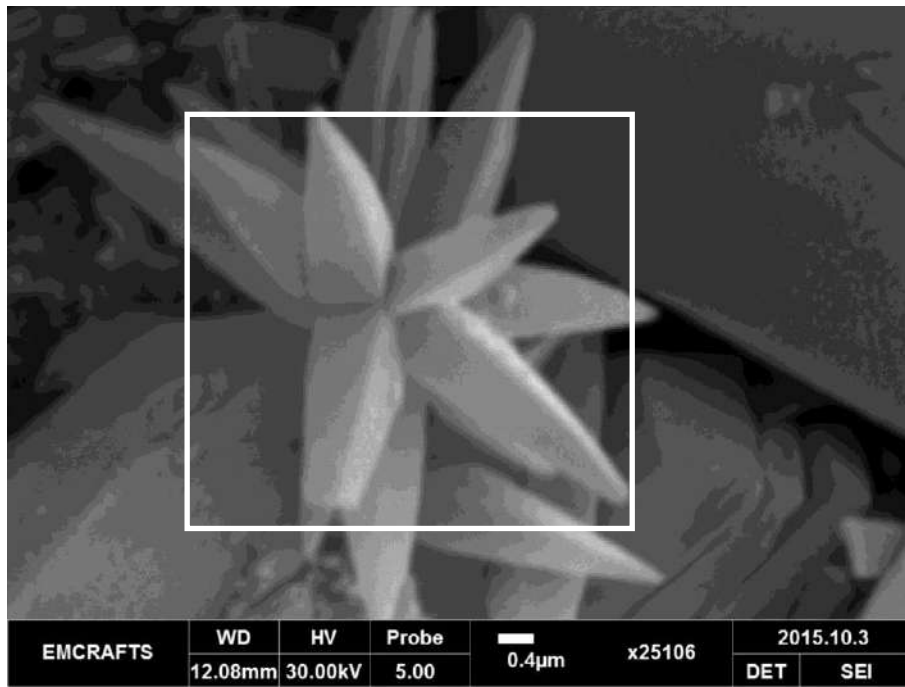


Figure 5.44 Micrograph and EDS result of the dendritic compounds that were formed in the transition zone of RGO paste (t+56)

Multiple numbers of EDS points were taken over the crystalline compounds having different morphology. The EDS analysis suggests the formation of a calcium sulfate – silicate – carbonate phase which is representative of thaumasite (Figures 5.43 and 5.44). Jallad et al. (2003) have reported that thaumasite ($\text{CaCO}_3 \cdot \text{CaSO}_4 \cdot \text{CaSiO}_3 \cdot 1.5\text{H}_2\text{O}$) could remain stable, when the pH of the system is greater than 12. In the transition zone ($\text{pH} > 11.5$), the release of sulfates from the calcium aluminosulfate phase and reduced graphene oxide (rGO) may have reacted with the Ca^{2+} leachates, leading to the formation of thaumasite-like phase.

Al₂O₃ mix

Figures 5.45 illustrates the micrograph and EDS result of the unaffected material (grey zone) of Al₂O₃ paste (t+28).

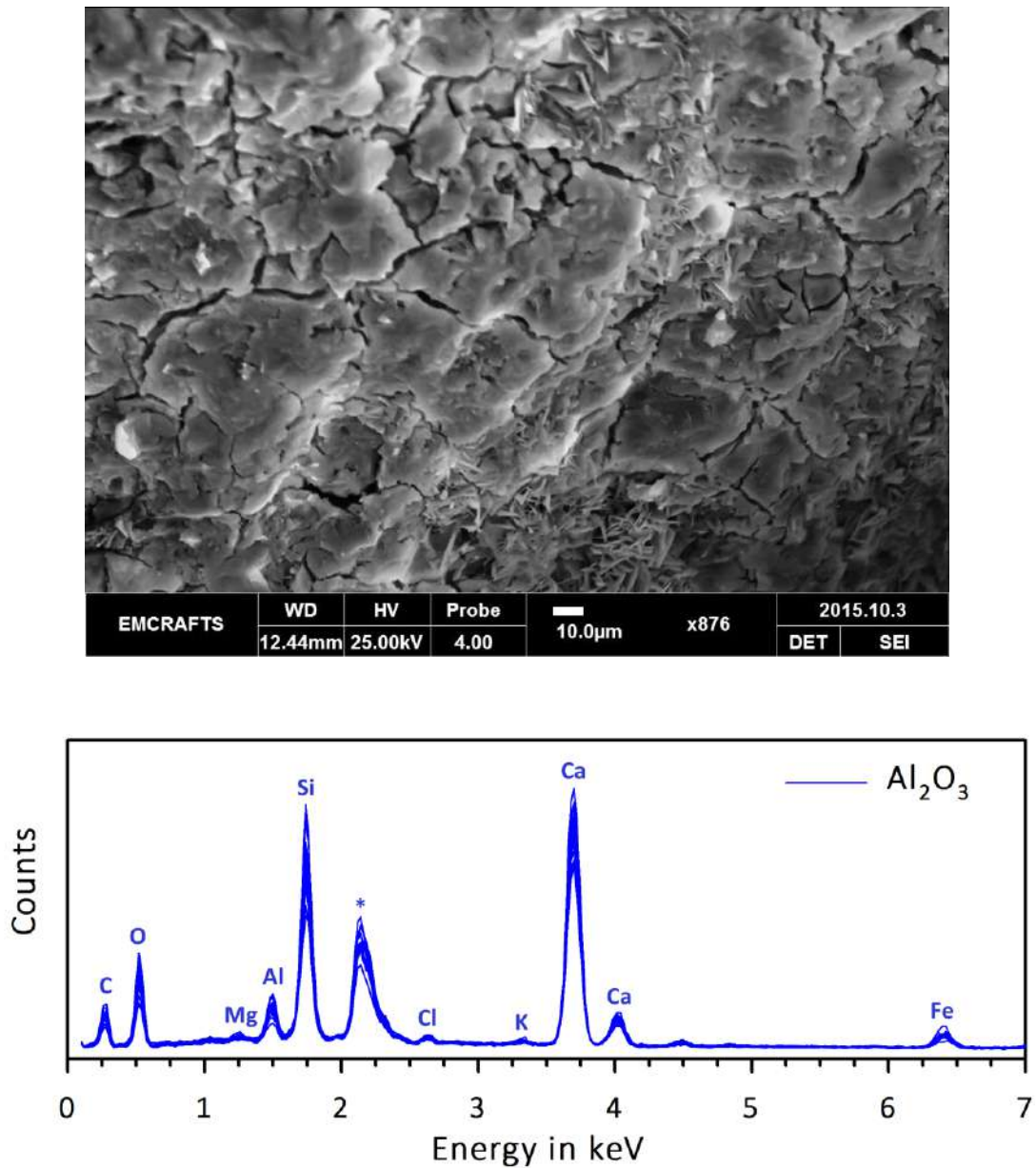


Figure 5.45 Micrograph and EDS result of the grey zone in the Al₂O₃ paste (t+28)

Several cracks were noticed in the grey zone of Al₂O₃ paste after storage in acidic solution for 28 days. These cracks could be formed because of the decalcification induced shrinkage. However, the EDS result suggests that the binder phases were not chemically altered by the

acid attack at such degradation period. Figures 5.46 and 5.47 illustrate the micrograph and EDS result of the degraded layer in the Al_2O_3 paste (t+28).

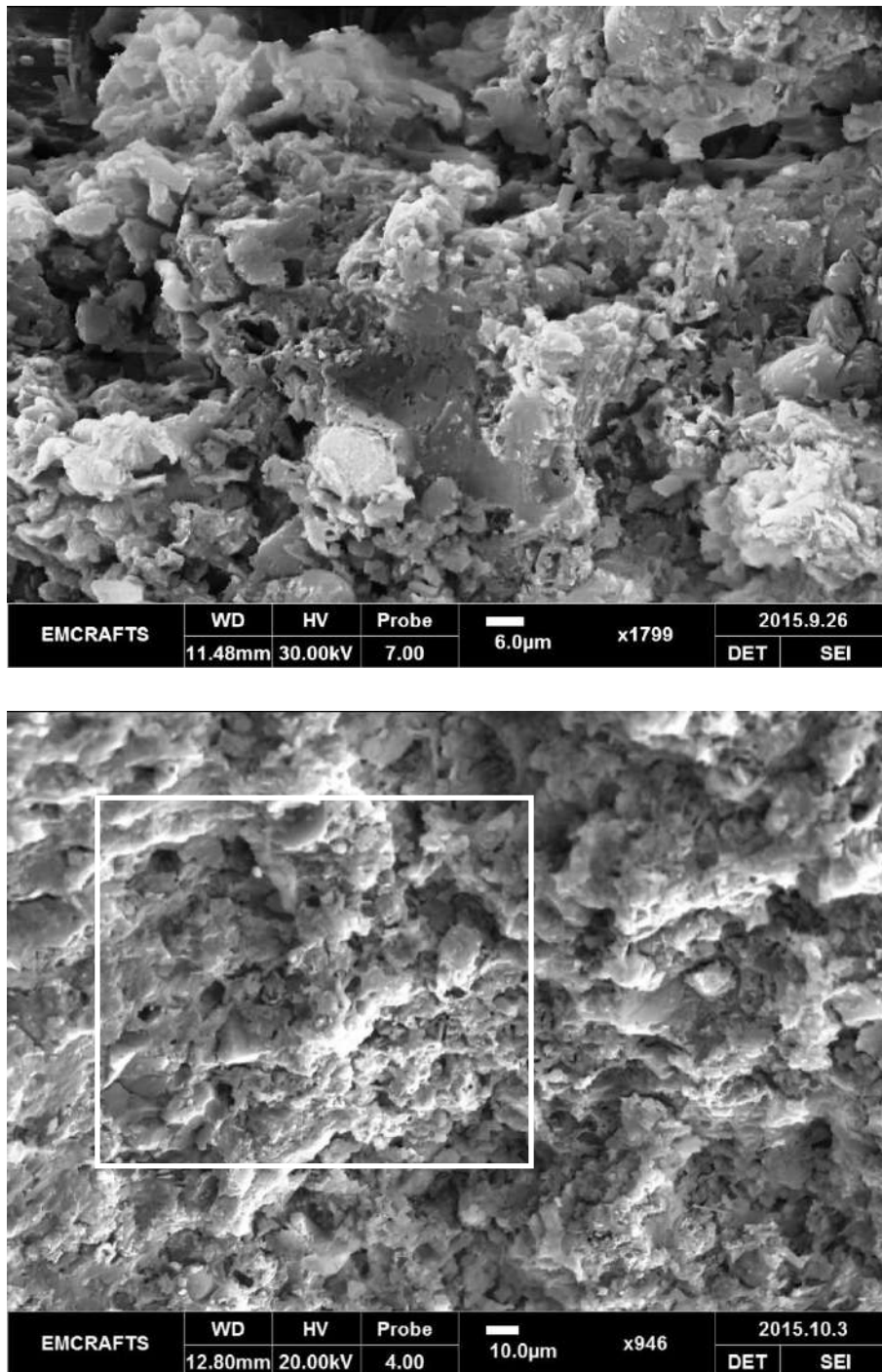


Figure 5.46 Micrograph illustrating the degraded layer in the Al_2O_3 paste (t+28) (top and bottom image)

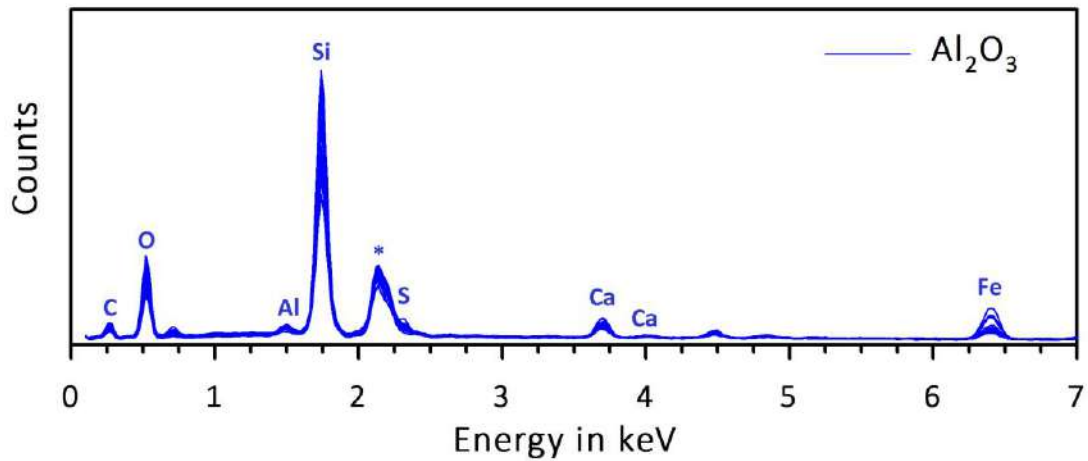


Figure 5.47 EDS result of the degraded layer in the Al_2O_3 paste (t+28)

The acid attack had significantly altered the chemical composition of the Al_2O_3 paste and thereby a degraded matrix having insoluble precipitate was formed (Figure 5.46). The EDS result suggests that the amount of Ca was marginal in the degraded layer of the paste after storage in HNO_3 solution (Figure 5.47). Micrographs and EDS results of the alteration phases in the transition zone of Al_2O_3 paste (t+28) are illustrated in Figure 5.48 and Figure 5.49.

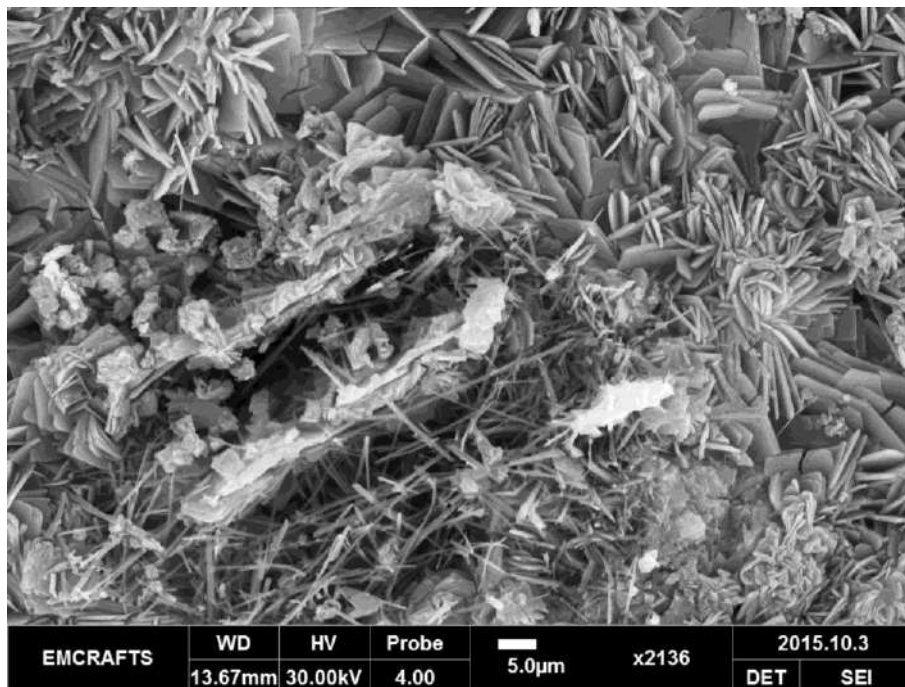


Figure 5.48 Micrograph illustrating the formation of needle like compounds in the transition zone of the Al_2O_3 paste (t+28)

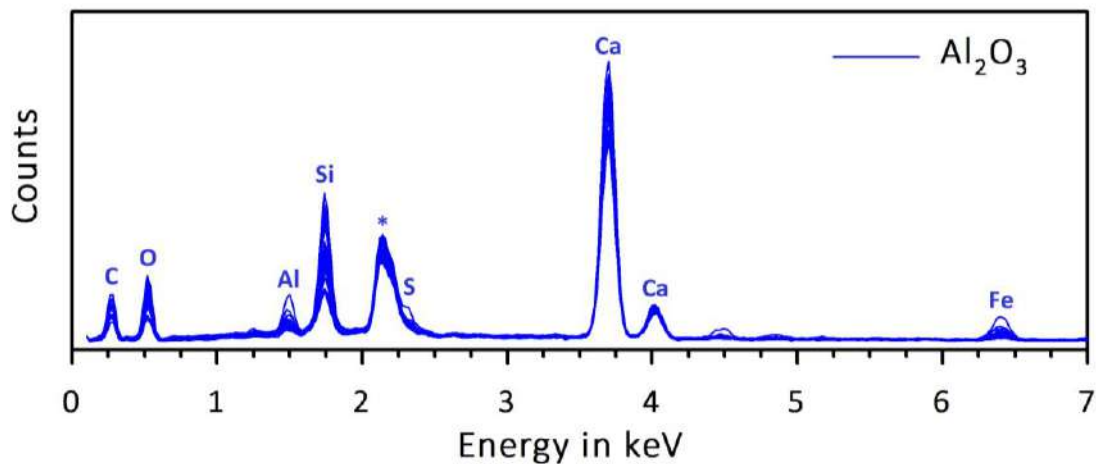
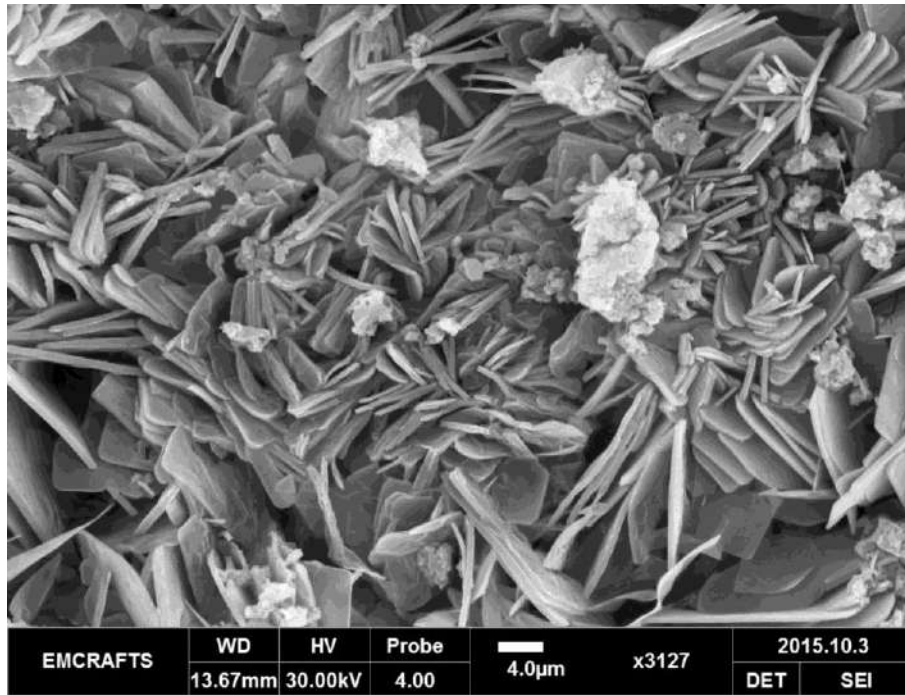


Figure 5.49 Micrograph and EDS result illustrating the plate like crystalline compounds that were formed in the transition zone of Al_2O_3 paste (t+28)

Thin radiated plate like and long needle shaped crystals were seen to be densely packed in the transition zone between the degraded layer and undamaged material of Al_2O_3 paste (Figures 5.48 and 5.49). The EDS result confirmed that those formations were calcium silicate based compounds. These crystalline products, which have a distinctly different morphology compared to C-S-H, may have formed because of the chemical interaction between the silica gel and calcium leachates in the degraded layer. Figure 5.50 and Figure 5.51 shows the

micrograph and EDS result of the alteration phases that were formed inside a void available in the Al_2O_3 paste (t+28).

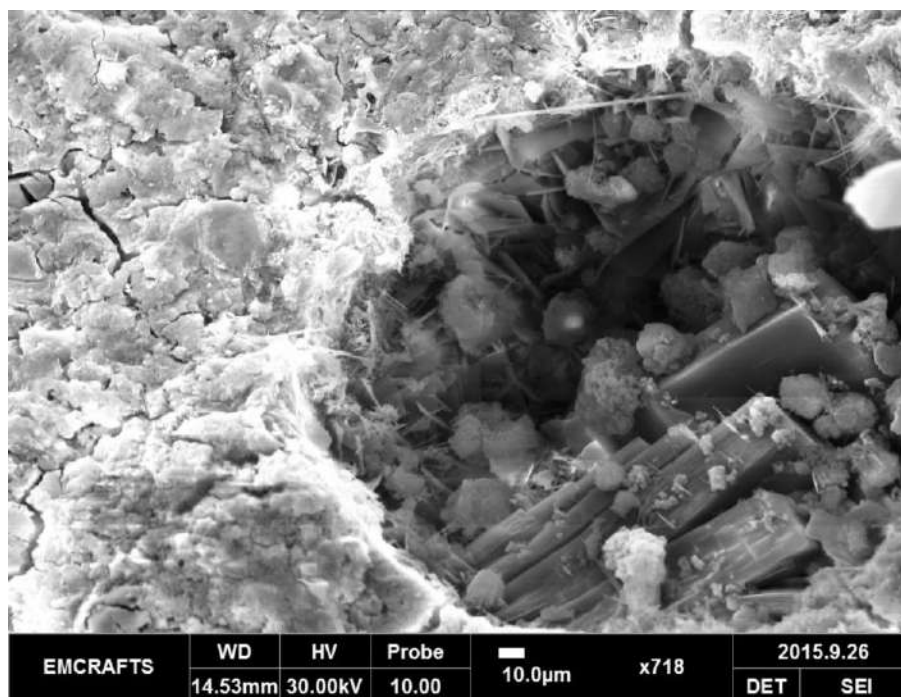
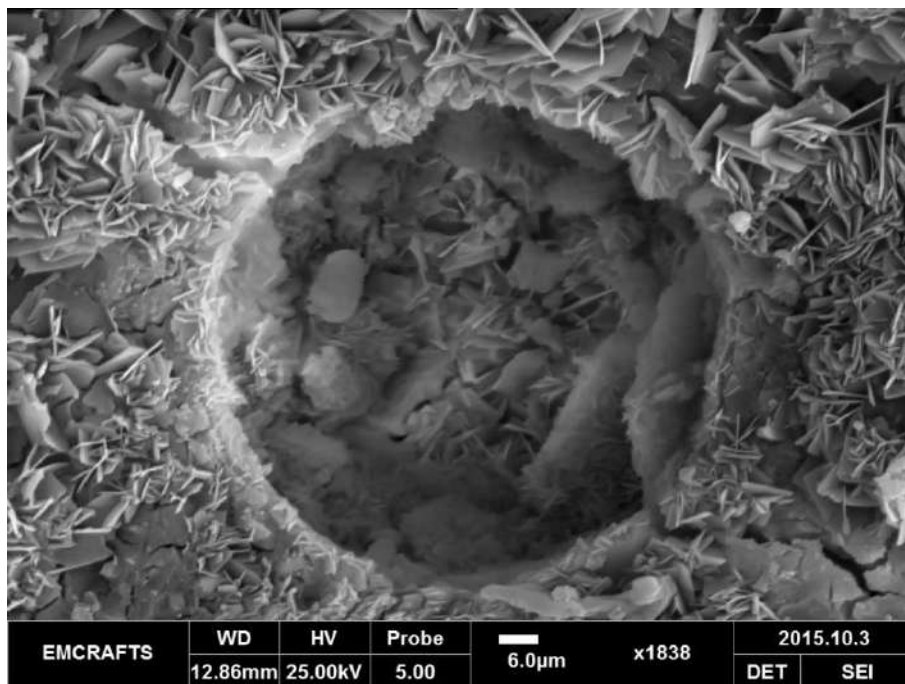


Figure 5.50 Micrographs illustrating the presence of voids in the Al_2O_3 paste (t+28) (top and bottom image)

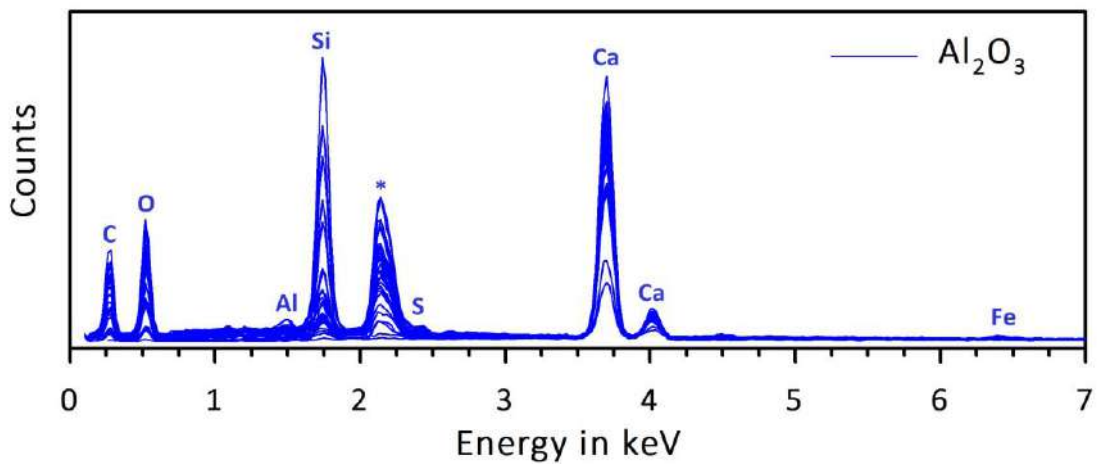
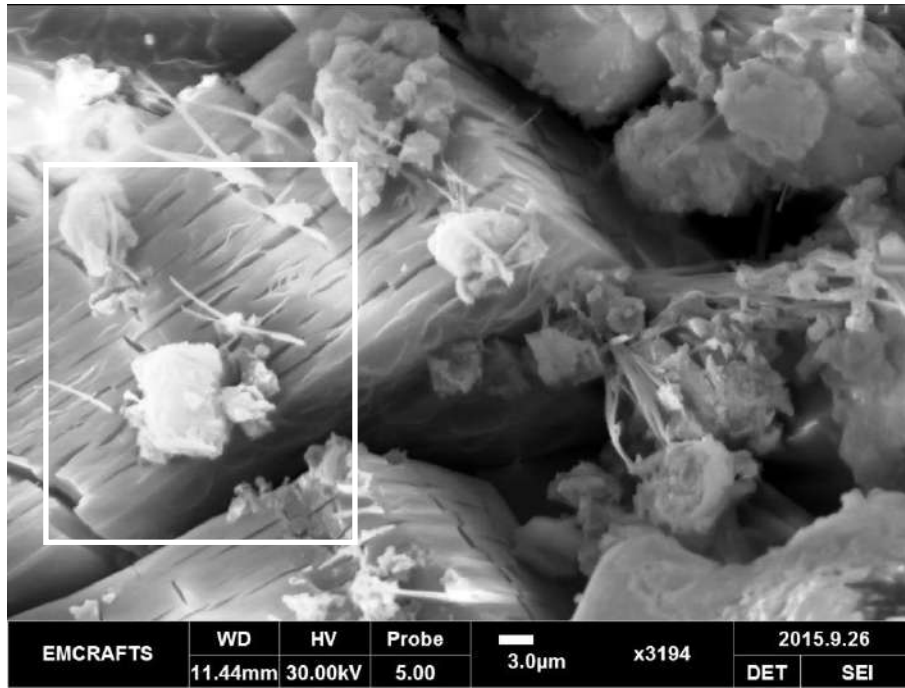


Figure 5.51 Micrograph and EDS result illustrating the formation of prismatic crystals inside the void of Al₂O₃ paste (t+28)

The formation of stacked, prismatic compounds having well defined crystalline structure was seen inside a void present in the Al₂O₃ paste (t+28) (Figure 5.51). The EDS result confirmed the formation of calcium silicate based compounds inside the void which appeared to be affected by the CO₂ from the environment.

SiO₂ mix

Figure 5.52 and Figure 5.53 shows the micrograph and EDS result illustrating the presence of agglomerated silica particles in the cut section of SiO₂ paste (t+28).

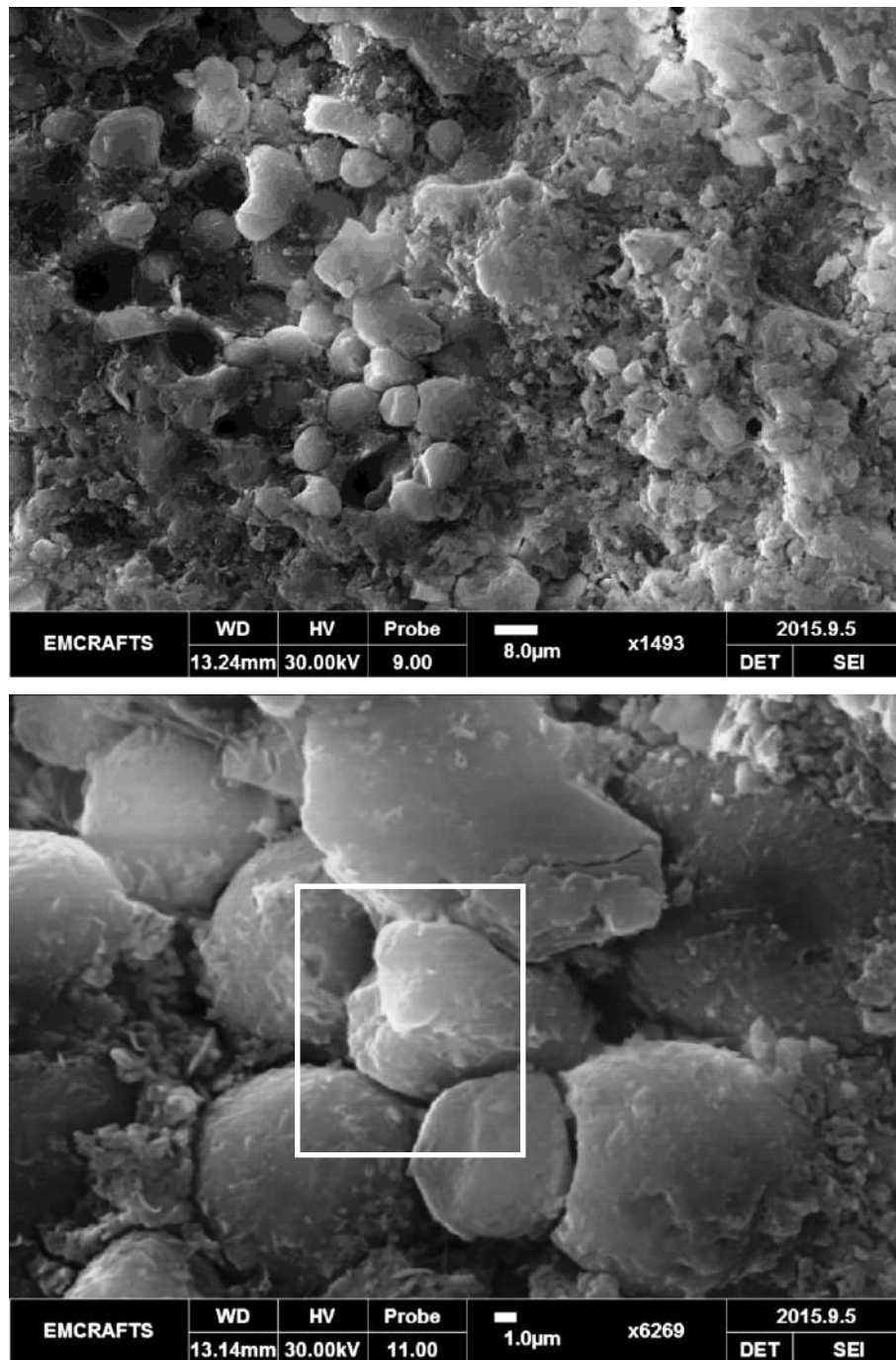


Figure 5.52 Low (top image) and high magnification (bottom image) SEM images illustrating the presence of agglomerated silica nanoparticles in the SiO₂ paste (t+28)

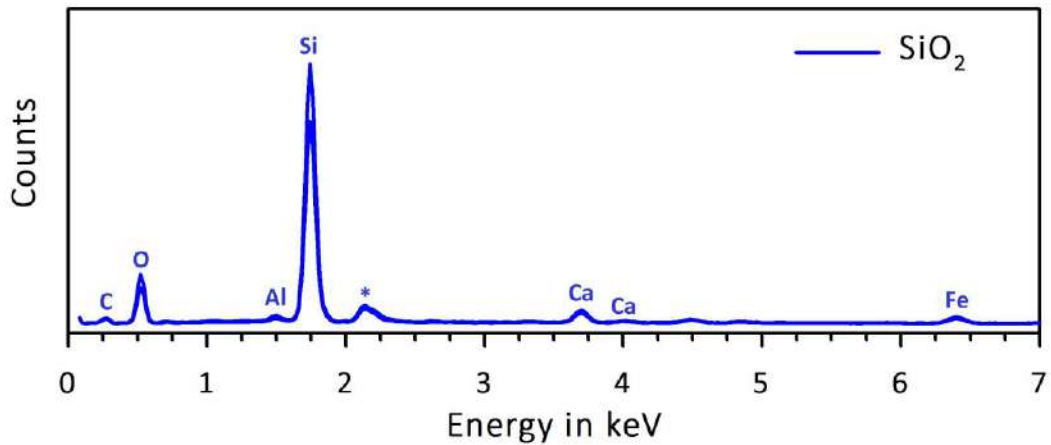


Figure 5.53 EDS result illustrating the presence of agglomerated silica particles in the cut section of SiO₂ paste (t+28)

The leached prism specimen was sectioned along the shorter direction for SEM analysis. Agglomerated silica particles were seen in the degraded layer of SiO₂ paste (t+28). After sectioning the specimen, the reminiscences of cut out silica particles were observed in its cross section. Figures 5.54 to 5.57 illustrate the micrographs and EDS result of the alteration phases that were formed in the transition zone of SiO₂ paste (t+28).

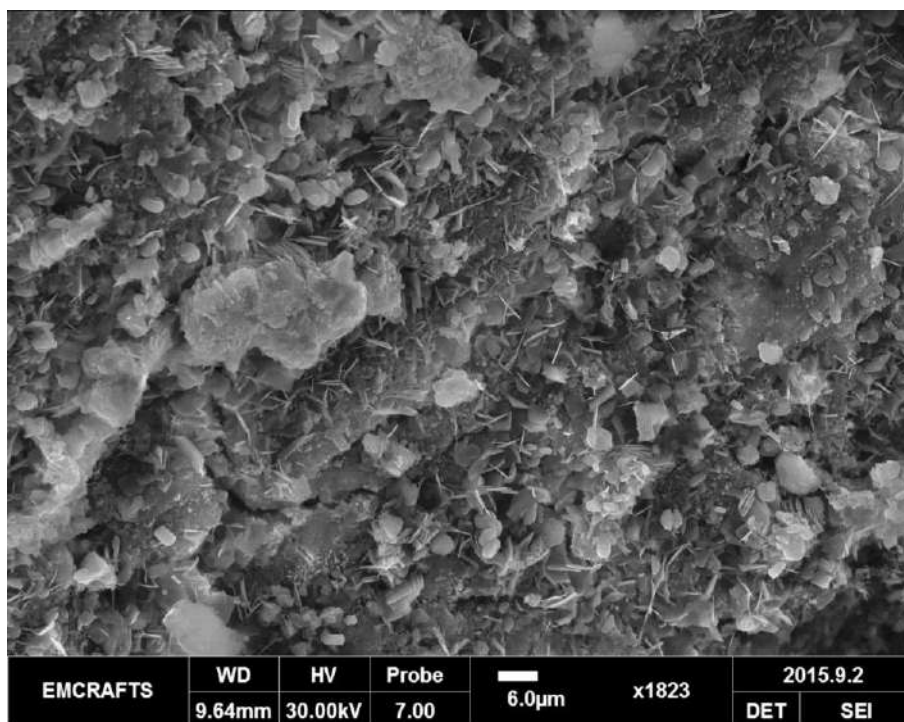


Figure 5.54 Micrograph illustrating the formation of alteration phases in the transition zone of SiO₂ paste (t+28)

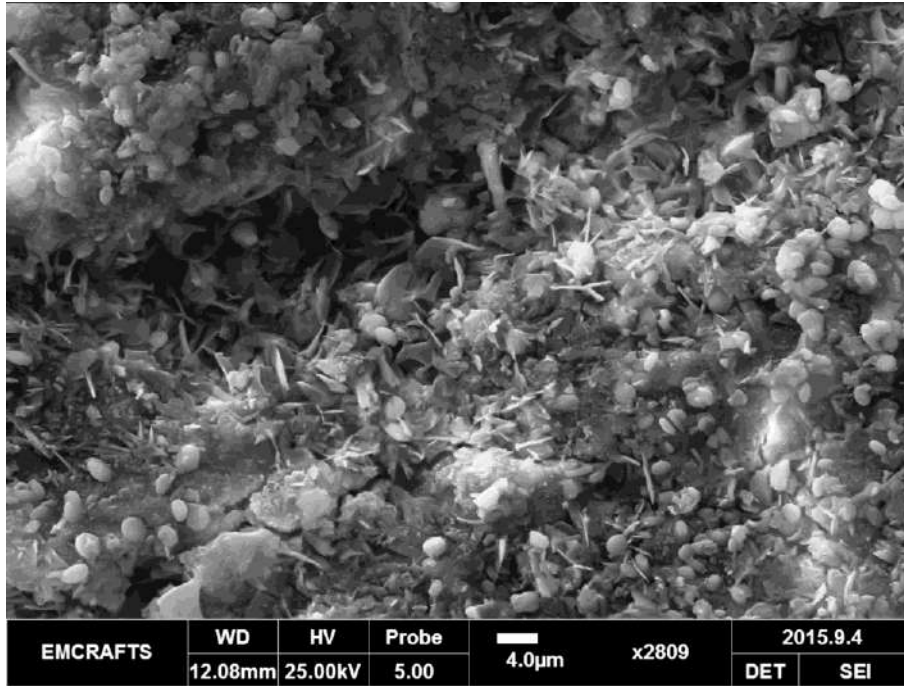


Figure 5.55 Micrograph illustrating the presence of spherical shaped particles and radiated, thin plate like compounds in the transition zone of SiO₂ paste (t+28)

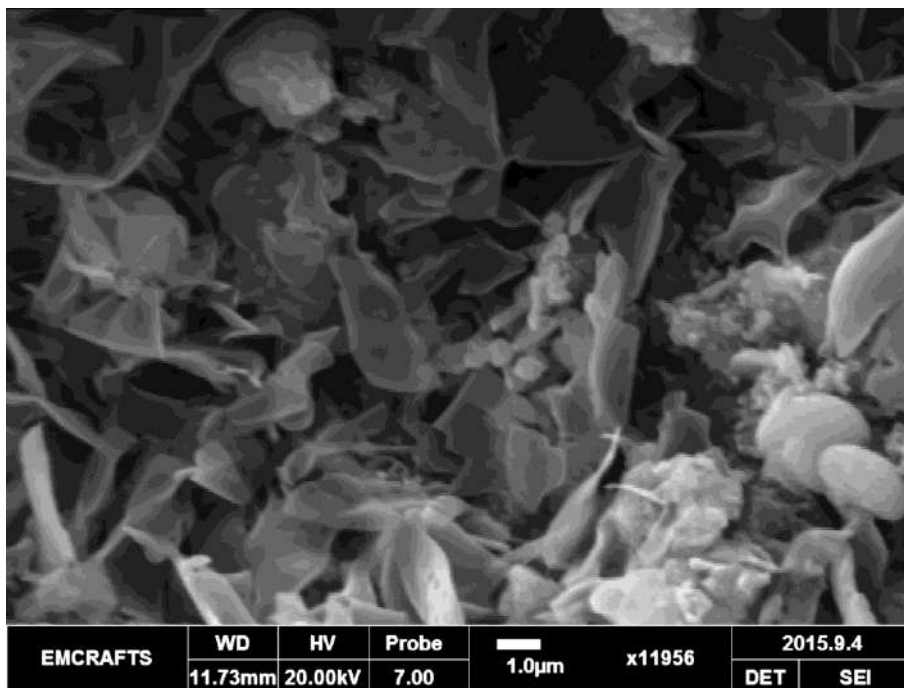


Figure 5.56 Micrograph illustrating the closer view of the non-uniform, radiated leaf like compounds that were formed in the transition zone of SiO₂ paste (t+28)

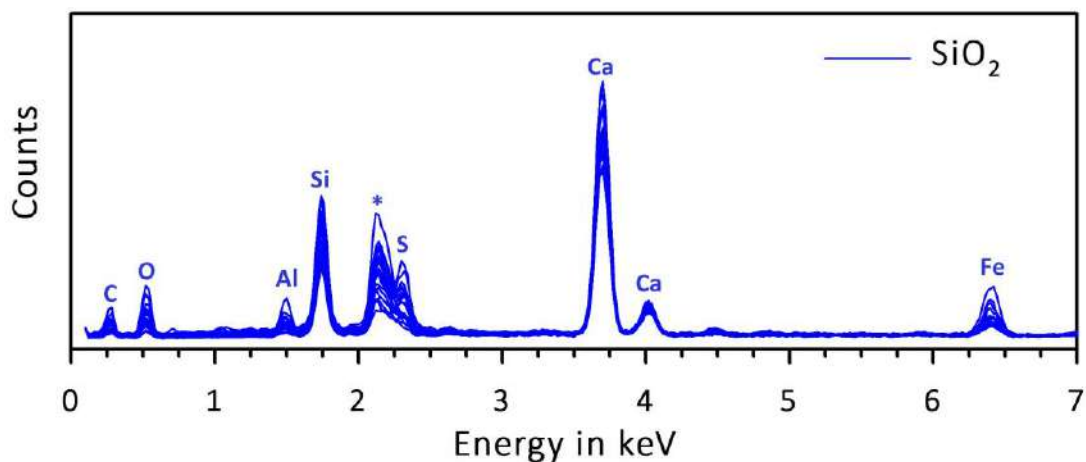
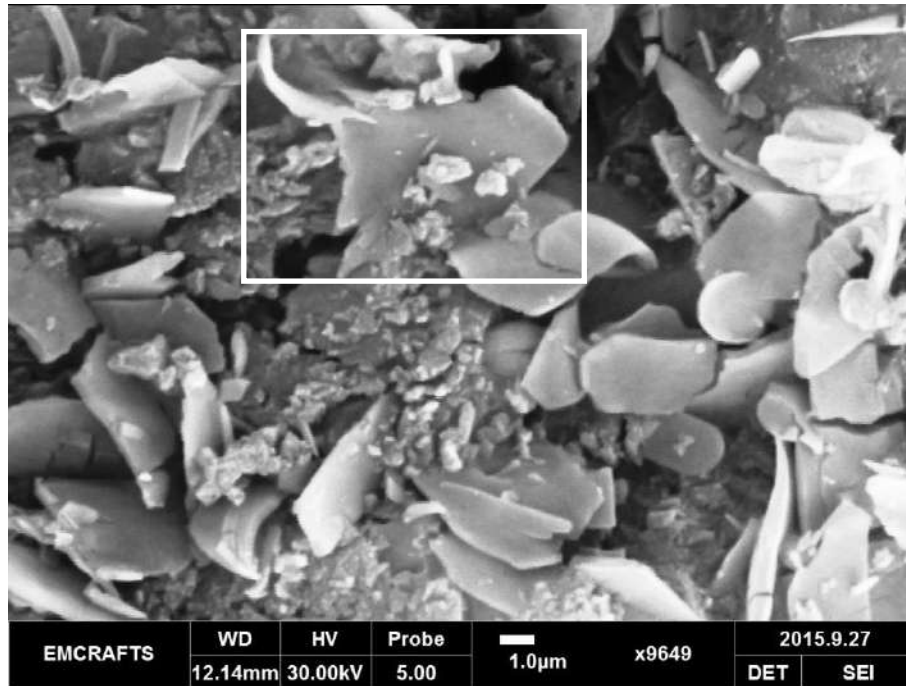


Figure 5.57 Micrograph and EDS result illustrating the closer view of the alteration phases that were formed in the transition zone of SiO_2 paste (t+28)

Non-uniform radiated thin plate like crystals were seen in the transition zone (Figure 5.57). This crystal was analysed to be a calcium sulfate silicate based compound that may have formed due to the chemical reaction between the calcium sulfate, nano silica and CO_2 from the environment. The formation of thaumasite like phases, therefore, is a common phenomenon seen in all the paste systems with nanomaterials. Figures 5.58 to 5.62 illustrate the micrograph and EDS result of the alteration phases that were noticed in the different locations of SiO_2 paste (t+28).

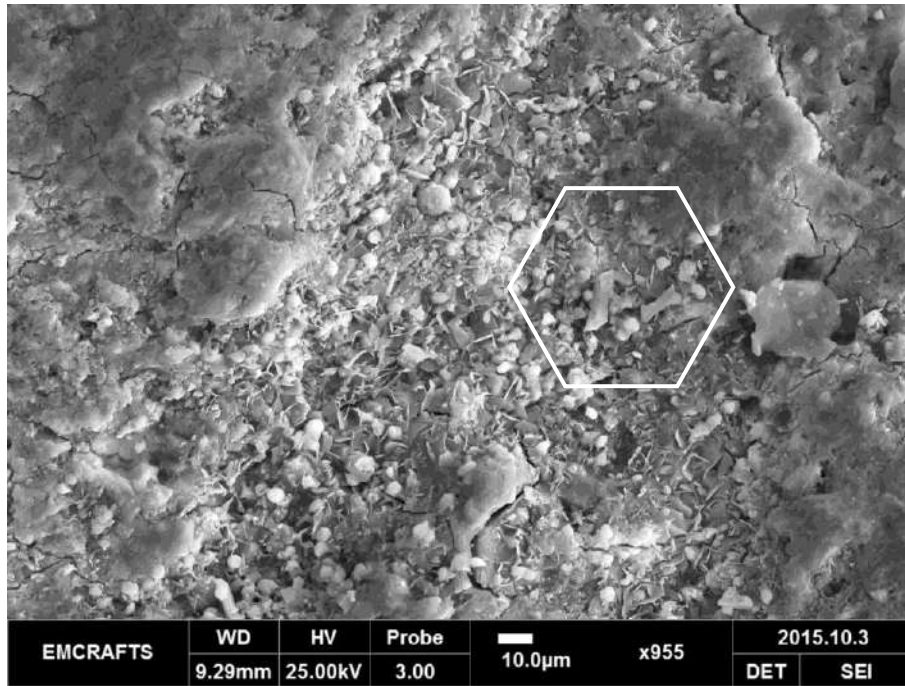


Figure 5.58 Micrograph illustrating the poorly dispersed silica nanoparticles in the transition zone of SiO₂ paste (t+28)

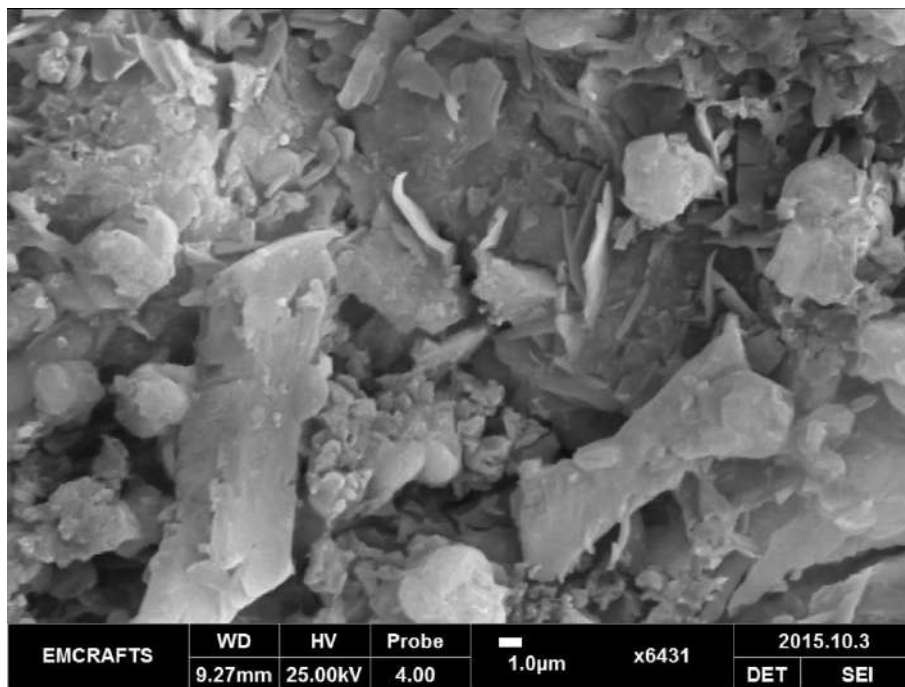


Figure 5.59 Micrograph illustrating the formation of well defined, prismatic shaped crystals in the transition zone of SiO₂ paste (t+28)

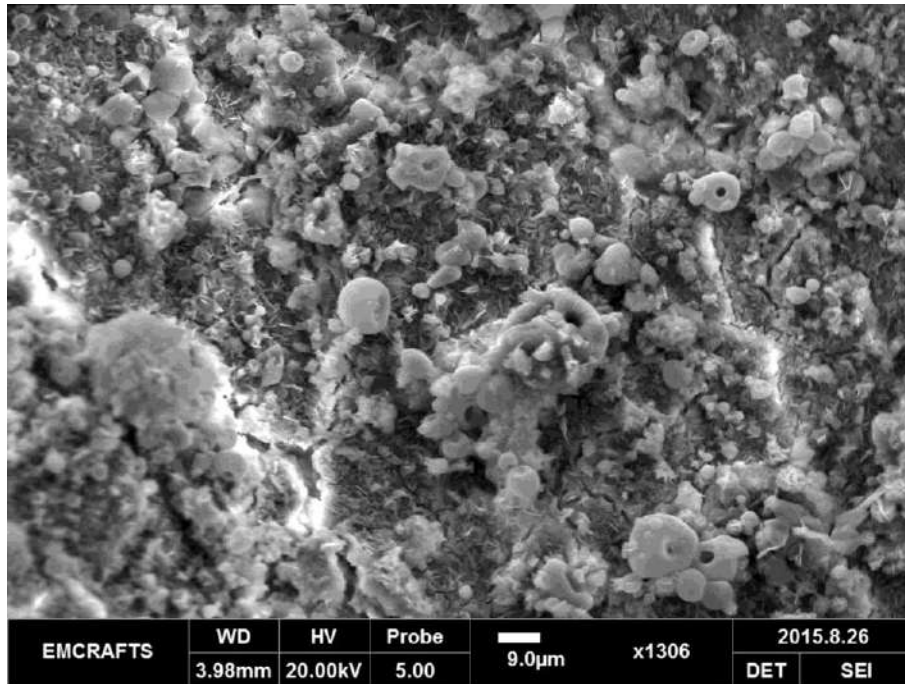


Figure 5.60 Micrograph illustrating the formation of spherical shaped crystals in the transition zone of SiO₂ paste (t+28)

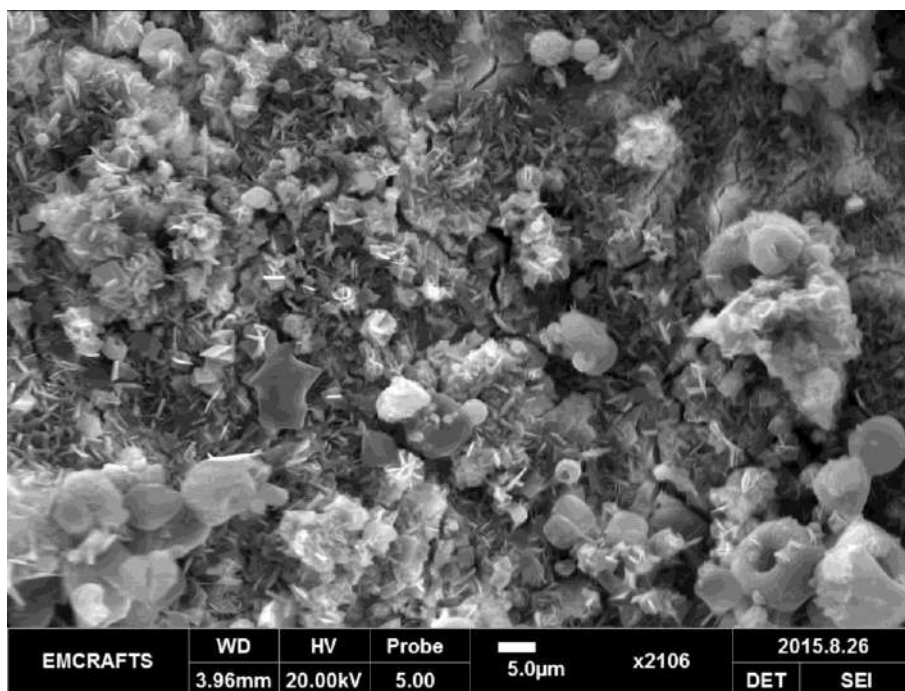


Figure 5.61 Micrograph illustrating the formation of thin plate like and spherical shaped crystalline compounds in the transition zone of SiO₂ paste (t+28)

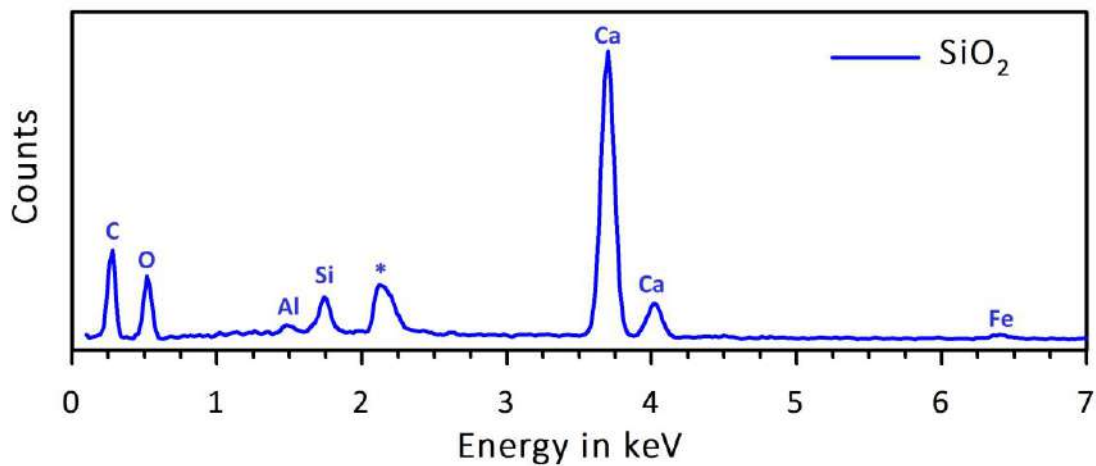
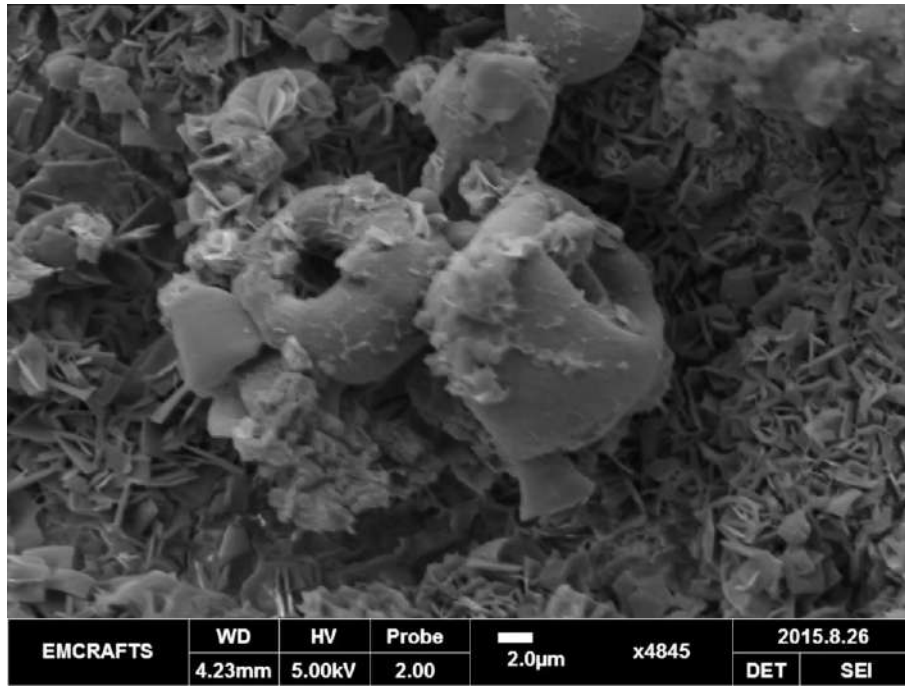


Figure 5.62 Micrograph and EDS result of the spherical shaped crystals having cavity in the middle of its structure in the SiO_2 paste (t+28)

Formations of well-defined, prismatic crystalline compounds were seen in the transition zone (Figures 5.58 and 5.59). In the locations nearer to the brown zone, spherical crystals having cavity at the middle was noticed (Figure 5.62). The EDS result suggests that this compound may be calcium carbonate based, which is likely to form when there is a chemical reaction between the calcium leachates and CO_2 from the environment.

5.4 SUMMARY

Digital photographs and the images acquired from OM, X-ray CT and SEM were found useful in delineating the degraded layer in the t+28 pastes. The alteration phases in the transition zone of the pastes after storage in acidic solution were analysed using SEM/EDS. Calcite and calcium silicate based compounds were noticed in the transition zone of Control and Al₂O₃ pastes respectively, whereas thaumasite like products were seen in the RGO and SiO₂ pastes. The porosimetry results suggest that the addition of reduced graphene oxide, alumina and silica nanoparticles in OPC paste had delayed the degradation due to acid attack. The addition of rGO in porous concrete can be thus expected to delay the deterioration of binder phases when exposed to aggressive acidic solutions, leading to an enhancement (service life) of porous concrete water filters. The finding also suggests that the presence of small amount of rGO may not induce any negative effect on the properties of porous concrete after subsequent passage of acidic solutions. The subsequent chapters explore the development and performance of the porous concrete systems with and without rGO addition.

CHAPTER 6

MIXTURE PROPORTIONING, SPECIMEN PREPARATION AND TESTING OF POROUS CONCRETE

6.1 INTRODUCTION

The research methodology of this study is comprised of two levels. In the first level, the role of rGO on the properties of cement paste was investigated as discussed in the previous chapters 4 and 5. The second level covers the investigation on the Pb removal in plain and rGO modified porous concrete system. The porous concretes are generally designed for high permeability for an easy passage of water. This criterion is not desirable for water filtration applications. In the present study, the porous concretes were designed for controlled levels of hydraulic conductivity. The mixture proportioning and specimen preparation of the porous concrete is discussed in this chapter. Additionally, the experimental methods to characterise the cylindrical porous concrete specimen intended for water filtration are also explained.

6.2 SPECIMEN PREPARATION

For experimental investigations on porous concrete, cylindrical cast iron moulds of size 100 × 200 mm ($\phi \times H$) were used for the preparation of test specimens. The compaction was performed with a Marshall Hammer having foot diameter, drop weight and free fall of 98.4 mm, 4.54 kg and 457 mm respectively. The fresh porous concrete was filled into the mould in three layers, which were weighed exactly before filling. After filling each layer, several numbers of blows were given using the Marshall hammer.

In the case of the top layer, the loose and fresh concrete was found to be filling above the mould surface, and could not be compacted properly. For better compaction of the top layer, a collar arrangement was added to the top of the iron mould. After the compaction of the top layer, the surface was carefully finished using a trowel. The specimens were demolded after 24 hours and then cured by immersing in tap water at room temperature (25 ± 2 °C) up to 7 days. This procedure was followed in accordance with the steps mentioned in the preparation of cylindrical porous concrete specimens by Bury et al. (2006).

The mass of the finished concrete along with the iron mould was measured using a weigh balance (of 0.1 g accuracy). After 24 hours, the mass of the hardened concrete and the mould was again measured. The fresh and hardened densities were then determined by dividing these masses by the volume of the iron mould (0.00157 m^3). The photographs of the above mentioned procedural steps are serially arranged in the Figures 6.1 to 6.9. This procedure could act as a guideline in the preparation of laboratory based cylindrical porous concrete specimens having controlled levels of hydraulic conductivity.



Figure 6.1 Aggregates of different sizes were separated using standard set of sieves conforming to IS 460-1 (1985)



Figure 6.2 Dry blending the 53 grade Portland cement and aggregate in a laboratory concrete mixer



Figure 6.3 Each layer in the concrete specimen was filled by weighing the fresh concrete and then poured inside the cylindrical iron mould



Figure 6.4 Consolidation was done using Marshall hammer having foot diameter, drop weight and free fall of 98.4 mm, 4.54 kg and 457 mm respectively



Figure 6.5 A collar arrangement was fixed to consolidate the top concrete layer that was poured inside the cylindrical iron mould



Figure 6.6 Top concrete layer was levelled and finished using a hand-held metal float



Figure 6.7 Mass of fresh and hardened porous concrete including mould was measured using a weigh balance of 0.01 g accuracy for density calculation



Figure 6.8 Porous concrete specimens of size 100×200 mm ($\phi \times H$) demolded after 24 hours from the mixing time of ingredients



Figure 6.9 Porous concrete specimens were cured in tap water for a period of 7 days before testing

6.3 EXPERIMENTAL PROGRAM

While finishing the concrete surfaces using trowel, the bleed water containing cement slurry was seen to occupy the coarser voids at the top of the specimen. Further, some cement slurry had also settled on the bottom part of the cylinder. To obtain a uniform sample of the porous concrete, slices from the top and bottom of the cured specimens of about 25 mm thickness were removed using a diamond-tipped saw, as shown in Figure 6.10 and Figure 6.11.



Figure 6.10 Non-permeable top and bottom concrete edges of about 25 mm thick in the specimen were removed using diamond-tipped saw



Figure 6.11 Porous concrete specimens of size 100 × 150 mm ($\phi \times H$) after sectioning using diamond-tipped saw

6.3.1 Falling head permeability test

The falling head permeability test set up model suggested by Sonebi and Bassuoni (2013) was fabricated for this study, and is shown in Figure 6.12.

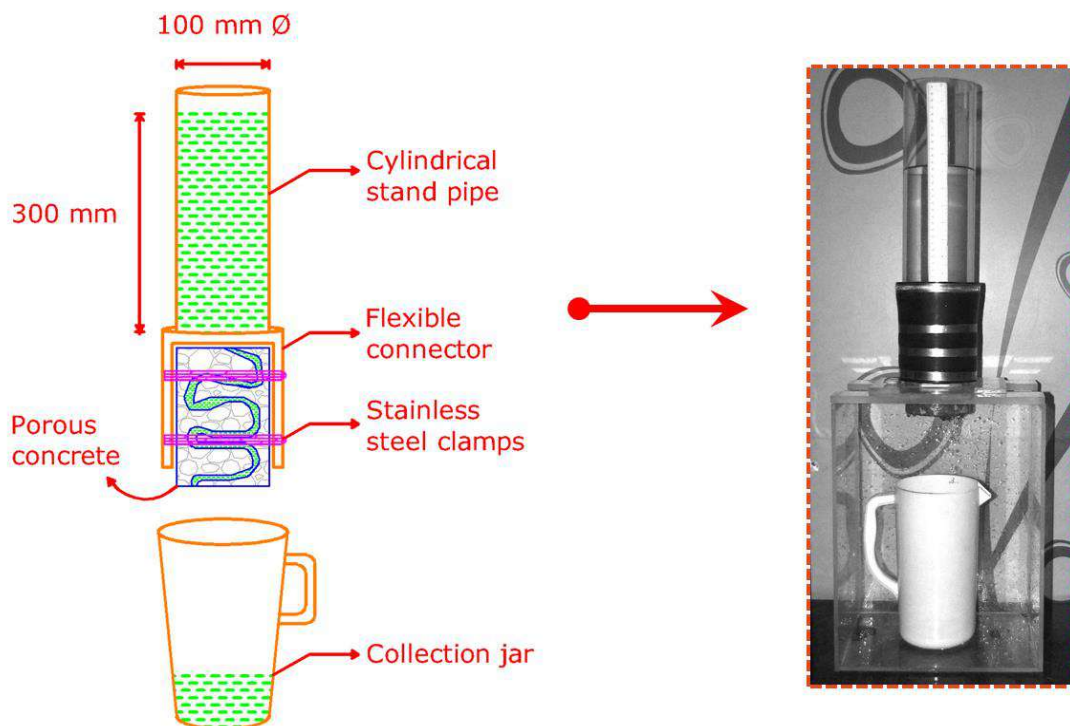


Figure 6.12 Determination of permeability of porous concrete using falling head permeability test set up which is similar to the set up suggested by Sonebi and Bassuoni (2013)

The cylindrical specimen of size 100 × 150 mm ($\phi \times H$) was enclosed inside a latex membrane. This was done to arrest the water percolation through its sides. Then the specimen was mounted on the set up using the flexible connector and stainless steel clamps. Fresh water was passed through this specimen for three to six cycles in order to decrease the air blockages in the flow channels of porous concrete. The permeability was then measured by observing the time taken between the difference in initial and final water levels. Darcy's law was used for calculating the coefficient of permeability, as shown in Equation 6.1.

$$\text{Permeability, } K = (A_1 / A_2) \times (L / t) \times \log_e (h_1 / h_2) \quad - (6.1)$$

where L is the length of the specimen, A_1 and A_2 are the cross sectional areas of the specimen and the stand pipe, h_1 and h_2 are the initial and final levels of water respectively, and t is the time required to reach the final level from the initial level of water.

6.3.2 Compressive strength test

The compressive strength test of the cylindrical concrete specimen (100 × 150 mm) was conducted according to IS 516 (1959). The specimens were tested at a loading rate of 1832 N/s in a compression testing machine having 3000 kN capacity. These tests were conducted on three specimens and their average compressive strength was determined.

6.3.3 Determination of void size using image analysis approach

Concrete specimens of size 40 × 100 mm ($\phi \times H$) were cored and sliced from the 100 × 200 mm concrete specimens using core cutting machine and Diamond-tipped saw respectively. These specimens (in dried condition) were then scanned using X-rays generated at a voltage and current of 120 kV and 70 μ A respectively. The scanning rate was maintained around 4 milliseconds per image. The GE phoenix v|tome|x s 3-D X-ray Computed Tomography (CT) machine, used for this study, was fitted with a Caesium Iodide flat panel based detector. The resultant 2-dimensional radiographs were extracted from the acquisition software named Phoenix datos|x CT. Next, their 3-dimensional reconstruction was performed using the software VGStudio MAX version 2.2. The acquired tomographic images were sectioned into multiple slices (~ 130) and then uploaded into the Image Pro Premier 9.1 software. The various tools such as crop and resize, auto calibration, segment, count and analyse, macro

recording, and batch processing from this software were subsequently used to analyse the CT image – these processes are schematically shown in Figure 6.13.

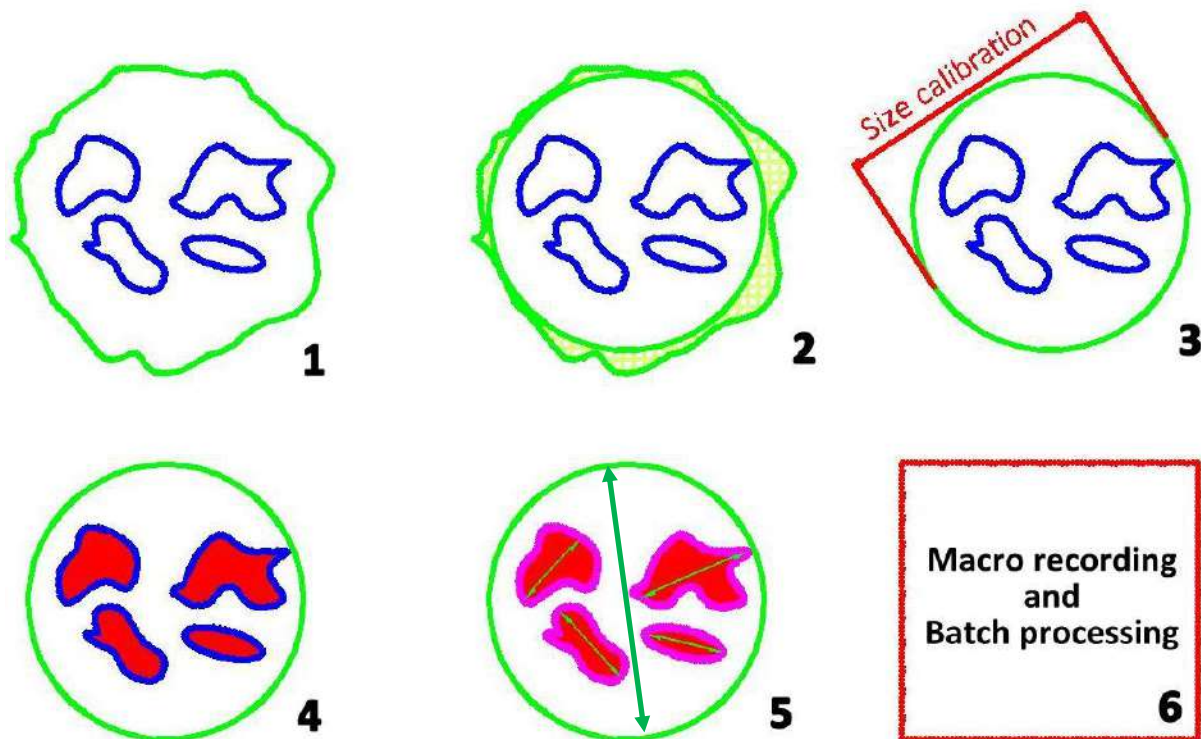


Figure 6.13 Schematic diagram illustrating the series of steps that were followed to analyse the CT slice using image analysis software

(1 – Original 2-D CT image was uploaded for analysis; 2 – The grey scale images were cropped to circular shape to reduce the edge irregularities; 3 – The cropped image was calibrated for realistic measurement; 4 – The calibrated image was converted into binary image by a thresholding operation to separate the void and solid phases; 5 – Counting and measurement of the diameter and surface area of 2-D image was done; 6 – The earlier steps were recorded and re-applied for the remaining images using batch processing tool)

Using this software, the scale of the cropped image was first calibrated to determine the realistic measurement of the specific features (voids) present in them. Then those features having lower attenuation coefficient in the CT image were segmented and measured for parameters such as Feret diameter and surface area respectively. Typically, Feret diameter is considered in the analysis of grain size and its distribution. The maximum and minimum Feret diameters are the longest and shortest distance between any two points in the contour of the closed polygon respectively (as depicted in Figure 6.14) and their average is considered

for the image analysis (Merkus 2009). The voids in the CT image were dominantly seen to be enclosed polygons that were irregular in shape, as seen in the thresholded 2-D CT slice in Figure 6.15.

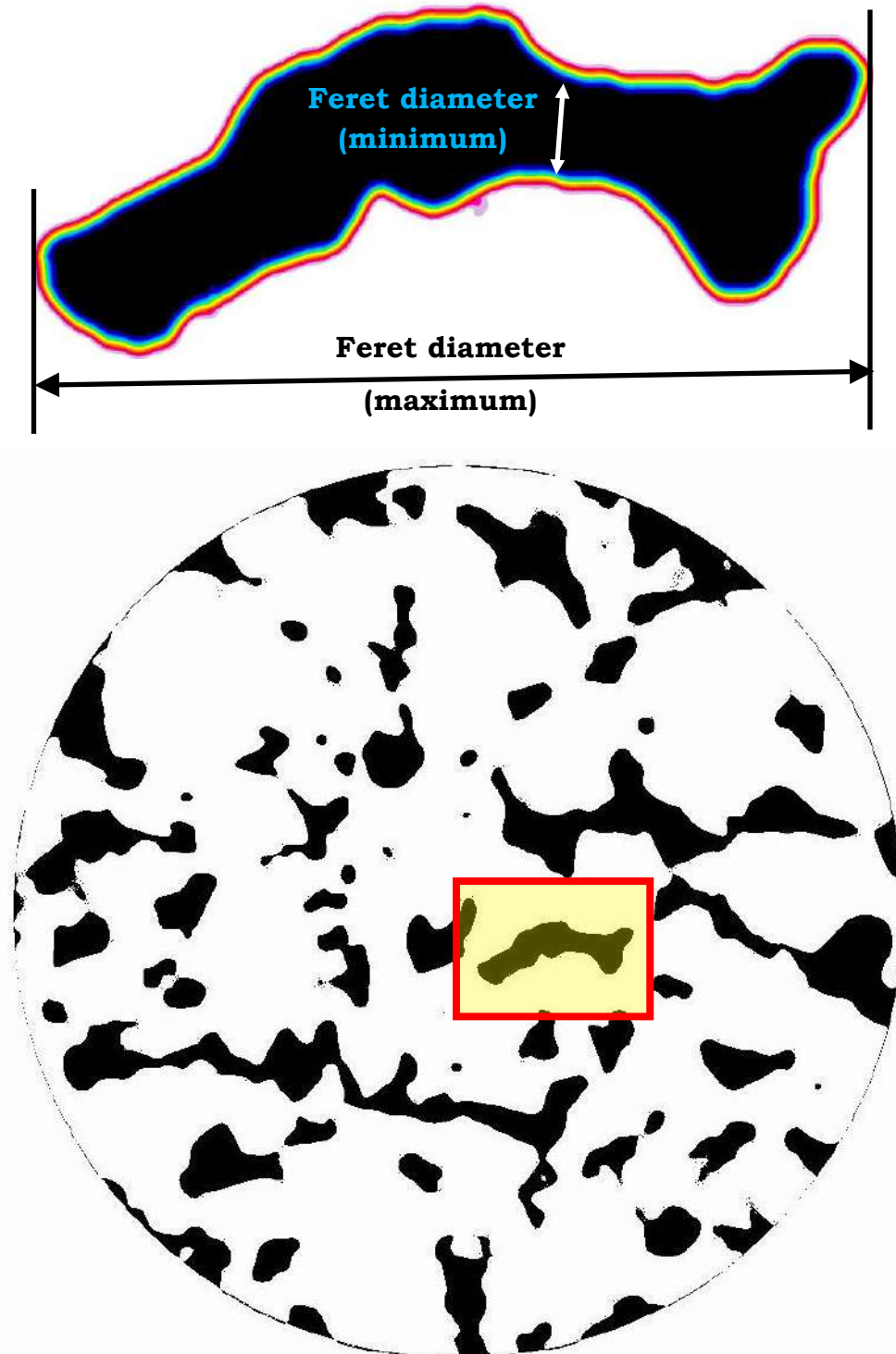


Figure 6.14 Feret diameter measurement (top image) of the polygons in the 2-D CT slice (bottom image) of the porous cement concrete

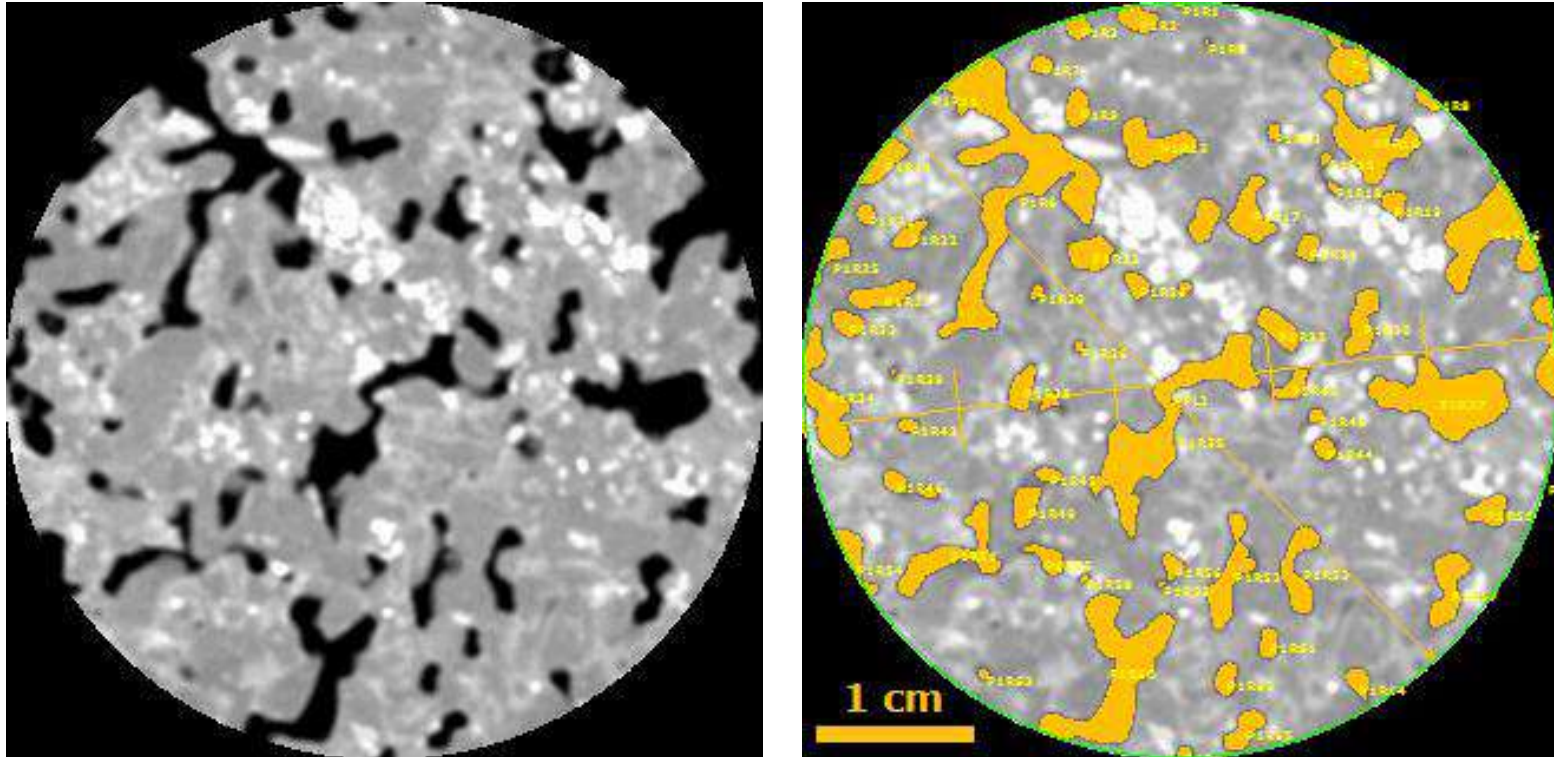


Figure 6.15 Plain (left image) and analysed (right image) CT image obtained from the software Image Pro Premier 9.1

After the analysis, the void size distribution in each slice was obtained. With this data, the area fraction of voids in each slice was calculated. Figure 6.16 illustrates the void area fraction of multiple CT slices along the depth of the specimen; the resultant porosity profile of the porous concrete specimen along its longitudinal section can be seen in this plot.

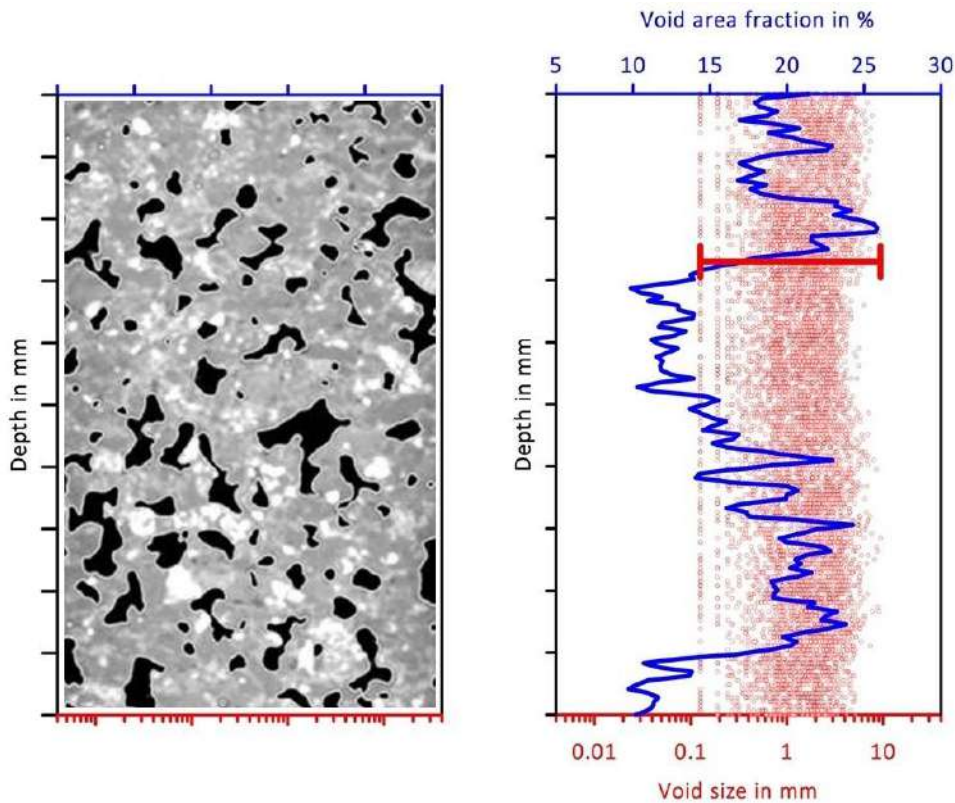


Figure 6.16 A typical slice from the CT (left image) and the void related features that were determined using image analysis approach (right image)

6.4 RESULTS AND DISCUSSION

6.4.1 Trial based experimental design

Porous concretes need to be designed with controlled hydraulic conductivity for better filtration performance. From the review of literature, it can be seen that permeability can be decreased by increasing the amounts of cementitious materials and compaction effort. Additionally, narrowly graded aggregates can decrease the formation of coarser voids. Considering these facts, five trial mixes were selected from a preliminary experimental investigation that involved more than 20 different combinations, and tested for their strength and permeability respectively. Based on the recommendations from the report of the

committee ACI 522R (2010), the typical values of w/c (water to cement) and a/c (aggregate to cement) ratio were considered for the design of all mixes. Among the common grading of aggregates suggested in ASTM C33 (2011) for the design of porous concrete, the narrowly graded sizes #8 (9.5 to 2.36 mm) and #89 (9.5 to 1.18 mm) were used in the preparation of trial mixes.

Marshall Hammer was used for the compaction of cylindrical specimens. The amounts of compaction energy were also altered between the mixes to determine its effect on the hydraulic properties. As seen from Table 4.1, Mixes M₁ and M₂ have similar grading of aggregates (#8). However, their porosities may be different because of the application of lower and higher compaction efforts respectively. In the cases of M₃ and M₄, the aggregate grading #89 was used. Subsequently, these mixes were prepared having lower and higher compaction efforts respectively. M₅ was designed with higher amounts of cementitious materials and smaller sized aggregates. The workability of all mixes was controlled by the addition of 0.5 wt% polycarboxylate ether (PCE) based superplasticizer. Table 6.1 shows the mixture proportioning of the different mixes and their strength and permeability results.

Table 6.1 Details of the different concrete mixes that were prepared for this study

Mixture Index	M ₁	M ₂	M ₃	M ₄	M ₅
Aggregate to cement (a/c) ratio	4.5	4.5	4.5	4.5	4
w/c	0.33	0.33	0.33	0.33	0.32
Number of layers	1	3	1	3	3
Blows per layer	5	26	5	26	26
12.5 to 10 mm	7	7	-	-	-
10 to 6.3 mm	25	25	19	19	-
6.3 to 4.75 mm	48	48	40	40	45
4.75 to 2.36 mm	15	15	21	21	25
2.36 to 1.18 mm	5	5	15	15	20
1.18 mm to 300 μm	-	-	5	5	5
≤ 300 μm	-	-	-	-	5
K value, in cm/min.	33.94 ± 2.69	19.96 ± 0.77	28.76 ± 2.84	18.13 ± 1.46	7.61 ± 2.11
Strength, in MPa	8.47 ± 1.07	16.72 ± 4.36	10.26 ± 0.57	17.19 ± 2.96	22.96 ± 1.76

All the mixes were found to allow the water to percolate. It is clear from the permeability results that the increase in binder content and compaction effort, and increased fraction of smaller sized aggregates used in the preparation lead to a decrease in the permeability. Typically, the filtration rate of slow and rapid sand filters are $0.1 - 0.4 \text{ m}^3/\text{m}^2/\text{h}$ and $5 - 15 \text{ m}^3/\text{m}^2/\text{h}$ respectively (Pani 2007). The filtration rate of M_5 specimens was calculated from the hydraulic conductivity to be on an average $4.8 \text{ m}^3/\text{m}^2/\text{h}$. This value was found similar to the sand filters that are used in water and wastewater treatment plants, and thereby porous concrete of the M_5 category was used for investigations associated to filtration performance in the present study.

6.4.2 Properties of porous concrete (M_5)

The interconnected and disconnected voids inside the porous concrete specimen could be visualised using its 3-D reconstructed CT images, which are shown in Figures 6.17 to 6.21.

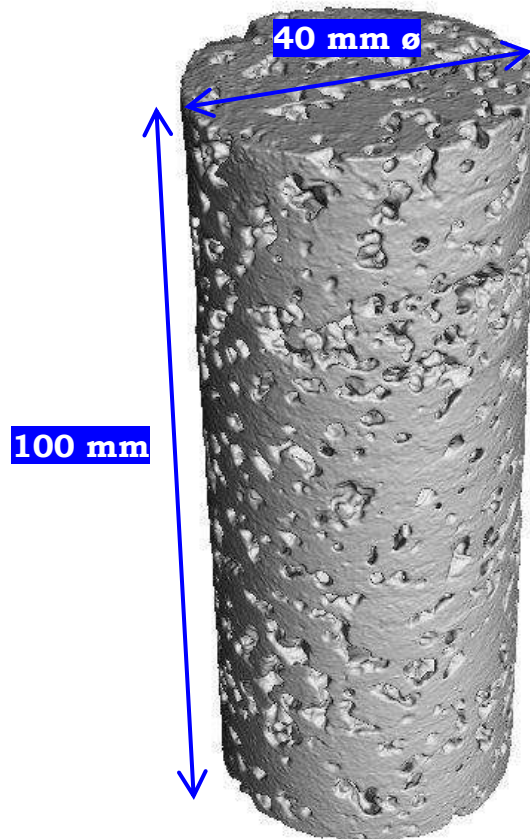


Figure 6.17 3-D CT image of the porous concrete specimen which was reconstructed using the software named VolumeGraphics Studio Max 2.2

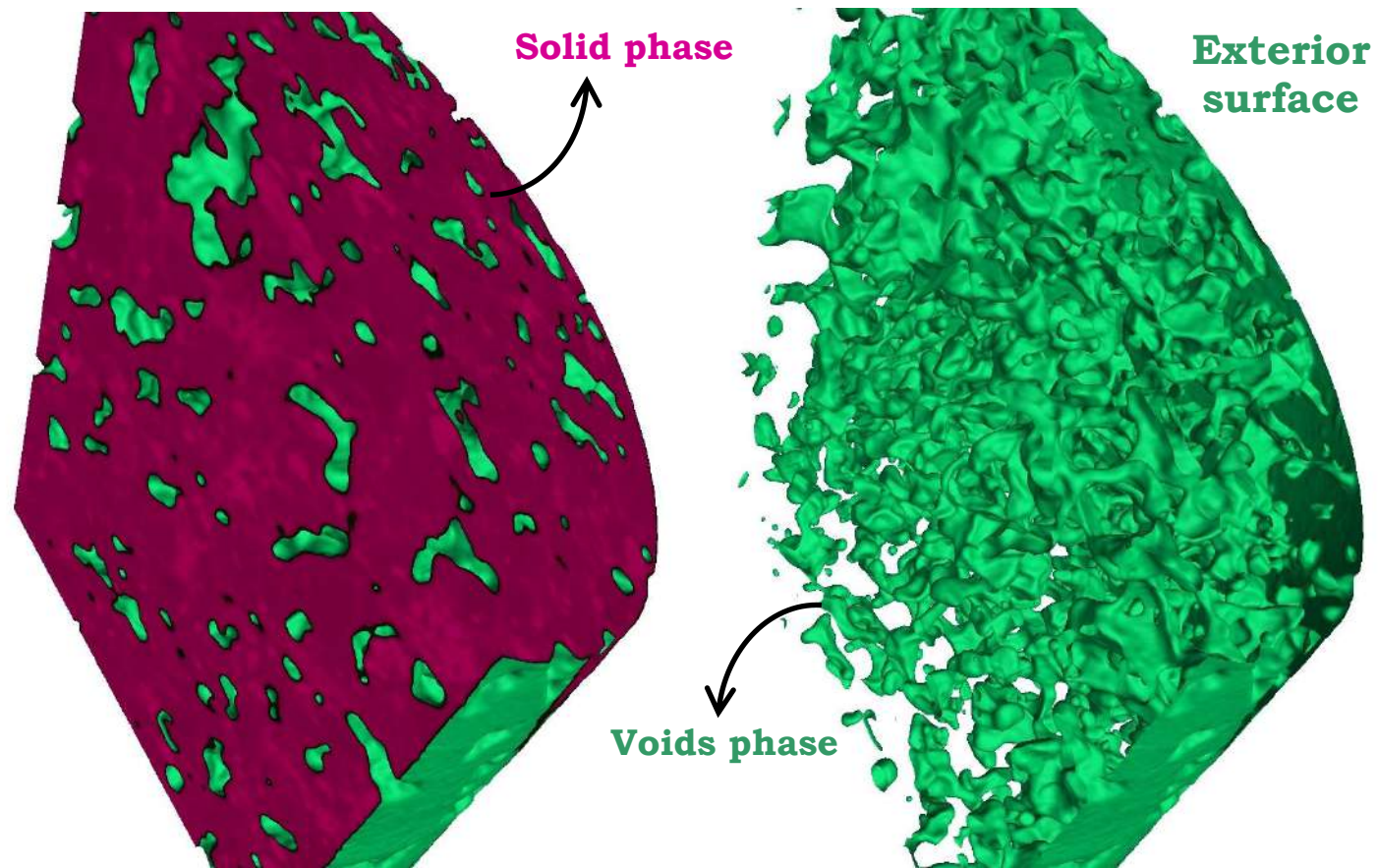


Figure 6.18 3-D Reconstructed CT image which was sectioned along horizontal and vertical axis (left image) and then processed to delineate the voids inside the material (right image) using the software VolumeGraphics Studio Max 2.2

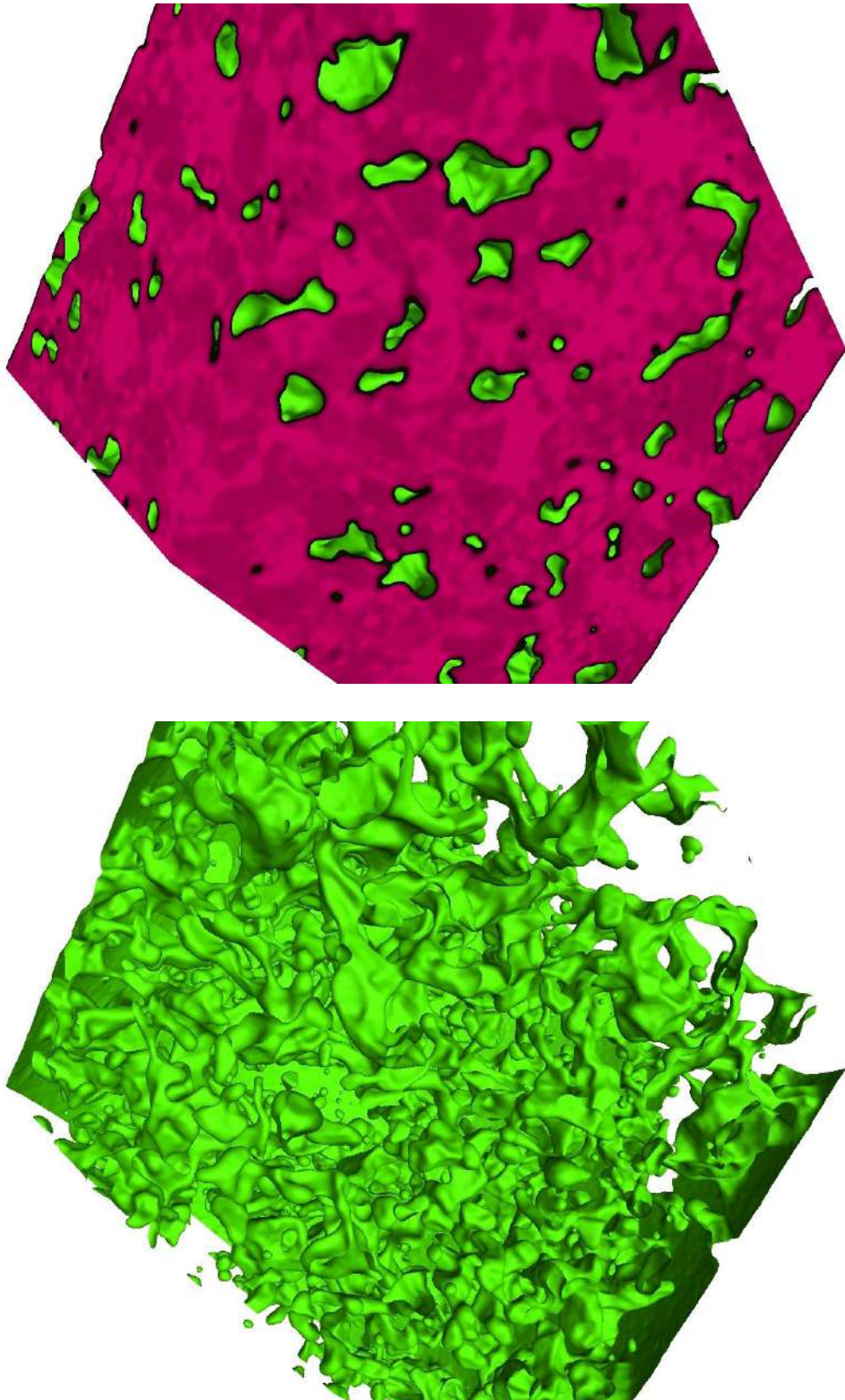


Figure 6.19 3-D Reconstructed CT image randomly sectioned along the primary axes (X, Y, Z) and then processed to clearly illustrate the porous structure inside the material

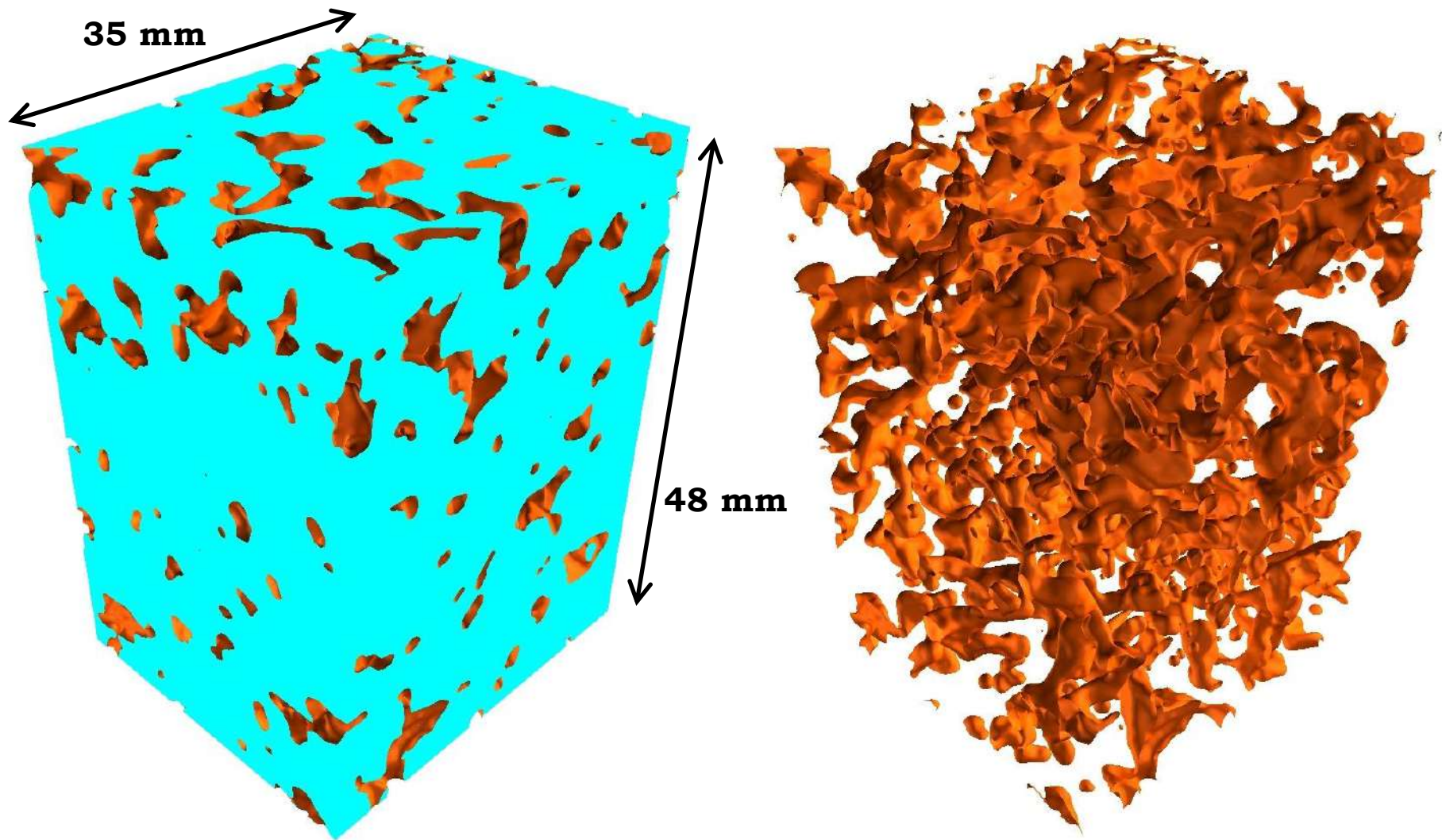


Figure 6.20 3-D reconstructed CT image (cylindrical shaped porous concrete specimen) sectioned out into a cuboid (left image) and then processed to show the porous structure inside the material (right image)

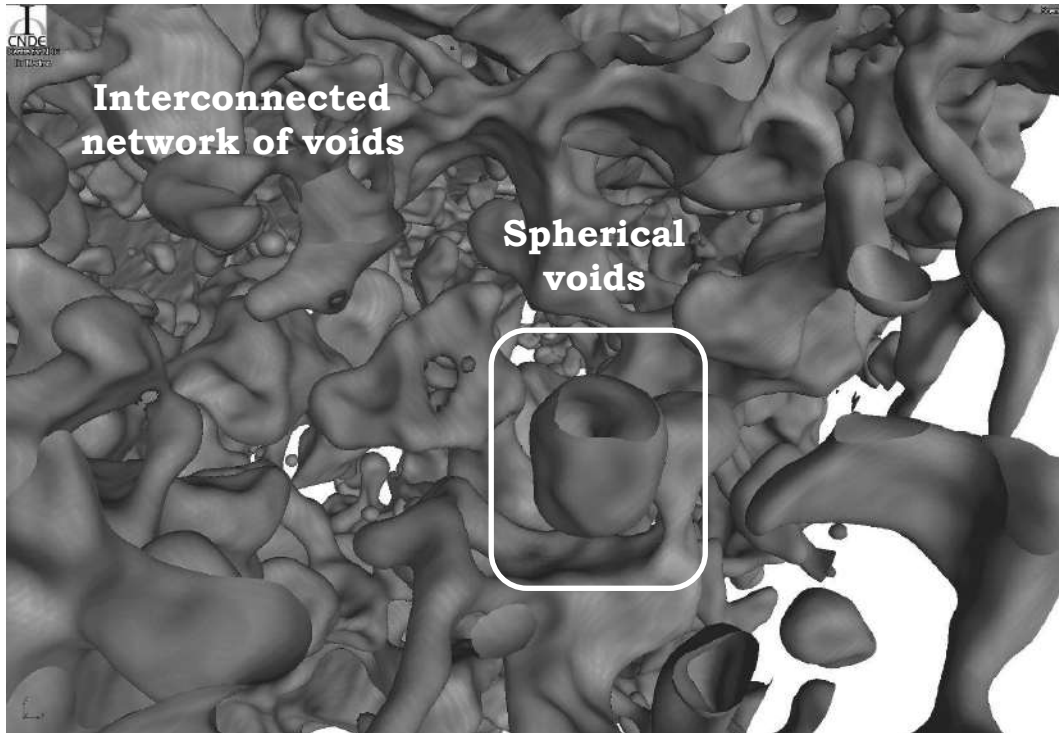


Figure 6.21 Closer view of the CT image illustrating the co-existence of interconnected and disconnected voids inside the porous concrete specimen

The connected voids were noticed to be irregular and highly tortuous, which suggests that the porous system could be highly prone to sediment blockage. The reconstructed software named VGStudio Max 2.2 has in-built algorithms and modes which can locate the pores or voids with high contrast inside the material. These algorithms control the grey scale histogram of the CT image.

First, the 3-D CT image of the porous concrete specimen was sectioned into multiple shapes to clearly visualise the interconnected voids inside the material. This was also done to remove the noise created by the exterior surface of the CT image which was in direct contact with the low density material (air). With the help of visualisation tools in the software, the grey scale histogram of the CT image was adjusted to only reveal the regions having lower attenuation coefficient, which is illustrated in the Figures 6.18 to 6.21.

Five concrete specimens of M₅ category were scanned using X-ray CT. These tomography images were sectioned into multiple slices and then analysed for their void size distribution and void area fraction respectively. Figure 6.22(a-b) compares the porosity profile of those five specimens along their longitudinal section.

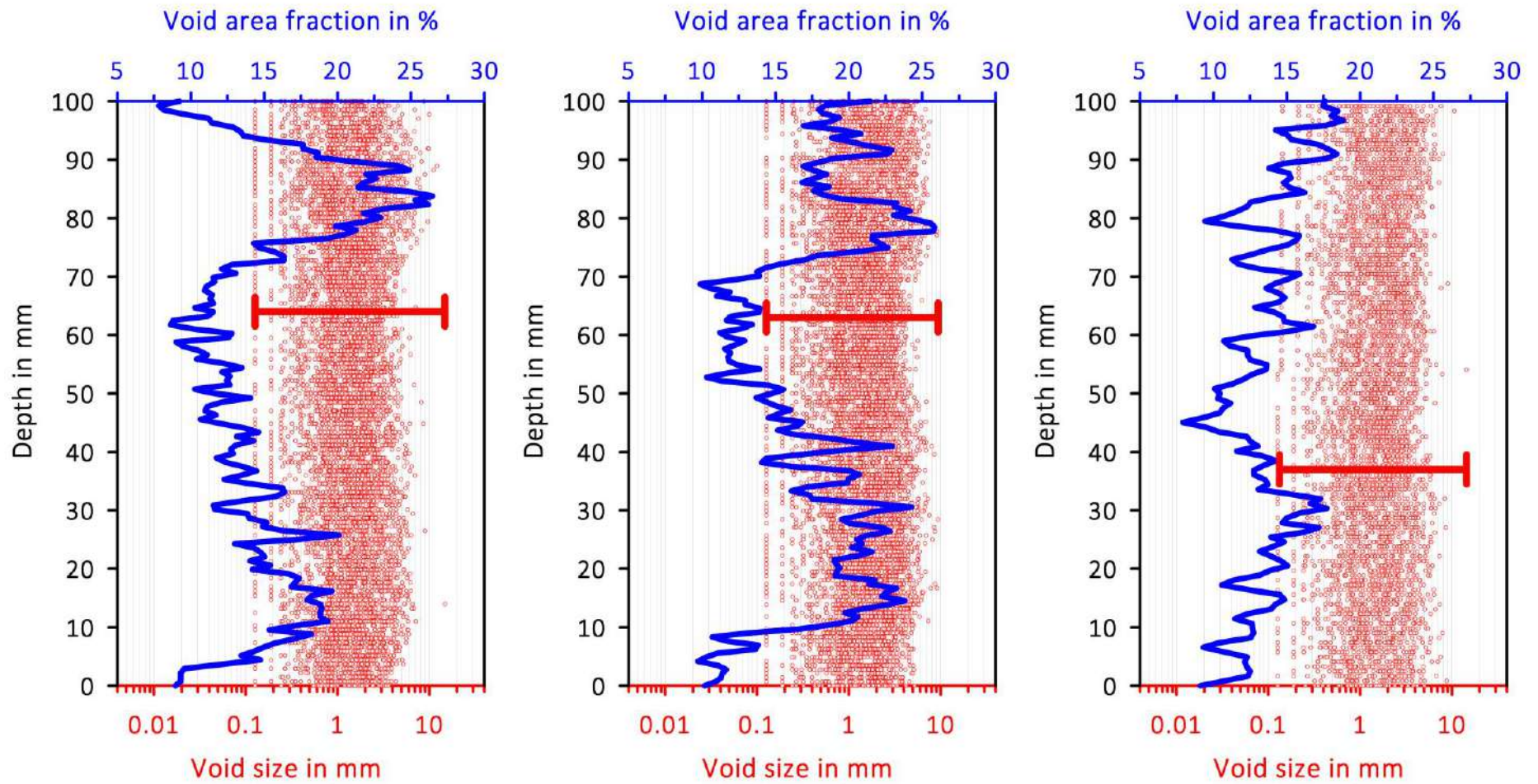


Figure 6.22a Porosity profiles of three M₅ category porous concrete specimens of size 40 × 100 mm (ϕ × H)

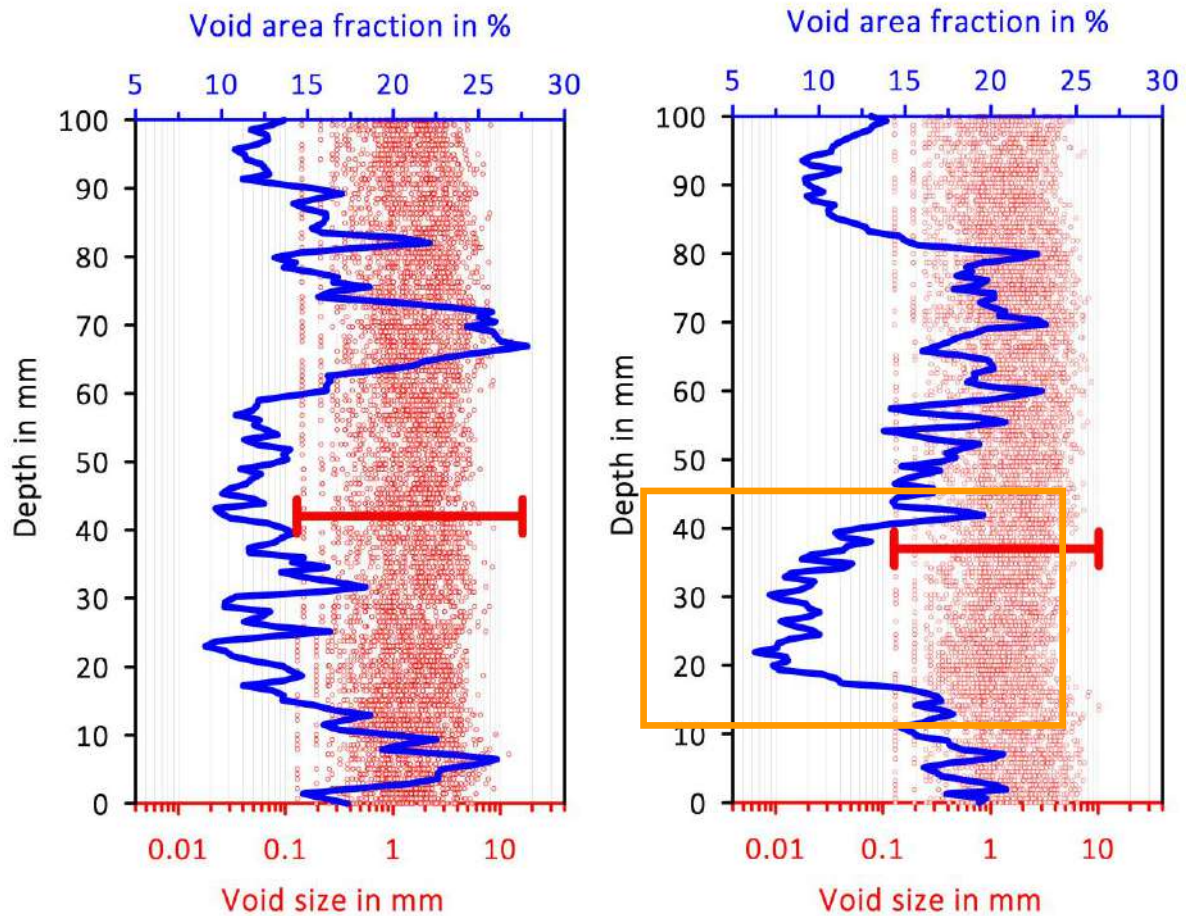


Figure 6.22b Porosity profiles of the remaining M_5 category concrete specimens of size 40×100 mm ($\phi \times H$)

It can be seen from the image analysis results that the void size and surface porosity (void area fraction) of M_5 concrete specimens (of size 40×100 mm) were found to be in the range $126 \mu\text{m}$ to 14.8 mm and 14.77 ± 4.21 % respectively. The porosity profiles suggest that the flow channels are highly tortuous, which increases the hydraulic retention time. In one of the profiles, a significant alteration in the porosity was observed at the interface between the middle and bottom concrete layer (marked by the orange box in Figure 6.22b). This might have occurred because of paste clogging at the top of the middle layer. In this study, to have a better bonding between the concrete layers, the surface of consolidated concrete was made rougher using an iron rod having a sharp tip. This action disturbs the cement slurry and thereby fresh surfaces were made rough in texture. The aggregates of different sizes packed inside the porous concrete specimen (of M_5 category) could also be visualised using the 3-D reconstructed CT image, which is illustrated in Figure 6.23.

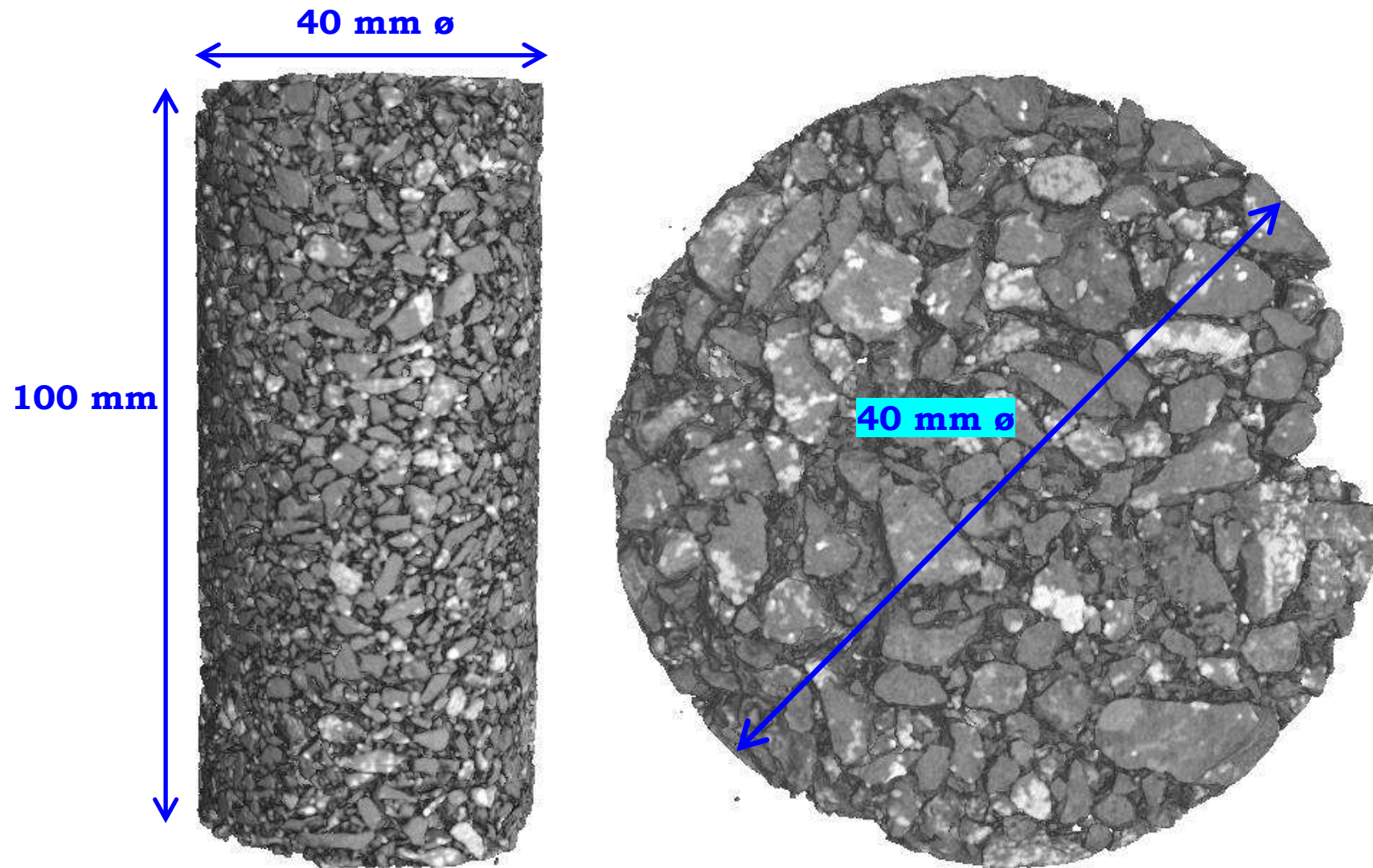


Figure 6.23 3-D Reconstructed CT image illustrating the aggregates of different sizes that were packed inside the porous concrete specimen

The aggregates coated by the cementitious binder in the porous concrete, as seen in Figure 6.17, were found to be brighter in the CT image of porous concrete, which could be due to their higher attenuation coefficient. It can be noticed that the presence of cementitious binder had not made the aggregates to be clearly visible on the surfaces in the CT image.

In order to bring about more clarity in imaging the distribution of aggregates, a short-term chemical attack was performed by the storage of specimens in 0.5 M HNO₃ solution for a period of 18 days, as shown in Figure 6.24.



Figure 6.24 Selective chemical attack of the porous concrete specimen by storage in 0.5 M HNO₃ solution

The result of this procedure was a removal of the paste layer from the surface. After this degradation, the specimen was carefully dried and then scanned using X-ray CT. The CT image from this scan, which was illustrated in Figure 6.23, was able to clearly show the presence of aggregates of different sizes that were packed inside the porous concrete specimen (M₅ category).

The compressive strength of porous concrete (M₅ category) was found to be 22.96 ± 1.76 MPa. In general, the compressive strength and density of porous concrete are in the range of 1600 – 1800 kg/m³ and 3.5 – 28 MPa respectively (Obla and Sabnis 2009). In this study, 40 specimens of M₅ category were prepared and then tested for their densities and permeability. The fresh and hardened densities were found to be 2159 ± 28 kg/m³ and 2155 ± 29 kg/m³ respectively. The permeability of M₅ specimens was found to be 7.98 ± 3.83 cm/min. This

value is much lower than in the existing literature on pervious concrete, as seen in Figure 6.25.

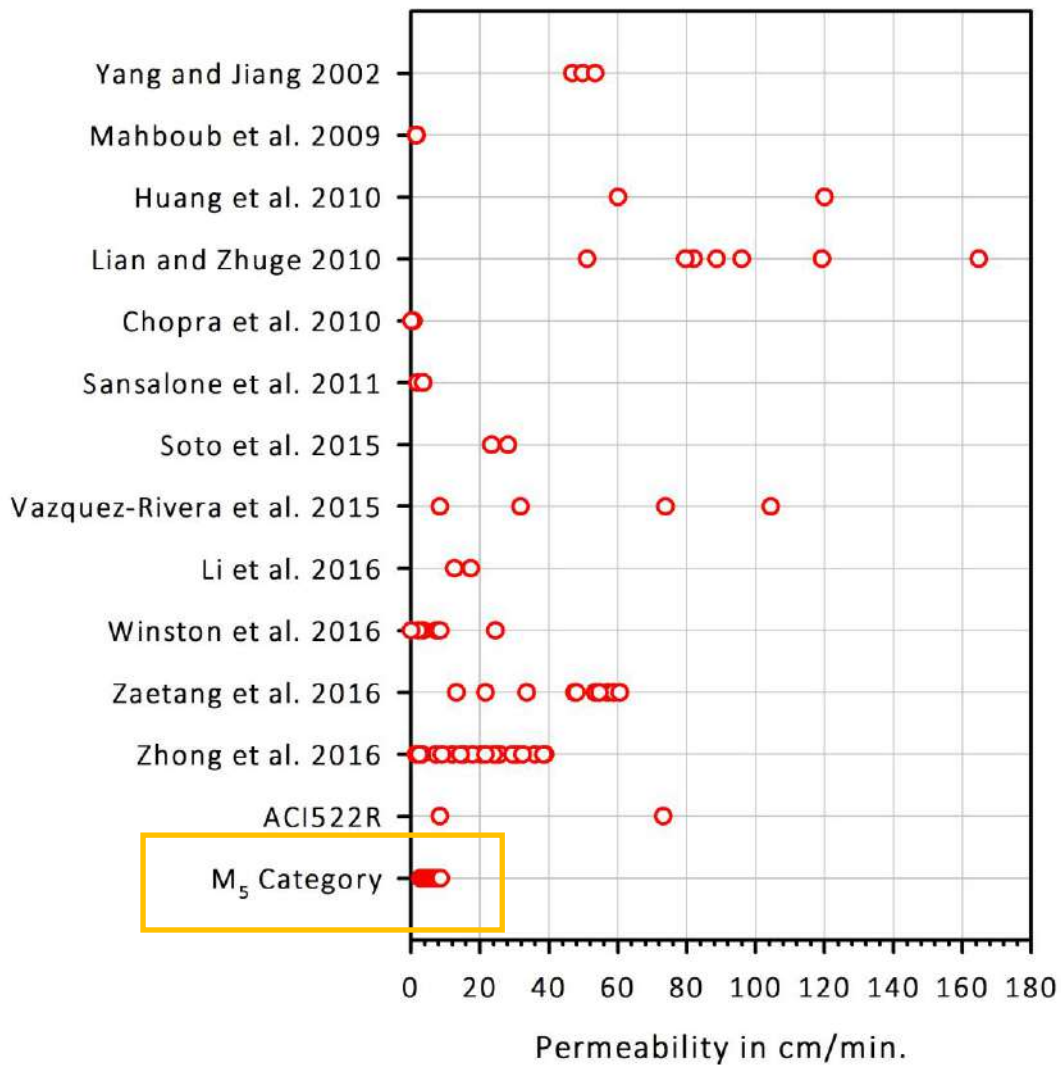


Figure 6.25 Comparison of permeability of M₅ specimens with the existing literature

Such low permeability values are not used in the design of pervious concrete pavements because of the tendency to clog easily by the stormwater runoff containing large amounts of sediments. However, this range was found similar to the permeability of sand filters that are used in water treatment plant and thereby porous concrete having such value was considered in the present study for the investigations associated to the removal of heavy metals from aqueous solutions.

6.5 SUMMARY

A trial based experimental design was followed in this study to obtain a porous concrete having controlled hydraulic permeability that is desired for filtration purposes. The interconnected voids inside this system were visualised using 3-D X-ray CT images, which suggested that the porous matrix was highly tortuous. The images of the slices from the CT study were analysed to calculate the void size distribution as well as the void area fractions. Additionally, the compressive strength and density of the porous concrete were also determined. From the experimental investigations, the M₅ category concrete, which was developed through extensive experimental trials, resulted in the optimal combination of permeability, density and strength, which made this system suitable for water filtration purposes. The next two chapters explore the performance of this concrete with respect to the removal of Pb from aqueous solutions.

CHAPTER 7

INVESTIGATION ON THE WATER FILTRATION CHARACTERISTICS OF POROUS CEMENT CONCRETE EXPOSED TO ACCELERATED CO₂ ENVIRONMENT

7.1 INTRODUCTION

One of the primary issues with the use of porous concrete for water filtration is the increase in alkalinity of the outlet water. A simple investigation was done to illustrate this problem. Six numbers of cylindrical porous concrete specimens (M₅ category) of size 100 × 200 mm (ø × H) were prepared by the procedure described in Chapter 6, and then demolded after 24 hours. These specimens were then immersed in 20 litres of distilled water, which was replenished every 24 hours, and the water characteristics were studied for a period of 6 days. Figure 7.1 and Figure 7.2 illustrate the alteration in the pH and turbidity of distilled water after storage.

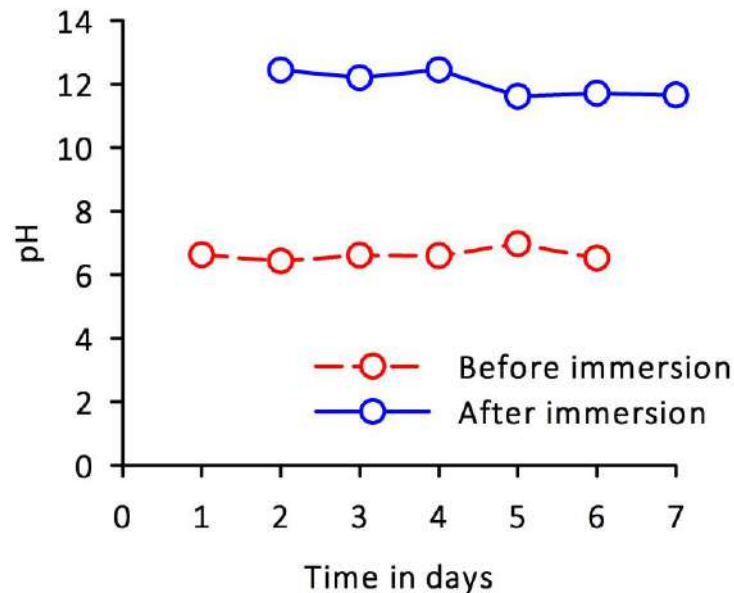


Figure 7.1 Alteration in the pH of distilled water which was used for storage (specimen to water volume ratio of 0.42)

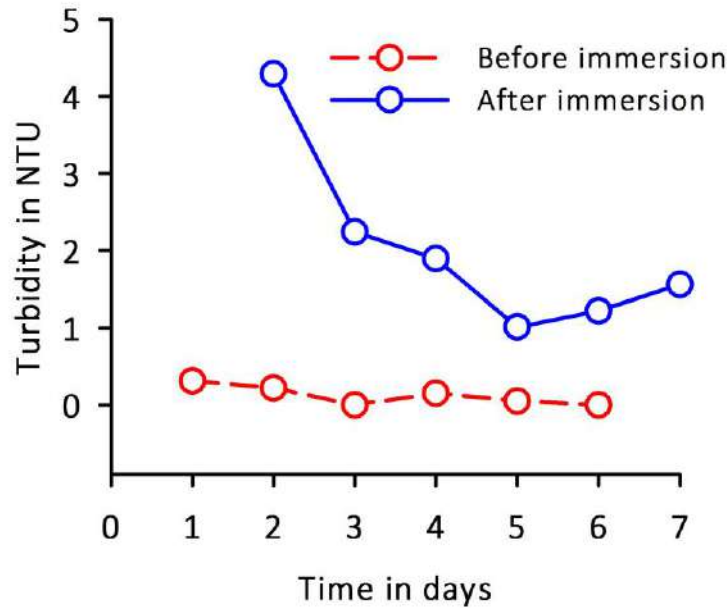


Figure 7.2 Alteration in the turbidity of distilled water that was used for storage (specimen to water volume ratio of 0.42)

The release of highly soluble alkalis (K and Na) and $\text{Ca}(\text{OH})_2$ (sparingly soluble) from the cementitious binder, otherwise known as leaching, is the major reason for the increase in turbidity and pH of distilled water from neutral to highly alkaline condition after storage.

There is a need to investigate methods to reduce this increase of pH. This has been attempted in the current study by the carbonation of porous concrete. Concrete carbonation is a natural phenomenon that results in the conversion of $\text{Ca}(\text{OH})_2$ (and in the long term, other Ca^{2+} bearing hydrate phases) into calcite based compounds in the presence of moisture. Figure 7.3 schematically illustrates the phase change which is likely to occur in the flow channels of porous cement concrete when exposed to CO_2 environment.

This chapter discusses the alteration in the physical characteristics of water passed through porous concrete exposed to accelerated CO_2 environment. In this study, aqueous solutions of different pH were passed through the porous concrete specimens after initial curing as well as after an accelerated carbonation exposure. The physical characteristics such as pH, turbidity and calcium ions remaining in those solutions after passage were analysed and are reported in the current chapter.

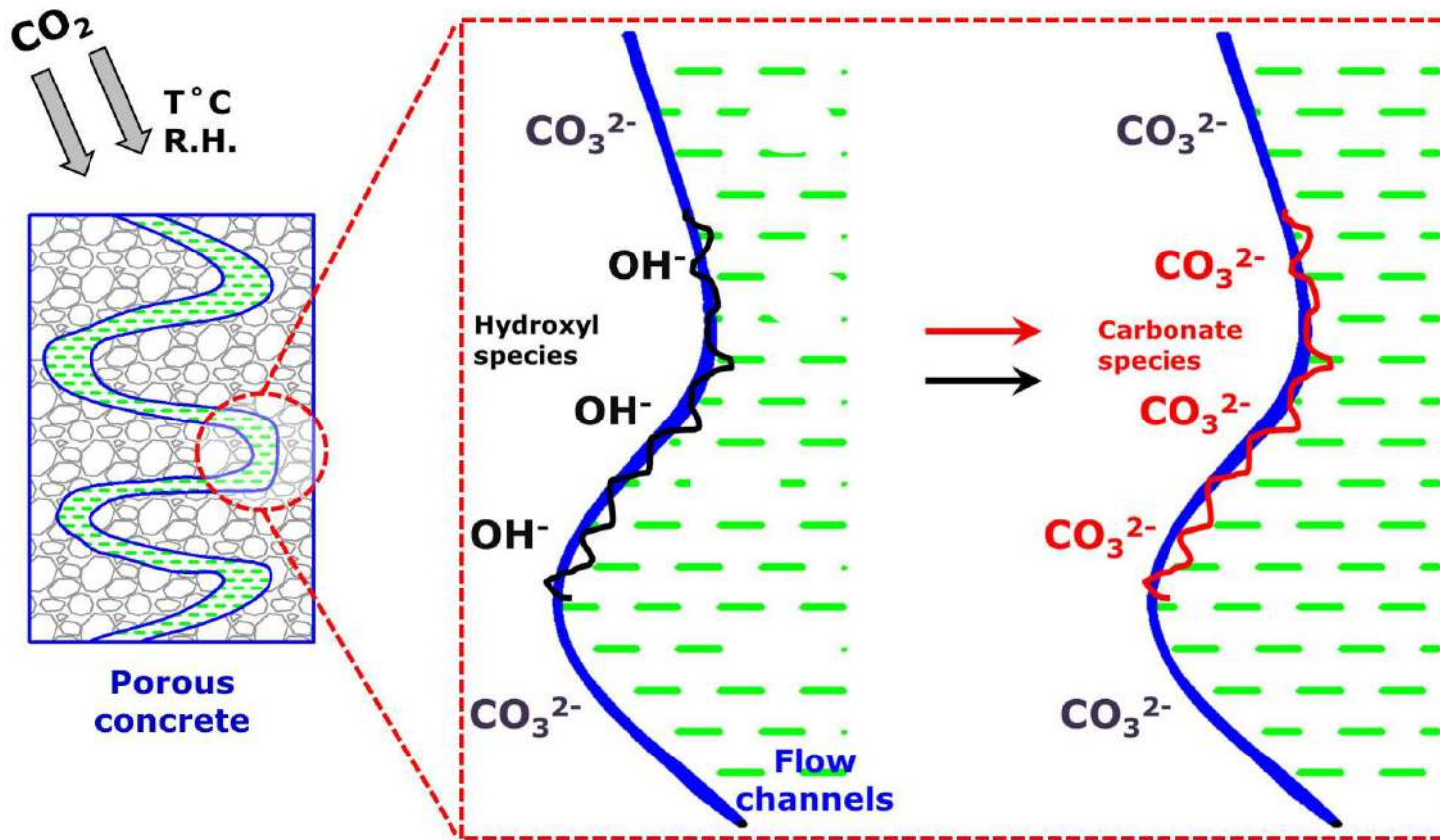


Figure 7.3 Phase alteration which is likely to occur in the flow channels of porous cement concrete when exposed to CO_2 (carbon dioxide) from the atmosphere

For preliminary filtration studies, aqueous solutions containing highly dangerous metal pollutants such as chromium (Cr), mercury (Hg), lead (Pb) and cadmium (Cd) were passed through the porous concrete after an accelerated carbonation exposure. This preliminary test was performed to finalise the model pollutant that could be used to investigate the filtration performance of porous concrete modified using reduced graphene oxide (rGO) sheets (dealt with in the next chapter). Finally, highly turbid solution containing bentonite clay was passed through the porous concrete after an accelerated carbonation exposure to investigate the changes in turbidity and permeability, in order to understand the potential for clogging in the system.

7.2 ACCELERATED CARBONATION EXPOSURE

The porous concrete specimens from the M₅ mix, having permeability of 7.98 ± 3.83 cm/min were used for the experimental investigations. In this study, carbonation test chamber was used to accelerate the effect of carbonation on these specimens. The CO₂ concentration in this chamber was maintained higher than that in the atmosphere. Further, the carbonation reaction was advanced by maintaining the test chamber with an optimum level of temperature and relative humidity (R.H.). Photograph of the carbonation test chamber that was used in this study is shown in Figure 7.4.



Figure 7.4 Carbonation test chamber that was used in this study

After 7 days of initial curing, as explained in Chapter 6, the specimens of size 100×150 mm ($\phi \times H$) were air dried at $25\text{ }^{\circ}\text{C}$ and 65% R.H. for the next 14 days. The dried specimens were then introduced into the carbonation chamber set at $25\text{ }^{\circ}\text{C}$, 65% R.H. and 1% CO_2 concentration for a period of 56 days. Micrographs illustrating the formation of hexagonal portlandite and short prismatic calcite crystals in the fractured surface of porous cement concretes after initial curing as well as after an accelerated carbonation exposure respectively, which are illustrated in Figure 7.5.

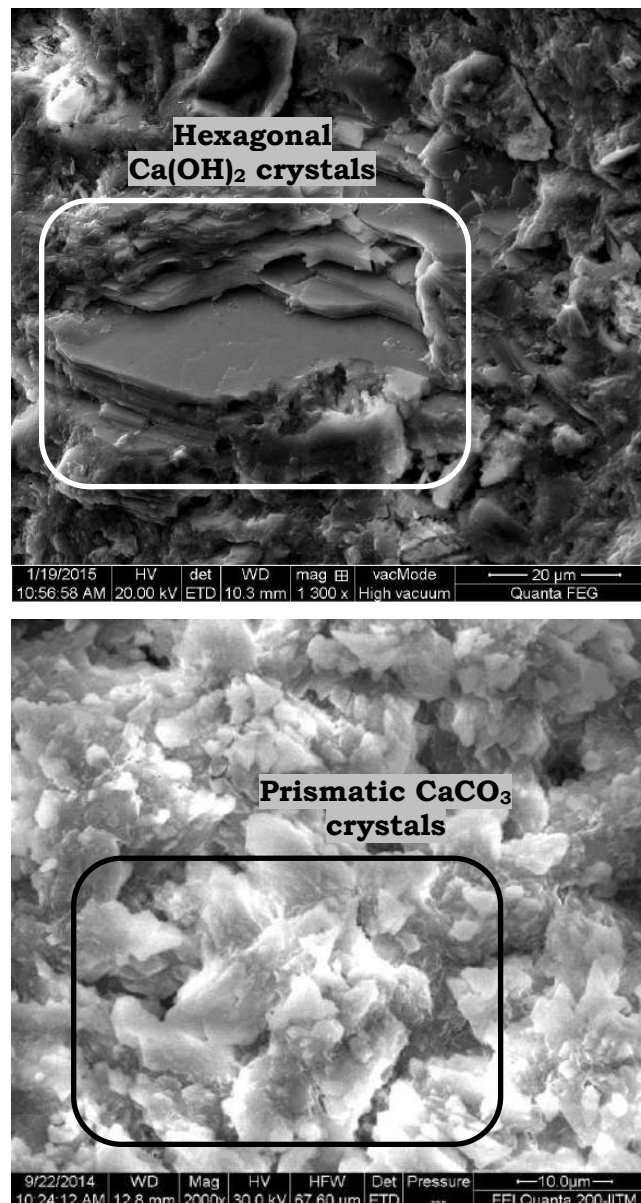


Figure 7.5 Micrographs illustrating the presence of Ca(OH)_2 (top image) and calcite (bottom image) crystals in the fractured surface of porous concretes after initial curing as well as after an accelerated carbonation exposure

7.3 EXPERIMENTAL METHODS

7.3.1 Repeat cycle permeability testing

Tap water, distilled water, and dilute solutions containing HCl, NaOH, lead, cadmium, mercury and chromium were passed through the porous concrete specimens using the falling head permeability test set up, which was described in Chapter 6 (section 6.3). The outlet water was fed back into the system, and this procedure was repeated ten times. For each solution, three concrete specimens were tested for statistical variance. A small amount of filtrate (~ 15 ml) was collected after each cycle and the remaining was again passed through the same specimen, which is schematically illustrated in Figure 7.6.

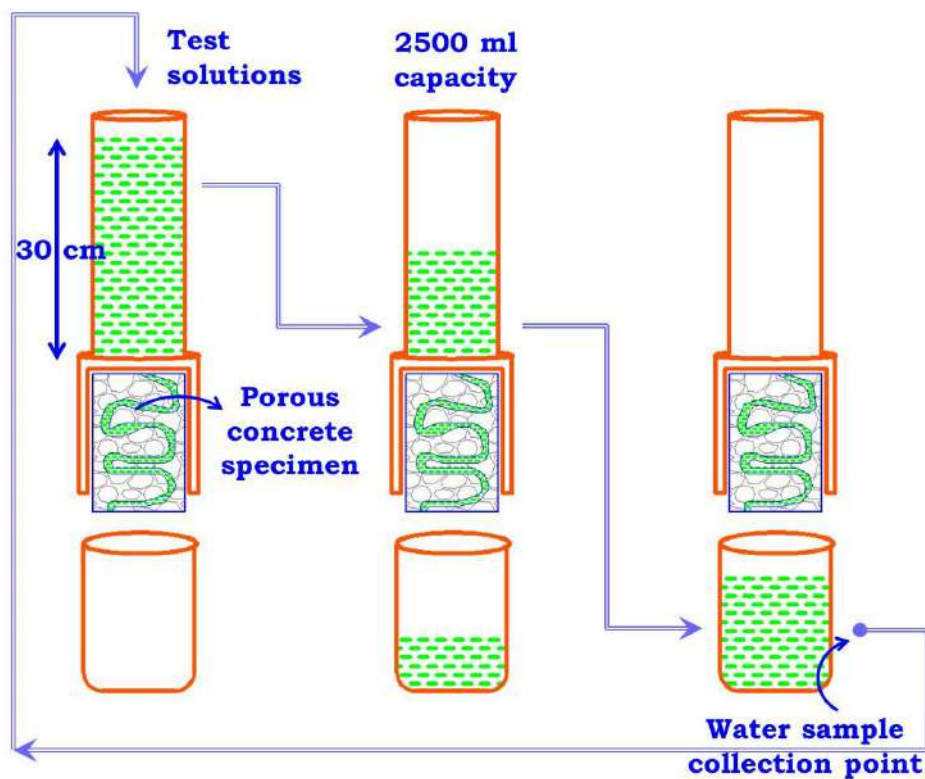


Figure 7.6 Schematic illustration of the repeat cycle permeability testing of cylindrical shaped porous concrete specimen of size 100×150 mm ($\phi \times H$)

ICP-MS (inductively coupled plasma mass spectrometry) was used to analyse the concentration of Ca, Cd, Cr, Pb and Hg ions remaining in the filtrate after passage. The physical characteristics such as pH and turbidity of the filtrate were measured using pH and turbidity meter respectively.

7.3.2 Bentonite clay loading test

In this study, a highly turbid solution containing sodium bentonite clay (~ 840 NTU) of 2500 ml capacity was passed through the porous concrete specimen, which is schematically illustrated in Figure 7.7.

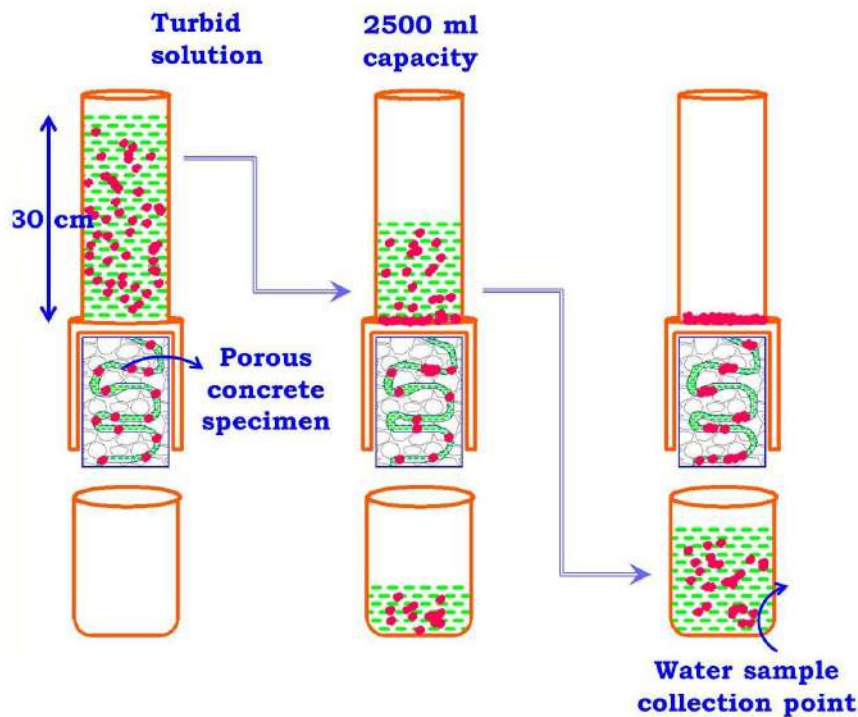


Figure 7.7 Schematic illustration of the highly turbid solution passed through the porous concrete specimens mounted in the permeability test set up

A small amount of filtrate was collected and the remaining solution was discarded. The turbidity of the collected water sample was measured using turbidity meter. Meanwhile, the permeability of such passage was also measured by observing the time taken between the difference in initial and final water levels. Darcy's law was used for calculating the coefficient of permeability, which is illustrated in Equation 7.1.

$$\text{Permeability, } K = (A_1 / A_2) \times (L / t) \times \log_e (h_1 / h_2) \quad - (7.1)$$

where L is the length of the specimen, A_1 and A_2 are the cross sectional areas of the specimen and the stand pipe, h_1 and h_2 are the initial and final levels of test solution (highly turbid

bentonite containing solution) respectively, and t is the time required to reach the final level from the initial level of test solution.

The turbid solution was magnetically stirred for 15 minutes to keep the fine clayey particles suspended in distilled water prior to the start of the test. Next, this procedure was repeated nine times on the same concrete specimen to study the effect of sediment blockage which is likely to alter the permeability of the porous material. From the laser diffraction analysis, the average particle size of dry bentonite clay powder was found to be $7.12\ \mu\text{m}$. Figure 7.8 shows the particle size distribution of bentonite clay that was determined using laser diffraction technique and the highly turbid bentonite containing solution that was used for this study.

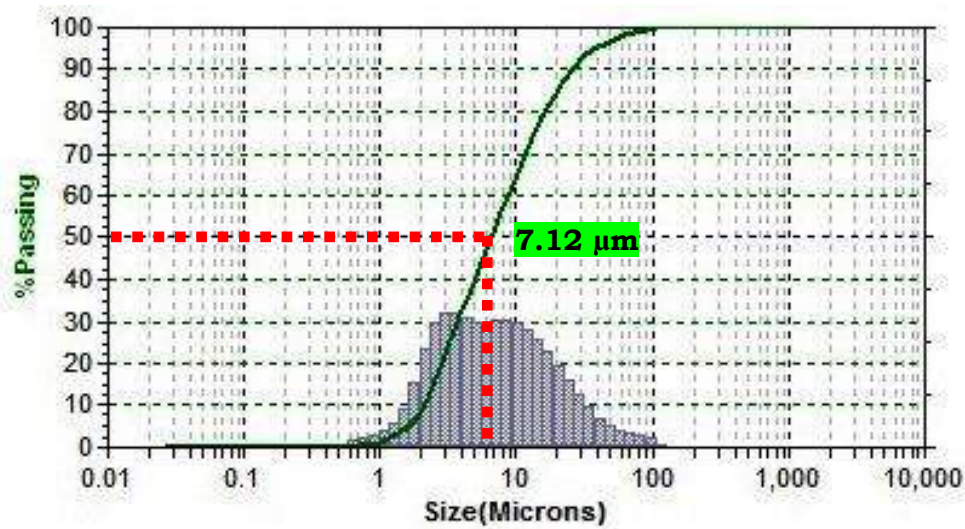


Figure 7.8 Particle size distribution of dry bentonite clay (top image) and the highly turbid bentonite containing solution (bottom image) that was prepared for this study

7.4 RESULTS AND DISCUSSION

7.4.1 Characteristics of distilled water and tap water, and dilute HCl and NaOH solutions after passage through the porous concrete

Figures 7.9 to 7.14 illustrate the alterations in the characteristics of distilled and tap water passed through the non-carbonated and carbonated porous concrete specimens for ten repeat cycles.

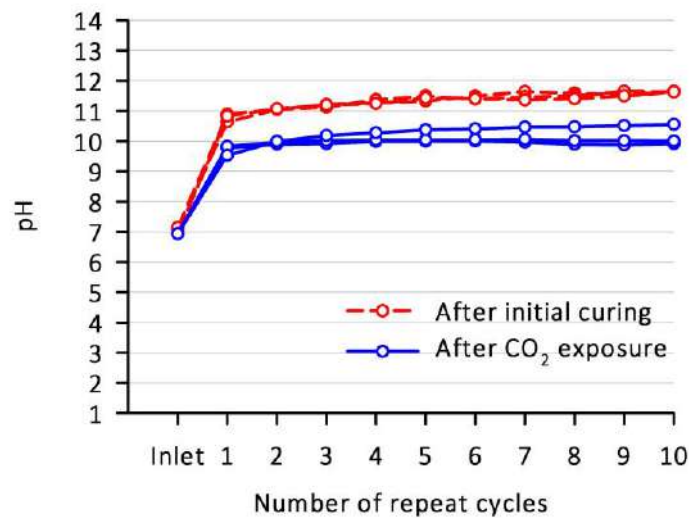


Figure 7.9 Alteration in the pH of distilled water passed through the porous concrete after initial curing as well as after an accelerated carbonation exposure, for ten repeat cycles

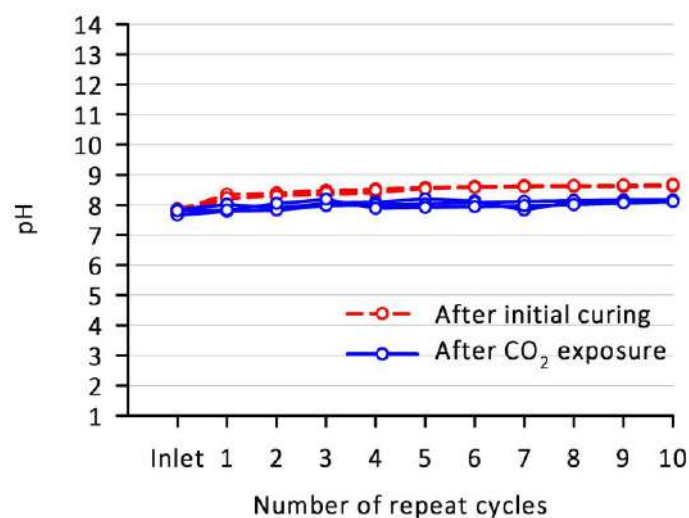


Figure 7.10 Alteration in the pH of tap water passed through the porous concrete after initial curing as well as after an accelerated carbonation exposure, for ten repeat cycles

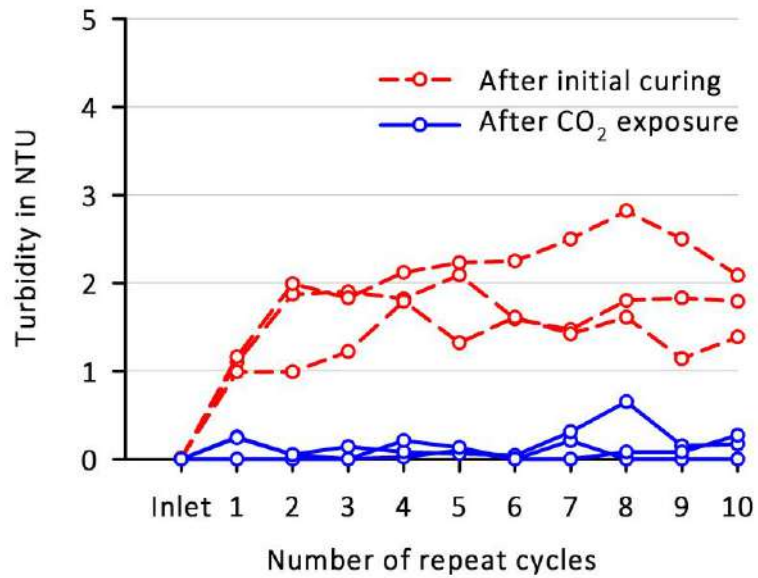


Figure 7.11 Alteration in the turbidity of distilled water passed through the porous concrete after initial curing as well as after an accelerated carbonation exposure, for ten repeat cycles

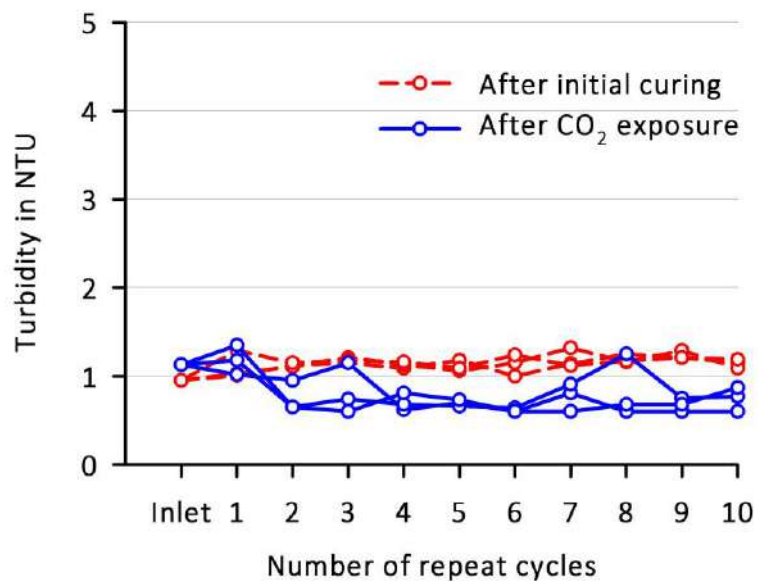


Figure 7.12 Alteration in the turbidity of tap water passed through the porous concrete after initial curing as well as after an accelerated carbonation exposure, for ten repeat cycles

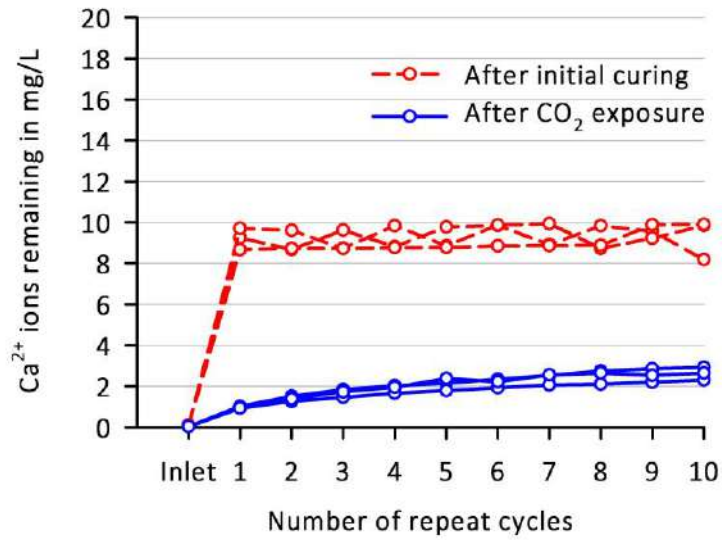


Figure 7.13 Calcium ions remaining in the filtrate obtained through the porous concrete specimens tested using distilled water, after initial curing as well as after an accelerated carbonation exposure, for ten repeat cycles

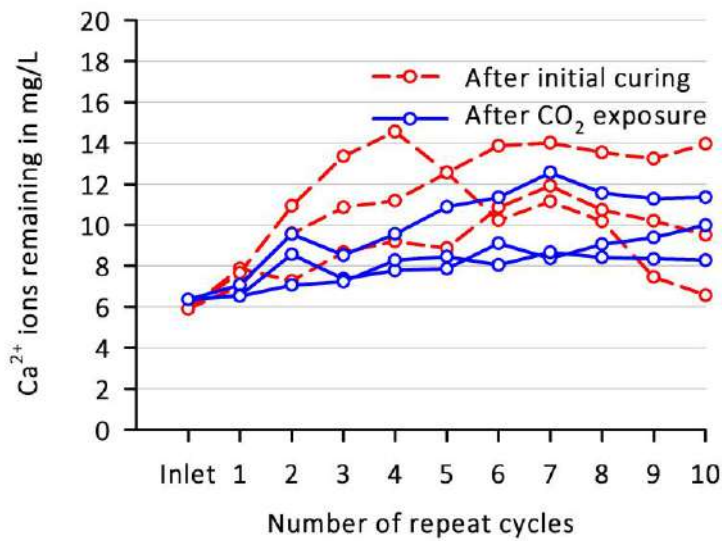


Figure 7.14 Calcium ions remaining in the filtrate obtained through the porous concrete specimens tested using tap water, after initial curing as well as after an accelerated carbonation exposure, for ten repeat cycles

The release of highly soluble $\text{Ca}(\text{OH})_2$ from the 7-day cured porous concrete specimens had altered the characteristics of tap and distilled water after passage. However, this alteration could be reduced by the effect of carbonation on the porous concrete specimens. In particular,

the removal of calcium ions from the carbonated specimens was decreased up to 3-fold in comparison to 7-day cured porous concrete specimens. The CO_2 interacts with the $\text{Ca}(\text{OH})_2$ crystals in the cementitious binder and thereby produces stable calcite compounds, reducing the propensity for leaching.

Figures 7.15 to 7.20 show the alteration in the characteristics of dilute HCl (made from laboratory reagent HCl 35% to 38%) and NaOH (made of NaOH pellets) solution after passage.

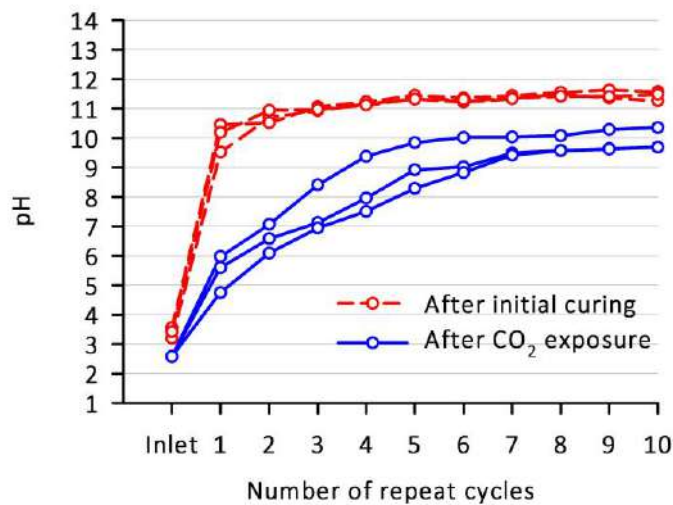


Figure 7.15 Alteration in the pH of dilute HCl solution passed through the porous concrete after initial curing as well as after an accelerated carbonation exposure, for ten repeat cycles

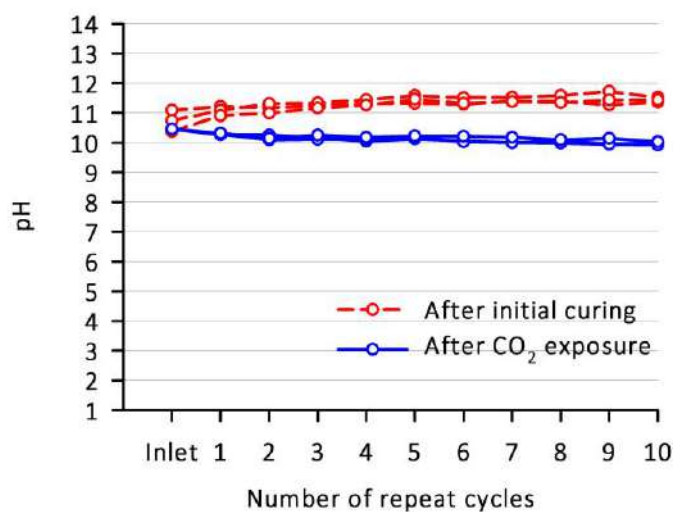


Figure 7.16 Alteration in the pH of dilute NaOH solution passed through the porous concrete after initial curing as well as after an accelerated carbonation exposure, for ten repeat cycles

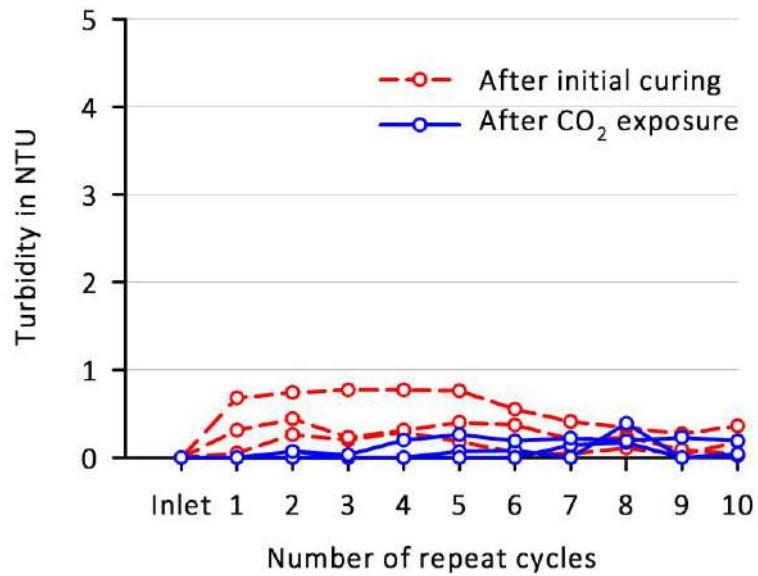


Figure 7.17 Alteration in the turbidity of dilute HCl solution passed through the porous concrete after initial curing as well as after an accelerated carbonation exposure, for ten repeat cycles

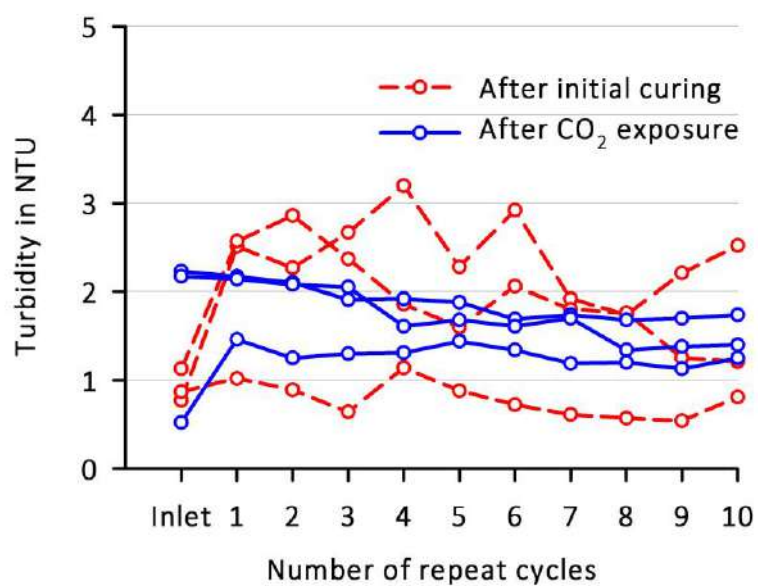


Figure 7.18 Alteration in the turbidity of dilute NaOH solution passed through the porous concrete after initial curing as well as after an accelerated carbonation exposure, for ten repeat cycles

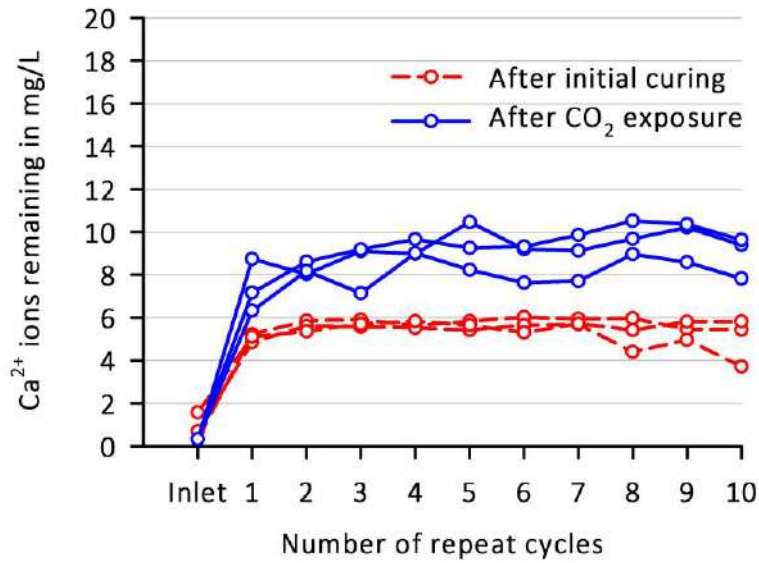


Figure 7.19 Calcium ions remaining in the filtrate obtained through the porous concrete specimens tested using dilute HCl solution, after initial curing as well as after an accelerated carbonation exposure, for ten repeat cycles

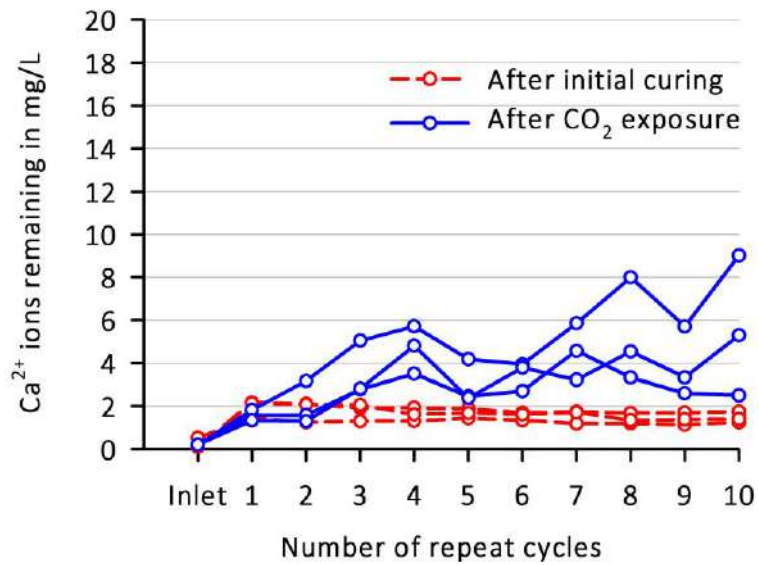
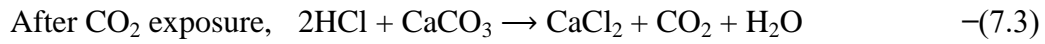
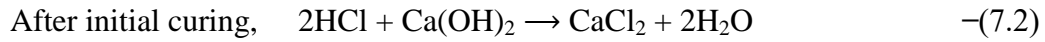


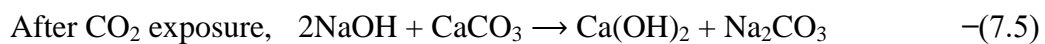
Figure 7.20 Calcium ions remaining in the filtrate obtained through the porous concrete specimens tested using dilute NaOH solution, after initial curing as well as after an accelerated carbonation exposure, for ten repeat cycles

The percolation of dilute HCl solution through the porous cement concrete specimens after initial curing as well as after an accelerated carbonation exposure is likely to form soluble calcium chloride salts as per Equation 7.2 and Equation 7.3.



It can be noticed from the results that the pH of filtrate obtained through the carbonated specimens was found to be decreased than the non-carbonated specimens. This may be due to the formation of H₂CO₃ (carbonic acid) in the filtrate after passage. However, the leaching of calcium ions from the cementitious binder was increased significantly when compared to remaining cases (distilled water, tap water and dilute NaOH solution), which may be due to the aggressiveness of the HCl solution that was used for passage. It is well known that the cementitious matrix is highly prone to attack by a low pH environment (Gutberlet et al. 2015).

In the case of dilute NaOH solution, the porous concrete specimens could have produced calcium based salts as per Equation 7.4 and Equation 7.5.



No salt was formed due to the common-ion effect between the highly soluble Ca(OH)₂ and dilute NaOH solution. The release of portlandite from the cementitious binder had increased the pH and amounts of calcium ions in the filtrate after passage. In the case of carbonated specimens, the calcite compounds may have chemically reacted with the dilute NaOH solution and thus produced calcium hydroxide and sodium carbonate. The solubility of Ca(OH)₂ may have increased the amounts of calcium ions in the filtrate after passage to a level greater than the case with the non-carbonated specimens.

7.4.2 Toxic metal pollutants

Gowd and Govil (2008) have investigated the heavy metals contamination in the surface water bodies situated near Ranipet industrial area, which is a part of Vellore district of Tamil Nadu (India), located in 79°19' – 79°22' E longitude and 12°53' – 12°57' N latitude. The surface water in this area shows very high concentrations of some of the heavy metals like Cr (average of 0.24 mg/L), Cd (0.05 mg/L), Pb (0.45 mg/L), Zn (3.76 mg/L), Cu (0.095 mg/L) and Ni (0.037 mg/L). Central Pollution Control Board of India (CPCB) has classified this area, which is one of the biggest exporting centres of tanned leather in India, as a chronic affected area.

The present study attempted to simulate the above real life environment by preparing aqueous solutions containing Cr^{6+} , Hg^{2+} , Cd^{2+} and Pb^{2+} of 0.97 mg/L, 0.78 mg/L, 2.43 mg/L and 0.87 mg/L concentrations respectively. These solutions were then passed through the porous concrete specimens, which had undergone accelerated carbonation exposure, for ten repeat cycles. Figures 7.21 to 7.24 illustrate the concentrations of these heavy metals remaining in the filtrate after passage.

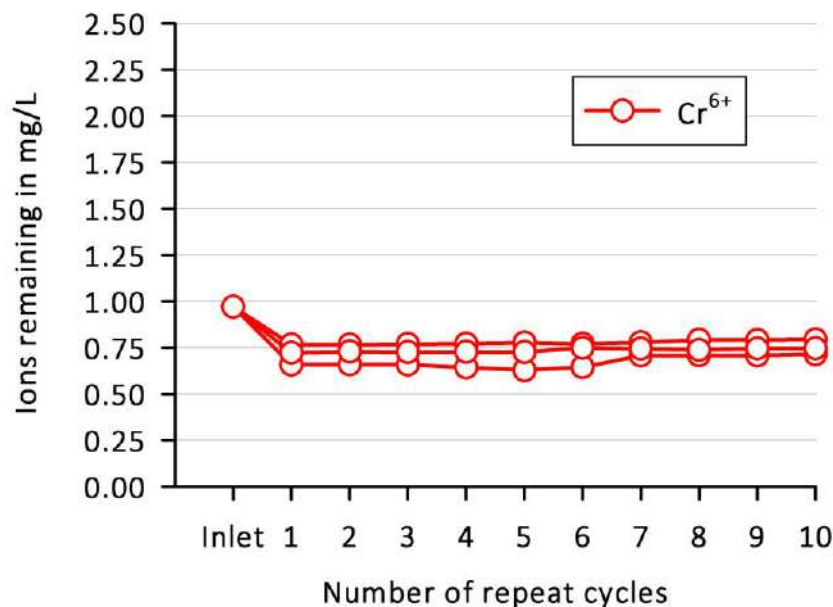


Figure 7.21 Chromium ions remaining in the filtrate obtained through the porous concrete specimens after accelerated carbonation exposure tested using a solution containing potassium dichromate (analytical grade)

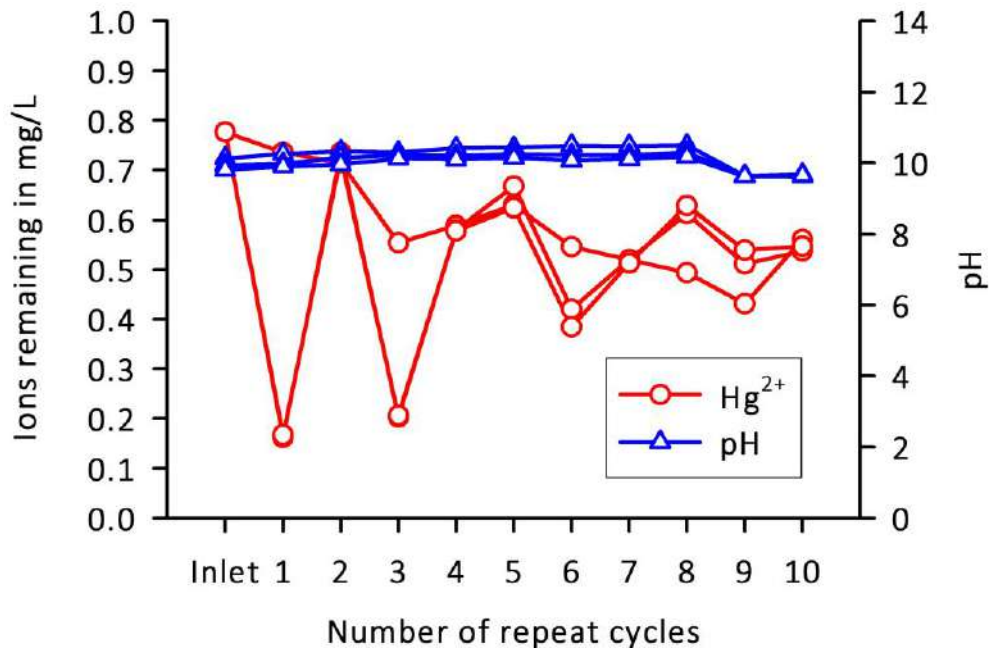


Figure 7.22 pH (of filtrate) and mercury ions remaining in the filtrate obtained through the porous concrete specimens after accelerated carbonation exposure tested using a solution containing mercuric chloride (analytical grade)

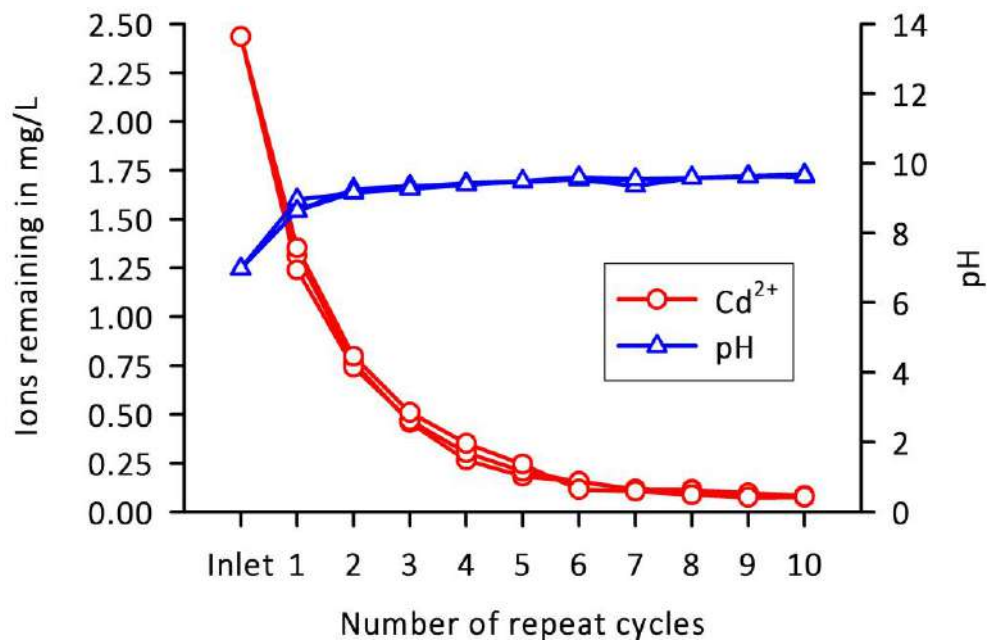


Figure 7.23 pH (of filtrate) and cadmium ions remaining in the filtrate obtained through the porous concrete specimens after accelerated carbonation exposure tested using a solution containing cadmium sulfate (analytical grade)

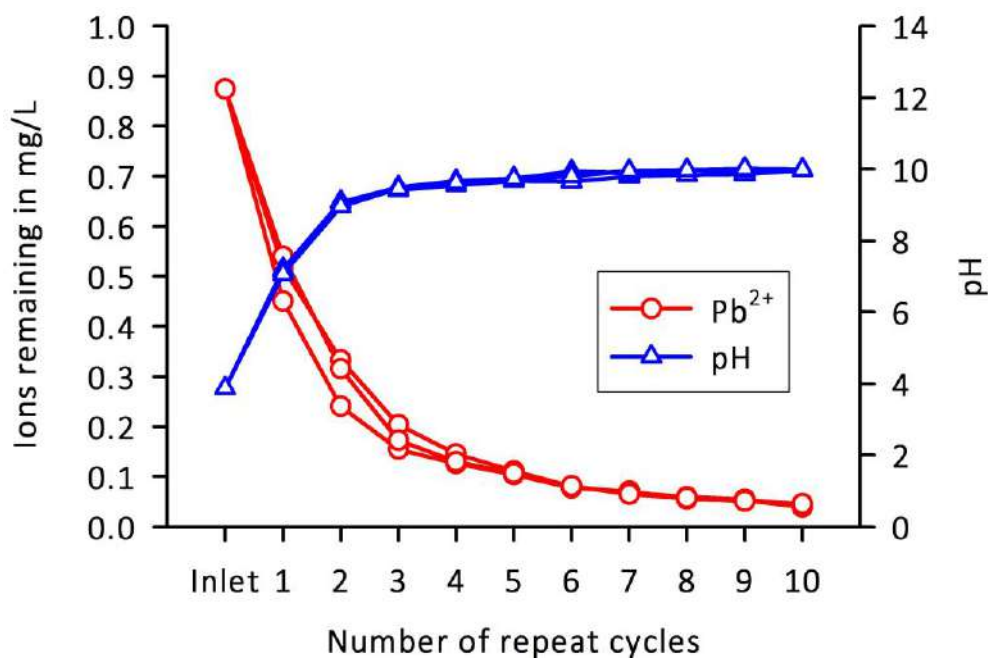


Figure 7.24 pH (of filtrate) and lead ions remaining in the filtrate obtained through the porous concrete specimens after accelerated carbonation exposure tested using a solution containing lead (II) nitrate (analytical grade)

Among the metal pollutants, Pb and Cd were found to be removed significantly by the porous concrete specimens after passage. This removal could be mainly due to the sorption or co-precipitation. Metal carbonates are likely to be formed because of the release of carbonate species from the cementitious binder. This carbonate precipitation should chemically trap the Pb and Cd ions from the aqueous solution. However, Cr and Hg are not known to form stable carbonates and therefore are not likely to be removed by the carbonated porous concretes after passage (Stumm and Morgan 2012).

The removal of Pb and Cd was marginal after the 7th cycle. The pH value (9.53 to 9.95) at such juncture suggests that the residual Pb and Cd ions remaining in the filtrate could exist either in the form of metal carbonates or metal hydroxides. However, these metal complexes were not precipitating further in the porous material which may be due to the concentration of total soluble species in the filtrate after 7th cycle could be lower than their solubility product constants (near 25 °C). These constants are indicated as the level at which a solute dissolves in solution (Stumm and Morgan 2012).

7.4.3 Bentonite clay loading test results

Highly turbid solution containing bentonite clay of initial turbidity 840 NTU was passed through several carbonated porous concrete specimens. Next, the passage of this solution was repeated nine additional times using the same concrete specimens. The percentage (%) decrease in turbidity and the change in the permeability were measured after each passage, and the results are illustrated in Figure 7.25 and Figure 7.26 respectively.

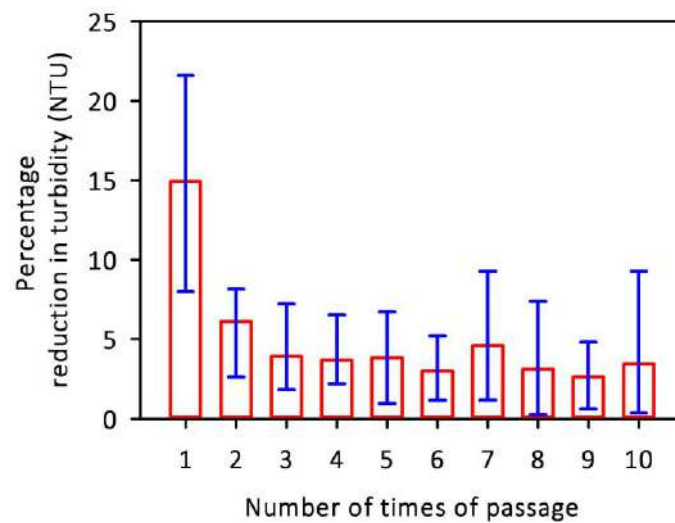


Figure 7.25 Change in the turbidity of bentonite containing solution after percolation through the porous concrete specimen that was reused ten times

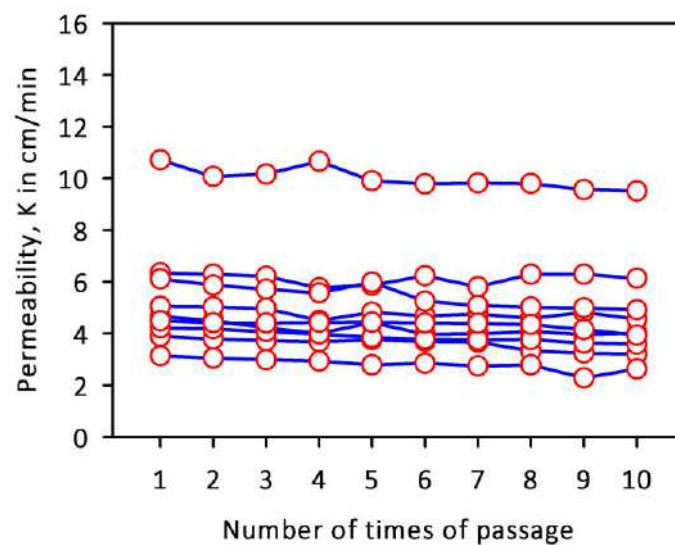


Figure 7.26 Permeability of the porous concrete specimen, measured after each passage of the bentonite containing solution

The turbidity results indicate that the porous concrete could only remove marginal amounts of bentonite clay (suspended particles) from the aqueous solution. This removal could be mainly due to physical trapping of bentonite particles inside the tortuous voids, which is schematically shown in Figure 7.27.

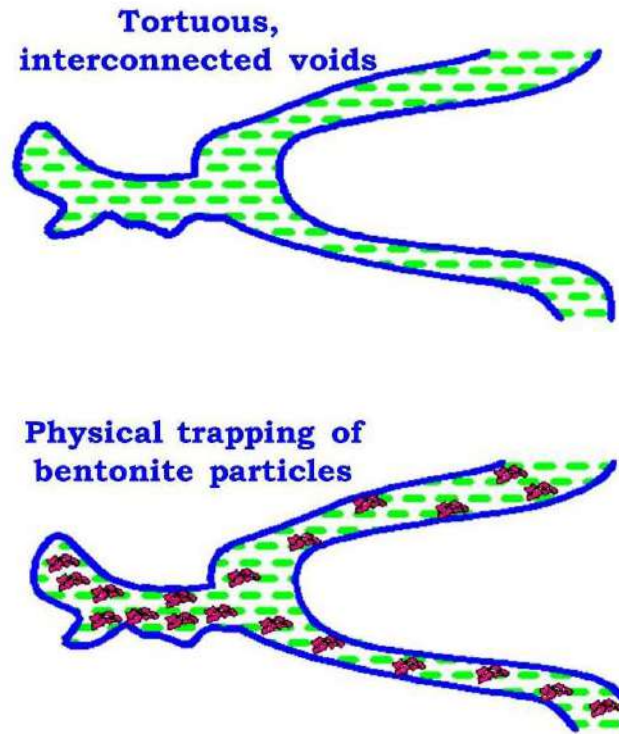


Figure 7.27 Schematic diagram illustrating the bentonite particles that were physically trapped inside the tortuous, interconnected voids of the porous cement concrete

In particular, the removal of clayey particles was higher when the porous concrete was used for the first time rather than when the same concrete was subsequently reused. Bentonite is negatively charged; therefore, its adsorption on the flow channels of porous concrete is retarded by the excess presence of hydroxyl (OH^-) and carbonate (CO_3^{2-}) species.

During the first use of the concrete, it is likely that bentonite adsorbs on the few sites at the concrete surface where such adsorption would be possible despite the presence of hydroxyl ions. Therefore, in the subsequent reuse of the porous concrete, the removal of bentonite clay is further reduced. Trapping of bentonite clay is likely to reduce the permeability of the porous material. However, in this study, the permeability of porous concrete was not affected significantly because of its limited capacity to trap bentonite clay from the aqueous solution.

7.5 SUMMARY

Table 7.1 lists the desirable physical characteristics and metal pollutant levels in drinking water conforming to IS 10500 (2012).

Table 7.1 Characteristics of drinking water conforming to IS 10500 (2012)

Parameter	Permissible limit in mg/L	Remarks
pH	6.5 to 8.5	No relaxation
Turbidity	1 to 5 NTU	No relaxation
Calcium	75	May be extended up to 200
Mercury	0.001	No relaxation
Cadmium	0.003	No relaxation
Lead	0.01	No relaxation
Chromium as Cr ⁶⁺	0.05	No relaxation

The pH of different solutions percolated through the porous concrete was exceeding the desirable limits of drinking water because of the release of Ca(OH)₂ from the cementitious binder. However, the turbidity and calcium ions remaining in the filtrate were found to be within the acceptable levels. These physical changes such as increase in the turbidity and leaching of calcium ions from the surfaces of flow channel were reduced marginally when the porous concrete specimens were exposed to CO₂ environment. The concrete carbonation had transformed the highly soluble Ca(OH)₂ into calcite and thereby reduced the solubility of binder phases that were available in the surface of flow channels of porous concrete. It is well known that the solubility of Ca(OH)₂ is much higher than the dissolution of CaCO₃ in water (Stumm and Morgan 2012).

Heavy metals including Pb and Cd were removed significantly by the porous concrete because of carbonate precipitation. The concentration of these metal ions in the filtrate (after 10th cycle) was marginally exceeding the acceptable limits in drinking water. However, this

removal mechanism (carbonate precipitation) was not favourable in the case of Cr and Hg ions from the aqueous solution after passage.

The porous concrete based water filtration system was able to remove the heavy metals more effectively compared to the removal of negatively charged bentonite clay, which is primarily due to the abundance of negatively charged species inside the cementitious matrix. The deposition of sediments in the flow channels of porous concrete is likely to affect the permeability of water. In this study, the permeability of porous concrete was not reduced because of its lesser capacity to physically trap the bentonite clay from the aqueous solution.

CHAPTER 8

EFFECT OF REDUCED GRAPHENE OXIDE ON THE FILTRATION PERFORMANCE OF POROUS CONCRETE

8.1 INTRODUCTION

In the present study, a novel concept of applying nanotechnology in porous concrete for the removal of heavy metals from aqueous solutions was attempted. Graphene, a strong adsorbent, was added into the porous concrete. It was shown in Chapter 7 that heavy metals such as lead (Pb) and cadmium (Cd) were trapped significantly by the carbonate and hydroxide species that were available in the surfaces of flow channel of porous concrete. In the case of graphene modified porous concrete, it was hypothesized that the presence of negatively charged graphene sheets, CO_3^{2-} (carbonate) and OH^- (hydroxide) species in the surfaces of flow channel may physically and chemically trap the metal cations from the aqueous solution, as is schematically illustrated in Figure 8.1.

Based on Environmental Protection Act 1986, the Central Pollution Control Board (CPCB) of India has specified that the maximum concentration of lead (Pb^{2+}) that can be discharged from the industries should not exceed 1 mg/L. Mahish et al. (2015) showed that the highest lead discharge from a petrochemical industry of Raipur city (Latitude 21°24' North and Longitude 81°63' East), Chhattisgarh, India was 11.58 mg/L. In this study, an aqueous solution having lead concentration of 8 mg/L was passed through the non-carbonated and carbonated specimens of control and graphene modified porous concretes under continuous flow for a period of one hour. In the case of plain porous concretes, after initial curing as well as after an accelerated carbonation exposure, the CO_3^{2-} and OH^- species could chemically react with the lead (II) nitrate solution and thereby precipitate as lead hydroxide and lead carbonate respectively, which is schematically shown in Figure 8.2. The results of this study are presented in the current chapter, which also compares the filtration efficiency and material cost of porous concrete with the existing water filtration methods such as activated carbon, ion exchange, reverse osmosis, and distillation. It also proposes a low cost concrete based water filtration arrangement which can filter the heavy metals effectively from industrial effluents.

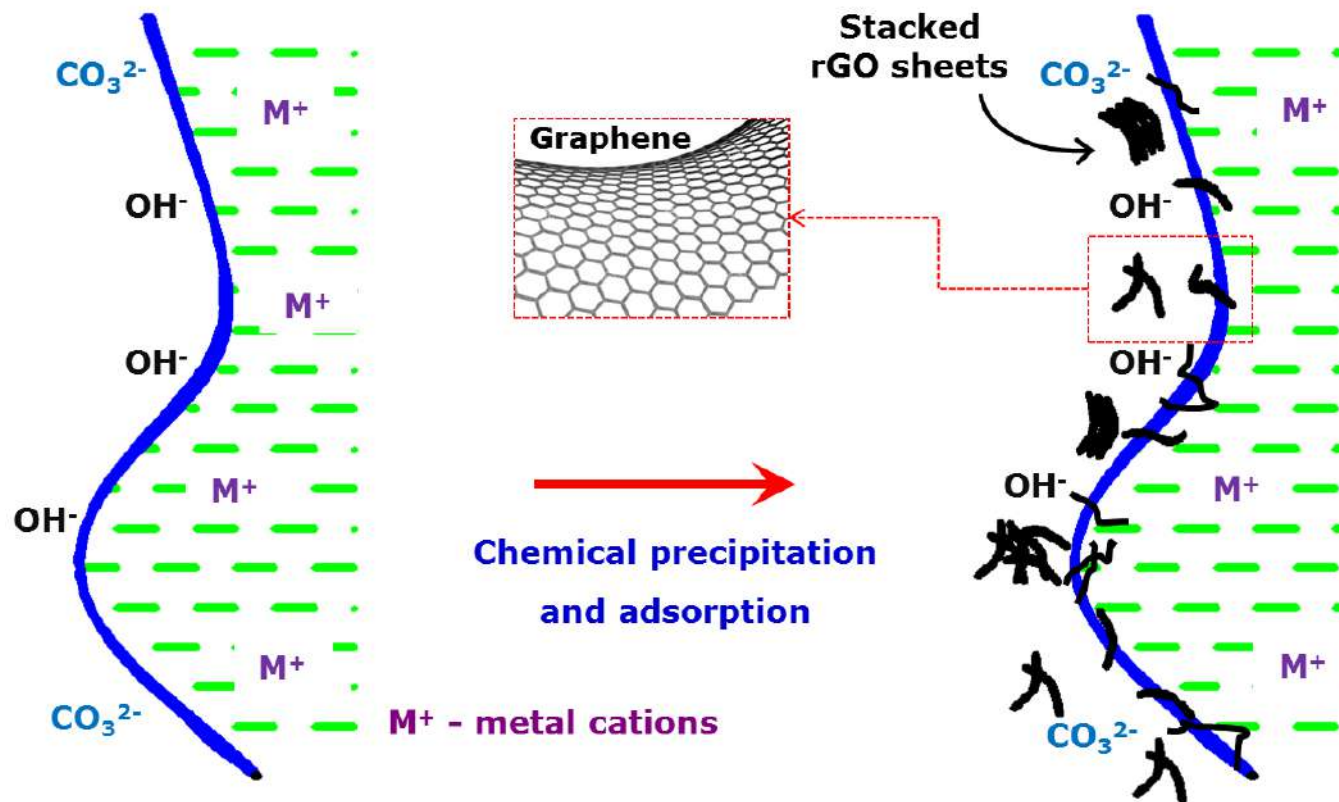


Figure 8.1 Schematic illustration of the presence of graphene nanosheets, carbonate and hydroxyl species along the flow channels of porous cement concrete

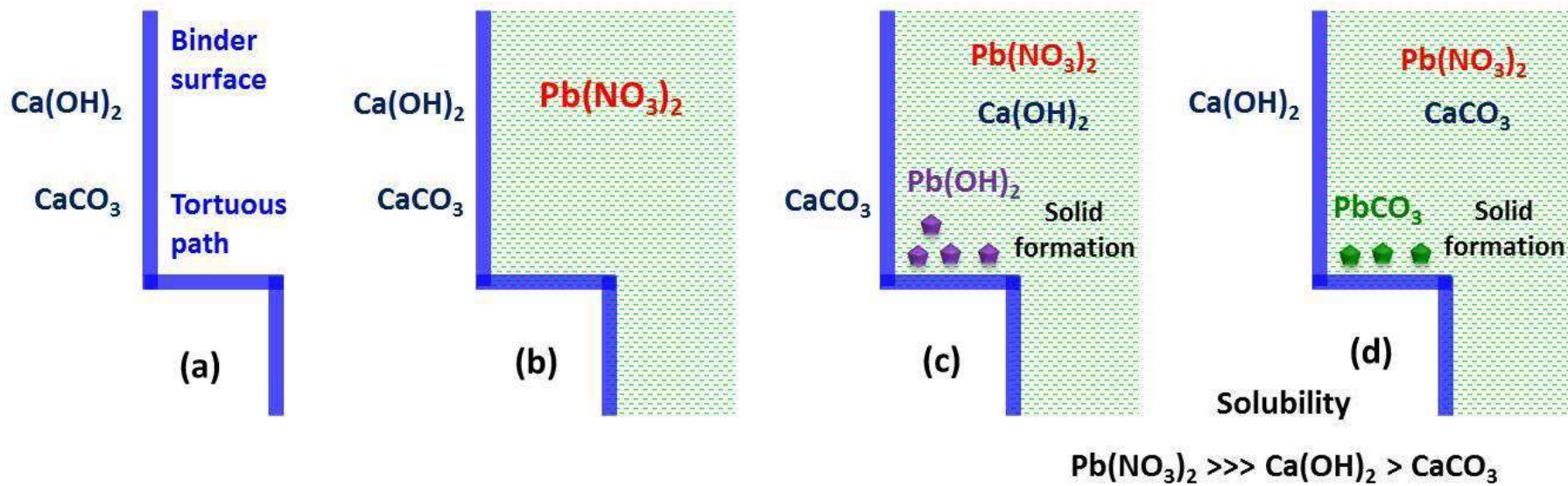


Figure 8.2 Schematic illustration of the lead removal by porous concrete: (a) Presence of Ca(OH)_2 and CaCO_3 on the pore channel surfaces (b-d) passage of $\text{Pb(NO}_3)_2$ solution through the flow channels results in the precipitation of lead hydroxide and lead carbonate

Desorption of chemically trapped heavy metal from such porous concretes was also analysed by passing the distilled water through the tested specimens mounted on the falling head permeability set up, which is shown in the section 6.3.1. This investigation was expected to help in assessing the binding capacity of metal precipitate on the concrete surfaces after passage.

8.2 SPECIMEN PREPARATION

The preparation procedure of plain porous concrete specimens of size 100×200 mm ($\phi \times H$) was discussed in detail in Chapter 6. In the case of graphene modified porous concrete, the solution containing 0.06 wt% nanosheets, distilled water (w/c ratio 0.32) and 0.5 wt% PCE was added to the concrete ingredients (53 grade Portland cement and aggregate). Prior to mixing, this solution was sonicated for 30 minutes using probe sonicator and thus nanosheets could be dispersed better within the cementitious matrix. The photographs in Figure 8.3 illustrate the sonication process of graphene containing solution and the freshly prepared concrete mixture modified using such a solution.



Figure 8.3 Sonication was done to the solution containing graphene using Sonics VCX-750 Vibra Cell Ultra Sonic Processor model probe sonicator (left image) and freshly prepared graphene modified porous concrete mixture (right image)

The freshly prepared concrete mixture, blended with black coloured reduced graphene oxide (rGO), was noticed to be of dark grey colour. Next, cylindrical specimens were cast using this mixture, demolded and cured in water for 7 days. Subsequently, some of the cured specimens

of size 100 × 150 mm (ø × H) were air-dried at 25 °C, 65% R.H. for a period of 14 days and then introduced into the carbonation chamber set at 25 °C, 65% R.H. and 1% CO₂ concentration for 56 days, as per the procedure mentioned in Chapter 7. Micrographs illustrating the reactive binder surface in the porous concrete after initial curing as well as after an accelerated carbonation exposure, shown in Figure 8.4 and Figure 8.5.

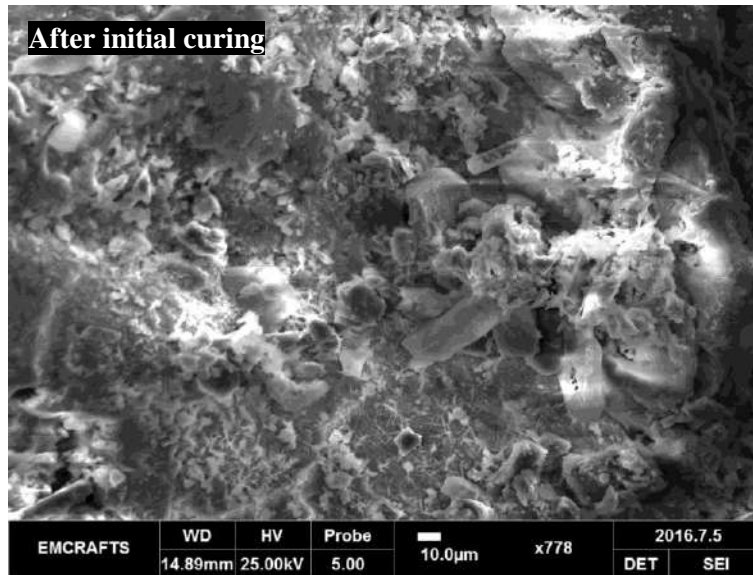


Figure 8.4 Micrograph illustrating the binder surface in the 7-day cured porous cement concrete

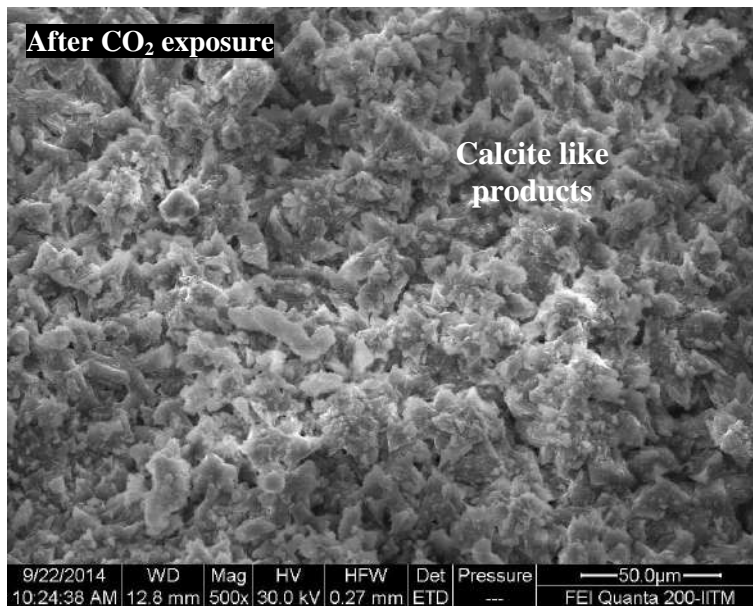


Figure 8.5 Micrograph illustrating the binder surface in the porous cement concrete after accelerated carbonation exposure

In this chapter, the plain and graphene modified porous concrete specimens are designated as Control and RGO respectively.

8.3 CONSTANT HEAD PERMEABILITY TEST

Lead containing solution of 8 mg/L concentration was prepared using lead (II) nitrate salts and then stored in a reservoir having flow control arrangement. This solution was passed under gravity through the Control and RGO specimens mounted in the permeability set up for a period of 60 minutes. A constant head of 30 cm was maintained over the concrete specimen for the whole testing period by precisely regulating the flow control valve of the solution reservoir. This is schematically illustrated in Figure 8.6.

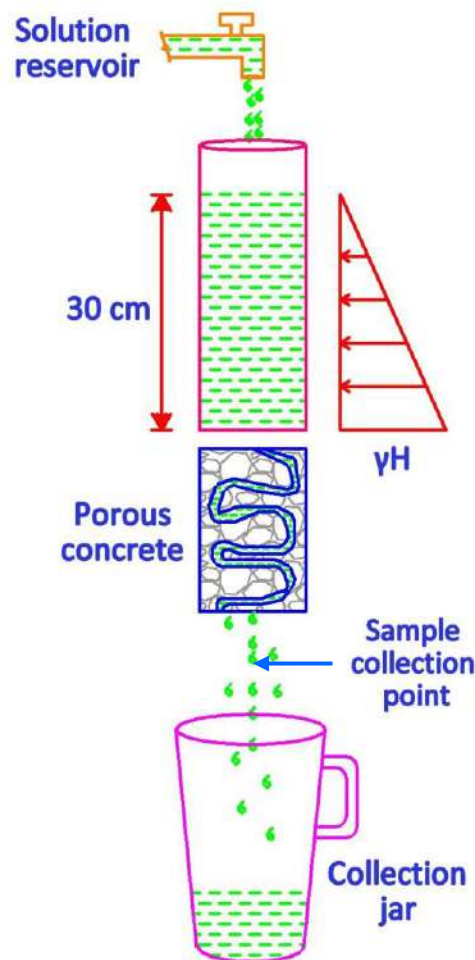


Figure 8.6 Constant head permeability testing of porous concrete

A small amount of filtrate (~ 15 ml) was collected at every 3 minutes and the remaining was collected in the plastic jar that was kept below the concrete specimen. The amounts of lead ions remaining in the collected filtrate was analysed using inductively coupled plasma mass spectrometry (ICP-MS). This procedure was once again repeated on the same concrete specimen by replacing the lead containing solution with distilled water, which was done to study the amounts of lead ions that are likely to be desorbed because of the possibly weak interaction between the heavy metal (Pb^{2+}) and the reactive binder surfaces.

8.4 RESULTS AND DISCUSSION

8.4.1 Effect of reduced graphene oxide on the lead removal

Lead containing solution (~ 8 mg/L) and subsequently distilled water was passed through the plain and RGO specimens (of two each) after initial curing as well as after an accelerated carbonation exposure. Figures 8.7 to 8.10 illustrate the amounts of Pb remaining in their filtrate after passage through the porous concrete specimens.

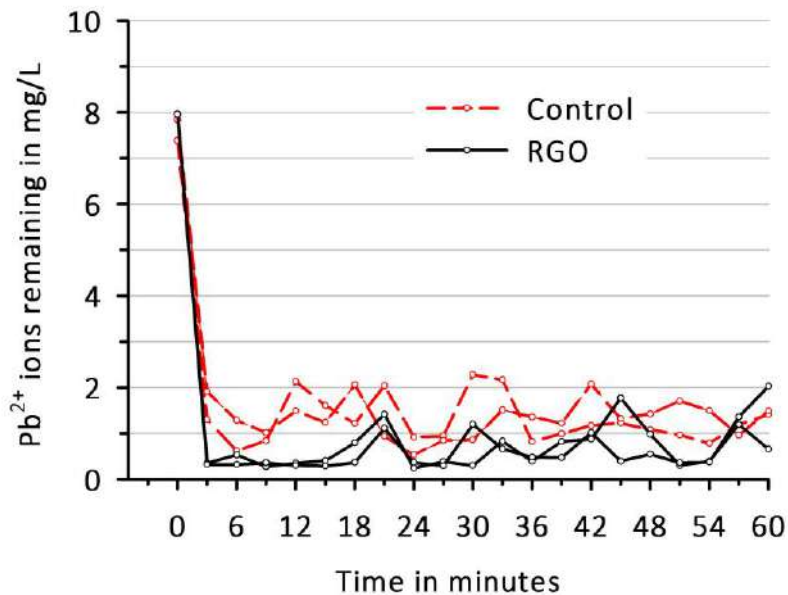


Figure 8.7 Lead ions remaining in the filtrate after passage of $Pb(NO_3)_2$ solution through the 7-day cured control and RGO specimens maintained with a constant head of 30 cm

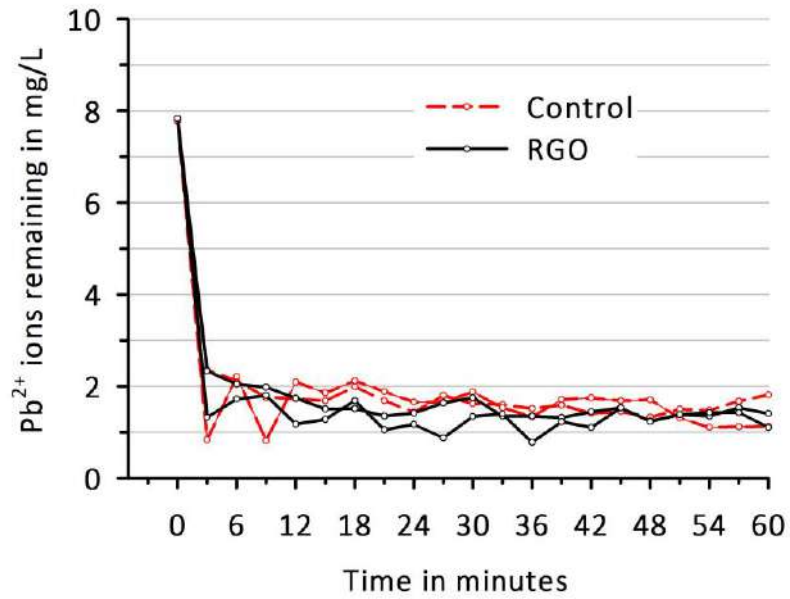


Figure 8.8 Lead ions remaining in the filtrate after passage of $Pb(NO_3)_2$ solution through the carbonated control and RGO specimens maintained with a constant head of 30 cm

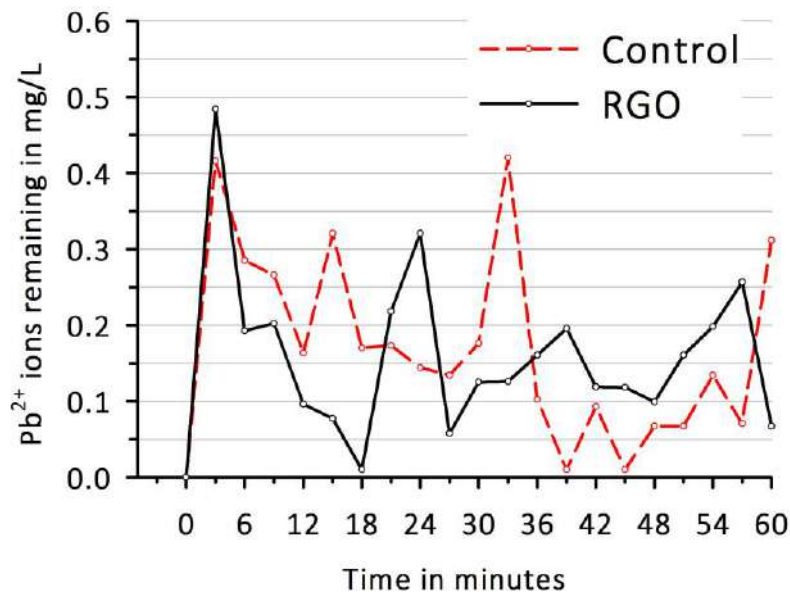


Figure 8.9 Lead ions desorbed in the filtrate after subsequent passage of distilled water through the 7-day cured control and RGO porous concrete specimens maintained with a constant head of 30 cm

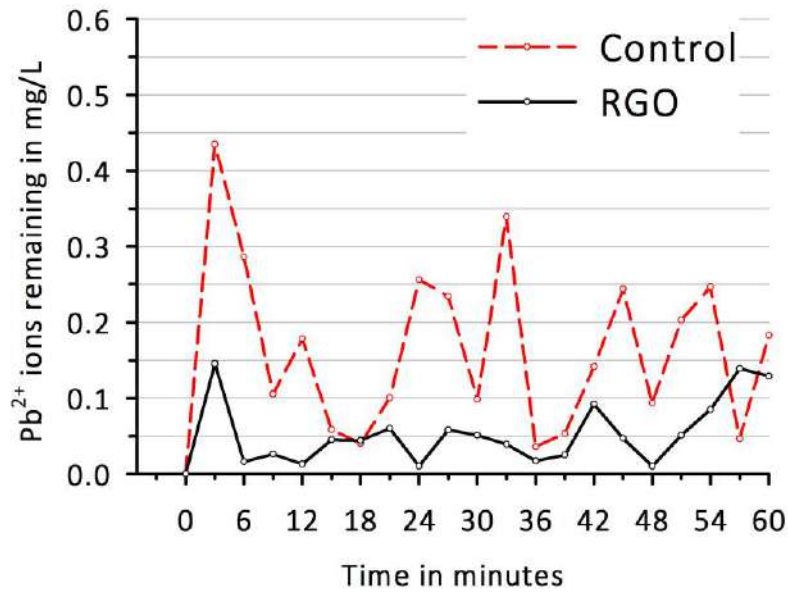


Figure 8.10 Lead ions desorbed in the filtrate after subsequent passage of distilled water through the carbonated control and RGO porous concrete specimens maintained with a constant head of 30 cm

It can be noticed from the results (Figures 8.7 and 8.8) that substantial amounts of Pb were trapped in the flow channels of the plain and RGO specimens after passage, regardless of its exposure condition. The removal of Pb by the porous concretes was nearly 6-fold, after initial curing as well as after an accelerated carbonation exposure. This change remained constant through the whole testing period of 60 minutes. However, the addition of 0.06 wt% graphene in porous concrete had no strong influence on the Pb removal, which may be due to the presence of lesser amounts of nanosheets at the reactive surface in the flow channels.

The subsequent passage of distilled water through the plain and RGO specimens (of one number each) caused minimal disturbance of the Pb precipitates, and therefore, desorption of the bound ions (Pb^{2+}) from the porous material was insignificant. This minute desorption suggests that the Pb precipitates were strongly bound to the binder surface and thereby the subsequent use of porous concretes could be encouraged. It also reduces the risk of secondary pollution that is likely to occur when such concretes are disposed after its effective use.

8.4.2 Effect of hydraulic retention time on the lead removal

As per IS 10500 (2012), the maximum permissible limit of Pb in the drinking water is 0.01 mg/L. It can be seen from the column test results that the porous concretes tested with higher constant head could remove the heavy metal (Pb^{2+}) significantly from the aqueous solution. However, the Pb remaining in the filtrate was still beyond the acceptable limit. This filtrate containing residual lead is designated as ‘first filtrate’ in this chapter.

To reach the desirable limit, the first filtrate was passed through a fresh set of porous concrete specimens (of one number each) maintained with two constant heads such as 30 cm (H) and 7.5 cm (H/4), and the test results are illustrated in Figures 8.11 to 8.14. This attempt is likely to increase the hydraulic retention time and thereby more amounts of heavy metal (Pb^{2+}) may get entrapped in the flow channels of porous concrete.

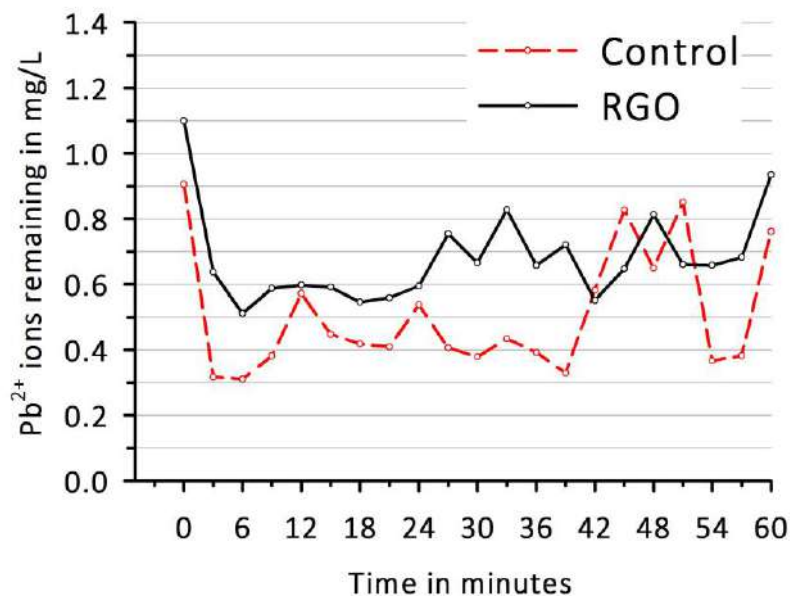


Figure 8.11 Lead ions remaining in the filtrate after passage of first filtrate through the 7-day cured control and RGO porous cement concrete specimens maintained with a constant head of 30 cm

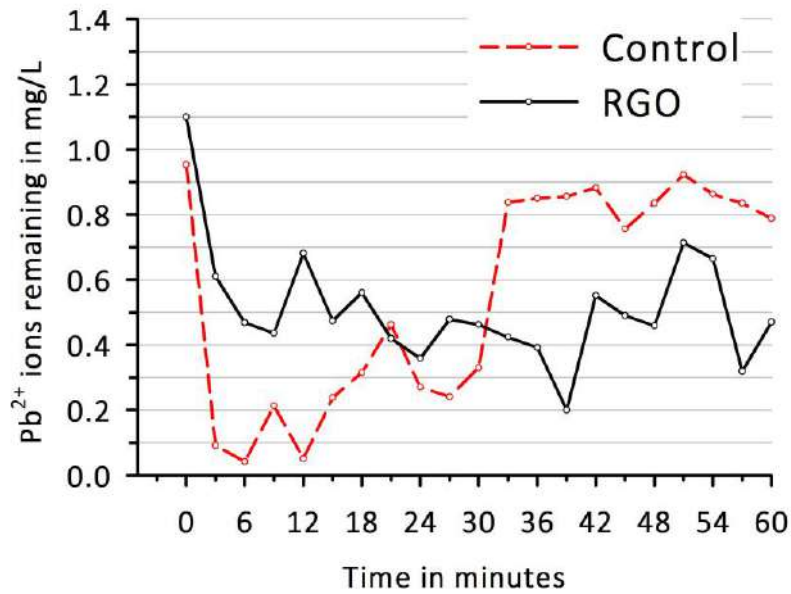


Figure 8.12 Lead ions remaining in the filtrate after passage of first filtrate through the carbonated control and RGO porous cement concrete specimens tested with a constant head of 30 cm

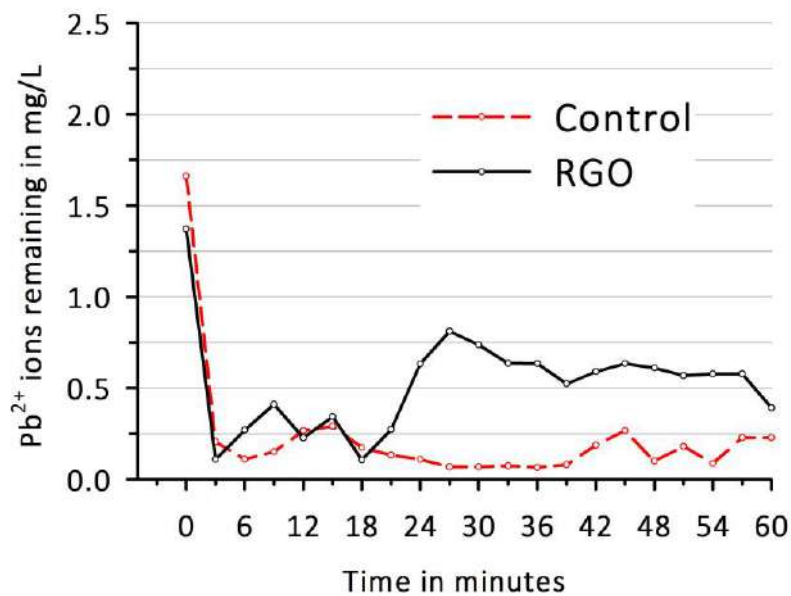


Figure 8.13 Lead ions remaining in the filtrate after passage of first filtrate through the 7-day cured control and RGO porous concrete specimens tested with a constant head of 7.5 cm

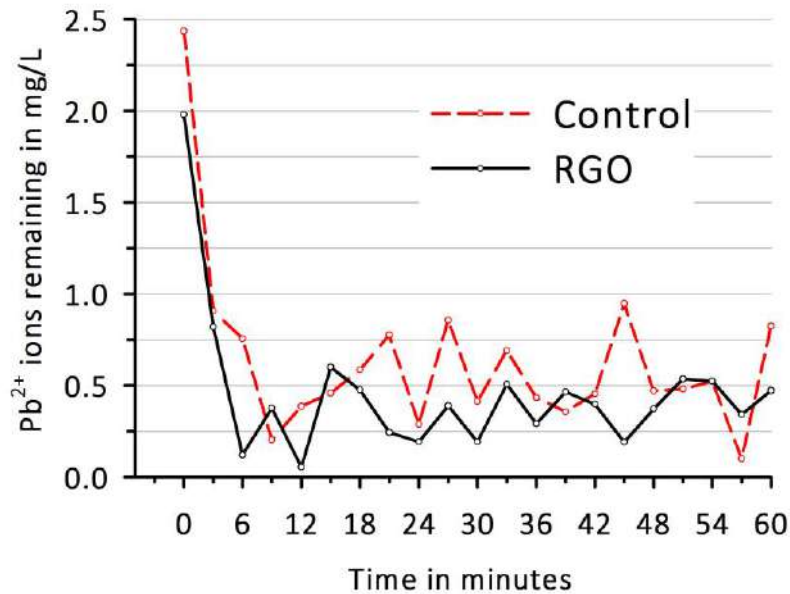


Figure 8.14 Lead ions remaining in the filtrate after passage of first filtrate through the carbonated control and RGO porous cement concrete specimens tested with a constant head of 7.5 cm

The porous concretes tested with 7.5 cm constant head were noticed to remove the Pb significantly compared to the concrete specimens tested with 30 cm constant head. The decrease in constant head is likely to increase the residence time of the metal cations to chemically bind with the hydroxyl and carbonate species of the cementitious binder. Further, the decrease in constant head may also reduce the pressure on the lead precipitates and thereby leaching of freshly bound Pb ions could be lesser. The flow rates through the porous concrete specimens maintained with 30 cm (H) and 7.5 cm (H/4) head were determined to be 350 mL/min and 280 mL/min; these fall safely within the range of slow sand filters used in wastewater treatment plants.

The lead ion concentration remaining in the filtrate of the porous concretes tested with 7.5 cm constant head was still found to be greater than the acceptable limits (0.01 mg/L). Hence, this filtrate was designated as ‘second filtrate’ which was further passed through a fresh set of porous concrete specimens tested with a trickling head of aqueous solution. The test results of this passage are illustrated in Figure 8.15 and Figure 8.16.

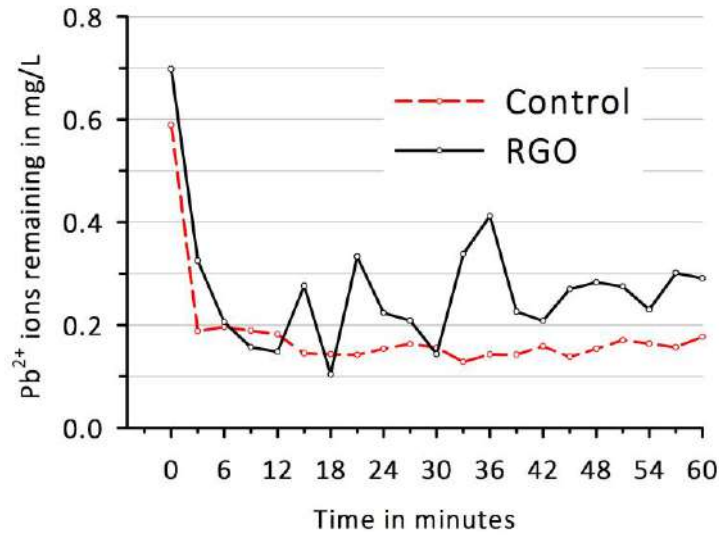


Figure 8.15 Lead ions remaining in the filtrate after passage of second filtrate through the 7-day cured control and RGO specimens tested with a trickling head of aqueous solution

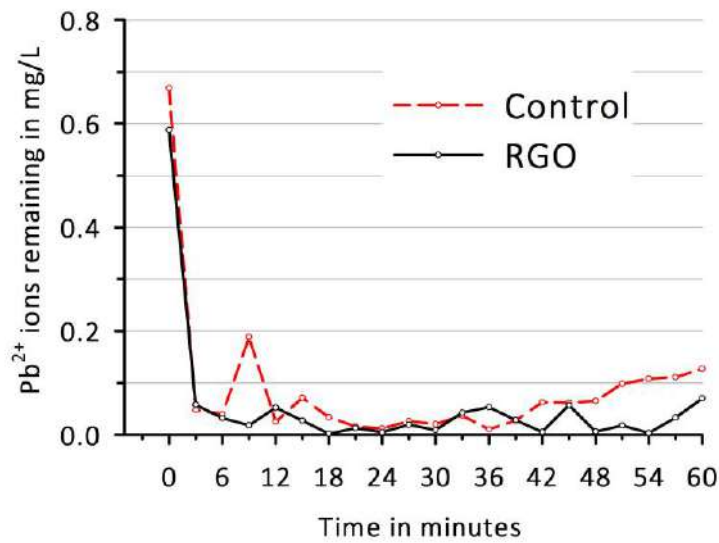


Figure 8.16 Lead ions remaining in the filtrate after passage of second filtrate through the carbonated control and RGO specimens tested with a trickling head of aqueous solution

It can be seen from the experimental results that the porous concretes maintained with a trickling head of water had further reduced the amounts of Pb in the aqueous solution after passage which could be mainly due to the increase in hydraulic retention time (residence time). The filtrate from this passage is designated as ‘third filtrate’ in this chapter. The Pb

concentration in the third filtrate was found to be only marginally higher than the desirable limits.

8.5 PROPOSED DESIGN AND COST ESTIMATE OF CONCRETE BASED WATER FILTRATION SYSTEM FOR HEAVY METALS REMOVAL

This section covers the design and likely field execution of concrete based water filtration system to remove the heavy metals from industrial effluents. Next, the cost estimate of such arrangement is also discussed.

8.5.1 Design and execution of concrete based water filtration system to filter the heavy metals from industrial effluents

Porous concrete was found to remove the heavy metal (Pb^{2+}) effectively from aqueous solutions. However, its filtration performance was mainly dependent on the hydraulic retention time (residence time). The experimental results from this chapter showed that the dilute solutions containing heavy metal (Pb^{2+}) could be filtered efficiently when a trickling head of water was maintained. This increases the contact time and thereby enhances the formation of Pb precipitates. The leaching of freshly bound chemical precipitates could also be reduced when lesser head of water was maintained over the porous concrete.

The experimental findings from the previous section were used as input to design the porous concrete based water filtration arrangement, which is illustrated in Figure 8.17. Three individual porous concrete cylinders of size 100×150 mm ($\phi \times H$) were arranged in series with progressively decreasing levels of hydraulic head such as 30 cm, 7.5 cm and 0 cm. Aqueous solution having Pb concentration of 8 mg/L was passed through these concretes under continuous flow for a period of one hour. This arrangement consisting of three porous concrete cylindrical specimens was able to retain 98% of Pb from the aqueous solution and the filtrate reached close to the acceptable limits of drinking water (0.01 mg/L). Similar amounts of Pb could also be retained when a plain and graphene modified porous concrete specimens of size 100×150 mm was maintained with a trickling head of lead containing solution. Aqueous solution having lead concentration of 9.4 mg/L was passed through this specimen under continuous flow for 8 hours and the concentration of Pb remaining in the filtrate was analysed, and the results are illustrated in Figure 8.18 and Figure 8.19.

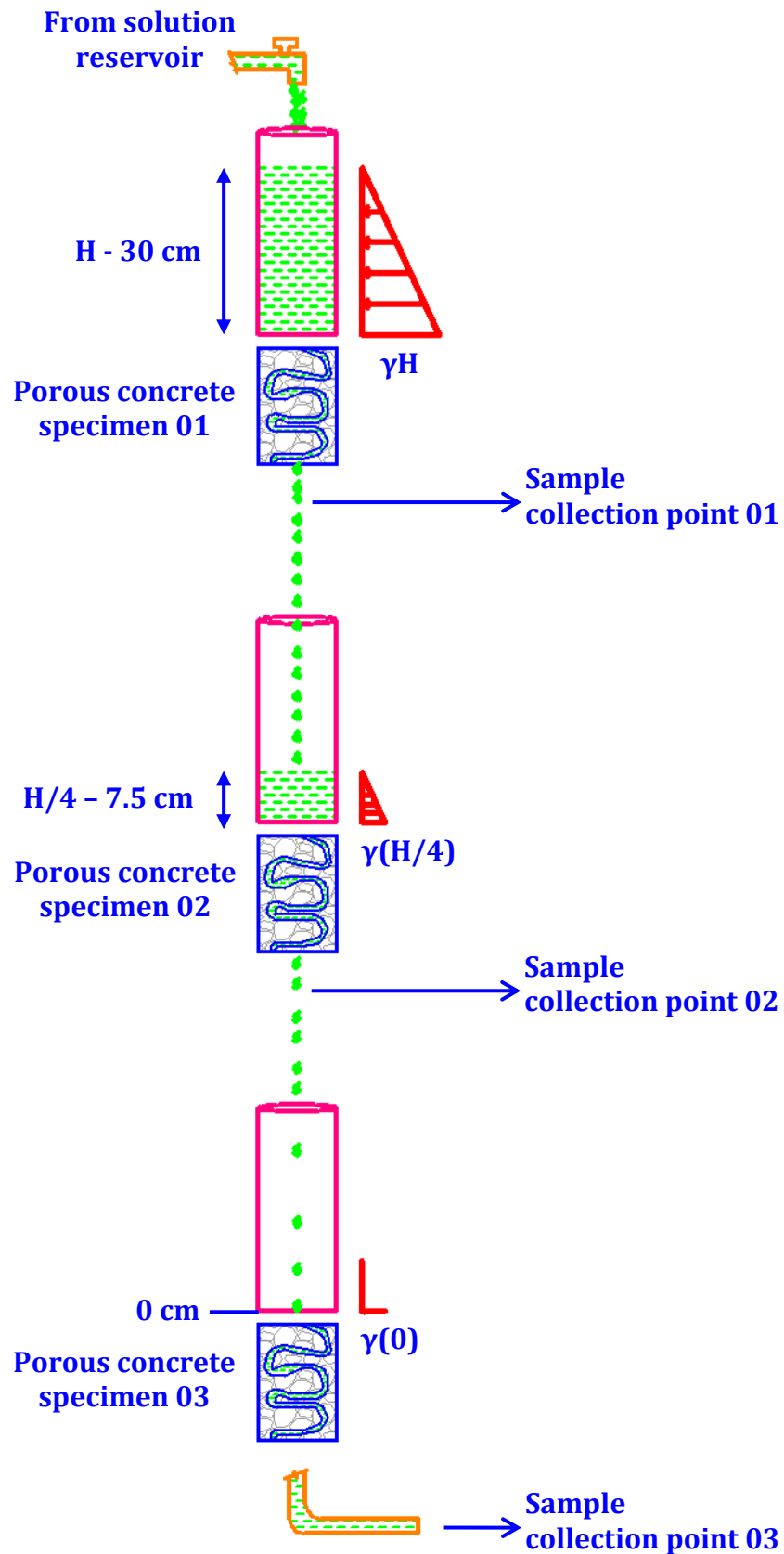


Figure 8.17 Filtration arrangement illustrating the series of porous concretes with decreasing levels of hydraulic head for the purpose of removing heavy metals from aqueous solutions

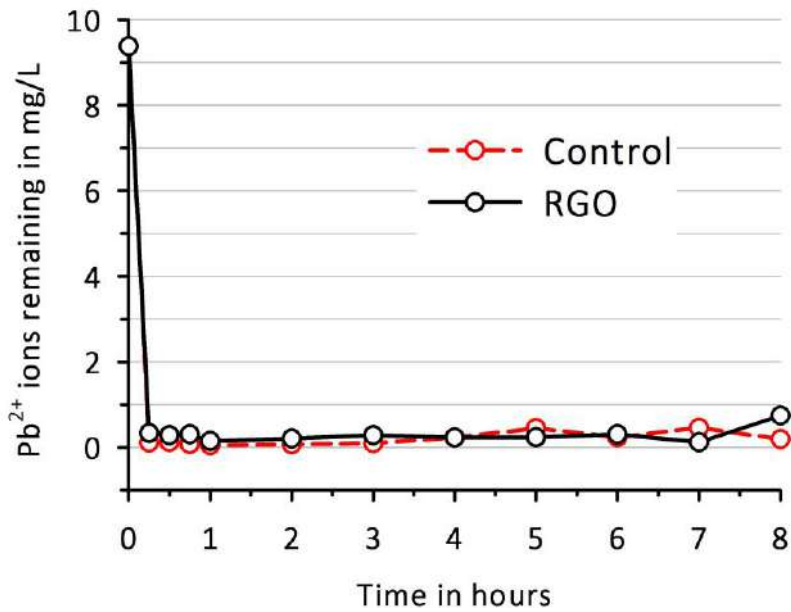


Figure 8.18 Lead ions remaining in the filtrate after passage of solution having lead concentrations of 9.4 mg/L through the 7-day cured control and RGO porous concrete specimens maintained with a trickling head of solution

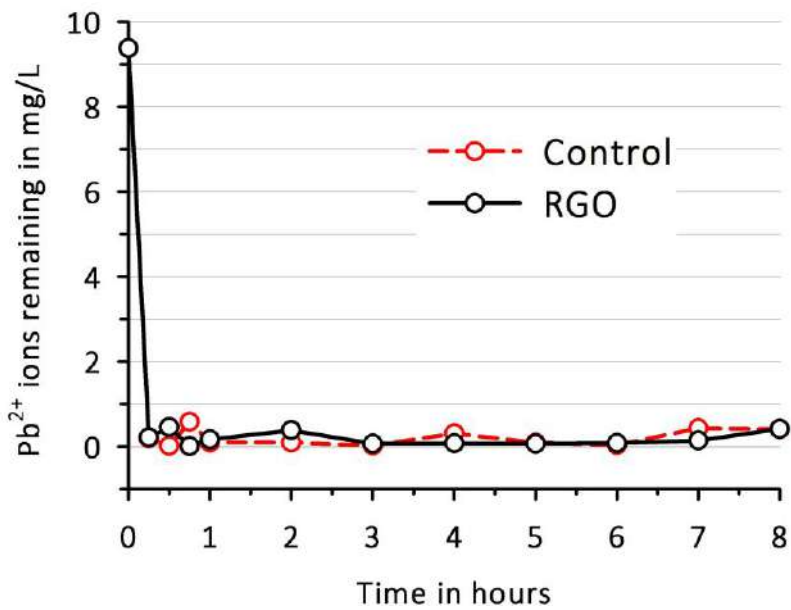


Figure 8.19 Lead ions remaining in the filtrate after passage of solution having Pb concentrations of 9.4 mg/L through the carbonated control and RGO porous concrete specimens maintained with a trickling head of solution

Substantial amounts of Pb from the aqueous solution were trapped by the non-carbonated and carbonated specimens when a trickling head of aqueous solution was maintained. Further,

this removal had remained consistent for the whole testing period of 8 hours. This result suggests that the surfaces of flow channel may have significant amounts of OH^- and CO_3^{2-} species, which thereby retain the heavy metal consistently from the aqueous solution after passage.

The volume of flow channels in the three-stage porous concrete based filtration system is much greater than in a single porous concrete maintained with a trickling head of aqueous solution, which implies an abundance of OH^- and CO_3^{2-} species in the former. Additionally, the choice of using the three stage filtration system is better because the metal cations that are not trapped by the first concrete are likely to get removed either in the second or third concrete in the filtration arrangement.

The filtration arrangement, as illustrated in Figure 8.17, was comprised of three numbers of porous concretes (of size 100×150 mm) having decreasing levels of hydraulic head such as 30 cm, 7.5 cm and 0 cm. The quantity of filtrate that could be collected from such concretes for one hour was measured as 27.5 L, 18.33 L and 0.24 L. Porous concrete could filter the heavy metal (Pb^{2+}) substantially from the industrial effluent. However, the trapping of suspended particles was only marginal. The materials used to prepare the porous concrete are relatively inexpensive and locally available. This concrete mixture can be molded into the required shape and structure and is also easy to fabricate. Lead is used in several industries as a pure metal, alloyed with other metals, or in the form of chemical compounds. The major industries discharging lead are illustrated in Figure 8.20.

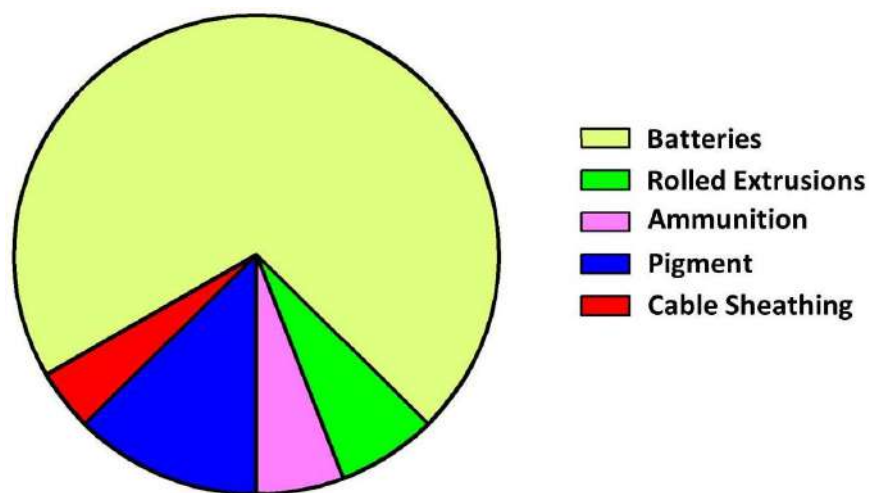


Figure 8.20 Industries that are major sources of lead containing effluents

(<http://www.gravitatechnomech.com/Lead-Metal/usesofLead.html>)

The discharge of Pb from these sources in an untreated manner can lead to the contamination of ground water. The porous concrete based water filtration system can treat such effluents and thereby treated water can be discharged into the environment or can be reused. Figure 8.21 schematically illustrates the layout of a treatment process which can effectively filter the heavy metals from the industrial effluent.

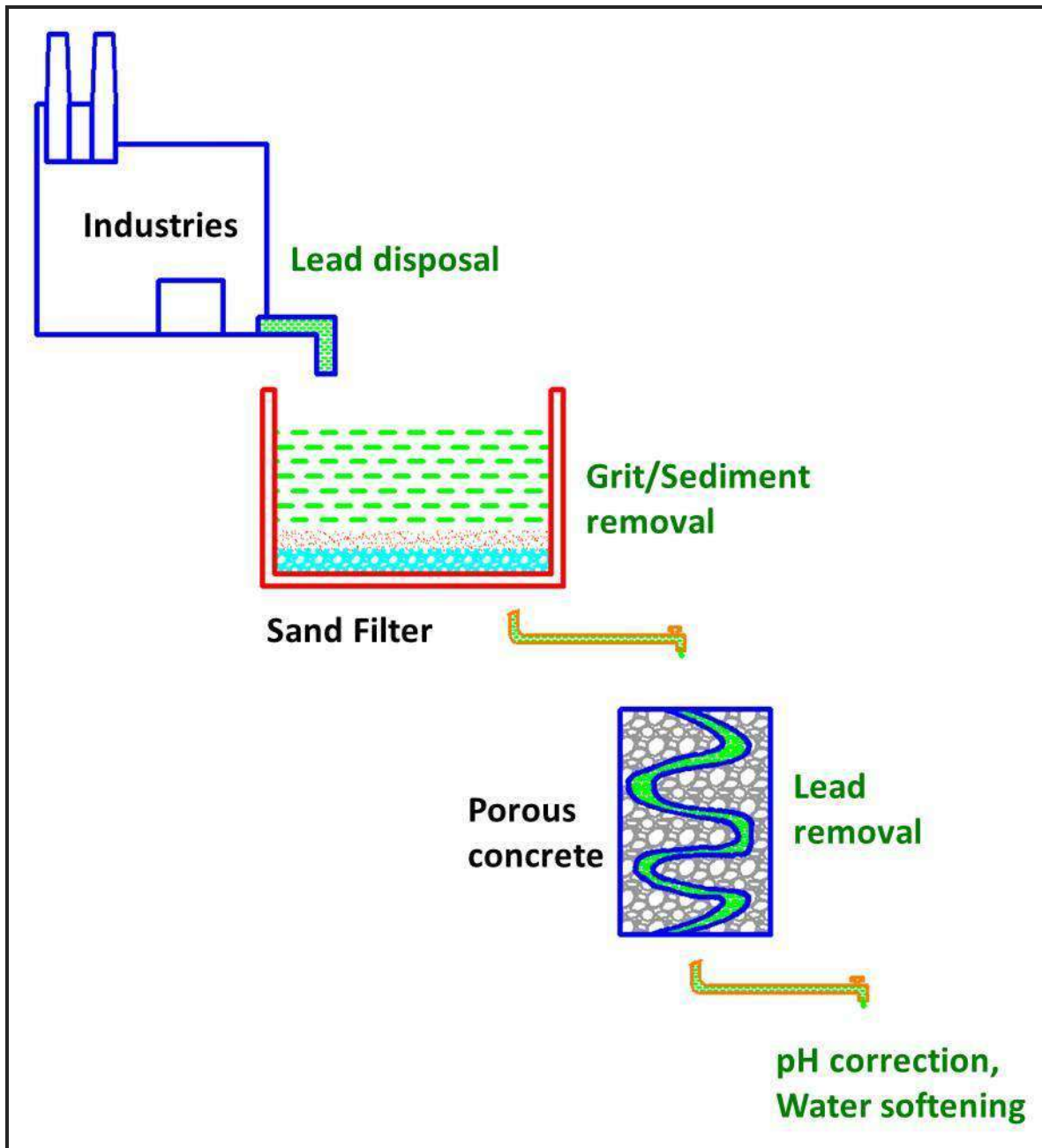


Figure 8.21 Schematic illustration of the treatment process which is proposed to filter the heavy metals and suspended particles from the industrial effluent

This treatment process combining sand filter and porous concrete can be proposed to the heavy industries that are disposing lead (Pb^{2+}) into the surface and ground water reserves in an untreated manner. Sand filter and porous concrete can retain the suspended particles and heavy metal (Pb^{2+}) respectively and thereby treated water, which may be alkaline in nature, is obtained. This alkalinity can be reduced by adding sodium carbonate (soda ash). Additionally, the increase in pH can also be controlled by carbonation of the porous concrete. The leaching of calcium ions may increase the hardness of water and thereby such hard water can be made soft by ion/cation exchange technique. However, a significant reduction in leaching can be brought about by the use of Reduced Graphene Oxide (rGO) in the porous concrete. The installation of sand filter is likely to decrease the problem of sediments blockage in the porous concrete. However, future studies are required to evaluate the service life and reusability of porous concrete, and its filtration performance over longer durations. These investigations on the porous concrete would help in proposing it as a potential candidate for treating the heavy metals, especially lead (Pb^{2+}) from the industrial effluents.

8.5.2 Cost estimation of plain and graphene modified porous concrete

The cost of reduced graphene oxide (synthesized by modified Hummers' method) from a leading manufacturer (United Nanotech Innovations Private Limited, India) is found to be ₹ 8115 per 50 grams. Table 8.1 lists the cost of materials that were used in the preparation of cylindrical graphene modified porous cement concrete specimen of size 100×200 mm ($\phi \times H$), which has a volume of 0.00157 m^3 .

Table 8.1 Estimation of material cost of 0.06 wt% graphene modified cylindrical porous cement concrete specimen

Volume of specimen	0.00157 m^3	Cost in INR
Cement	695 g	₹ 4.4
Crushed stone	2789 g	₹1.6
Water	219 g	₹ 0.1
Superplasticizer	4 g	₹ 0.3
Reduced graphene oxide	0.42 g	₹ 162.3
Total cost		₹ 168.7

The cost involved in mixing the ingredients of plain and graphene modified porous concrete mixtures using a laboratory concrete mixer was excluded. The material costs of plain and 0.06 wt% graphene modified porous concretes were calculated as ₹ 6.4 and ₹ 168.7, which suggests that the incorporation of graphene had increased the material cost of rGO modified porous concrete by 26.4 times than the plain porous concrete.

Furthermore, the operation cost involved in the uptake of CO₂ by those specimens was calculated from the following data:

- The repeat cycle permeability test results from Chapter 7 had showed that the concrete carbonation could help in decreasing the pH and turbidity of aqueous solutions after passage. A Carbonation Chamber of 600 litres capacity, running at 32 Amps and 440 Volts (VAC) was used for carbonating the specimens. The specimens were kept inside this chamber for 56 days at 1% CO₂, 25 °C and 65% R.H. The net volume of concrete specimens that can be accommodated inside the chamber is 500 litres.
- Tariff rate of electrical power as approved by the Tamil Nadu Electricity Regulatory Commission, Tamil Nadu, India (in effect from July 2010 - present), for Educational Institutions is ₹ 4.8 per Kilowatt-hour. The carbonation chamber set at 1% CO₂, 25 °C and 65% R.H was found to consume an electrical power of 338 Kilowatt-hour per day. The cost of this consumed electrical power was calculated as ₹ 1622.4 (338 Kilowatt-hour × ₹ 4.8). The quantity of CO₂ gas consumed by the chamber for such specified condition per day was observed to be 1.6 kg (equivalent) and its consumption cost was calculated as ₹ 27.4.
- Total cost involved to carbonate 500 litres of porous concrete using accelerated carbonation method (1% CO₂, 25 °C and 65% R.H.) per day is the sum of cost of electrical power and cost of CO₂ gas consumed, which is ₹ 1649.8 (₹ 1622.4 + ₹ 27.4).

The cost involved in the uptake of CO₂ by the plain porous concrete specimen of size 100 × 200 mm (ø × H) having a volume of 1.57 litres can be thus calculated as ₹ 5.2 per day. In this study, the specimen was kept inside the carbonation chamber for 56 days and thereby the operation cost was ₹ 291.2.

Table 8.2 summarizes the cost of filtration arrangement that was comprised of three numbers of porous concretes exposed to accelerated CO₂ environment.

The operation cost involved in the uptake of CO₂ had increased the cost of filtration arrangement comprising of three numbers of 7-day cured porous concretes by 46.5 times. The experimental results had suggested that the addition of graphene had no strong influence on the performance of filtration arrangement. However, their addition may enhance the mechanical and durability properties of porous concrete, particularly the resistance to leaching.

Table 8.2 Cost of filtration arrangement comprising of three numbers of porous concretes (of 0.00157 m³) exposed to accelerated CO₂ environment

Sl.No	Filtration material	Number of stages	0.06 wt% rGO	CO ₂ exposure	Total Cost in INR
1	Plain porous concrete after curing for 7 days	3	✗	✗	₹ 19.2
2	Plain porous concrete after curing for 7 days	3	✗	✓	₹ 892.8
3	Graphene modified porous concrete after curing for 7 days	3	✓	✗	₹ 506.1
4	Graphene modified porous concrete after curing for 7 days	3	✓	✓	₹ 1379.7

Table 8.3 lists the material cost, estimated filter life, lead removal capacity and flow rate of porous concrete and the commercially available water filtration methods that can be used to trap the heavy metals from aqueous solutions. Out of these filtration methods, the better one in terms of cost and performance could not be easily pointed out because of lesser amount of details that were covered in such table.

Majersky (2008) reported that the service life of porous cement concrete block that could treat the acid mine drainage significantly was estimated to be 2 to 4 months. This may be similar when porous concretes are tested with aqueous solutions containing Pb²⁺, which are acidic in nature. The service life and filtration efficiency of reverse osmosis is reported to be better than the remaining filtration methods such as activated carbon, ion exchange using natural zeolite, and the proposed three stage carbonated porous cement concrete. However, the major drawbacks of the reverse osmosis are its high energy consumption and cost.

Table 8.3 Details of commercially available filtration methods with the porous cement concrete that was proposed in this study

Filtration methods	Estimated life	Flow rate	Pb²⁺ Loading	Pb²⁺ Uptake	Cost (INR)	Remarks
Granular activated carbon	1 to 6 months ^[1]	-	50 mg/L (Asuquo et al. 2017)	81%	₹ 900 / kg ^[2]	<ul style="list-style-type: none"> • It is easy to operate, removes bad taste and odour • The disadvantages are it is expensive, needs to be replaced periodically
Ion exchange using natural zeolite	2 years ^[3]	-	100 mg/L (Kim et al. 2013)	93%	₹ 450 / kg ^[4]	<ul style="list-style-type: none"> • It can remove the inorganic pollutants effectively • The biological pollutants are not removed
Reverse osmosis	10 years ^[5]	78.6 litres / hour ^[6]	-	98%	₹ 10000 / unit ^[7]	<ul style="list-style-type: none"> • It can desalinate the sea water, and can remove the bacteria and viruses • It requires high energy and removes the nutrient minerals from the water
Three stage porous cement concrete	2 - 4 months (Majersky 2008)	0.24 litres / hour	8 mg/L	96.5% to 98%	₹ 892 / unit	<ul style="list-style-type: none"> • It is easy to fabricate, cheap and can remove the heavy metals such as lead, cadmium, zinc and copper effectively • Its operation can fail due to pore blockages

[1] http://www.watertreatmentguide.com/activated_carbon_filtration.htm [2] <http://www.amazon.in/Activated-Carbon-Pellets-Aquarium-Filter/dp/B002VXE82K>

[3] <http://www.zeocem.com> [4] <https://www.zauba.com/export-ZEOLITE+POWDER-hs-code.html>

[5] <http://www.freedrinkingwater.com/support/questions-answers-discussions/what-is-the-average-life-time-of-your-reverse-osmosis-system>

[6] <http://www.filterwater.com/c-36-commercial-reverse-osmosis.aspx> [7] <https://www.snapdeal.com/product/aquaguard-enhance-green-ro-water/635854472530>

Similar to reverse osmosis, porous concretes were able to trap the heavy metal (Pb^{2+}) from aqueous solutions. However, their cost, maintenance period and service life can vary. Next to these filtration methods, activated carbon and natural zeolite could be the potential candidates in treating the industrial effluents. Ion exchange method is commonly used to filter the heavy metals from the effluents. This method is preferred by the industries in place of activated carbon because of its high service life and less maintenance cost.

8.6 SUMMARY

It can be seen from the experimental results that the plain and RGO specimens had removed the Pb significantly from the aqueous solution. The addition of 0.06 wt% graphene in porous concrete had no strong influence on the removal of Pb from the aqueous solution. The proposed hypothesis that was earlier mentioned in the case of graphene modified porous concrete may remain possible only when the surfaces of flow channel in the porous material are largely occupied with graphene nanosheets. Possibly, at the low concentrations of graphene used in the system, this does not occur. In other words, better approaches to incorporation of graphene in the flow channels need to be worked out. Nevertheless, the increased resistance to leaching provided by rGO modified concrete would make the quality of the filtered water better. It was found that the chemically trapped metal cations (Pb^{2+}) on the surfaces of flow channel could be desorbed only marginally with the subsequent passage of distilled water. This indicates the reliability of the filtration system.

The experimental findings suggest that the hydraulic retention time is likely to influence filtration of heavy metals using porous cement concrete. The present study had suggested a low cost filtration arrangement consisting of three porous concrete specimens to filter the heavy metals significantly from the aqueous solution. A combination of sand filter and porous cement concrete can effectively treat the lead containing industrial effluents discharged from various industries like battery manufacturing, metal plating, soldering, paint and pigment producing and oil refining.

CHAPTER 9

CONCLUSIONS

9.1 SUMMARY OF THE PROJECT WORK

Heavy metal contamination in water is a growing problem worldwide, which is due to urban growth and rapid industrialisation. The major drawbacks that affect the practice of using conventional treatment methods such as adsorption, precipitation, ion exchange and reverse osmosis are high initial capital cost, operational and maintenance costs. These drawbacks could be resolved by developing new methods and materials for water filtration, which could be made of inexpensive and locally available ingredients.

The present study led to the development of a concrete based water filtration system which could trap the heavy metals, especially lead (Pb) substantially from simulated effluents. This porous concrete was designed to have controlled levels of hydraulic conductivity similar to the sand filters that are used in water and wastewater treatment plants. Further, it was noticed that the quality of the filtered water could be enhanced when such proposed filtration system was exposed to accelerated carbonation for a period of 56 days at 1% CO₂, 25 °C and 65% R.H. The net effect of carbonation is a reduction in the pH of the cementitious matrix, which causes depassivation of the rebars. However, this seemingly negative effect can potentially be used in a positive manner with respect to the passage of polluted water through the porous concrete, because of the expected reduction in the leaching.

The leachability characteristics were assessed by passing tap water, distilled water, dilute HCl and NaOH solutions through the 7-day cured and carbonated pervious concrete specimens. The results suggest that concrete carbonation had decreased the propensity for calcium leaching during the filtration process. Furthermore, the turbidity of the filtrates was also lower for the pervious concrete system exposed to accelerated carbonation environment. Nevertheless, in both systems (normal and carbonated), the turbidity and Ca²⁺ ions remaining in the filtrates were within the acceptable levels.

A novel attempt of applying nanotechnology in porous concrete for the removal of heavy metals from aqueous solutions was investigated. Graphene, a strong adsorbent, was added

into the porous cement concrete in an attempt to improve its pollutant removal characteristics. The effect of 0.06 wt% reduced graphene oxide (rGO) on the filtration performance of porous cement concrete was investigated by passing Pb containing solution under continuous head for a period of 60 minutes. Prior to its use in porous concrete, the influence of rGO on the properties of Portland cement paste was investigated in comparison to alumina and silica nanoparticles. One mix was kept as control whereas the remaining three mixes were added with rGO, alumina and silica nanoparticles at concentrations of 0.02%, 0.2% and 4% by weight of cement respectively and thereby such mixes were designated as Control, RGO, Al₂O₃ and SiO₂ in the present study. All these pastes were prepared using the w/c ratio and PCE content of 0.32 and 0.05 wt% respectively.

The addition of rGO in cement paste had refined the pore structure and thereby increased the mechanical strengths. This suggests that the rGO addition at 0.06 wt% concentration could also enhance the strength of porous cement concrete. The binder phases in such porous systems are expected to deteriorate due to the passage of Pb containing solution, which is acidic in nature. To investigate the role of rGO in such aggressive conditions, the influence of rGO, alumina and silica nanoparticles on the deterioration characteristics of 28-day cured cementitious pastes after storage in 0.5 M HNO₃ solution for a period of 56 days were analysed at different time periods using various characterisation techniques like SEM/EDS, XRD, TGA, FTIR, MIP, OM, X-ray CT and nanoindentation. It was noticed from the porosimetry result that the porosity of rGO paste was comparatively less than the control paste after storage in 0.5 M HNO₃ solution for a period of 28 days. With this investigation, it can be suggested that the presence of rGO in porous concrete may contribute in resisting the calcium leaching which occurs due to the subsequent passage of acidic solution.

Up to 98% of Pb was retained by the filtration experiment comprising of three numbers of porous concrete specimens that were arranged in series with progressively decreasing levels of water head such as H (stage 1), H/4 (stage 2) and trickling head (stage 3). However, the presence of marginal amount of rGO in porous concrete system had no strong influence in the binding of Pb from aqueous solutions. The hydraulic retention time played a crucial role in achieving this significant removal of Pb from aqueous solutions. Similar amount of Pb was retained in both the porous concrete systems, which were tested right after initial curing as well as after an accelerated carbonation exposure. The material cost and time required to treat 1000 litres of Pb containing influent by 88% (only in stage 1) were calculated as ₹ 238 and 36

hours. The results of the study demonstrate that the low cost porous concrete treatment system can be a potential candidate in treating the industrial effluents.

9.2 SPECIFIC CONCLUSIONS

9.2.1 Effect of graphene, alumina and silica nanoparticles on the properties of Portland cement paste

- The mini slump test results showed that the spread of graphene, alumina and silica modified pastes was decreased up to 13%, 11% and 24% compared to the control paste respectively, which may be due to the adsorption of maximum amounts of water by those nanomaterials that are having higher surface area to volume ratio. However, the 7-day compressive and flexural strengths of the nanomaterials modified pastes had increased up to 20%, 32%, 45% and 70%, 104%, 118% than the control paste for graphene, alumina and silica modified pastes respectively.
- It can be noticed from the porosimetry results that the amounts of gel pores (< 10 nm) in the RGO, Al₂O₃ and SiO₂ pastes had increased up to 37%, 152% and 119% than the 28-day cured control paste respectively. This suggests that the addition of graphene, alumina and silica nanoparticles could have increased the production of C-S-H gel because of their ability to promote nucleation.
- The addition of graphene had decreased the amounts of capillary pores (10 nm to 10 μm) in OPC paste up to 32% than the 28-day cured cementitious paste, which may be due to the refinement of such pores by the presence of 2-dimensional nanosheets in the matrix.
- The 3-dimensional image analysis of the X-ray CT scans of the pastes indicated that the addition of graphene, nano alumina and nano silica had decreased the amounts of entrapped air voids (of size 0.25 mm to 0.95 mm) up to 57%, 38% and 36% than the 28-day cured control paste. Particularly, the refinement of voids (of size > 0.25 mm) in RGO paste was found higher than in the remaining mixes.

9.2.2 Effect of graphene, alumina and silica nanoparticles on the deterioration characteristics of Portland cement paste exposed to acidic environment

- The addition of graphene, alumina and silica nanoparticles resulted in lesser increase in the capillary porosity compared to the control paste after storage in acidic solution, which was deduced from the porosimetry results. In particular, the presence of graphene and nano alumina had substantially decreased the amounts of capillary pores up to 46% and 51% than the control paste (t+28) respectively.
- Digital photographs and the images acquired from optical microscopy (OM), X-ray CT and SEM were found useful in delineating the degraded layer in the cementitious matrix after storage in 0.5 M HNO₃ solution for a period of 28 days. In particular, the 3-D CT technique proved effective in illustrating the degree of degradation in the t+28 pastes. More than three brown rings could be noticed in the cut section of t+28 pastes, which were imaged using optical microscopy. The EDS (line scan) results suggested that the degraded layer was occupied with iron and silica based precipitates.
- Acid attack on cement paste is characterised by the presence of a degraded layer surrounding the unaffected material. The nanoindentation results indicated that the Young's modulus and hardness of degraded layer had decreased up to 91% and 93% respectively than the unaffected material in the control paste after 28 days of leaching.
- The formation of calcium based salts in the degraded layer of paste specimens was analysed using SEM/EDS. The t+28 control paste was noticed to be occupied with calcite deposits which could be mainly due to natural carbonation, while in the case of Al₂O₃ and SiO₂ pastes (t+28), the degraded layer was deposited with calcium silicate and thaumasite-like minerals respectively. Evidence of thaumasite-like deposits was noticed in the degraded layer of RGO pastes (t+56). The carbonate bearing phases could have formed because of the atmospheric exposure of the paste sections after removal from the acidic solution.

9.2.3 Design of porous concrete having controlled levels of hydraulic conductivity

- Based on trial and error, a porous concrete system having permeability of 7.98 ± 3.83 cm/min, which is in the desired range for water filtration purposes, was developed. The

filtration rate of this concrete was found to be similar to the sand filters that are used in water treatment plants.

- The 2-dimensional image analysis technique was used to determine the size of voids (from X-ray CT images) inside the porous concrete specimen of size 40×100 mm ($\phi \times H$). The size range of voids in this porous concrete was found to fall within $126 \mu\text{m}$ to 14.8 mm and its compressive strength and density was determined to be 22.96 ± 1.76 MPa and 2155 ± 29 kg/m³ respectively.

9.2.4 Effect of carbonation on the characteristics of water percolated through the porous cement concrete

- Alterations in the physical characteristics of water (pH, turbidity and calcium ions remaining in the filtrate) after passage through the porous concrete were reduced when the concrete was exposed to accelerated CO₂ environment (at 1% CO₂, 25 °C, 65% R.H. for 56 days) prior to the water filtration study. In particular, the pH of distilled water had increased from 6.9 to 11.5 after passage through the porous concrete specimens after initial curing, but after carbonation, the pH was increased only up to 10.
- The pH of tap water, distilled water, diluted HCl and NaOH solutions percolated through the porous concrete was exceeding the desirable limits of drinking water because of the release of Ca(OH)₂ from the cementitious binder. However, the turbidity and calcium ions remaining in the filtrate were found to be within the IS 10500 (2012) acceptable levels. In the case of the carbonated systems, the reduced propensity for leaching of the carbonates (as opposed to hydroxides) led to a lowering of the pH of the outlet water.
- After ten repeat cycles, the toxic heavy metals such as Pb and Cd were removed up to 95% and 97% by the carbonated porous concrete specimens because of metal carbonate precipitation. This chemical trapping mechanism (carbonate precipitation) was found to be not favourable in the case of Cr and Hg from aqueous solutions after passage.

9.2.5 Effect of reduced graphene oxide on the filtration performance of concrete based water filtration system

- Plain and RGO modified porous concrete specimens maintained with a hydraulic head of 30 cm were able to remove nearly 82% of heavy metal (lead) from the aqueous solution. However, the addition of 0.06 wt% graphene in porous concrete had no strong influence on the lead removal, which may be due to the presence of lesser amounts of nanosheets at the surfaces of the flow channels.
- The experimental findings suggest that the hydraulic retention time is likely to influence the concentration of heavy metals that are required to be filtered using porous cement concrete. The cost of materials used in the preparation of cylindrical porous concrete having size of 100 × 200 mm ($\phi \times H$) exposed to accelerated CO₂ environment was determined to be ₹ 892 (13.6 USD). The results from the present study were used to formulate an inexpensive water filtration arrangement consisting of three numbers of cylindrical porous concretes of size 100 × 150 mm ($\phi \times H$), which could trap 98% of heavy metal (Pb²⁺) from the aqueous solution after passage.

9.3 MAJOR CONTRIBUTIONS FROM THIS STUDY

- A better understanding of the influence of graphene, alumina and silica nanoparticles on the deterioration characteristics of OPC (ordinary Portland cement) paste exposed to aggressive (acidic) environment was developed in the present study. Alterations in the pore structure of cementitious matrix modified using these nanomaterials were comprehensively studied using a combination of mercury porosimetry and image analysis technique, which are significant contributions to the existing literature.
- The preparation procedure of laboratory based cylindrical shaped porous concrete specimen that was suggested in this study, could act as guideline to obtain controlled levels of permeability in such porous concretes. Apart from this, the present study has shown that accelerated carbonation can decrease the propensity for leaching of binder phases from the porous concrete. This application of accelerated carbonation in the concrete based water filtration system can also lead the way to a new means of CO₂ uptake from the environment.

- The addition of rGO in porous concrete for the removal of heavy metals was attempted in this study. The application of nanotechnology in porous concrete for water filtration is a completely new field of study. The operation of plain porous concrete could be cost effective and can be a potential benefit to industrial wastewater treatment.

9.4 RECOMMENDATIONS FOR FURTHER STUDY

- In the present study, the filtration of Pb (heavy metal) through pervious concrete was investigated for 8 hours. However, further investigation is required to determine the filtration performance of porous cement concrete over longer durations. Apart from this, investigation on the safe removal of chemically trapped heavy metals can add value to the concrete's utility for treatment of industrial effluents. This desorption addresses the recyclability challenge related to contaminant-saturated concrete-based water filter and the associated risk of secondary pollution. The effective service life of such concrete filters can be determined by investigating the filtration and deterioration characteristics over longer durations. An attempt of making porous concrete based water filter using construction and demolition waste can open up new challenges and opportunities.
- The addition of rGO into porous concrete had not improved the filtration performance in this study. This may change when the surfaces of flow channels in porous concrete are largely occupied with graphene nanosheets. A different approach of adding rGO into the freshly prepared porous concrete is required to expose such nanosheets effectively in the flow channels. However, future investigations are required to determine whether the incorporation of rGO would help in reducing the leaching of chemically trapped metal cations from the flow channels of porous concrete.
- The experimental results from this study have shown that the negatively charged ions such as hydroxyl and carbonate species in the porous concrete had chemically trapped the positively charged metal cations from the aqueous solution after passage. This suggests that a scientific understanding of the ion exchanging property of the cementitious matrix in porous concrete is required to determine its potential for filtration of various toxic pollutants from the industrial wastewater.

REFERENCES

- AASHTO T 180** (2015). "Standard Method of Test for Moisture-Density Relations of Soils Using a 4.54-kg (10-lb) Rammer and a 457-mm (18-in.) Drop." *American Association of State Highway and Transportation Officials (AASHTO), USA*, 14 pages.
- AASHTO T 245** (2015). "Standard Method of Test for Resistance to Plastic Flow of Asphalt Mixtures Using Marshall Apparatus." *American Association of State Highway and Transportation Officials (AASHTO), USA*, 8 pages.
- ACI 522R** (2010). "Report on Pervious Concrete." *American Concrete Institute, Farmington Hills, Michigan, USA*, 42 pages.
- Alexander, M., Bertron, A. and De Belie, N.** (2013). *Performance of cement-based materials in aggressive aqueous environments*, Springer.
- Aligizaki, K. K.** (2005). "Pore Structure of cement-Based Materials: Testing, Interpretation and Requirements." *Taylor & Francis Group*, 432.
- ASTM C33** (2011). "Standard Specification for Concrete Aggregates." *American Society for Testing and Materials, USA*, 11 pages.
- ASTM C204** (2011). "Standard Test Methods for Fineness of Hydraulic Cement by Air-Permeability Apparatus." *American Society for Testing and Materials, USA*, 9 pages.
- Asuquo, E., Martin, A., Nzerem, P., Siperstein, F. and Fan, X.** (2017). "Adsorption of Cd(II) and Pb(II) ions from aqueous solutions using mesoporous activated carbon adsorbent: Equilibrium, kinetics and characterisation studies." *Journal of Environmental Chemical Engineering*, 5(1), 679-698.
- Axtell, N. R., Sternberg, S. P. K. and Claussen, K.** (2003). "Lead and nickel removal using *Microspora* and *Lemna minor*." *Bioresource Technology*, 89(1), 41-48.
- Badoe, D. A., Honeycutt, K. R., Crouch, L., Cates, M. A. and Dotson, V. J.** (2003). "Measuring the effective air void content of Portland cement pervious pavements." *Cement, concrete and aggregates*, 25(1), 1-5.

- Bai, Z.-Q., Li, Z.-J., Wang, C.-Z., Yuan, L.-Y., Liu, Z.-R., Zhang, J., Zheng, L.-R., Zhao, Y.-L., Chai, Z.-F. and Shi, W.-Q.** (2014). "Interactions between Th (IV) and graphene oxide: experimental and density functional theoretical investigations." *RSC Advances*, 4(7), 3340-3347.
- Barbhuiya, S., Mukherjee, S. and Nikraz, H.** (2014). "Effects of nano-Al₂O₃ on early-age microstructural properties of cement paste." *Construction and Building Materials*, 52, 189-193.
- Barnett, S. J., Macphee, D. E., Lachowski, E. E. and Crammond, N. J.** (2002). "XRD, EDX and IR analysis of solid solutions between thaumasite and ettringite." *Cement and Concrete Research*, 32(5), 719-730.
- Beauchemin, D.** (2010). "Inductively coupled plasma mass spectrometry." *Analytical chemistry*, 82(12), 4786-4810.
- Beddoe, R. E. and Dorner, H. W.** (2005). "Modelling acid attack on concrete: Part I. The essential mechanisms." *Cement and Concrete Research*, 35(12), 2333-2339.
- Berner, U.** (1988). "Modelling the incongruent dissolution of hydrated cement minerals." *Radiochimica Acta*, 44(2), 387-394.
- Bertron, A., Duchesne, J. and Escadeillas, G.** (2005). "Attack of cement pastes exposed to organic acids in manure." *Cement and Concrete Composites*, 27(9–10), 898-909.
- Brown, R., Line, D. and Hunt, W.** (2011). "LID treatment train: Pervious concrete with subsurface storage in series with bioretention and care with seasonal high water tables." *Journal of Environmental Engineering*, 138(6), 689-697.
- Bury, M. A., Mawby, C. A. and Fisher, D.** (2006). "Making Pervious Concrete Placement Easy Using a Novel Admixture System." *National Ready Mixed Concrete Association*, Silver Spring, Maryland, 55-59.
- Camilleri, J.** (2011). "Characterization of modified calcium-silicate cements exposed to acidic environment." *Materials Characterization*, 62(1), 70-75.

- Carde, C., François, R. and Torrenti, J.-M.** (1996). "Leaching of both calcium hydroxide and CSH from cement paste: Modeling the mechanical behavior." *Cement and concrete research*, 26(8), 1257-1268.
- Chandra, S.** (1988). "Hydrochloric acid attack on cement mortar — An analytical study." *Cement and Concrete Research*, 18(2), 193-203.
- Chandra, V., Park, J., Chun, Y., Lee, J. W., Hwang, I.-C. and Kim, K. S.** (2010). "Water-dispersible magnetite-reduced graphene oxide composites for arsenic removal." *ACS nano*, 4(7), 3979-3986.
- Chandrappa, A. K. and Biligiri, K. P.** (2016). "Pervious concrete as a sustainable pavement material—Research findings and future prospects: A state-of-the-art review." *Construction and Building Materials*, 111, 262-274.
- Chatveera, B. and Lertwattanakul, P.** (2014). "Evaluation of nitric and acetic acid resistance of cement mortars containing high-volume black rice husk ash." *Journal of environmental management*, 133, 365-373.
- Chen, J. J., Thomas, J. J. and Jennings, H. M.** (2006). "Decalcification shrinkage of cement paste." *Cement and concrete research*, 36(5), 801-809.
- Chopra, M., Kakuturu, S., Ballock, C., Spence, J. and Wanielista, M.** (2009). "Effect of rejuvenation methods on the infiltration rates of pervious concrete pavements." *Journal of Hydrologic Engineering*, 15(6), 426-433.
- Chuah, S., Pan, Z., Sanjayan, J. G., Wang, C. M. and Duan, W. H.** (2014). "Nano reinforced cement and concrete composites and new perspective from graphene oxide." *Construction and Building Materials*, 73, 113-124.
- Collins, F., Lambert, J. and Duan, W. H.** (2012). "The influences of admixtures on the dispersion, workability, and strength of carbon nanotube–OPC paste mixtures." *Cement and Concrete Composites*, 34(2), 201-207.
- Ćosić, K., Korat, L., Ducman, V. and Netinger, I.** (2015). "Influence of aggregate type and size on properties of pervious concrete." *Construction and Building Materials*, 78, 69-76.

- DeFloriani, L. and Spagnuolo, M.** (2008). *Shape analysis and structuring*, Springer.
- Ding, C., Cheng, W., Sun, Y. and Wang, X.** (2014). "Determination of chemical affinity of graphene oxide nanosheets with radionuclides investigated by macroscopic, spectroscopic and modeling techniques." *Dalton Transactions*, 43(10), 3888-3896.
- Du, H. and Dai Pang, S.** (2015). "Enhancement of barrier properties of cement mortar with graphene nanoplatelet." *Cement and Concrete Research*, 76, 10-19.
- Duan, P., Yan, C., Zhou, W. and Ren, D.** (2016). "Development of fly ash and iron ore tailing based porous geopolymer for removal of Cu (II) from wastewater." *Ceramics International*.
- Ekolu, S. O., Azene, F. Z. and Diop, S.** (2014). "A concrete reactive barrier for acid mine drainage treatment." *Proceedings of the Institution of Civil Engineers*, 167(7), 373.
- Fan, Y., Zhang, S., Wang, Q. and Shah, S. P.** (2016). "The effects of nano-calcined kaolinite clay on cement mortar exposed to acid deposits." *Construction and Building Materials*, 102, Part 1, 486-495.
- Fernández-Carrasco, L., Torréns-Martín, D. and Martínez-Ramírez, S.** (2012). "Carbonation of ternary building cementing materials." *Cement and Concrete Composites*, 34(10), 1180-1186.
- Gaitero, J., Sáez de Ibarra, Y., Erkizia, E. and Campillo, I.** (2006). "Silica nanoparticle addition to control the calcium-leaching in cement-based materials." *physica status solidi (a)*, 203(6), 1313-1318.
- Gaitero, J., Zhu, W. and Campillo, I.** (2009). "Multi-scale study of calcium leaching in cement pastes with silica nanoparticles." *Nanotechnology in Construction 3*, Springer, 193-198.
- Gaitero, J. J., Campillo, I. and Guerrero, A.** (2008). "Reduction of the calcium leaching rate of cement paste by addition of silica nanoparticles." *Cement and concrete research*, 38(8), 1112-1118.

Galan, I., Glasser, F., Baza, D. and Andrade, C. (2015). "Assessment of the protective effect of carbonation on portlandite crystals." *Cement and Concrete Research*, 74, 68-77.

Geim, A. K. and Novoselov, K. S. (2007). "The rise of graphene." *Nat Mater*, 6(3), 183-191.

Ghafoori, N. and Dutta, S. (1995). "Building and Nonpavement Applications of No-Fines Concrete." *Journal of Materials in Civil Engineering*, 7(4), 286-289.

Gong, K., Pan, Z., Korayem, A. H., Qiu, L., Li, D., Collins, F., Wang, C. M. and Duan, W. H. (2014). "Reinforcing effects of graphene oxide on portland cement paste." *Journal of Materials in Civil Engineering*, 27(2), A4014010.

Gowd, S. and Govil, P. K. (2008). "Distribution of heavy metals in surface water of Ranipet industrial area in Tamil Nadu, India." *Environmental Monitoring and Assessment*, 136(1), 197-207.

Groves, G. W., Rodway, D. I. and Richardson, I. G. (1990). "The carbonation of hardened cement pastes." *Advances in Cement Research*, 3(11), 117-125.

Gutberlet, T., Hilbig, H. and Beddoe, R. E. (2015). "Acid attack on hydrated cement — Effect of mineral acids on the degradation process." *Cement and Concrete Research*, 74, 35-43.

Haselbach, L., Poor, C. and Tilson, J. (2014). "Dissolved zinc and copper retention from stormwater runoff in ordinary portland cement pervious concrete." *Construction and Building Materials*, 53, 652-657.

Haselbach, L. M. (2009). "Potential for clay clogging of pervious concrete under extreme conditions." *Journal of Hydrologic Engineering*, 15(1), 67-69.

Horszczaruk, E., Mijowska, E., Kalenczuk, R. J., Aleksandrak, M. and Mijowska, S. (2015). "Nanocomposite of cement/graphene oxide—Impact on hydration kinetics and Young's modulus." *Construction and Building Materials*, 78, 234-242.

Hua, M., Zhang, S., Pan, B., Zhang, W., Lv, L. and Zhang, Q. (2012). "Heavy metal removal from water/wastewater by nanosized metal oxides: a review." *Journal of Hazardous Materials*, 211, 317-331.

Huang, B., Wu, H., Shu, X. and Burdette, E. G. (2010). "Laboratory evaluation of permeability and strength of polymer-modified pervious concrete." *Construction and Building Materials*, 24(5), 818-823.

Huang, J., Valeo, C., He, J. and Chu, A. (2016). "Three types of permeable pavements in cold climates: hydraulic and environmental performance." *Journal of Environmental Engineering*, 142(6), 04016025.

Hummers, W. S. and Offeman, R. E. (1958). "Preparation of Graphitic Oxide." *Journal of the American Chemical Society*, 80(6), 1339-1339.

Hwang, H.-M., Fiala, M. J., Park, D. and Wade, T. L. (2016). "Review of pollutants in urban road dust and stormwater runoff: part 1. Heavy metals released from vehicles." *International Journal of Urban Sciences*, 20(3), 334-360.

Hyvert, N., Sellier, A., Duprat, F., Rougeau, P. and Francisco, P. (2010). "Dependency of C–S–H carbonation rate on CO₂ pressure to explain transition from accelerated tests to natural carbonation." *Cement and Concrete Research*, 40(11), 1582-1589.

IS 383 (1970). "Specification for Coarse and Fine Aggregates from Natural Sources for Concrete." *Bureau of Indian Standards, Manak Bhavan, New Delhi 110002*, 19 pages.

IS 516 (1959). "Methods of tests for strength of concrete." *Bureau of Indian Standards, Manak Bhavan, New Delhi 110002, India*, 27 pages.

IS 2386-3 (1963). "Methods of Test for Aggregates for Concrete." *Bureau of Indian Standards, Manak Bhavan, New Delhi 110002*, 17 pages.

IS 10500 (2012). "Drinking Water Specification." *Bureau of Indian Standards, Manak Bhavan, 9 Bahadur Shah Zafar Marg, New Delhi 110002*, 18 pages.

IS 12269 (2013). "Ordinary Portland Cement, 53 Grade - Specification." *Bureau of Indian Standards, Manak Bhavan, New Delhi 110002*, 10 pages.

Jain, J. and Neithalath, N. (2009). "Analysis of calcium leaching behavior of plain and modified cement pastes in pure water." *Cement and Concrete Composites*, 31(3), 176-185.

Jallad, K. N., Santhanam, M. and Cohen, M. D. (2003). "Stability and reactivity of thaumasite at different pH levels." *Cement and Concrete Research*, 33(3), 433-437.

Jiang, W., Sha, A., Xiao, J., Li, Y. and Huang, Y. (2015). "Experimental study on filtration effect and mechanism of pavement runoff in permeable asphalt pavement." *Construction and Building Materials*, 100, 102-110.

Kadirvelu, K., Faur-Brasquet, C. and Cloirec, P. L. (2000). "Removal of Cu (II), Pb (II), and Ni (II) by adsorption onto activated carbon cloths." *Langmuir*, 16(22), 8404-8409.

Kapdan, I. K. and Kargi, F. (2002). "Simultaneous biodegradation and adsorption of textile dyestuff in an activated sludge unit." *Process Biochemistry*, 37(9), 973-981.

Kawashima, S., Hou, P., Corr, D. J. and Shah, S. P. (2013). "Modification of cement-based materials with nanoparticles." *Cement and Concrete Composites*, 36, 8-15.

Kayhanian, M., Anderson, D., Harvey, J. T., Jones, D. and Muhunthan, B. (2012). "Permeability measurement and scan imaging to assess clogging of pervious concrete pavements in parking lots." *Journal of Environmental management*, 95(1), 114-123.

Kazi, T. G., Jalbani, N., Kazi, N., Jamali, M. K., Arain, M. B., Afridi, H. I., Kandhro, A. and Pirzado, Z. (2008). "Evaluation of Toxic Metals in Blood and Urine Samples of Chronic Renal Failure Patients, before and after Dialysis." *Renal Failure*, 30(7), 737-745.

Kemp, K. C., Seema, H., Saleh, M., Le, N. H., Mahesh, K., Chandra, V. and Kim, K. S. (2013). "Environmental applications using graphene composites: water remediation and gas adsorption." *Nanoscale*, 5(8), 3149-3171.

Ketcham, R. A. and Carlson, W. D. (2001). "Acquisition, optimization and interpretation of X-ray computed tomographic imagery: applications to the geosciences." *Computers & Geosciences*, 27(4), 381-400.

Kim, S. A., Kamala-Kannan, S., Lee, K.-J., Park, Y.-J., Shea, P. J., Lee, W.-H., Kim, H.-M. and Oh, B.-T. (2013). "Removal of Pb (II) from aqueous solution by a zeolite–nanoscale zero-valent iron composite." *Chemical Engineering Journal*, 217, 54-60.

Konios, D., Stylianakis, M. M., Stratakis, E. and Kymakis, E. (2014). "Dispersion behaviour of graphene oxide and reduced graphene oxide." *Journal of colloid and interface science*, 430, 108-112.

Konsta-Gdoutos, M. S., Metaxa, Z. S. and Shah, S. P. (2010). "Highly dispersed carbon nanotube reinforced cement based materials." *Cement and Concrete Research*, 40(7), 1052-1059.

Kuang, X., Kim, J.-Y., Gnecco, I., Raje, S., Garofalo, G. and Sansalone, J. (2007). "Particle separation and hydrologic control by cementitious permeable pavement." *Transportation Research Record: Journal of the Transportation Research Board*(2025), 111-117.

Kuang, X., Sansalone, J., Ying, G. and Ranieri, V. (2011). "Pore-structure models of hydraulic conductivity for permeable pavement." *Journal of Hydrology*, 399(3), 148-157.

Kuila, T., Bose, S., Mishra, A. K., Khanra, P., Kim, N. H. and Lee, J. H. (2012). "Chemical functionalization of graphene and its applications." *Progress in Materials Science*, 57(7), 1061-1105.

Kul, A. R. and Koyuncu, H. (2010). "Adsorption of Pb (II) ions from aqueous solution by native and activated bentonite: kinetic, equilibrium and thermodynamic study." *Journal of Hazardous materials*, 179(1), 332-339.

Lee, M.-G., Tia, M., Chuang, S.-H., Huang, Y. and Chiang, C.-L. (2013). "Pollution and purification study of the pervious concrete pavement material." *Journal of Materials in Civil Engineering*, 26(8), 04014035.

Li, B., Cao, H. and Yin, G. (2011). "Mg (OH) 2@ reduced graphene oxide composite for removal of dyes from water." *Journal of Materials Chemistry*, 21(36), 13765-13768.

Li, D., Muller, M. B., Gilje, S., Kaner, R. B. and Wallace, G. G. (2008). "Processable aqueous dispersions of graphene nanosheets." *Nat Nano*, 3(2), 101-105.

Li, X., Wei, W., Qin, H. and Hu, Y. H. (2015). "Co-effects of graphene oxide sheets and single wall carbon nanotubes on mechanical properties of cement." *Journal of Physics and Chemistry of Solids*, 85, 39-43.

- Lian, C. and Zhuge, Y.** (2010). "Optimum mix design of enhanced permeable concrete—an experimental investigation." *Construction and Building Materials*, 24(12), 2664-2671.
- Liu, S., Zeng, T. H., Hofmann, M., Burcombe, E., Wei, J., Jiang, R., Kong, J. and Chen, Y.** (2011). "Antibacterial activity of graphite, graphite oxide, graphene oxide, and reduced graphene oxide: membrane and oxidative stress." *Acs Nano*, 5(9), 6971-6980.
- Liu, X., Zhang, H., Ma, Y., Wu, X., Meng, L., Guo, Y., Yu, G. and Liu, Y.** (2013). "Graphene-coated silica as a highly efficient sorbent for residual organophosphorus pesticides in water." *Journal of Materials Chemistry A*, 1(5), 1875-1884.
- Lv, S., Liu, J., Sun, T., Ma, Y. and Zhou, Q.** (2014). "Effect of GO nanosheets on shapes of cement hydration crystals and their formation process." *Construction and Building Materials*, 64, 231-239.
- Lv, S., Ma, Y., Qiu, C., Sun, T., Liu, J. and Zhou, Q.** (2013). "Effect of graphene oxide nanosheets of microstructure and mechanical properties of cement composites." *Construction and Building Materials*, 49(0), 121-127.
- Mahboub, K., Canler, J., Rathbone, R., Robl, T. and Davis, B.** (2009). "Pervious Concrete: Compaction and Aggregate Gradation." *ACI Materials Journal*, 106(6).
- Mahish, P. K., Tiwari, K. and Jadhav, S.** (2015). "Biodiversity of Fungi from Lead Contaminated Industrial Waste Water and Tolerance of Lead Metal Ion by Dominant Fungi." *Research Journal of Environmental Sciences*, 9(4), 159.
- Mainguy, M. and Ulm, F.-J.** (2001). "Coupled diffusion-dissolution around a fracture channel: the solute congestion phenomenon." *Transport in porous media*, 45(3), 479-495.
- Majersky, G. M.** (2008). *Filtration and life span analysis of a pervious concrete filter*, ProQuest.
- Makar, J. M. and Chan, G. W.** (2009). "Growth of Cement Hydration Products on Single-Walled Carbon Nanotubes." *Journal of the American Ceramic Society*, 92(6), 1303-1310.
- Malhotra, V. M.** (1976). "No-Fines Concrete - Its Properties and Applications*." *Journal Proceedings*, 73(11).

Maliyekkal, S. M., Sreeprasad, T., Krishnan, D., Kouser, S., Mishra, A. K., Waghmare, U. V. and Pradeep, T. (2013). "Graphene: a reusable substrate for unprecedented adsorption of pesticides." *Small*, 9(2), 273-283.

Mallikarjunachari, G. (2016). "Interface Characterization of Polymer Thin Films on Polymer Substrates and its Applications." Doctor of Philosophy, Indian Institute of Technology Madras, Chennai.

Manahiloh, K. N., Muhunthan, B., Kayhanian, M. and Gebremariam, S. Y. (2012). "X-ray computed tomography and nondestructive evaluation of clogging in porous concrete field samples." *Journal of Materials in Civil Engineering*, 24(8), 1103-1109.

Maniquiz-Redillas, M. C. and Kim, L.-H. (2016). "Evaluation of the capability of low-impact development practices for the removal of heavy metal from urban stormwater runoff." *Environmental technology*, 1-8.

Marolf, A., Neithalath, N., Sell, E., Wegner, K., Weiss, J. and Olek, J. (2004). "Influence of aggregate size and gradation on acoustic absorption of enhanced porosity concrete." *ACI Materials Journal-American Concrete Institute*, 101(1), 82-91.

Mehta, P. K. and Aïtcin, P.-C. (1990). "Principles underlying production of high-performance concrete." *Cement, concrete and aggregates*, 12(2), 70-78.

Meininger, R. C. (1988). "No-fines pervious concrete for paving." *Concrete International*, 10(8), 20-27.

Merkus, H. G. (2009). *Particle Size Measurements: Fundamentals, Practice, Quality*, Springer Netherlands.

Metaxa, Z. S., Konsta-Gdoutos, M. S. and Shah, S. P. (2013). "Carbon nanofiber cementitious composites: Effect of debulking procedure on dispersion and reinforcing efficiency." *Cement and Concrete Composites*, 36(0), 25-32.

Mohammed, A., Sanjayan, J., Duan, W. and Nazari, A. (2015). "Incorporating graphene oxide in cement composites: A study of transport properties." *Construction and Building Materials*, 84, 341-347.

- Mohammed, A., Sanjayan, J., Duan, W. and Nazari, A.** (2016). "Graphene Oxide Impact on Hardened Cement Expressed in Enhanced Freeze–Thaw Resistance." *Journal of Materials in Civil Engineering*, 04016072.
- Mondal, P., Shah, S., Marks, L. and Gaitero, J.** (2010). "Comparative study of the effects of microsilica and nanosilica in concrete." *Transportation research record: journal of the transportation research board*(2141), 6-9.
- Morales-Florez, V., Findling, N. and Brunet, F.** (2012). "Changes on the nanostructure of cementitious calcium silicate hydrates (C–S–H) induced by aqueous carbonation." *Journal of Materials Science*, 47(2), 764-771.
- Moranville, M., Kamali, S. and Guillon, E.** (2004). "Physicochemical equilibria of cement-based materials in aggressive environments—experiment and modeling." *Cement and Concrete Research*, 34(9), 1569-1578.
- Nagappa, B. and Chandrappa, G.** (2007). "Mesoporous nanocrystalline magnesium oxide for environmental remediation." *Microporous and Mesoporous Materials*, 106(1), 212-218.
- Nambiar, E. K. K. and Ramamurthy, K.** (2007). "Air-void characterisation of foam concrete." *Cement and Concrete Research*, 37(2), 221-230.
- Neithalath, N., Sumanasooriya, M. S. and Deo, O.** (2010). "Characterizing pore volume, sizes, and connectivity in pervious concretes for permeability prediction." *Materials characterization*, 61(8), 802-813.
- Neithalath, N., Weiss, J. and Olek, J.** (2006). "Characterizing enhanced porosity concrete using electrical impedance to predict acoustic and hydraulic performance." *Cement and Concrete Research*, 36(11), 2074-2085.
- Nguyen, V., Colina, H., Torrenti, J. M., Boulay, C. and Nedjar, B.** (2007). "Chemo-mechanical coupling behaviour of leached concrete: Part I: Experimental results." *Nuclear Engineering and Design*, 237(20), 2083-2089.
- Nishikawa, T., Suzuki, K., Ito, S., Sato, K. and Takebe, T.** (1992). "Decomposition of synthesized ettringite by carbonation." *Cement and Concrete Research*, 22(1), 6-14.

- Obla, K. H. and Sabnis, G.** (2009). "Pervious concrete for sustainable development."
- Olek, J., Weiss, W. J., Neithalath, N., Marolf, A., Sell, E. and Thornton, W.** (2003). "Development of quiet and durable porous Portland cement concrete paving materials."
- Özdemir, M., Durmuş, Ö., Şahin, Ö. and Saka, C.** (2015). "Removal of methylene blue, methyl violet, rhodamine B, alizarin red, and bromocresol green dyes from aqueous solutions on activated cotton stalks." *Desalination and Water Treatment*, 1-11.
- Pacheco-Torgal, F. and Jalali, S.** (2011). "Nanotechnology: advantages and drawbacks in the field of construction and building materials." *Construction and Building Materials*, 25(2), 582-590.
- Pan, N., Deng, J., Guan, D., Jin, Y. and Xia, C.** (2013). "Adsorption characteristics of Th (IV) ions on reduced graphene oxide from aqueous solutions." *Applied Surface Science*, 287, 478-483.
- Pan, Z., He, L., Qiu, L., Korayem, A. H., Li, G., Zhu, J. W., Collins, F., Li, D., Duan, W. H. and Wang, M. C.** (2015). "Mechanical properties and microstructure of a graphene oxide–cement composite." *Cement and Concrete Composites*, 58, 140-147.
- Pani, B.** (2007). *Textbook of environmental chemistry*, IK International Pvt Ltd.
- Park, S.-B. and Tia, M.** (2004). "An experimental study on the water-purification properties of porous concrete." *Cement and Concrete Research*, 34(2), 177-184.
- Pavlík, V.** (1994). "Corrosion of hardened cement paste by acetic and nitric acids part I: Calculation of corrosion depth." *Cement and Concrete Research*, 24(3), 551-562.
- Pavlík, V.** (1994). "Corrosion of hardened cement paste by acetic and nitric acids part II: Formation and chemical composition of the corrosion products layer." *Cement and Concrete Research*, 24(8), 1495-1508.
- Pavlík, V.** (1996). "Corrosion of hardened cement paste by acetic and nitric acids Part III: Influence of water/cement ratio." *Cement and Concrete Research*, 26(3), 475-490.

Peyvandi, A., Soroushian, P., Balachandra, A. M. and Sobolev, K. (2013). "Enhancement of the durability characteristics of concrete nanocomposite pipes with modified graphite nanoplatelets." *Construction and Building Materials*, 47, 111-117.

Quercia, G., Hüskén, G. and Brouwers, H. J. H. (2012). "Water demand of amorphous nano silica and its impact on the workability of cement paste." *Cement and Concrete Research*, 42(2), 344-357.

Ramesha, G., Kumara, A. V., Muralidhara, H. and Sampath, S. (2011). "Graphene and graphene oxide as effective adsorbents toward anionic and cationic dyes." *Journal of colloid and interface science*, 361(1), 270-277.

Revertgat, E., Richet, C. and Gégout, P. (1992). "Effect of pH on the durability of cement pastes." *Cement and concrete research*, 22(2), 259-272.

Robati, D., Mirza, B., Rajabi, M., Moradi, O., Tyagi, I., Agarwal, S. and Gupta, V. (2016). "Removal of hazardous dyes-BR 12 and methyl orange using graphene oxide as an adsorbent from aqueous phase." *Chemical Engineering Journal*, 284, 687-697.

Romanchuk, A. Y., Slesarev, A. S., Kalmykov, S. N., Kosynkin, D. V. and Tour, J. M. (2013). "Graphene oxide for effective radionuclide removal." *Physical Chemistry Chemical Physics*, 15(7), 2321-2327.

Said, A. M., Zeidan, M. S., Bassuoni, M. and Tian, Y. (2012). "Properties of concrete incorporating nano-silica." *Construction and Building Materials*, 36, 838-844.

Sanchez, F. and Sobolev, K. (2010). "Nanotechnology in concrete—a review." *Construction and building materials*, 24(11), 2060-2071.

Sansalone, J., Kuang, X. and Ranieri, V. (2008). "Permeable pavement as a hydraulic and filtration interface for urban drainage." *Journal of irrigation and drainage engineering*, 134(5), 666-674.

Sansalone, J., Kuang, X., Ying, G. and Ranieri, V. (2012). "Filtration and clogging of permeable pavement loaded by urban drainage." *Water research*, 46(20), 6763-6774.

Šauman, Z. (1971). "Carbonization of porous concrete and its main binding components." *Cement and Concrete Research*, 1(6), 645-662.

Schwotzer, M., Scherer, T. and Gerdes, A. (2015). "Immediate impact on the rim zone of cement based materials due to chemical attack: A focused ion beam study." *Materials Characterization*, 99, 77-83.

Sen Gupta, S., Manoj Siva, V., Krishnan, S., Sreeprasad, T. S., Singh, P. K., Pradeep, T. and Das, S. K. (2011). "Thermal conductivity enhancement of nanofluids containing graphene nanosheets." *Journal of Applied Physics*, 110(8), 084302.

Sevelsted, T. F. and Skibsted, J. (2015). "Carbonation of C–S–H and C–A–S–H samples studied by ¹³C, ²⁷Al and ²⁹Si MAS NMR spectroscopy." *Cement and Concrete Research*, 71, 56-65.

Shabalala, A. N., Ekolu, S. O., Diop, S. and Solomon, F. (2017). "Pervious concrete reactive barrier for removal of heavy metals from acid mine drainage– column study." *Journal of Hazardous Materials*, 323, 641-653.

Sharma, S. and Kothiyal, N. (2016). "Comparative effects of pristine and ball-milled graphene oxide on physico-chemical characteristics of cement mortar nanocomposites." *Construction and Building Materials*, 115, 256-268.

Sharma, S. K. (2015). *Green Chemistry for dyes removal from waste water: research trends and applications*, John Wiley & Sons.

Shi, C. and Stegemann, J. (2000). "Acid corrosion resistance of different cementing materials." *Cement and concrete research*, 30(5), 803-808.

Shirke, N. A. and Shuler, S. (2009). "Cleaning porous pavements using a reverse flush process." *Journal of transportation engineering*, 135(11), 832-838.

Shu, X., Huang, B., Wu, H., Dong, Q. and Burdette, E. G. (2011). "Performance comparison of laboratory and field produced pervious concrete mixtures." *Construction and Building Materials*, 25(8), 3187-3192.

- Singh, L. P., Karade, S. R., Bhattacharyya, S. K., Yousuf, M. M. and Ahalawat, S.** (2013). "Beneficial role of nanosilica in cement based materials – A review." *Construction and Building Materials*, 47, 1069-1077.
- Singh, R., Gautam, N., Mishra, A. and Gupta, R.** (2011). "Heavy metals and living systems: An overview." *Indian journal of pharmacology*, 43(3), 246.
- Singh, V., Joung, D., Zhai, L., Das, S., Khondaker, S. I. and Seal, S.** (2011). "Graphene based materials: Past, present and future." *Progress in Materials Science*, 56(8), 1178-1271.
- Solpuker, U., Sheets, J., Kim, Y. and Schwartz, F.** (2014). "Leaching potential of pervious concrete and immobilization of Cu, Pb and Zn using pervious concrete." *Journal of contaminant hydrology*, 161, 35-48.
- Sonebi, M. and Bassuoni, M.** (2013). "Investigating the effect of mixture design parameters on pervious concrete by statistical modelling." *Construction and Building Materials*, 38, 147-154.
- Sreeprasad, T., Maliyekkal, S. M., Lisha, K. and Pradeep, T.** (2011). "Reduced graphene oxide–metal/metal oxide composites: facile synthesis and application in water purification." *Journal of hazardous materials*, 186(1), 921-931.
- Sreeprasad, T. and Pradeep, T.** (2012). "Graphene for environmental and biological applications." *International Journal of Modern Physics B*, 26(21), 1242001.
- Sreeprasad, T. S., Gupta, S. S., Maliyekkal, S. M. and Pradeep, T.** (2013). "Immobilized graphene-based composite from asphalt: Facile synthesis and application in water purification." *Journal of hazardous materials*, 246, 213-220.
- Status of Trace and Toxic Metals in Indian Rivers** (2014). "Report by Central Water Commission, Ministry of Water Resources, Government of India." 207 pages.
- Stumm, W. and Morgan, J. J.** (2012). *Aquatic chemistry: chemical equilibria and rates in natural waters*, John Wiley & Sons.

Suleiman, M., Kevern, J., Schaefer, V. and Wang, K. "Effect of compaction energy on pervious concrete properties." *Proc., Submitted to Concrete Technology Forum-Focus on Pervious Concrete, National Ready Mix Concrete Association, Nashville, TN, May, 23-25.*

Sumanasooriya, M. S., Deo, O. and Neithalath, N. (2012). "Particle packing-based material design methodology for pervious concretes." *ACI Materials Journal*, 109(2), 205-214.

Sumanasooriya, M. S. and Neithalath, N. (2009). "Stereology-and Morphology-Based Pore Structure Descriptors of Enhanced Porosity (Pervious) Concretes." *ACI Materials Journal*, 106(5).

Sumanasooriya, M. S. and Neithalath, N. (2011). "Pore structure features of pervious concretes proportioned for desired porosities and their performance prediction." *Cement and Concrete Composites*, 33(8), 778-787.

Tan, L., Wang, J., Liu, Q., Sun, Y., Jing, X., Liu, L., Liu, J. and Song, D. (2015). "The synthesis of a manganese dioxide–iron oxide–graphene magnetic nanocomposite for enhanced uranium (VI) removal." *New Journal of Chemistry*, 39(2), 868-876.

Tennis, P. D., Leming, M. L. and Akers, D. J. (2004). *Pervious concrete pavements*, Portland Cement Association Skokie, IL.

Thiery, M., Villain, G., Dangla, P. and Platret, G. (2007). "Investigation of the carbonation front shape on cementitious materials: Effects of the chemical kinetics." *Cement and Concrete Research*, 37(7), 1047-1058.

Tyson, B. M., Abu Al-Rub, R. K., Yazdanbakhsh, A. and Grasley, Z. (2011). "Carbon nanotubes and carbon nanofibers for enhancing the mechanical properties of nanocomposite cementitious materials." *Journal of Materials in Civil Engineering*, 23(7), 1028-1035.

Velez, K., Maximilien, S., Damidot, D., Fantozzi, G. and Sorrentino, F. (2001). "Determination by nanoindentation of elastic modulus and hardness of pure constituents of Portland cement clinker." *Cement and Concrete Research*, 31(4), 555-561.

Villain, G., Thiery, M. and Platret, G. (2007). "Measurement methods of carbonation profiles in concrete: thermogravimetry, chemical analysis and gammadensimetry." *Cement and Concrete Research*, 37(8), 1182-1192.

Wang, M., Wang, R., Yao, H., Farhan, S., Zheng, S. and Du, C. (2016). "Study on the three dimensional mechanism of graphene oxide nanosheets modified cement." *Construction and Building Materials*, 126, 730-739.

Wei, D. and Liu, Y. (2010). "Controllable synthesis of graphene and its applications." *Advanced Materials*, 22(30), 3225-3241.

Winston, R. J., Al-Rubaei, A. M., Blecken, G. T., Viklander, M. and Hunt, W. F. (2016). "Maintenance measures for preservation and recovery of permeable pavement surface infiltration rate—The effects of street sweeping, vacuum cleaning, high pressure washing, and milling." *Journal of environmental management*, 169, 132-144.

Yang, J. and Jiang, G. (2003). "Experimental study on properties of pervious concrete pavement materials." *Cement and Concrete Research*, 33(3), 381-386.

Yazdanbakhsh, A., Grasley, Z., Tyson, B. and Abu Al-Rub, R. (2010). "Distribution of carbon nanofibers and nanotubes in cementitious composites." *Transportation Research Record: Journal of the Transportation Research Board*(2142), 89-95.

Zhang, K., Dwivedi, V., Chi, C. and Wu, J. (2010). "Graphene oxide/ferric hydroxide composites for efficient arsenate removal from drinking water." *Journal of hazardous materials*, 182(1), 162-168.

Zhao, G., Li, J., Ren, X., Chen, C. and Wang, X. (2011). "Few-layered graphene oxide nanosheets as superior sorbents for heavy metal ion pollution management." *Environmental Science and Technology*, 45(24), 10454-10462.

Zhao, G., Ren, X., Gao, X., Tan, X., Li, J., Chen, C., Huang, Y. and Wang, X. (2011). "Removal of Pb (II) ions from aqueous solutions on few-layered graphene oxide nanosheets." *Dalton Transactions*, 40(41), 10945-10952.

Zhong, R., Xu, M., Netto, R. V. and Wille, K. (2016). "Influence of pore tortuosity on hydraulic conductivity of pervious concrete: Characterization and modeling." *Construction and Building Materials*, 125, 1158-1168.

Zhu, J., Wei, S., Gu, H., Rapole, S. B., Wang, Q., Luo, Z., Haldolaarachchige, N., Young, D. P. and Guo, Z. (2011). "One-pot synthesis of magnetic graphene nanocomposites

decorated with core@ double-shell nanoparticles for fast chromium removal." *Environmental science & technology*, 46(2), 977-985.

Zivica, V. r. and Bajza, A. (2001). "Acidic attack of cement based materials — a review.: Part 1. Principle of acidic attack." *Construction and Building Materials*, 15(8), 331-340.

Zong, P., Wang, S., Zhao, Y., Wang, H., Pan, H. and He, C. (2013). "Synthesis and application of magnetic graphene/iron oxides composite for the removal of U (VI) from aqueous solutions." *Chemical engineering journal*, 220, 45-52.

LIST OF PAPERS ON THE BASIS OF THIS THESIS

JOURNALS

1. **Murugan M.**, Manu Santhanam, Soujit Sen Gupta, T. Pradeep and Surendra P. Shah, “Influence of 2D rGO nanosheets on the properties of OPC paste”, *Cement and Concrete Composites*, 70: 48-59, March 2016.
2. **Murugan M.** and Manu Santhanam, “Effect of reduced graphene oxide, alumina and silica nanoparticles on the deterioration characteristics of OPC paste exposed to acidic environment”, *Cement and Concrete Composites* [Submitted]
3. **Murugan M.**, Manu Santhanam and Mathava Kumar, “Pb removal in pervious concrete system: Effects of carbonation and hydraulic retention time”, *Construction and Building Materials* [Submitted]
4. **Murugan M.**, Manu Santhanam, Krishnan C.R., Murali Rangarajan, Mathava Kumar, Anil Kumar Avula and Pradeep Thalappil, “Binding of Pb, Cu, Zn and Cd by the porous concrete modified using reduced graphene oxide”, *Journal of Hazardous Materials*, XX:XX [in preparation]

PRESENTATION IN INTERNATIONAL CONFERENCES / SEMINARS

1. **Murugan M. and Manu Santhanam**, “Influence of rGO, n-Al₂O₃ and n-SiO₂ nanomaterials on the microstructure of OPC paste immersed in 0.5 M HNO₃ solution”, Proceedings of the 4th International Conference on Sustainable Construction Materials and Technologies (SCMT4), Las Vegas, Nevada, USA, August 7-11, 2016.
2. **Murugan M., Manu Santhanam, Mallikarjunachari G. and Pijush Ghosh**, “Study on the calcium leaching of OPC paste modified using nanomaterials”, Advanced Materials for Sustainable Infrastructure Development – Gordon Research Conference (GRC), Hong Kong, China, July 31 – August 5, 2016.
3. **Ramaswamy K.P., Murugan M. and Manu Santhanam**, “Characterization of cement

paste modified with nanomaterials using X-ray computed microtomography”, Proceedings of the 3rd International Conference on Modeling and Simulation in Civil Engineering (ICMSC 2015), Kollam, Kerala, India, December 9-11, 2015.

4. **Murugan M. and Manu Santhanam**, “Extracting the pore structure features of cement based materials using 3D X-ray computed tomography”, Proceedings of the 25th National Seminar and Exhibition on Non-Destructive Evaluation, Hyderabad, India, November 26-28, 2015.
5. **Murugan M. and Manu Santhanam**, “Characterizing the influence of nanomaterials on the pore refinement of OPC paste”, 4th Annual Seminar on Bringing the Nanoworld Together (BTNT), Chennai, India, November 3-4, 2015.
6. **Murugan M. and Manu Santhanam**, “Investigation on the water filtration characteristics of enhanced porosity concrete”, 2nd International Conference on Emerging Technologies for Clean Water, Chennai, India, October 23-24, 2014.

DOCTORAL COMMITTEE

CHAIR PERSON

Dr. K. Ramamurthy
Professor and Head
Department of Civil Engineering

GUIDE

Dr. Manu Santhanam
Professor
Department of Civil Engineering

MEMBERS

Dr. Devdas Menon
Professor
Department of Civil Engineering

Dr. Srinivasan Chandrasekaran
Professor
Department of Ocean Engineering

Dr. Pijush Ghosh
Associate Professor
Department of Applied Mechanics

Dr. Radhakrishna G. Pillai
Assistant Professor
Department of Civil Engineering

CURRICULUM VITAE

Name : Murugan M.

Date of Birth : 01 October 1988

Education qualification

2007 : **Diploma**
Institution : Central Polytechnic College, Tamil Nadu, India
Department : State Board of Technical Education and Training,
Department of Technical Education, India
Specialization : Civil Engineering

2010 : **Bachelor of Engineering (B.E.)**
Institution : Misrimal Navajee Munoth Jain Engineering College
University : Anna University, Chennai, Tamil Nadu, India
Specialization : Civil Engineering

2012 : **Master of Engineering (M.E.)**
Institution : College of Engineering, Guindy
University : Anna University, Chennai, Tamil Nadu, India
Specialization : Construction Engineering and Management

2017 : **Doctor of Philosophy (Ph.D.)**
Institution : Indian Institute of Technology Madras,
Chennai, Tamil Nadu, India
Specialization : Building Technology and Construction Management
Registration date : 16 July 2012